

University of Alberta

Microstructural investigation of D2 tool steel during rapid solidification

by

Pooya Delshad Khatibi

A thesis submitted to the Faculty of Graduate Studies and Research
in partial fulfillment of the requirements for the degree of

Doctor of Philosophy
in
Materials Engineering

Chemical and Materials Engineering

©Pooya Delshad Khatibi

Spring 2014

Edmonton, Alberta

Permission is hereby granted to the University of Alberta Libraries to reproduce single copies of this thesis and to lend or sell such copies for private, scholarly or scientific research purposes only. Where the thesis is converted to, or otherwise made available in digital form, the University of Alberta will advise potential users of the thesis of these terms.

The author reserves all other publication and other rights in association with the copyright in the thesis and, except as herein before provided, neither the thesis nor any substantial portion thereof may be printed or otherwise reproduced in any material form whatsoever without the author's prior written permission.

Abstract

Solidification is considered as a key processing step in developing the microstructure of most metallic materials. It is, therefore, important that the solidification process can be designed and controlled in such a way so as to obtain the desirable properties in the final product. Rapid solidification refers to the system's high undercooling and high cooling rate, which can yield a microstructure with unique chemical composition and mechanical properties. In order to control the rapidly solidified microstructure and achieve the decent mechanical properties, an understanding of the effects of some important processing parameters such as undercooling and cooling rate on the microstructure need to be considered. An area of interest in rapid solidification application is high-chromium, high-carbon tool steels which experience considerable segregation of alloying elements during their solidification in a casting process.

In this dissertation, the effect of rapid solidification (undercooling and cooling rate) of D2 tool steel on the microstructure and carbide precipitation during annealing was explored. In order to produce rapidly solidified particles and spray deposits of D2 tool steel, impulse atomization technique was used. A methodology is described to estimate the eutectic and primary phase undercooling of solidifying droplets. The estimate of primary phase undercooling was confirmed using an online measurement device that measured the radiation energy of the droplets (this device is

termed DPV-2000). It was found that DPV-2000 can provide an estimate of the droplet temperature post recalescence.

The results showed that in D2 tool steel, the primary phase and eutectic undercooling, as well as cooling rate, have a significant effect on the development of the microstructure and constituent phase fractions. With increasing primary phase and eutectic undercooling and higher cooling rate, the amount of supersaturation of alloying element in metastable retained austenite phase also increases. Large amounts of supersaturation of alloying elements in powder particles result in the formation of fine carbide precipitates during post-annealing of particles. Microstructural investigation of spray deposits showed similar amounts of eutectic fraction and, as a result, similar eutectic undercooling in the spray deposits, as compared with individual single powder particles.

In the case of powders, the optimum hardness after heat treatment is achieved at different temperatures for constant periods of time. Higher supersaturation of austenite results in obtaining secondary hardness at higher annealing temperature. An intermediate level of supersaturation of about 25 yielded the best hardness after heat treating at 550°C for two hours. Supersaturation is defined as supersaturated concentration of alloying elements divided by equilibrium concentration of alloying elements in the austenite.

D2 steel ingots generated using spray deposition have high eutectic undercooling and, as a result, high supersaturation of alloying elements.

This can yield near net shape D2 tool steel components with good mechanical properties (specifically hardness). The data developed in this work would assist in better understanding and development of near net shape D2 steel spray deposit products with good mechanical properties.

Acknowledgements

I would like to offer my sincere gratitude and thanks to my supervisor, Professor Hani Henein, who has supported me throughout my thesis. His advice on both research as well as on my career has been priceless.

I would like to thank Dr. Andre Phillion from University of British Columbia, who was always willing to help and give his best suggestions.

I would like to thank Dr. Dimitry Sediako from National Research Council Canada (NRC) for conducting neutron diffraction analysis and Chris Schade from Hoeganaes Company for providing water atomized powders.

Thanks to Bob Smith and Clark Bicknell (machine shop) and Walter Bodez, Les Dean and Richard Cooper (instrument shop) for their technical support.

I would like to extend my appreciation to my colleague, Dr. Arash Ilbagi for all his help giving me new ideas to achieve my project goals.

Most importantly, none of this would have been possible without the love and patience of my family. My mother, Mahrokh Saedi, and my father, Jalal Delshad Khatibi have been a constant source of love, concern, support and strength all these years. I also want to thank my brother, Payam Delshad Khatibi, for his help and support.

I owe my heartfelt thanks toward my wife, Mona Saedi, whose infallible love and support has always been my strength. Her patience and sacrifice will remain my inspiration throughout my life.

Funding from Natural Sciences and Engineering Research Council (NSERC) of Canada and Canadian Space Agency (CSA) is greatly appreciated.

Table of Contents

1. INTRODUCTION	1
1.1. THESIS OUTLINE	5
2. LITERATURE REVIEW	7
2.1. TOOL STEELS	7
2.1.1. Manufacturing of tool steels	8
2.1.2. Categories of tool steels	9
2.1.3. Carbides in tool steels	11
2.1.4. Phase diagram and microstructure	13
2.2. RAPID SOLIDIFICATION	17
2.2.1. Nucleation	17
2.2.2. Growth	20
2.2.3. Undercooling	21
2.2.4. Atomization	25
2.2.5. Microstructure and properties	26
2.2.6. Precipitation in the solid state	28
2.3. RAPID SOLIDIFICATION TECHNIQUES	37
2.3.1. Gas atomization (GA)	38
2.3.2. Water atomization (WA)	40
2.3.3. Impulse atomization (IA)	41
2.3.4. Spray deposition	44
2.4. MODELING OF HEAT LOSS DURING DROPLET FREE FALL	49
2.5. METHODS OF CHARACTERIZATION	54

2.5.1.	Rietveld refinement analysis.....	55
2.6.	THESIS OBJECTIVE	57
3.	EXPERIMENTAL PROCEDURES.....	59
3.1.	MELTING, ATOMIZATION AND SPRAY DEPOSITION OF D2 STEEL.....	59
3.1.1.	Atomization and spray deposition	59
3.1.2.	Annealing of the particles	66
3.1.3.	Powders and spray deposits polishing and etching.....	67
3.1.4.	Characterization	68
3.1.5.	Sensors on the atomization units.....	79
4.	MICROSTRUCTURAL INVESTIGATION OF D2 TOOL STEEL DURING RAPID SOLIDIFICATION.....	85
4.1.	INTRODUCTION.....	85
4.2.	EXPERIMENTAL	89
4.3.	RESULTS.....	91
4.3.1.	Qualitative description of the microstructure	91
4.3.2.	Quantitative analysis.....	95
4.3.3.	Solidification kinetics	99
4.4.	DISCUSSION.....	109
4.4.1.	Sensitivity analysis on chemical composition of D2 tool steel	113
4.5.	SUMMARY	114
5.	ONLINE REAL-TIME DIAGNOSTICS OF A SINGLE FLUID ATOMIZATION SYSTEM	116

5.1.	INTRODUCTION.....	116
5.1.1.	DPV-2000 hypotheses	122
5.1.2.	DPV-2000 temperature measurement.....	123
5.1.3.	DPV-2000 diameter measurement.....	123
5.2.	RESULTS AND DISCUSSION.....	124
5.2.1.	DPV-2000 diameter measurement calibration.....	124
5.2.2.	Online measurements.....	125
5.2.3.	Droplets temperature calculations.....	132
5.2.4.	Calculated temperature and measured radiant energy correlation.....	133
5.2.5.	Radiant energy analysis of droplets at difference falling distances.....	139
5.3.	SUMMARY.....	146
6.	EFFECT OF HEAT TREATMENT ON MICROSTRUCTURE AND MECHANICAL PROPERTIES OF RAPIDLY SOLIDIFIED D2 TOOL STEEL	148
6.1.	INTRODUCTION.....	148
6.2.	EXPERIMENTAL	149
6.2.1.	Sub-zero treatment.....	149
6.2.2.	Finding the upper limits of the temperature for annealing ..	149
6.2.3.	Annealing of D2 tool steel	150
6.2.4.	Solidification at low cooling rates	150
6.3.	RESULTS AND DISCUSSION.....	151

6.3.1.	Finding the upper limits of the temperature for annealing ..	151
6.3.2.	Solidification at slow cooling rates.....	152
6.3.3.	Sub-zero treatment of rapidly solidified particles.....	154
6.3.4.	Supersaturation during rapid solidification.....	157
6.3.5.	Phase identification and quantification analysis of annealed particles	165
6.3.6.	Microstructure of annealed particles.....	182
6.4.	SUMMARY	205
7.	SPRAY DEPOSITION OF D2 TOOL STEEL.....	207
7.1.	INTRODUCTION.....	207
7.2.	RESULTS AND DISCUSSION.....	207
7.2.1.	Modeling of solid fraction and temperature of droplets	210
7.2.2.	Formation of different phases in deposits.....	214
7.2.3.	Microstructure of spray deposits.....	215
7.3.	SUMMARY	237
8.	CONCLUSION AND FUTURE WORK.....	239
8.1	CONCLUSIONS	239
8.2	FUTURE WORK.....	244
	REFERENCES.....	246
9.	APPENDIX A	259
10.	APPENDIX B	262

List of Table

Table 2.1. Characteristics of alloy carbides in tool steels.....	11
Table 2.2. Chemical composition of D2 tool steel.....	14
Table 3.1. Chemical composition of D2 tool steel used in this study.....	60
Table 3.2. Atomization run conditions as well as particle size distribution of produced powders.....	62
Table 3.3. IA run conditions for atomized D2 tool steel deposits.....	64
Table 3.4. Experimental conditions for XRD analysis	73
Table 3.5. Summary of 11-BM technical specifications.....	73
Table 4.1. EDX analysis results from dark and light gray regions in D2 steel (shown in Figure 4.3) (wt.%).....	94
Table 4.2. SDAS as a function of particle size and cooling gas	96
Table 4.3. Solidification time and solidification temperature range for particles solidified at different conditions	103
Table 6.1. Sample calculation results for the amount of supersaturated chromium at room temperature in the retained austenite for the droplets IA in helium.....	160
Table 6.2. Weight percent of carbides at different annealing temperature for droplets atomized in nitrogen as well as equilibrium amount of carbides at those temperatures.	196

List of Figures

Figure 2.1. The effect of chromium content on the austenite phase stability region in Fe-Cr-C alloys	13
Figure 2.2. Vertical section of the Fe-C-Cr system at 13 wt.% Cr.	15
Figure 2.3. The free energy change associated with homogeneous nucleation of a sphere of radius r	19
Figure 2.4. Increase in dendrite growth rate as a function of undercooling for Ni-Sn alloy	24
Figure 2.5. CCT diagrams of (a) the as-received and (b) the as-sprayed Cr12MoV steel	29
Figure 2.6. TTT diagram of D2 tool steel. Ms: Martensite start temperature, A: Austenite, K: Carbide, P: Pearlite, M: Martensite, B: Bainite.....	30
Figure 2.7. Lattice parameter (a_0), percent transformation (Y) of D2 steel as a function of temperature.....	33
Figure 2.8. SEM images of (a) gas-atomized and (b) water-atomized H13 tool steel powder.....	41
Figure 2.9. Schematic of the IA unit. The numerical labels describe the different parts of the unit	42
Figure 2.10. Microstructure of spray deposited Al-4wt.%Cu in various locations: (a) adjacent to the substrate, (b) in the central portion and (c) near the upper surface.....	46
Figure 2.11. Schematic of the forces acting on a falling droplet.	50

Figure 2.12. Cooling curve of a falling droplet in an atomization chamber. Undercooling (B-C), Nucleation point (C), Recalescence (C-D), Isothermal solidification (D-E).....	53
Figure 3.1. (a) schematic of spray depositon in the small tower and (b) image of spray deposition.....	63
Figure 3.2. D2 tool steel spray deposits (a) IA with substrate at 38cm below the nozzle plate atomized in helium, oxygen level of 10ppm, (b) IA with substrate at 20cm below the nozzle plate atomized in nitrogen, oxygen level of 10ppm (c) IA with substrate at 20cm below the nozzle plate atomized in nitrogen, oxygen level of 1000ppm and (d) IA with substrate at 28cm below the nozzle plate atomized in nitrogen, oxygen level of 10ppm.	65
Figure 3.3. Schematic of spray deposits sectioning.....	68
Figure 3.4. SDAS measurements for (a) 650 μ m particle atomized in helium (110112) and (b)1000 μ m particle atomized in nitrogen (100310).	70
Figure 3.5. A 2 μ m grid is randomly superimposed on the SEM image of a 650 μ m droplet atomized in nitrogen (110310).....	72
Figure 3.6. Image of a properly prepared sample for the 11-BM high energy powder diffraction.	74
Figure 3.7. FIB steps in order to remove a TEM sample from a 650 μ m IA- He particle, (a) SEM micrograph of the sample before FIB process, (b) depositing tungsten on the area of interest, (c) milling regions around the area of interest, (d) lift-out of sample piece by means of a manipulator	

mounted inside the FIB chamber, (e) and (f) sample mounted to a copper grid to be thinned for TEM analysis.....	76
Figure 3.8. Hardness of 300-355 μ m as-atomized particles as a function of applying the load during the hardness measurement.....	78
Figure 3.9. Schematic of spray deposits sectioning for porosity measurements.....	79
Figure 3.10. Translation stage, as well as online measurement devices, installed on the tower 's door.....	81
Figure 3.11. (a) DPV-2000 trigger tuning screen showing accepted and rejected droplets and (b) shadowgraph captured picture showing unfocused rejected droplets.....	83
Figure 4.1. Calculated phase diagram for D2 tool steel from TCFE6 database using Thermocalc software.....	88
Figure 4.2. Particles of D2 tool steel atomized using: (a) Impulse Atomization (in helium) and (b) Water Atomization methods. Particle size of 655 μ m.....	90
Figure 4.3. D2 tool steel particles formed by IA: (a) 325 μ m particle atomized in helium, (b) 325 μ m particle atomized in nitrogen and (c) 655 μ m particle atomized in nitrogen. Arrows show porosities.....	92
Figure 4.4. D2 tool steel particles formed by WA: (a) 325 μ m particle and (b) 650 μ m particle (c).....	93
Figure 4.5. XRD patterns for 600-710 μ m particles produced via IA in helium and nitrogen as well as WA.....	95

Figure 4.6. High-magnification SEM images of D2 tool steel: (a) 1200 μm IA particle in helium, (b) 1200 μm IA particle in nitrogen and (c) 655 μm WA particle.....	97
Figure 4.7. Eutectic area fraction as a function of particle size and cooling gas for IA and WA.....	98
Figure 4.8. D2 tool steel phase diagram showing metastable extension of liquidus and solidus lines using Thermocalc software.	101
Figure 4.9. Effect of eutectic undercooling on the amount of eutectic in IA and WA D2 tool steel.	102
Figure 4.10. Effect of primary phase undercooling on the amount of eutectic in IA and WA D2 tool steel.	104
Figure 4.11. Effect of particle size on the primary phase undercooling.	105
Figure 4.12. Effect of cooling rate of primary phase on the amount of eutectic in IA and WA D2 tool steel.....	106
Figure 4.13. Primary phase undercooling versus f_R of D2 tool steel droplets.	108
Figure 4.14. (a) Critical radius of austenite nucleant as a function of primary phase undercooling, (b) Activation energy for formation of austenite nucleants as a function of critical radius of nucleants.	110
Figure 4.15. Number of unitcells in the austenite nucleants during homogenous nucleation of austenite.....	111
Figure 5.1. General view of a shadowgraph system	118
Figure 5.2. Inverting the shadow image using a reference image.....	119
Figure 5.3. Thresholds for the first segmentation	120

Figure 5.4. Thresholds for the first segmentation	120
Figure 5.5. shadowgraph images of droplets during free fall, (a) molten D2 tool steel at 4cm below the nozzle plate and (b) molten copper at 10cm below the nozzle plate.	123
Figure 5.6. Velocity as a function of droplet size of falling droplets collected by shadowgraph system at 15cm below the nozzle plate.....	126
Figure 5.7. Average velocity of IA droplets measured at 15cm below the nozzle plate by shadowgraph for range of droplets within 7% precision measurement range of DPV-2000.	126
Figure 5.8. Boxplot showing velocity of droplet in different particle size range at 15cm below the nozzle plate.....	127
Figure 5.9. Velocity as a function of droplet size of falling droplets collected by shadowgraph system at 28cm below the nozzle plate.....	128
Figure 5.10. The signal counts measured at two different wavelengths for a single droplet, (b) Radiant energy vs. droplet diameter measured by DPV-2000 at 15cm below the nozzle plate (copper).	129
Figure 5.11. Radiant energy vs. droplet diameter measured by DPV-2000 at (a) 4cm, (b) 18cm and (c) 28cm below the nozzle plate (D2 tool steel). (c) power curve fitted radiant energy of $Q(\lambda_1)$ as a function of droplet diameter for the fully liquid D2 tool steel droplets.	131
Figure 5.12. Power curve fitted radiant energy of $Q(\lambda_1)$ as a function of droplet diameter for the fully liquid copper droplets.....	132

Figure 5.13. Velocity as a function of distance of droplets from the nozzle plate for different droplet sizes, generated from the model.....	133
Figure 5.14. Temperature vs. distance from nozzle plate (plotted using the model), using initial velocities calculated from Figure 5.13. Dashed line shows distance from the nozzle plate (15cm).....	134
Figure 5.15. Calculated temperature of copper droplets at different falling distances.....	134
Figure 5.16. Solidified fraction of copper droplets at 15cm and 50cm of nozzle plate, as well as initial velocity of droplets exiting from the orifices.	135
Figure 5.17. Primary and eutectic undercooling values as a function of particle size of droplets atomized in the nitrogen atmosphere.	137
Figure 5.18. Temperature of falling D2 steel droplets in heights calculated by the heat loss model.	138
Figure 5.19. $Q(\lambda_1)/d^2$ versus K_1 graph at different heights for the D2 steel liquid droplets.	141
Figure 5.20. $Q(\lambda_1)/d^2$ versus K_1 graph at different heights for copper liquid droplets.	141
Figure 5.21. $Q(\lambda_1)/d^2$ and fraction solidified versus K_1 graphs at different heights for the semi-solid droplets.....	143
Figure 5.22. $Q(\lambda_1)/d^2$ versus K_1 graphs at different heights for the both liquid and semi-solid droplets at (a) 18cm and (b) 28cm heights.	145
Figure 6.1. DSC graph of 600-710 μ m particles atomized in nitrogen (heating reate of 10K/min).	151

Figure 6.2. SEM micrograph of D2 tool steel under cooling rate of 0.166°C/sec.....	152
Figure 6.3. SEM micrograph of D2 tool steel under cooling rate of 0.166°C/sec. White arrows show some measured dendrites.	154
Figure 6.4. Microvickers' hardness of different sized particles as-atomized and quenched in the liquid nitrogen.	155
Figure 6.5. Equilibrium curve of chromium and carbon at 550°C, 650°C and 750°C in the austenite phase.....	159
Figure 6.6. Level of supersaturation of final D2 steel structure at different temperatures as function of cooling rate.....	162
Figure 6.7. Level of supersaturation of final D2 steel structure at different temperatures as a function of eutectic undercooling.	163
Figure 6.8. Precipitation driving force for M_7C_3 carbides in the supersaturated rapidly solidified retained austenite at different temperatures as function of cooling rate.....	164
Figure 6.9. Precipitation driving force for M_7C_3 carbides in the supersaturated rapidly solidified retained austenite at different temperatures as function of eutectic undercooling.	165
Figure 6.10. XRD patterns for 300-355 μm particles atomized in nitrogen and annealed for 2 hour at different temperatures.....	166
Figure 6.11. XRD patterns for 300-355 μm particles atomized in helium and annealed for 2 hours at different temperatures.	167

Figure 6.12. XRD patterns for 600-710 μm particles atomized in nitrogen and annealed for 2 hour at different temperatures.....	168
Figure 6.13. XRD patterns for 600-710 μm particles atomized in helium and annealed for 2 hour at different temperatures.....	168
Figure 6.14. High Energy XRD patterns for 300-355 μm particles atomized in nitrogen and annealed for 2 hours at 650C.....	170
Figure 6.15. High Energy XRD patterns for 600-710 μm particles atomized in nitrogen and annealed for 2 hours at 650°C.	171
Figure 6.16. Profile refinement of D2 tool steel particles with the diameter size range of 600-710 μm atomized in nitrogen using the GSAS computer code in (a) As-atomized with $\chi^2=4.80$, (b) annealed at 350°C with $\chi^2=1.14$, (c) annealed at 550°C with $\chi^2=1.03$ and (d) annealed at 750°C with $\chi^2=1.08$	174
Figure 6.17. Lattice parameter of austenite and percent transformation of austenite to ferrite as a function of annealing temperature.....	175
Figure 6.18. Percent of transformation of austenite to ferrite at annealed for two hours at 550°C as a function of cooling rate of droplets.	177
Figure 6.19. Austenite lattice parameter of different-sized droplets WA and IA in helium and nitrogen, using Rietveld analysis of (a) XRD and (b) ND. Fe-0.8wt.% C and Fe-gamma lattice parameters are also shown, (a.	181
Figure 6.20. SEM image of 650 μm D2 steel atomized in nitrogen, annealed for 2 hours at (a) 550°C, (b) 650°C, (c) 750°C and (d) 810°C.....	183

Figure 6.21. SEM image of 600-710 μ m particle atomized in nitrogen and then annealed at 550C for 2 hours. Region (I) is austenite and Region (II) is ferrite + carbides	185
Figure 6.22. SEM image of a 600-710 μ m particle atomized in nitrogen and then annealed at 650°C for 2 hours. (b) is the higher magnification view of image (a).....	186
Figure 6.23. (a) SEM image of 600-710 μ m particle atomized in nitrogen and then annealed at 750°C for 2 hours and (b) higher magnification.....	187
Figure 6.24. SEM image of 600-710 μ m particle atomized in nitrogen and then annealed at 810°C for 2 hours and (b) higher magnification.....	188
Figure 6.25. SEM image of 600-710 μ m particle atomized in helium and then annealed at 810°C for 2 hours.	189
Figure 6.26. SEM image of 600-710 μ m particle atomized in helium and then annealed at 810°C for 2 hours (samples tilted at 40° angle).....	190
Figure 6.27. TEM BF image of the interdendritic region of a 655 μ m particle of D2 tool steel, atomized in helium and annealed for 2 hour at 350°C. (b) SAD pattern from the austenite primary phase.	192
Figure 6.28. (a) Higher magnification TEM BF image from the eutectic area of the sample annealed at 350°C (Figure 6.27); (b) SAD pattern from the interdendritic (eutectic) region.	192
Figure 6.29. (a) and (b) TEM-BF images of a 655 μ m D2 tool steel sample, annealed at 923 K. SAD patterns from (c) a ferrite grain; (d) ferrite and	

carbide. Region I shows area with carbides used for the SAD pattern in (d).....	195
Figure 6.30. Precipitates diameter as a function of dropelts cooling rates for different annealing temperatures.	197
Figure 6.31. Vickers hardness of as-atomized droplets in different size ranges atomized in different atmospheres, as well as annealed samples at different temperatures.....	202
Figure 6.32. Hardness as a function of precipitate spacing of particles annealed at different temperatures.....	205
Figure 7.1. Temperature of the melt and weight of deposit as a function of time of atomization, for deposit at (a) 20cm below the nozzle plate at 10ppm oxygen level, (b) 20cm below the nozzle plate at 1000ppm oxygen level and (c) 28cm below the nozzle plate at 10ppm oxygen level.	209
Figure 7.2. Temperature of the droplet and distance of droplet from nozzle plate as a function of fraction solidified in the droplets, for 360 μ m droplet atomized in nitrogen, with the superheat of 205 $^{\circ}$ C as calculated by the model.	211
Figure 7.3. Effect of droplet size and superheat on the distance at which 40% solid forms in a nitrogen atmosphere.	213
Figure 7.4. XRD graphs of bottom and middle part of impulse atomized deposits. XRD peaks of ferrite, austenite and M7C3 carbides are also shown in the graph.....	215

Figure 7.5. OM images of IA spray deposits at (a) 20cm and (b) 28cm distances from nozzle plate.....	217
Figure 7.6. SEM micrograph of IA spray deposits, (a) 2810 and (b) 2010 samples.	218
Figure 7.7. OM o IA spray deposited sample at 28cm from the bottom of the sample to the top. The arrow shows the direction to the top part of the sample.....	220
Figure 7.8. SDAS at the center line of the deposits for (a) 2010, (b) 201000 and (c) 2810.....	221
Figure 7.9. Cooling rate of IA and GA spray deposits as a function of height of deposits. (a) 2010, (b) 201000 and (c) 2810.	224
Figure 7.10. Eutectic volume fraction of impulse atomized deposits, (a) 2010 sample, (b) 2810 sample and (c) 201000 sample.	227
Figure 7.11. Eutectic undercooling of spray deposit as a function of height of samples.....	229
Figure 7.12. SEM micrograph of spray deposited samples at middle section of deposits, (a) 201000 and (b) 2810 samples. Red arrows show spray direction.....	232
Figure 7.13. Hardness map of IA (a) 2010 and (b) 2810 spray deposits.	233
Figure 7.14. Porosity of D2 steel spray deposits at different locations according to the sample sectioning shown in Figure 3.9, (a) 2010 sample, (b) 2810 sample and (c) 201000 sample.....	236

Figure 8.1. Effect of primary phase and eutectic undercooling on the amount of supersaturation of the primary phase.242

List of symbols and abbreviations

A	Surface area of droplet, m^2
C_d	Drag coefficient
C_p	Heat capacity, $JKg^{-1}K^{-1}$
C_l^m	Composition of the last liquid to solidify
C_0	Original alloy composition
D	Diffusion coefficient, m^2s^{-1}
$E(\lambda_i)$	Thermal radiation energy, J
ΔG	Free energy of formation of a nucleus, J/mole
ΔG°	Standard free energy, J/mole
ΔH	Latent heat of solidification, J/g
M	Coarsening factor
M_s	Martensite start temperature, K
M_f	Martensite finish temperature, K
P	Porosity level, Vol. %
$Q(\lambda_i)$	Value proportional to thermal radiation energy
R	Precipitate radius, m
dR/dt	Growth rate of precipitate, ms^{-1}
SDAS	Secondary dendrite arm spacing, μm
T_0	Surrounding gas temperature of a droplet, K
T_g	Temperature of gas, K
T_p	Temperature of a droplet, K
\dot{T}	Cooling rate, Ks^{-1}
T_L	Liquidus temperature, K
T_S	Solidus temperature, K
T_e	Eutectic temperature, K
ΔT	Amount of undercooling, K
ΔT_r	Solidification range, K
ΔT_p	Primary phase undercooling, K
ΔT_{hyp}	Hypercooling limit, K
V_p	Volume of droplet, m^3

X_{eM}	Equilibrium concentrations of M, wt. %
X_{eC}	Equilibrium concentrations of C, wt. %
c_E	Equilibrium concentration, wt. %
c_β	Concentration at the interface of the precipitate, wt. %
$c(t)$	Amount of supersaturation in the matrix, wt. %
d	Falling droplet diameter, m
f_R	Volume fraction of a droplet solidifying during the recalescence
f_s	Solidified volume fraction of droplet during free fall
h_{eff}	Effective heat transfer coefficient, $Wm^{-2}K^{-1}$
k	Partition coefficient
k_g	Conductivity of gas, $Wm^{-1}K^{-1}$
k_s	Equilibrium constant (solubility product)
m	Equilibrium liquidus slope, $T(\text{wt. \%})^{-1}$
n_e	Number of points falling within the eutectic region
n_b	Number of points on the eutectic-dendrite boundary
n_t	Total number of grid points on the image
r^*	Critical radius of stable nucleus, m
t_{SL}	Solidification time, s
v	Relative velocity between the falling droplet and gas, ms^{-1}
v_e	Volume percent eutectic
w_i	Weighting factor for each observation point
y^{calc}	Calculated profile
y^{obs}	Observed profile

Greek symbols

α	Ferrite
λ_2	Secondary dendrite arm spacing, μm
λ_i	Wavelength, μm
γ	Austenite
γ_a	Activity coefficient
μ_g	Dynamic viscosity of gas, $\text{Kgm}^{-1}\text{s}^{-1}$
ρ_t	Theoretical full density, Kgm^{-3}
ρ_m	Experimentally measured density, Kgm^{-3}
ρ_p	Density of particle, Kgm^{-3}
ρ_g	Density of surrounding gas, Kgm^{-3}
Γ	Gibbs-Thomson coefficient, mK

Chapter 1

1. Introduction

The properties of metals and alloys are determined by their microstructure and chemical composition. One of the important steps in generating a microstructure is the solidification step. Currently, many alloys undergo post-cast heat treatment or hot/cold working and are not used in the as cast condition. Despite this fact, the primary microstructure obtained from solidification plays an important role in the final microstructure.

Therefore, it is so important to design and control the solidification process in such a way that the final product obtains the desirable properties. For instance, materials with a fine microstructure have higher yield strength and fracture toughness compared to materials with a coarser microstructure [1]. In order to control the solidification step, some important parameters such as undercooling and cooling rate need to be considered. Variation of these two parameters can produce different structures in materials. Cooling rate is the rate at which the heat is extracted from the sample. Undercooling is the process by which the temperature of the liquid is lowered below its equilibrium solidification temperature while still remaining a liquid. More detailed information about cooling rate and undercooling will be given in Section 2.2.

Microsegregation is another parameter which affects mechanical properties of the final product. Non-uniform distribution of alloying

elements within the volume of a solidified microstructure is termed segregation [2]. If this non-uniformity is at the scale of dendrite spaces and/or grain size, it is called microsegregation. For example, when some binary alloys solidify, the solute is rejected by the solid during solidification. This leaves a solute-poor composition profile in the center of the dendrite and a solute-rich composition profile at the position where a dendrite impinges on the one growing next to it (the last region to freeze). This is called coring. If the spatial variation in composition occurs in the alloy ranges in scale from several millimetres to centimetres or even meters, it is called macrosegregation [3].

In order to refine the microsegregated structure, homogenization heat treatment can be done at long enough time and temperature. This makes homogenization an expensive process. According to Kurz and Fisher [4], the homogenization time is proportional to the square of the length scale of the material's microstructure due to diffusional processes. Therefore, a coarse microstructure of a casting sample takes longer to homogenize compared to that of a fine microstructure. Therefore, it would be best to refine the microstructure by means of different techniques in order to reduce the amount of time spent to remove the microsegregation in the microstructure.

Rapid solidification modifies the microstructure of the alloys in order to get a finer microstructure with less microsegregation. The term rapid solidification refers to the system's high undercooling and cooling

rate, which result in a deviation of the formed phases and their composition from equilibrium condition [5]. Three different definitions of the term “cooling rate” have been provided by Eskin et al. [6]:

1. Ratio of solidification temperature range and the time that takes for an alloy to pass this temperature range,
2. Slope of the time-temperature graph (thermal history),
3. The heat extraction rate during solidification.

Definition number 1 for cooling rate are used in this work and can be written as:

$$\dot{T} = \frac{\Delta T_r}{t_{SL}} \quad \text{Eq. 1.1}$$

where ΔT_r is the solidification range and t_{SL} is the time required for an alloy to pass this temperature range. Cooling rate is usually expressed in Ks^{-1} .

In order to have nucleation of a new phase, a nucleation energy barrier must be overcome. Undercooling is required to overcome this energy barrier. This undercooling also provides a driving force for the nucleation of a particular solid phase [4].

As described previously, rapid solidification can yield a microstructure with unique chemical composition and mechanical properties. An area of interest in rapid solidification applications is high-chromium high-carbon tool steels which experience considerable segregation of alloying elements during their solidification in the casting process. The major alloying element in this group of steels is chromium

(nominal concentration of 12%). Higher amounts of other alloying elements such as manganese, silicon, nickel, molybdenum and vanadium may also be added to these tool steels. The first solidified crystals have high concentration of iron. During solidification, other alloying elements such as carbon and chromium are rejected into the interdendritic regions and carbides will form in these regions [7]. Size and distribution of these carbides play important roles in the final properties of tool steels. It has been shown by Blaha et al. [8] that the formation of fine and well-distributed carbides in the matrix result in good mechanical properties for the alloy in the case of hardness, fracture toughness and wear properties.

The goal of this project is to study the effect of rapid solidification (different cooling rate and undercooling values) on the microstructure and mechanical properties through quantification of the microstructure. Although considerable work has been done on rapid solidification of high-alloy steel, a systematic effort on the effect of undercooling and cooling rate on the final properties on high-chromium high-carbon steels is still missing. D2 tool steel has been chosen for this work because there are significant amounts of carbon and carbide forming elements in this alloy which increase the chance of microsegregation of alloying elements in the microstructure. The study also looks at the carbide precipitation behaviour of the supersaturated primary phase as a result of rapid solidification, since the size and distribution of these carbides play an important role in determining the final properties of the alloy and carbide precipitation

behaviour is strongly affected by the rapid solidification characteristics. Impulse Atomization (IA) has been utilized in order to study the rapid solidification of D2 tool steel droplets.

In order to measure the real undercooling values of the droplets during rapid solidification, experimental and modelling analyses are combined and the possibility of such measurements using a two color pyrometer is investigated.

Correlation of rapid solidification characteristics in a droplet to a near-net shape product (produced by spray deposition) is also interesting. Therefore, this study presents an understanding of some properties in spray deposits based on rapid solidification concepts applied in the solidification of droplets.

Neutron diffraction (ND), x-ray diffraction (XRD), scanning electron microscopy (SEM), transmission electron microscopy (TEM) and the hardness measurements have been used in order to evaluate the powders and spray deposited samples. Also, using online measurements techniques, thermal and solidification behaviour of the falling droplets during the IA process are investigated.

1.1. Thesis outline

Chapter 2 will review general information associated with solidification, rapid solidification techniques, tool steels and methods of characterization associated with this work. At the end of this chapter, the objectives and

motivation of this work will be defined. Chapter 3 presents the experimental procedures that were used to achieve the study objectives. Chapter 4 mainly focuses on the microstructural analysis of D2 tool steel as a result of rapid solidification and the effect of undercooling and cooling rate on the final microstructure and phases. Chapter 5 includes efforts for the online real-time diagnostics of the droplets during free fall in order to measure real values of undercooling during solidification. In Chapter 6, the effect of annealing on the rapidly solidified D2 tool steel will be discussed. Chapter 7 is devoted to the microstructural investigation of spray deposited D2 tool steel using the IA technique. Chapter 8 contains general discussion and conclusions along with recommendations for future work.

Chapter 2

2. Literature Review

There are different processes to generate microstructures that are metastable or non-equilibrium. Some examples are mechanical alloying, rapid solidification (e.g., atomization, melt spinning, etc.), chemical and vapor deposition, and spray processes (e.g., plasma spraying, thermal spraying and spray atomization and deposition) [9]. Before explaining the rapid solidification methods addressed in this work, it is necessary to describe the D2 tool steel which has been used in this project. Therefore, the following section will discuss different types of tool steels, especially D2 tool steel and its microstructure. Since carbide formation from a supersaturated microstructure during rapid solidification is important, a section will address the precipitation phenomena especially carbide precipitation from a supersaturated matrix. Also, in order to better understand rapid solidification, the fundamentals of solidification, specifically nucleation, growth and undercooling will be discussed. Some methods of characterization that are used in analysis of rapidly solidified microstructures will be introduced briefly at the end of this chapter.

2.1. Tool steels

Tool steels usually contain significantly more alloying elements than alloy steels [7]. Alloying elements are added to plain carbon steel to obtain certain properties such as high wear resistance for cutting or abrasion, high

toughness or strength and “red hardness” defined as the tool’s ability to do its work at high temperatures that would soften plain carbon steel [10].

Each alloying element in a tool steel, such as tungsten, chromium, molybdenum and vanadium, has a specific effect on the mechanical properties [11]. Addition of alloying elements can change the nature and amount of the carbide phases that form in the steel. Also, they can change different characteristics such as: the amount of carbide solution, stability of carbides, grain growth during heating, hardenability, martensite start and finish temperatures, etc. [7]. Mechanical properties of tool steels can be improved by the formation of finer grain sizes, finer carbides and a uniform distribution of carbides for a given volume fraction of carbides [11]. When a tool steel is slowly cooled during solidification, the carbides form as a result of segregation during solidification. Under such conditions, these carbides would have a non-uniform distribution and would tend to be coarse in size leading to detrimental ductility and wear of the alloy [11].

2.1.1. Manufacturing of tool steels

Traditionally, tool steels are produced using ingot casting processes (conventionally processed tool steels). During these processes, a tool steel is produced and melted using different processes such as electric arc furnace (EAF), electroslag remelting (ESR) and vacuum arc remelting (VAR). Based on the application, tool steels undergo different forging and/or rolling steps. Hot workability of tool steels strongly depends on the range of alloying elements in the steel. Tool steels with a high amount of alloying

elements are the most difficult ones to hot work. In addition to achieving the required shape and dimensions in the final products, another purpose of hot working is to improve the properties of the final tool steel product. Based on the application, in some cases hot and cold drawing are also applied to the tool steels [7].

Recently, advances in powder metallurgy (PM) techniques have resulted in the production of high alloyed steels using this technique. Slow cooling rates in ingot casting processes result in the formation of coarse grains as well as coarse carbides. Breaking down these coarse carbides during the hot working step is difficult. Gas and water atomization techniques are usually used in PM techniques (these methods will be further discussed in Section 2.3). The final product can be produced by compacting and sintering the produced powder by the PM process. Because of formation of fine and well-distributed carbides during PM process, machinability of the PM parts is improved [7].

2.1.2. Categories of tool steels

There are several varieties of tool steels and therefore, they need to be categorized into different alloy steel systems. Based on their chemical compositions and application, tool steels are categorized into different groups. One of the methods to classify tool steels is proposed by the American Iron and Steel Institute (AISI) [11]. The major categories of the tool steels are listed as follows [7]:

- Water-hardening tool steels (W)

- Shock-resisting tool steels (S)
- Special-purpose tool steels (L and F)
- Cold work tool steels (O, A and D)
- Hot work tool steels (H)
- High speed tool steels (T and M)

In all tool steel groups, the properties and application are the main criteria for comparison, except for the first group, water-hardening tool steels. In this group, the classification is based on the manner of the heat treatment. Some groups are divided into sub-categories. For example, cold work tool steels are divided into oil-hardening types (O), medium-alloy air hardening types (A) and high-carbon high chromium types (D).

D-type tool steels are among the most important tool steels. Five D-series tool steels are commonly available. Basically, all five have the same type of microstructure (carbides, but in different amounts) and they differ only by minor changes of chemical composition. The nominal composition of chromium is about 12wt.%, which is the major alloying element. The high carbon and alloy content in these alloys results in a large volume fraction of high-hardness alloy carbides which is the main reason these alloys have excellent wear resistance [7]. Although there is high amount of chromium in D-type tool steels, chromium content is not high enough to achieve a high level of corrosion resistance as compared to stainless steels. This is mainly because most of the chromium is used in forming alloy

carbides. However, there is a good oxidation resistance behaviour at high temperatures [7].

2.1.3. Carbides in tool steels

Different types of carbides available in tool steels are listed in Table 2.1.

Some of the characteristics of these carbides are also described in Table 2.1.

The letter M in the carbide formula indicates the metal content of the carbide (which can be more than one metal component) [7,12].

Table 2.1. Characteristics of alloy carbides in tool steels [7]

Type of carbide	Lattice type	Remarks
M_3C	Orthorhombic	Cementite (Fe_3C) type carbide. M: iron, manganese, chromium and a little tungsten, molybdenum, vanadium.
M_7C_3	Hexagonal	This carbide found mostly in chromium alloy steels. At higher temperatures, resistant to dissolution. Hard and abrasion resistant. Product of tempering.
$M_{23}C_6$	FCC	Found in high-chromium steels and all high-speed steels.
M_6C	FCC	Carbide rich in tungsten or molybdenum. Contains some amounts of chromium, vanadium, cobalt. Formed in all high-speed steels. Highly resistant to abrasion
M_2C	Hexagonal	W_2C type of carbide. Rich in tungsten or molybdenum. Product of tempering. A considerable amount of chromium can be dissolved in this carbide.

All these carbides are harder than a martensite matrix. Therefore, in order to achieve better performance for the tool steel in different

applications, it is required to incorporate more carbide dispersion inside the matrix [7].

The alloy carbides can be produced during different processes such as solidification, hot working or heat treatment. In the liquid state, all alloying components in a tool steel are soluble in liquid iron. On cooling, carbides form during a eutectic reaction. This eutectic structure appears similar to the pearlitic structure (which contains lamellae of matrix and carbide) that is common in carbon steels. Sometimes the eutectic forms in the grain boundaries and network carbide is formed. These carbides are the main reasons that high alloyed tool steels become brittle [13].

In D2 tool steels, M_7C_3 carbides are formed due to the high-chromium content of these steels. There is a mutual solubility of chromium and iron in high alloy steel. Iron and chromium can replace each other in the carbide structure (carbide with formula of $(Cr,Fe)_7C_3$). These carbides can be written as M_7C_3 in a simplified format [14]. Viale et al. [15] reported after heat treatment of modified D2 steel (with 1wt.% carbon and 8wt.% chromium and more molybdenum and titanium contents) produced by PM processes, M_7C_3 carbide would form with $(Fe_{29.64}Cr_{31.01}V_{3.14}Mo_{3.82}Mn_{0.36}Si_{0.03}Ti_{0.09})C_{31.91}$ chemical composition. Characterization of these precipitates was carried out by electron microprobe analysis.

2.1.4. Phase diagram and microstructure

Elements such as chromium, molybdenum, silicon, tungsten, vanadium and zirconium are ferrite stabilizers and carbon, cobalt, copper, manganese, nickel and nitrogen are austenite stabilizers. Austenite stabilizers lower the eutectoid temperature and ferrite stabilizers raise the eutectoid temperature [7]. Figure 2.1 displays the iron-carbon phase diagram in which different amounts of chromium from 0 to 19% chromium are superimposed. The addition of chromium significantly changes the size of the austenite region in iron-carbon phase diagram. It should be noted that by increasing the chromium content, the range of stability of austenite is reduced [16].

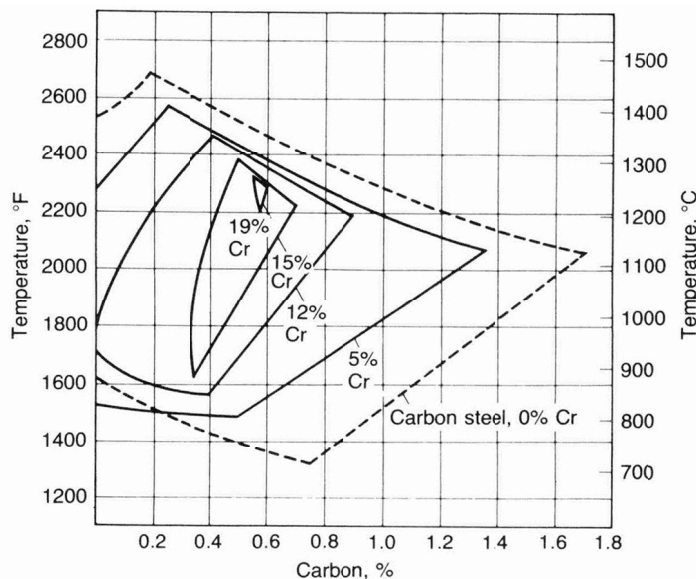


Figure 2.1. The effect of chromium content on the austenite phase stability region in Fe-Cr-C alloys [7]. Reprinted with permission of ASM International. All rights reserved. www.asminternational.org.

The effect of carbon on the austenite region also can be determined from Figure 2.1. It can be seen that increasing carbon content (in all chromium contents) increases the size of austenite regions.

The chemical composition of D2 tool steel is shown in Table 2.2. There is a large amount of chromium in this tool steel, which results in the formation of large chromium carbides in the microstructure of solidified D2 tool steel. Thus, for D2 tool steel the equilibrium primary phase should be ferrite.

Table 2.2. Chemical composition of D2 tool steel [7]

Chemical composition (wt. %)						
C	Mn	Si	Cr	Ni	Mo	V
1.40-1.60	≤0.60	≤0.60	11.00-13.00	≤0.30	0.70-1.20	≤1.10

Figure 2.2 shows the vertical section of Fe-Cr-C alloy system with the constant chromium content of 13 wt.% (close to the D2 tool steel chromium content which is about 12 wt.%). The resulting phase diagram is similar to the Fe-C diagram but, due to formation of alloy carbides (availability of high amount of chromium), there are more phase regions available in this phase diagram [7]. According to this diagram, it is obvious that by decreasing the temperature of an alloy which contains about 1.55 wt.% carbon (close to the carbon content of D2 tool steels), the solidification sequence is primarily the crystallization of austenite and then

the eutectic decomposition of the interdendritic liquid: $L \rightarrow \gamma + (\text{Cr,Fe})_7\text{C}_3$ [18]. Since the phase diagram shown in

Figure 2.2 is the projection of a three-dimension Fe-Cr-C phase diagram, the eutectic transformation is not in the form of a line but has its own eutectic region. Residual interdendritic liquid eventually transforms to austenite and carbide throughout this region.

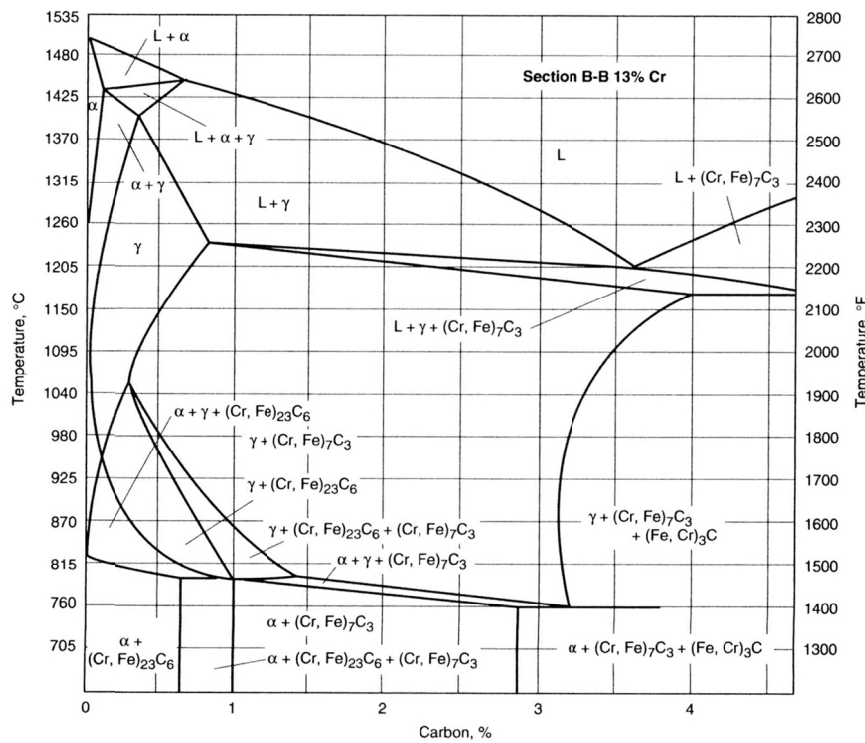


Figure 2.2. Vertical section of the Fe-C-Cr system at 13 wt.% Cr [7]. Reprinted with permission of ASM International. All rights reserved. www.asminternational.org.

When the high chromium steels solidify, the alloying elements segregate considerably. The first solidified crystals are rich in iron. Other elements such as carbon, chromium are then rejected to the interdendritic

liquid regions. This is the region where eventually alloy carbides form [7]. If any hot work is applied to the as solidified structure, the segregated solidification structure is broken up. Since the alloy carbides are stable at the temperature at which hot working is done (around 1150°C), they get elongated in the rolling direction [7].

As discussed previously, austenite and ferrite stabilizers can change the range of stability that these phases have in the phase diagram resulting in the formation of different contents of austenite and ferrite. Austenite and ferrite stabilizers can also affect M_s and M_f temperatures. An empirical equation is given by Puttgen et al. [19], in which the M_s (°C) is described as a function of mass percent carbon and mass percent chromium and manganese, in austenite (Eq. 2.1).

$$M_s = 636 - 475C - 17Cr - 33Mn \quad \text{Eq. 2.1}$$

This equation shows that alloying elements such as carbon, chromium and manganese decrease the martensite start temperature. The M_s temperature for the austenitic steel is below the room temperature. Therefore, austenite phase is available in the final microstructure which is in the form of retained austenite [19]. If solidification happens in high cooling rates, primary austenite traps alloying elements in its structure before there is time for them to be rejected to the interdendritic liquid. The amount of alloying element saturated inside the austenite is affected by the amount of undercooling and cooling rate during solidification. Therefore,

rapid solidification (non-equilibrium solidification) will provide a different microstructure than what the equilibrium phase diagram predicts. The following section will address the basic principles of rapid solidification.

2.2. Rapid solidification

In order to better understand the rapid solidification phenomena, it is vital to understand the solidification mechanism and the way in which different parameters such as undercooling and cooling rate affect the solidification process. These parameters are highly effective in order to control the final properties of the product. Solidification can be divided into two stages: nucleation and growth.

2.2.1. Nucleation

The driving force of solidification for a liquid which is cooled below its equilibrium melting point is represented by the difference in Gibbs free energy between the solid and liquid ($G_{\text{Solid}} - G_{\text{Liquid}}$). Because the free energy of solidification in this condition is negative, it is expected that the liquid will solidify. When a unit volume of solid is formed, there is a decrease in free energy of the system, equal to ΔG_V . Therefore, the free energy of formation for a small volume of solid has a negative effect on the total free energy of solidification (i.e., it reduces the total free energy of the system). On the other hand, because solid-liquid interface is formed, there is a positive contribution to the total free energy of solidification (i.e., the total free energy of solidification is increased). If we assume the nucleus is a

sphere, the free energy of formation of this nucleus can be defined as Eq. 2.2 [1]:

$$\Delta G = \frac{4}{3}\pi r^3 \Delta G_V + 4\pi r^2 \gamma_{SL} \quad \text{Eq. 2.2}$$

where, γ_{SL} is the solid-liquid interfacial energy, ΔG_V is the change in free energy per unit volume of the nucleus and r is the radius of the nucleus. ΔG_V is zero at the melting temperature. By increasing the undercooling of the metal below the solidification temperature, the free energy of solidification becomes more negative. Because of this, the solidification process is initiated. According to Figure 2.3, for a given undercooling, there is a nucleus with a critical radius r^* which has reached the critical free energy of nucleation (ΔG^*). If the radius of the crystallites is smaller than r^* , the energy of the system will be lowered by dissolving these crystallites. If the nucleus increases its size, the free energy of the system is decreased and the nucleated solid phase will grow.

The formation of a solid phase inside the liquid phase without the help of any foreign material is called homogenous nucleation. Due to its high amount of ΔG^* , this type of nucleation is seldom observed in practice. The other type of nucleation, heterogeneous nucleation, plays the most important role in the solidification of materials. During heterogeneous nucleation, crystallization occurs on foreign bodies such as the container walls or metal oxides. At such preferential sites, the surface energy is lower

and this decreases the amount of thermodynamic energy barrier for solidification compared to homogenous nucleation [1].

For homogenous nucleation, r^* and ΔG^* are represented as Eq. 2.3 and Eq. 2.4, respectively [1].

$$r^* = \frac{-2\gamma_{SL}T_m}{\Delta H\Delta T} \quad \text{Eq. 2.3}$$

$$\Delta G^* = \frac{16\pi\gamma_{SL}^3T_m^2}{3\Delta H^2\Delta T^2} \quad \text{Eq. 2.4}$$

where T_m is the equilibrium melting temperature of the material, γ_{SL} is the surface energy of the solid in contact with the liquid phase, ΔT is the amount of undercooling below the solidification temperature and ΔH is the latent heat of solidification.

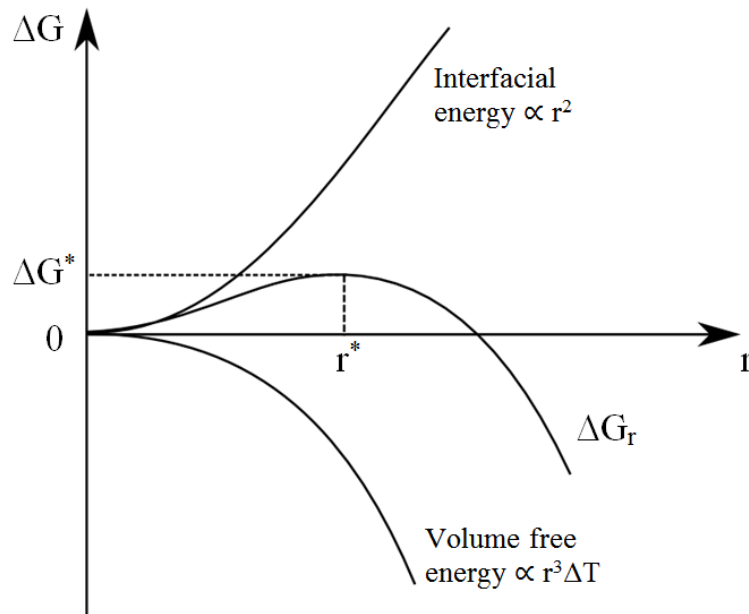


Figure 2.3. The free energy change associated with homogeneous nucleation of a sphere of radius r [1].

According to the nucleation theory presented by Flemings [20], Eq. 2.3 gives the critical radius of a nucleus (r^*), stable at undercooling ΔT . This equation reveals that as the undercooling increases, the critical radius of a stable nucleus will decrease. Subsequent to the formation of this stable nucleus, growth will follow.

2.2.2. Growth

The growth process begins after the stable nucleus forms. Generally speaking, growth occurs when atoms are joined from the liquid to the solid phase. According to the thermal gradient and growth rate, different types of growth can be achieved: planar, cellular and dendritic. When the amount of undercooling is increased, any small bump on the surface of the solid/liquid interface, which is as a result of any small perturbation on the liquid-solid interface, will be located in the lower temperature region. The growth rate is controlled by the rate of diffusion of solute atoms to the interface (more frequently, there is rejection of solute). With further growth, other small bumps can form on the surface of the primary arm of the dendrite and secondary branches are formed; as a result, dendrite growth starts [1]. The spacing between secondary dendrite arms is related to the cooling rate. As the cooling rate increases, dendrite arm spacing decreases and the microstructure will consist of finer dendrites. The secondary dendrite arm spacing can be expressed as Eq. 2.5 [18] :

$$\lambda_2 = B \left(\frac{\Delta T_r}{t_{SL}} \right)^{-n} \quad \text{Eq. 2.5}$$

where, λ_2 is SDAS (secondary dendrite arm spacing) (μm); B and n are constants related to the material characteristics and $\frac{\Delta T_r}{t_{SL}}$ is the cooling rate [18]. To show the effect of the cooling rate on the refinement of the microstructure, Wiskel et al. [21], atomized different Al-Cu alloys in two different cooling gases (helium and nitrogen) via impulse atomization (IA) technique. They found that by decreasing the droplet size, the dendrite arm spacing and solidification time also decreases. In addition to this, because of the higher heat conductivity of helium gas compared to nitrogen, using helium as the cooling gas results in a finer microstructure for the same droplet size.

2.2.3. Undercooling

In solidification, changing the undercooling can lead to the creation of different structures. Rapid solidification makes it possible to achieve undercooling of materials below their equilibrium liquidus temperature. Undercooling below the liquidus temperature can form metastable phases according to the lower Gibb's free energy of the metastable phase. The difference between the equilibrium liquidus temperature and the nucleation temperature is called primary phase undercooling. For eutectic undercooling, it is defined as the temperature difference between the equilibrium eutectic temperature and the eutectic nucleation temperature. It has been shown that during rapid solidification, high amount of undercoolings can be achieved for pure liquid metals (as high as $0.3T_m$) [5]. In this equation, T_m is the melting temperature of the metal in Kelvin.

Undercooling is needed to overcome the nucleation energy barrier of the new phase. The driving force for forming these metastable solid phases is also provided by undercooling.

Another important aspect of solidification affected by undercooling is segregation in alloys resulting from the difference in solute solubility between the solid and the liquid phases. Using rapid solidification, it is possible to reduce microsegregation. Because during rapid solidification, growth velocity of solid-liquid interface becomes larger than diffusive speed of solute atoms and as a result, atoms of the solute are trapped inside the solid phase [22].

Different amount of undercooling can be applied to materials along with different cooling rates. There have been several studies on the microstructure of material with high amounts of undercooling and low cooling rates. For example, Kattamis et al. [23] reported solidification of a Fe-25wt.%Ni alloy undercooled to different temperatures. In this experiment, about 100g of the alloy were placed between layers of crushed glass inside an alumina crucible. A glass coating formed surrounding the molten alloy by melting the mixture of alloy and glass for several times. The possibility of nucleation in the liquid alloy starting from the crucible wall was reduced because of the glass coating. The melt temperature was measured using a thermocouple. Different levels of undercooling from 0K to as high as 300K was applied, and using optical microscopy, the structure of the solidified material was studied. Results showed that the structure

from dendritic to fine dendritic to multiple equiaxed grains was achieved by increasing the undercooling. In another study, Li et al. [24] produced different levels of undercooling in a $\text{Cu}_{70}\text{Ni}_{30}$ droplet produced via the emulsion technique (measured by a thermocouple). As a results of different undercooling values, different microstructures and mechanical properties were obtained in the droplets. By applying an undercooling of 13K, a dendritic structure was formed. By increasing the undercooling to 200K, fine equiaxed grains were formed. Improved mechanical properties were also reported in the consolidated material produced from the undercooled particles in the mentioned work. For example, a 160% increase in maximum elongation at 180K of undercooling was achieved as compared to samples with no undercooling.

Levitation melting technique is an effective way to obtain a specific undercooling in a droplet. This is another technique in which high amount of undercooling can be achieved with low cooling rates. This technique is used to levitate a droplet using electromagnetic forces without any contact with a solid or liquid medium, and offers the possibility of undercooling droplets [25]. Using Electromagnetic levitation (EML), it is possible to have a directly observe the undercooling and solidification of droplet. In order to prevent the nucleation to achieve the desired undercooling, there should not be any contact between the droplet and any contamination, since it starts heterogeneous nucleation. An optical pyrometer or photosensing diodes can be used in order to measure the temperature of the droplet. To start the

nucleation at a desired undercooling, the surface of the droplet is touched with an Al_2O_3 needle to start the nucleation at the surface of the droplet. Therefore, in the EML technique, it is possible to control the amount of nucleation undercooling in the droplets [5].

There is a relationship between the amount of undercooling, growth rate and crystal morphology. It is generally accepted that increasing the amount of undercooling also increases the dendrite growth rate (Figure 2.4).

In the levitation method, it is possible to study the effect of high undercooling values with low cooling rates. In atomization techniques (which will be discussed in next section), a high amount of undercooling can be achieved along with high cooling rates. In this process, however, it is not possible to control the time or temperature at which nucleation occurs.

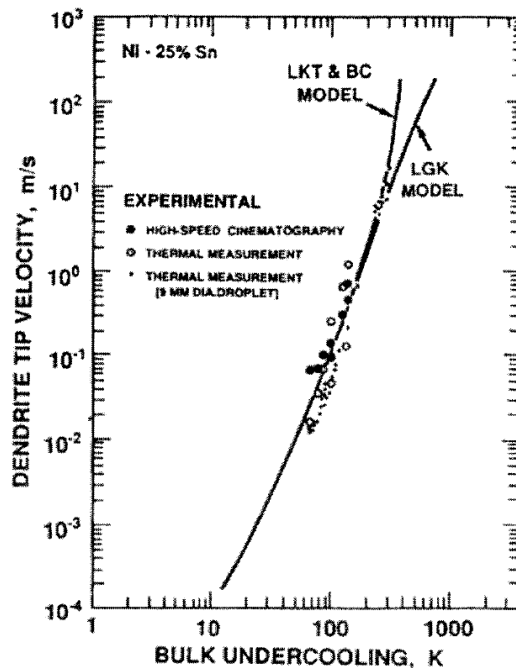


Figure 2.4. Effect of undercooling on dendrite growth rate for Ni-Sn alloy [26].

2.2.4. Atomization

It is widely accepted that the nucleation process is initiated by a heterogeneous process. In a large volume of a liquid, variety of nucleation sites are available and these nucleation sites can prevent achieving large undercooling values prior to solidification. If one transfers the liquid bulk into fine droplets, it is possible to isolate the potential nucleation centers into small fraction of droplets, instead of the whole liquid bulk. This leaves a large number of droplets without any nucleating sites. As a result, during cooling of the droplets, those with large fraction of nucleation sites experience low undercooling while the most of the droplets solidify with higher amount of undercooling. During atomization, small liquid metal droplets are formed and large values of undercooling can be achieved in the liquids with small nucleation centers [27,28]. Therefore, formation of small particles can result in higher cooling rates due to enhanced heat transfer, as well as larger possibilities in achieving higher levels of undercooling [29]. Therefore in an atomization process, various levels of undercooling in molten droplets are achieved and therefore different microstructures can develop in a rapidly solidified particle. Pryds [30] stated that the level of undercooling prior to nucleation can result in one or more of the following changes: 1) refined microstructure; 2) extension of solid solubility in the primary phase; 3) change in the morphology of eutectic and/or primary phase; 4) metastable phases formation. However, no undercooling data measured directly during the atomization process have been reported because of the difficulty to monitor the temperatures of small droplets

moving at relatively high velocity. One of the main objectives of this project is the evaluation of a method for measuring the undercooling of falling droplets generated via the IA method.

Due to the large amount of undercooling and cooling rate during the atomization process, rapid solidification is achieved during this process. Therefore, using atomization, it is possible to improve the properties final product. By changing the different parameters affecting the atomization process, it is possible to control the different characteristics (such as size and shape) of the produced powder [29,31–33]. For tool steels, comparing atomization and casting processes, carbide precipitates with more uniform size are formed in the products made from the atomization process [7].

2.2.5. Microstructure and properties

Microstructure and properties of rapidly solidified materials are different from those in the material which are solidified more slowly. The main differences are in morphologies, formation of non-equilibrium phases and extended solute solubility. The improvements achieved by rapid solidification can be in mechanical strength, corrosion resistance and magnetic properties [5]. Rapid solidification can result in formation of metastable phases in the final microstructure. As an example, according to phase diagram of high-chromium high-carbon steel shown in

Figure 2.2 (with 1.55 wt. % carbon), the formed phases at room temperature are ferrite and $(Cr, Fe)_7C_3$. But, it has been reported by several researchers [19,34,35] that by rapid solidification of this type of alloy, martensite and

retained austenite phases are found in the final microstructure. Al_6Fe (in Al-Fe system) and Al_4Mn (in Al-Mn system) are another example of the metastable phases reported in the final microstructure after rapid solidification [36–38].

During rapid solidification of tool steels, metastable austenite can be present in the microstructure even at room temperature as a result of high solidification rates. Bhargava [39] reported that by rapidly solidifying of D2 tool steel using the chill block melt spinning process (CBMS), metastable austenite form and martensite formation is completely suppressed. In fact, supersaturation of the austenite during rapid solidification lowers the martensite start temperature [39].

During rapid solidification process, finer carbides form compared to the microstructures the tool steels with slow solidification rate. Due to rapid solidification, carbide precipitate size is refined by 20 to 40 times compared to conventionally processed tool steels. It has been reported that carbide precipitates are about 20 times finer in overaged-rapidly solidified D2 tool steel ribbons compared to those in conventionally processed D2 steel [39].

Since carbide precipitation from a supersaturated solid phase (as a result of rapid solidification) plays an important role in defining the final microstructure and mechanical properties of tool steels, especially D2 steel, the following section will briefly present the fundamentals of solid state precipitation followed by the precipitation of carbides from a supersaturated matrix.

2.2.6. Precipitation in the solid state

According to Porter et al. [1], most of the phase transformations in the solid state occur by the temperature dependant atomic movements. One of the transformations in solid state is precipitation:



where F' is the metastable supersaturated solid solution, P is a precipitate (stable or metastable) and F is a more stable solid solution. F has same crystal structure as F' , but its composition is closer to equilibrium [1].

During precipitation in the solid state, two stages can be distinguished: nucleation and growth. During the first stage, nuclei of the new phase form from the matrix phase. New phase can nucleate preferentially at imperfection sites (e.g. grain boundaries). During the second stage, the nuclei which exceed a critical size, grow. The growth rate of the new phase is proportional to the amount of the untransformed matrix phase. Growth of the new phase is fast when it initially starts, but as the amount of the matrix phase decreases, the growth rate of the new phase also decreases [40].

One limitation of phase diagrams is that it is not possible to attain any information regarding the rate (e.g. the kinetics of a phase transformation). Using isothermal transformation diagrams (TTT), it is possible to get information regarding a transformation start and finish time, at a given temperature. Continuous cooling transformation (CCT) diagrams

can provide information regarding the transformation occurring during continuous cooling.

Figure 2.5 shows CCT diagrams for Cr12MoV tool steel at two different conditions: an as-received sample and a spray deposited sample.

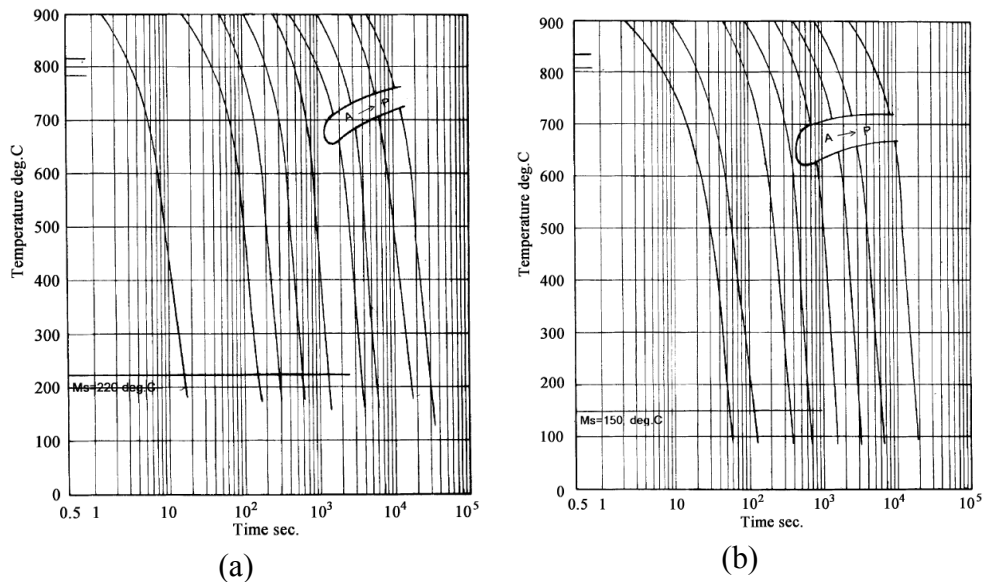


Figure 2.5. CCT diagrams of (a) an as-received and (b) an as-sprayed Cr12MoV steel, A: Austenite, P: Pearlie [41].

These diagrams can show what phases are formed at different cooling rates. By comparing the CCT diagrams for the as-sprayed steel and the as-received steel, it can be seen that the as-sprayed steel has a lower M_s temperature compared to that in the as-received steel. Because of rapid solidification during spray forming, austenite phase is supersaturated by the alloying elements which results in depression of the M_s temperature.

The TTT diagram for D2 tool steel is reported in Figure 2.6 [42]. This diagram shows the time required, at a given temperature, for austenite to transform (incubation time). It also shows the temperature at which, with

enough time, austenite begins to transform to pearlite and bainite. At low degrees of undercooling, it takes longer time for austenite to transform into pearlite. The transformation rate increases with decreasing temperatures, until it reaches a maximum at approximately at 650°C. The transformation rate decreases again at temperatures lower than 650°C. As a result, the TTT plots are in the form of the S-shape which show a nose at which there is a maximum transformation rate [40]. This is mainly because of the balance between the required driving force for the nucleation and movement energy needed for diffusion of atoms.

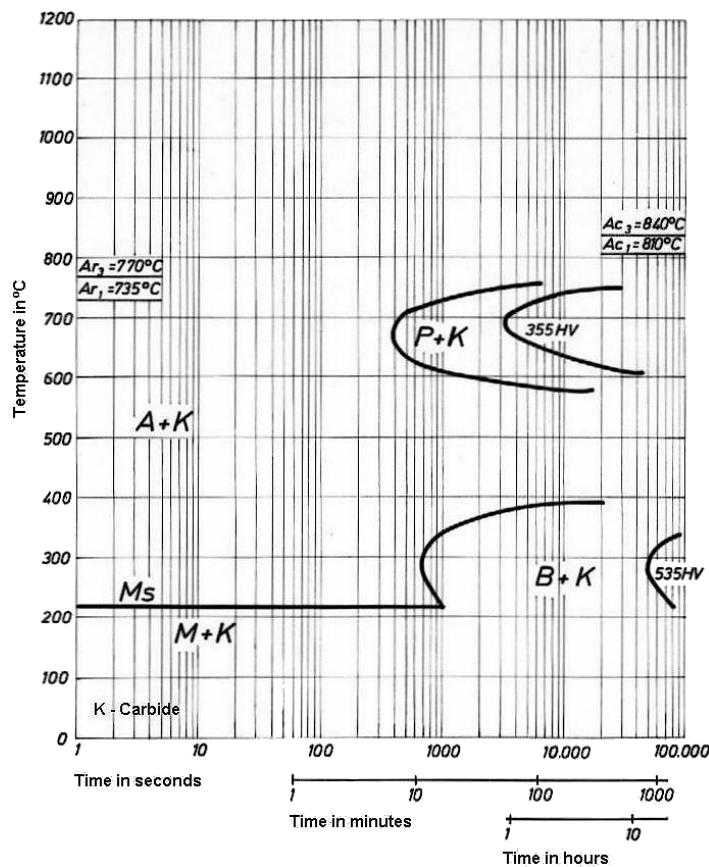


Figure 2.6. TTT diagram of D2 tool steel. Ms: Martensite start temperature, A: Austenite, K: Carbide, P: Pearlite, M: Martensite, B: Bainite [42].

2.2.6.1 Precipitation of carbides from a supersaturated matrix

Carbon stabilizes the austenite structure and there is a great thermodynamic affinity between carbon and chromium. Because of this affinity, whenever carbon reaches the level of supersaturation in austenite, chromium carbides form. In this condition, the diffusion rates are sufficient for carbon and chromium to form the precipitates [43]. In order to understand what happens during rapid solidification, it is important to determine the relationship between the cooling rate and the resulting microstructure. A rapidly solidified microstructure in a high alloy steel may consist of martensite and retained austenite phases which are supersaturated with carbon and other alloying elements. The thermodynamic driving force for precipitation of fine carbides during the tempering process is provided by this supersaturation. At the first stage of tempering, transition carbide precipitates, which can be either hexagonal ϵ -carbide ($\text{Fe}_{2.4}\text{C}$) or orthorhombic η -carbide [7,44,45]. Das et al. [35] did not find η -carbides during the analysis of precipitates in D2 steels. These carbides are not thermodynamically stable [45]. In the next stage, diffusion of carbon is increased and the retained austenite is transformed to ferrite and cementite [44,45]. In highly alloyed tool steels such as high speed and D-series tool steels, this transformation takes place at the higher temperatures [7]. In the subsequent stages, transition carbides convert to cementite. Also, previously formed carbides become more coarse [44]. As tempering continues, the ability of retained austenite to transform to martensite during cooling increases due to the precipitation of alloy carbides during tempering since it

removes carbon and alloying elements from the solution. According to Eq. 2.1, this increases the M_s . It will be discussed in the next section that due to the high cooling rate in rapid solidification process, alloying elements (mostly carbon and chromium) will supersaturate in the austenite. When the cooling rate increases, the A_{r3} line in the Fe-C phase diagram moves towards the lower temperatures. This shows that by increasing the cooling rate, the temperature of the eutectic (or eutectoid) transformation is lowered and also there are lower amount of carbon in the eutectic structure. This can also explain why austenite is supersaturated during rapid cooling.

Bhargava and Tiwari [39] showed that the value of the lattice parameter (a_0) of the retained austenite in D2 tool steels obtained from rapidly solidified processes is greater than that of the same steel obtained from conventional processed D2 steel. This is due to the supersaturation caused by rapid solidification. The a_0 of austenite in rapidly solidified D2 steel was about 1.5% larger than the lattice parameter of gamma-iron. This shows that substantial amounts of carbon and chromium are dissolved of in the austenite. Therefore, rapid solidification results in the formation of supersaturated metastable austenite and a decrease in carbide precipitation in D2 tool steel [39].

Bhargava et al. [39] showed that tempering rapidly solidified D2 tool steels up to about 1000K results in the decomposition of the metastable austenite. The lattice parameter of the supersaturated austenite matrix phase as a function of aging temperature is shown in Figure 2.7. By plotting the

percent of transformation, Y , as a function of aging temperature, it is possible to illustrate the austenite transformation to a BCC matrix phase.

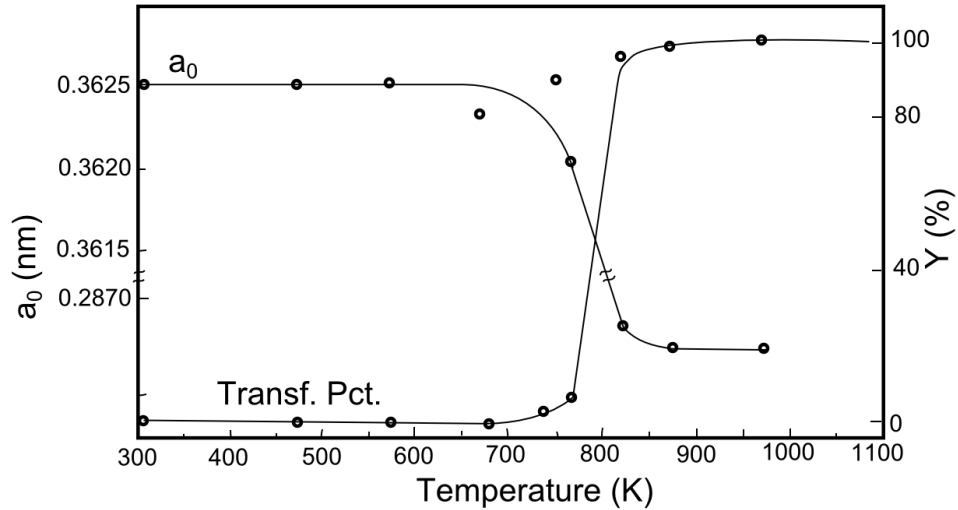


Figure 2.7. Lattice parameter (a_0), percent transformation (Y) of D2 steel as a function of temperature. Reproduced from [39].

Figure 2.7 shows that the value of lattice parameter of metastable austenite is constant (about 0.3625nm) at aging temperatures up to 723K. Aging between 773K and 823K shows a sharp drop in the a_0 value from 0.3620nm to 0.2868nm and there is not any significant change in the a_0 value above 823K. The observed drop is due to the decomposition of austenite to the ferrite phase. XRD analysis showed that M_7C_3 , Fe_3C and $M_{23}C_6$ are the types of carbide which precipitate during aging of D2 ribbons. Carbide precipitates in the tempered D2 steel have the size between 0.20 μ m and 12 μ m [39]. For high speed tool steels, Andren et al. [46] stated that different types of small carbides such as cubic MC and hexagonal M_2C (and in higher carbon alloys, $M_{23}C_6$) precipitate during secondary precipitation. They also showed that when the aging time increases, the

matrix composition is depleted of carbon, chromium, vanadium, and molybdenum, and the volume fraction of carbides increases. This increases the hardness of the steel. Andren et al. [46] believed that after tempering, substantial amounts of carbon and alloying elements (carbide forming elements) remain in solution. Therefore, during using of the tool, these element will act as a source for further precipitation [46]. However, Bhargava and Tiwari [39] showed that aging above a certain temperature (823K for D2 tool steel) does not cause any major change in the amount of precipitation transformation. According to Figure 2.7, precipitation transformation approaches 100% after ageing up to 1100 K, which means the precipitation transformation is completed. Das et al. [35] also showed that by increasing the heating time, the volume fraction of precipitated carbides increases and remains unchanged after a given time. This confirms Bhargava's results [39].

In order to understand the precipitation of supersaturated carbides, some information is required about the solubility of different carbides and their precipitation behavior in the liquid and austenite phase. During carbide precipitation, chromium will react with carbon to form chromium carbide. If there are other carbide formers such as vanadium and molybdenum, they may limit the available carbon for chromium and complex carbides will form.

Considering precipitation of Cr_7C_3 carbide during tempering of D2 tool steel, precipitation analysis for these precipitates are shown in this

section. But, in this study, the analysis on the precipitation behaviour of M_7C_3 carbides has been done using Thermocalc software which will be described in Section 6.3.4.

The solubility limit may be defined according to Eq. 2.7 and Eq. 2.8, (by assuming formation of one mole of Cr_7C_3) [47]:



$$k_s = \frac{a_{Cr_7C_3}}{(\gamma_{a[Cr]}[Cr])^7 \cdot (\gamma_{a[C]}[C])^3} \quad \text{Eq. 2.8}$$

where k_s is the equilibrium constant and γ_a is the activity coefficient. According to Gladman [47], activity coefficients for chromium and carbon, $\gamma_{a[Cr]}$ and $\gamma_{a[C]}$, are equal to unity (this is by assuming a low concentration of the components in the steel). The activity of pure Cr_7C_3 ($a_{Cr_7C_3}$) is equal to 1. The activities are directly proportional to the weight percentages and Eq. 2.8 will change to Eq. 2.9 [47]:

$$k_s = \frac{1}{[Cr]^7[C]^3} \quad \text{Eq. 2.9}$$

On the other hand, according the thermodynamic data provided by Eremenko and Sidorko [48], the standard free energy for Cr_7C_3 (ΔG°) at 298-1673K is:

$$\Delta G^\circ \left(\frac{J}{mole} \right) = -174473 - 25.73T \quad \text{Eq. 2.10}$$

More accurate thermodynamic data for each temperature can be found in the JANAF Thermochemical Tables [49].

According to thermodynamic information [50]:

$$\Delta G^\circ = -2.303 \times RT \log k_s \quad \text{Eq. 2.11}$$

From Eq. 2.9, Eq. 2.10 and Eq. 2.11, it can be concluded that:

$$k_s = [Cr]^7 [C]^3 = 10^{(-1.34 - \frac{9112.64}{T})} \quad \text{Eq. 2.12}$$

Using Eq. 2.12, it is possible to draw the solubility diagram for [Cr] versus [C]. Using this solubility diagram and using either the linear method or/and calculation methods proposed by Gladman [47], it is possible to determine the equilibrium concentration of chromium and carbon in the liquid or austenite phases (depending on the temperature used in Eq. 2.12). The only remained requirement is the chemical composition of the supersaturated matrix. If one uses the solubility diagram for chromium carbide, it is possible to calculate how much chromium carbide should precipitate in the supersaturated matrix at the temperature at which the solubility diagram is plotted.

There are some limitations using this method. The most significant limitation of this method is the existence of complex carbides. For example, carbides in tool steels are usually in the form of $M_n C_m$, where M can consist of different elements such as iron, chromium, molybdenum, vanadium, etc. This complicates the associated equations and makes it difficult to find the true solubility constant. There is not enough research focused on the relationship between precipitation from supersaturated matrix and

solidification conditions. Further research needs to be conducted on this subject.

Tool steel (exclusively D2 tool steel) properties and their microstructure were mostly discussed in the previous sections. Solidification path, carbide precipitation and phase transformation as a result of rapid solidification were also introduced. The following section will describe methods that can be utilized in order to rapidly solidify D2 tool steel. Thus, the following section mostly addresses some common atomization techniques of relevance to this work.

2.3 Rapid solidification techniques

Different processes are available to achieve a rapidly solidified microstructure. These methods can be categorized to spray spinning, chill methods, surface melting and weld technologies [51,52].

In the melt spinning process, liquid metal is exited from a nozzle in the form of a jet on the surface of a wheel which is rotating fast. As a result, long thin ribbons form. Cooling rates between 10^5 and 10^7 Ks^{-1} have been achieved using this method [30]. In the chill method process, a thin layer of liquid metal is deposited on a substrate with low temperature. The melt loses heat through the chilled substrate and rapid solidification occurs [51]. In the surface melting technologies, the surface of sample is rapidly melted. This is followed by a rapid freezing which is due to the rapid heat extraction from the surface to the bulk of the sample. In these methods, it is possible to

achieve high undercoolings (hundreds of degrees Kelvin) with cooling rates of 10^{10} Ks^{-1} in a small cross sections (as small as $0.1 \mu\text{m}$) with [51].

In the spray technologies, a bulk liquid is breaking up into individual droplets. These droplets then rapidly solidify by rapid heat loss. Atomization is the method that can produce metal droplets. Metal particles are produced by injecting gas or water into a stream of molten metal. The molten metal is then broken into spherical droplets. This technique is considered a containerless method which can provide non-equilibrium microstructures. Atomization can be divided into single-fluid and two-fluid atomization methods. Gas Atomization (GA) and Water Atomization (WA) are the most well-known two-fluid atomization methods. In two-fluid atomization, the melt is disintegrated by blowing high pressure fluid (e.g., gas or water). After disintegration, the atomized droplets fall through a cold medium and rapidly solidify. In single-fluid atomization, the melt stream becomes unstable as a result of Raleigh instability in a stagnant gas atmosphere [53]. Impulse Atomization (IA) and centrifugal atomization can be categorized under single-fluid atomization techniques [54].

2.3.1. Gas atomization (GA)

The GA process is one the most common powder production technique. In this is the two fluid technique, a fairly broad particle size distribution ($\sigma=1.9-2.2$) can be achieved [55], where σ is the geometric standard deviation. GA is a relatively old technology. This technique have been used since the 1930's [30]. In GA process, the disintegration of a liquid metal

stream is happened by a high-velocity gas jet. As a result, spherical droplets form which then cool down while they are falling in the atomizing tower [56].

Properties of the products that are made from atomization metal powders depend on different parameters such as particle shape, size, size distribution and particle chemistry. A large number of the process variables should be considered in GA to control powder properties. These variables are metal viscosity, surface tension of the liquid, amount of superheating, diameter of the nozzle, geometric configuration between melt nozzle and gas jets, atomization pressure and velocity of the atomizing fluid. The relationship between the process parameters in GA and the resulting microstructure has been published for many alloy systems, such as aluminum [56,57] and ferrous alloys [58].

It has been reported that in GA, since high pressure gas is blowing, a significant velocity gradient forms in the droplet in both radial and axial directions. This phenomenon is different based on the design of the atomization unit. For example the design of gas nozzles and position of gas jets affect the GA results. The result is a wide droplet size distribution, in which there is a different local gas velocity and temperature for each droplet [54,59]. Also, Freyberg et al. [60] showed that there is a level of two-way thermal coupling in GA particles. Briefly, because of high quantity of gas with high velocities, there is high efficiency in heat removal from droplets in GA. Since there is a low relative velocity between the gas and droplet,

the temperature of the gas increases and as a result, the subsequent heat removal from droplets is reduced. Depending on how much the thermal coupling effect happens and how the droplets move with the atomizing gas, the microstructure varies in GA particles. Therefore, it is difficult to understand the effect of individual process variables on the characteristics of solidified droplets [54].

2.3.2. Water atomization (WA)

It has been stated that WA is probably the cheapest method to produce powders in most metals which is broadly used in the powder production of iron and stainless steel [61]. The particle size in WA depends on the water velocity. Other effective variables are superheat, water/metal mass ratios and chamber cooling atmosphere [62].

The most distinguishing characteristic of the powders produced via WA from GA is the particle shape. The GA powders are generally spherical and have smooth surface texture, while in the WA powders, irregular, ligamental structure and coarser surface texture can be found [62]. Figure 2.8 shows SEM micrographs of a GA and WA of H13 tool steel powder.

Both WA and GA powders show a log-normal size distribution, although there is slightly lower standard deviation in the distribution of the GA powder. It has been noted that the surface oxide layer on WA particles is normally less than 20nm thick. Also, EDS (energy-dispersive x-ray spectrometry) analysis of laser melted GA and WA powder particles

revealed a higher oxygen level on the surface of the WA powder samples than that on the GA powder samples [63]. Formation of Fe_3O_4 type of iron oxide has been reported on the surface of WA tool steels [62].

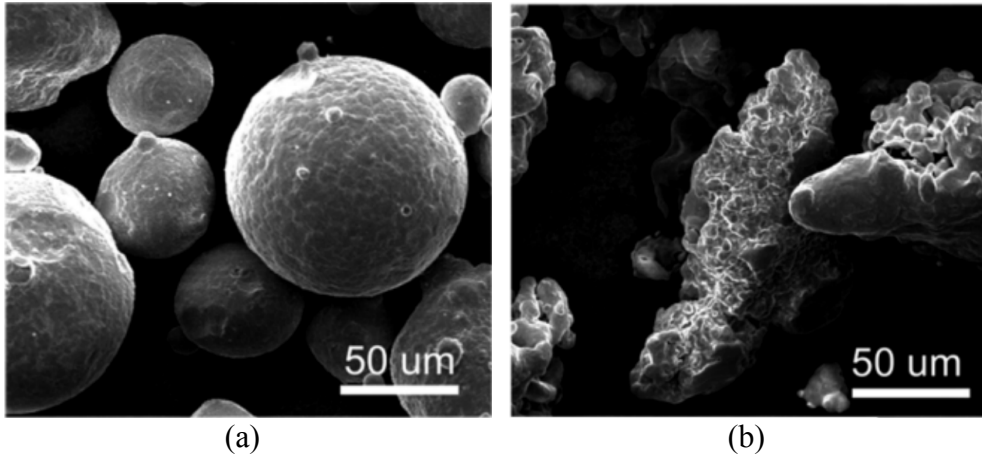


Figure 2.8. SEM images of (a) gas-atomized and (b) water-atomized H13 tool steel powder [63].

2.3.3. Impulse atomization (IA)

This method was developed and patented at the University of Alberta, Canada [64]. Figure 2.9 shows a schematic of the atomization unit.

In IA unit, liquid metal forms by the heat generated from an induction furnace (3). The pulsator (1) then moves the impulse applicator (2) and by movement of the impulse applicator, energy transfers to the liquid metal and feeds the liquid metal through the orifices inside the nozzle plate at the bottom of the crucible. This provides liquid metal stream and the surface tension of the liquid results in instability of the stream and breaks up the liquid stream into the smaller droplets. Nitrogen or helium gases are available in the IA tower as cooling media and therefore, droplets

with different sizes experience rapid solidification during their free fall. Produced powders then can be collected at the bottom of the tower.

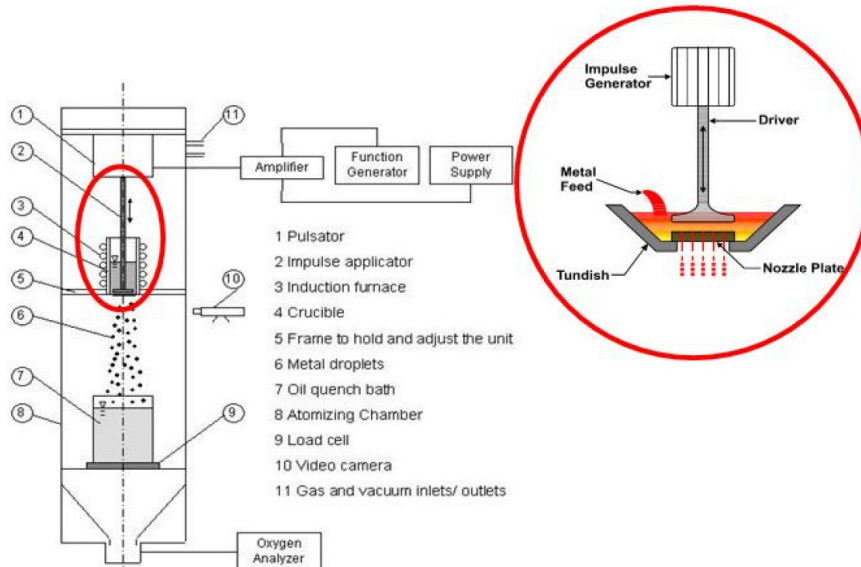


Figure 2.9. Schematic of the IA unit. The numerical labels describe the different parts of the unit [53].

Two IA units are used in the current study. Both are atmospherically sealed and can be filled with different gases which, for this study, are helium and nitrogen (or argon). In both units, the impulse unit is located at the top part of the chamber. Also, there is an induction coil in the top part of the units which prepares the melt. After melting, the melt is pushed through the holes in the nozzle plate. One of these units is about two meters tall, half a meter deep and three meters wide on which the some online measurement devices have been installed and is referred to as the “Box Tower.” The other unit is longer in length (four meters) and half a meter in diameter. It is referred to as the “Small Tower.” The former is used for in-situ

measurements of droplet properties. The latter is used to generate samples of the powder and spray deposits.

Prasad [5] has stated that the IA process can yield rapidly solidified powders with a narrow size distribution and a cooling rate as high as 10^4 K/s. Since there is a stagnant gas used in this process, it is easier to study and model the behavior of the droplets. Wiskel et al. [21] concluded that because heat flow conditions are known for the IA method, IA is a suitable method in order to understand the solidification phenomena during free fall. Therefore, IA is used for experiments in this study. Also, Prasad et al. [65] showed that the internal circulation inside the droplets is limited in the IA technique. Depending on the viscosities of the droplet and surrounding fluid, some internal circulation may happen inside the droplets. According to the high ratio of viscosities of the droplet and surrounding media, produced droplets with IA experience limited internal circulation. Comparing to the electromagnetic levitation methods, this limited circulation can be considered as an advantage [22], where there are strong internal flows inside the particles which affect solidification of the droplets.

IA has been chosen in this work to rapidly solidify D2 tool steel. During IA, droplets are falling through a stagnant media and there is no agitation of droplets and media (like GA and WA). Therefore, the conditions at which gas behaves around the droplet are simpler compared to GA and WA. Therefore, it is easier to model behaviour of droplets (temperature and velocity) during free fall. As a result, there is a greater

likelihood to reproduce the atomization conditions for each droplet in order to do better quantitative analysis. Also, WA D2 steel powders will be used in order to compare the results from a bench mark process (IA) with an industrial process which is used to produce D2 powders.

2.3.4. Spray deposition

Among the various rapid solidification techniques, spray deposition processes are of interest to produce near-net-shaped products since they can provide fine grained materials with high deposition rates in the range of 0.25-2.5 kg/s [66]. The general principle of spray deposition technique is to deposit a distribution of droplets into a mould or onto a substrate. These droplets can be in the form of either fully liquid or semi-solid droplets, when they hit the substrate [66]. As discussed by Grant [67], one of the advantages of this process is a very fine scale microstructure with low levels of segregation, formation of fine precipitates and extended solid solubility of the alloying elements. Formation of porosity in the final product is one of the main disadvantages of this method. Final products are usually consolidated to achieve full density by means of different techniques such as extrusion, hot/cold rolling or hot isostatic pressing (HIP).

Different methods such as plasma arc or induction furnace can be used to melt the materials in the spray deposition technique. In plasma deposition, the initial material is the solid powders which then melt through the hot plasma and are deposited on the substrate. The metal droplets can

also be produced with atomization techniques (mostly gas and centrifugal atomization) and then impinge on the substrate [66]. Spray deposition also has been done on alloys including Al-Fe and Cu-Sn using the IA technique [68,69].

Clarification of several important factors is required to understand the evolution of microstructure in spray deposited materials. Understanding the fraction of the solid and the temperature of the droplets are necessary in order to better establish the initial conditions for depositions. Another important factor is the thermal and solidification conditions present during deposition. Using equations presented in Section 2.4, it is possible to estimate the temperature and solid fraction of a droplet as a function of droplet diameter and time (or flight distance). Also, during atomization, it is important to investigate the effect of droplet size on the solidification history since a broad range of particle sizes is produced [66].

The microstructural image of a study about spray deposition of Al-4wt.%Cu by Grant et al. [70] is shown in

Figure 2.10. This figure shows that close to the substrate, where cooling rate is high, finer grains have been formed. It can be seen from this figure that by going through the thickness of the sample to the surface, coarse grains have been formed. Grant et al. [70] reported that the average grain size close to the substrate was approximately 30 μm , while the grain size in the middle region was 75 μm .

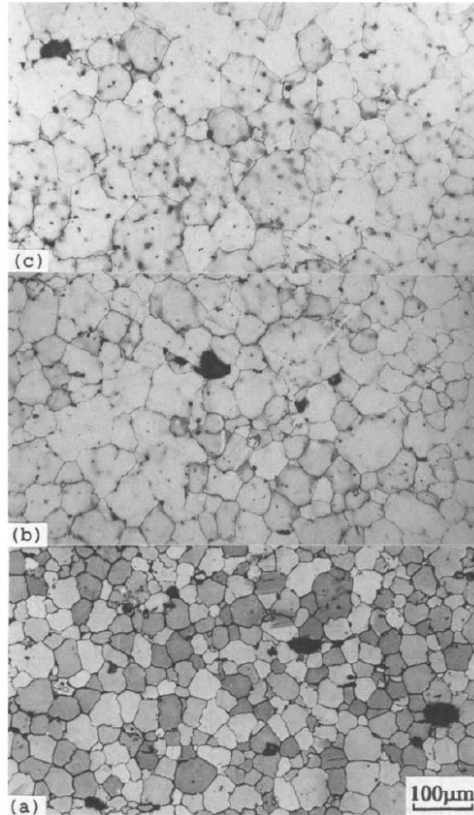


Figure 2.10. Microstructure of spray deposited Al-4wt.%Cu in various locations: (a) adjacent to the substrate, (b) in the central portion and (c) near the upper surface [70].

2.3.4.1. Porosity

One of the characteristics of spray formed materials is porosity. Different reasons, such as gas entrapment and inadequate liquid feeding due to solidification shrinkage and rapid cooling, can result in the formation of porosity in the deposit [66]. Based on the application of the spray formed samples, there is a need to reduce the amount of porosity in the sample (for example, in the applications which require high strength, there is a need to have low amount of porosities). Also, in applications such as damping, self-lubrication and thermal insulation, certain amount of porosity is required.

Therefore, for applications in which high strength is required, the goal is to reduce the amount of porosity in as-sprayed sample. This will reduce post-processing steps such as forging, pressing, HIPing or CIPing [71].

Some works show that parameters such as surface temperature of the deposit and impact angle of droplets are effective in porosity formation [71]. One method to quantify the porosity level is sample density measurement and its comparison with the theoretical density:

$$P = \left(\frac{\rho_t - \rho_m}{\rho_t} \right) \times 100 \quad \text{Eq. 2.13}$$

where P is porosity level, ρ_m is the experimentally measured density and ρ_t is the theoretical full density.

Porosity level is different at different part of the spray deposited sample. This is due the fact that there are different solidification conditions at different regions of the spray deposited sample. For example, in the radial distance from the centerline, Schaeffler et al. [72] measured the porosity content of a high-strength low-alloy steel (HSLA) spray deposit. The results show that at 20mm above the substrate, by increasing the radial distance from the centerline, porosity increases from 0.12% to 16.2% from centerline to 12cm from the centerline. Another factor affecting the porosity level is the deposit thickness. In the same work by Schaeffler et al. [72], porosity of the deposit at different heights was also measured. They reported that the porosity of a HSLA deposit is higher in the area close to the substrate and by going toward the top part of the deposit, the porosity level decreases

(from 7.4% porosity in the bottom part to 0.09% porosity in the top part of deposit). Three different regions are available for porosity distribution in a deposit: an upper band (surface porosity), a lower band (substrate porosity) and a central portion (steady state porosity). The amount of porosity in both upper and lower bands of the deposit are relatively high, while there is less porosity in the central portion [73,74]. As stated by Apelian et al. [75], in the initial stages of deposition, the deposition rate is higher than the amount of heat introduced to the deposits. Therefore, in the first millimetre of the deposit, some interconnected porosity form. When the metal-to-gas ratio in gas atomization systems is reduced, some porosities can form at the surface of the deposit. Also, at the end of the deposition, sometimes the spray formation is not consistent and as a result, there is not enough liquid to fill the spaces between the droplets. Steady state porosity which forms in the bulk of the deposit, contains less porosity with small diameters (less than 1% porosity with the pores $<1\mu\text{m}$ in diameter in HSLA)[75].

The effect of deposition distance on the steady state porosity level was studied by Grant and Cantor [76]. It has been argued that when there is not enough liquid in the spray deposited samples, porosity level also increases. Uhlenwinkel and Ellendt [71] also showed that increasing the surface temperature of low carbon steel deposit results in a low amount of local porosity. They showed the same effect on spray formed Inconel 718 alloy. Substrate porosity is formed in the deposit close to the substrate since there is high thermal extraction from droplets when they hit the substrate.

Annavarapu et al. [77] reported that in low carbon steel deposits, the amount of steady state and substrate porosity decreases by decreasing the deposition distance. This can be due to the fact that by reducing the deposition distance, there would be a higher temperature and a larger fraction of liquid which can reduce the fraction of porosity formed in the deposit.

During atomization of droplets and spray deposition, the main factor for controlling the cooling rate of the droplets is the heat extraction mode from the droplet to the surrounding atmosphere. Therefore, it is important to understand the heat loss of the droplets during their free fall.

2.4. Modeling of heat loss during droplet free fall

One of the most important parameters during solidification of a droplet is heat flow. Therefore, understanding the thermal transport between a droplet and a surrounding gas medium is essential. Cooling rate, droplet temperature at different heights and droplet flight time can be better understood by understanding the thermal history and the trajectory path of the falling droplets during free fall. The model can calculate droplet velocity and temperature as a function of time and distance traveled. When a molten droplet is moving down through a cooling surrounding atmosphere, there will be thermal energy transfer within the droplet by conduction. There will also be convection, conduction and radiation between the droplet and surrounding gas [78]. The heat energy loss at the droplet surface is shown by Eq. 2.14:

$$q = h_{eff}A(T_m - T_0) \quad \text{Eq. 2.14}$$

where h_{eff} is the effective heat transfer coefficient and consists of the additive contribution of the convection, the conduction and the radiation heat transfer mechanisms between the falling droplet and surrounding gas. A is the surface area of the droplet, T_m is the droplet surface temperature and T_0 is the surrounding gas atmosphere temperature [78].

Droplets begin their free fall with an initial velocity. The trajectory of the droplets depends on their initial velocity and the forces of gravity, buoyancy and drag as shown schematically in Figure 2.11.

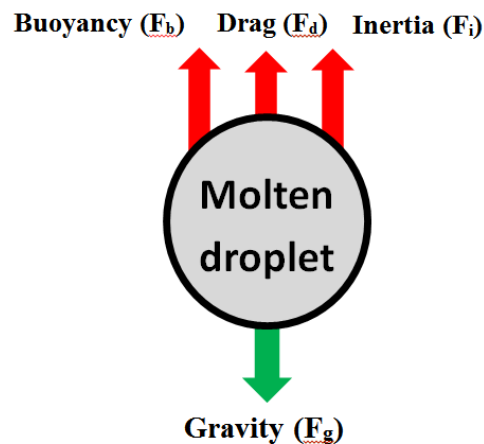


Figure 2.11. Schematic of the forces acting on a falling droplet [79].

The main forces acting on a falling droplet are gravity $F_g=m \cdot g$; inertia $F_i=m \cdot a$, with a being the acceleration, F_b the buoyancy force and the drag or resistance force F_d with the drag coefficient C_d . When a metal is moving inside a gas, the buoyancy effect can be neglected since there is a large difference between density of the metal and the surrounding gas. Therefore, the balance of forces can be written as:

$$\rho_p \cdot V_p \cdot \frac{dv}{dt} = \rho_p \cdot V_p \cdot g - \frac{\rho_g}{2} \cdot v^2 \cdot A \cdot C_d \quad \text{Eq. 2.15}$$

where ρ_p and ρ_g are the density of the particle and surrounding gas, A is volume of the droplet, v is the relative velocity between the falling droplet and gas, d is the droplet diameter and V_p is the droplet volume [80]. The drag coefficient can be calculated by an empirical equation:

$$C_d = 0.28 + \frac{6}{\sqrt{Re}} + \frac{21}{Re} \quad \text{Eq. 2.16}$$

where Re is the Reynolds number ($0.2 < Re < 2 \times 10^3$) and for a particle with diameter d, that moves in a gas with the dynamic fluid viscosity of μ_g , Re equal to,

$$Re = \frac{\rho_g \cdot v \cdot d}{\mu_g} \quad \text{Eq. 2.17}$$

Substituting Eq. 2.16 and Eq. 2.17 in Eq. 2.14 gives:

$$\frac{dv}{dt} = \frac{(\rho_p - \rho_g)g}{\rho_p} - 0.21 \frac{\rho_g v^2}{\rho_p d} - 4.5 \frac{\rho_g^{0.5} \mu_g^{0.5} v^{1.5}}{\rho_p d^{1.5}} - 15.75 \frac{\mu_g v}{\rho_p d^2} \quad \text{Eq. 2.18}$$

By numerical integration of above equation, time, t, can be calculated. Eq. 2.18 is valid until the droplet reaches its terminal velocity when its acceleration becomes zero. After that point, calculation of the time of the flight for each particle becomes straightforward.

To calculate the thermal history of a falling droplet, Eq. 2.14 is used which described the rate of heat energy loss from the surface of the droplet to the surrounding gas. Since the internal temperature gradient within the

droplet is negligible (Biot <0.1), In Eq. 2.14 equation, it is assumed that the surface temperature of the droplet represents the temperature of the droplet [78]. Temperature increase due to surface oxidation is also assumed negligible. The following equation gives the general heat transfer equation for a droplet of mass m_p [81]:

$$m_p C_p \frac{dT_p}{dt} = -hA(T_d - T_g) - A\varepsilon\sigma(T_p^4 - T_g^4) + \rho_p V_p H_f \frac{df_s}{dt} \quad \text{Eq. 2.19}$$

where V_p is volume of the droplets, ε is emissivity, d is the droplet diameter, f_s is the solid fraction, σ is the Stefan-Boltzman constant, T_d is the droplet temperature, T_g is the gas temperature, ρ_p is the droplet density and C_p is heat capacity of the gas. Before nucleation starts, the last term on the right-hand side of the Eq. 2.19 is zero. Therefore, it possible to calculate the temperature history of the droplet before solidification starts. In Eq. 2.19, h , the heat transfer coefficient (convective component of h_{eff}), can be calculated through the use of semi-empirical equations (e.g., Ranz-Marshall or Whitaker) [5,78] where the Nusselt number (Nu) is averaged over the entire droplet surface:

$$Nu = \frac{h \cdot d}{k_g} = A + B \cdot Pr^m \cdot Re^n \quad \text{Eq. 2.20}$$

where the Prandtl number, Pr , in Eq. 2.20 is given by:

$$Pr = \frac{C_p \mu_g}{k_g} \quad \text{Eq. 2.21}$$

and k_g and μ_g are the conductivity and viscosity of the gas, respectively, and all other parameters are constants.

When a droplet falls through a stagnant gas, it loses heat to the gas. After reaching a certain temperature, which is less than its equilibrium melting temperature (point C in Figure 2.12), the droplet starts to solidify. During this stage of solidification, the release rate of the latent heat of solidification is greater than the heat removal at the surface of the droplet. Therefore, the droplet's temperature goes up which is called recalescence (C-D in Figure 2.12). During recalescence, the solid interface grows with a reduced velocity. As a result, the evolved latent heat is reduced. This ends the period of recalescence and the temperature of droplet starts reducing again.

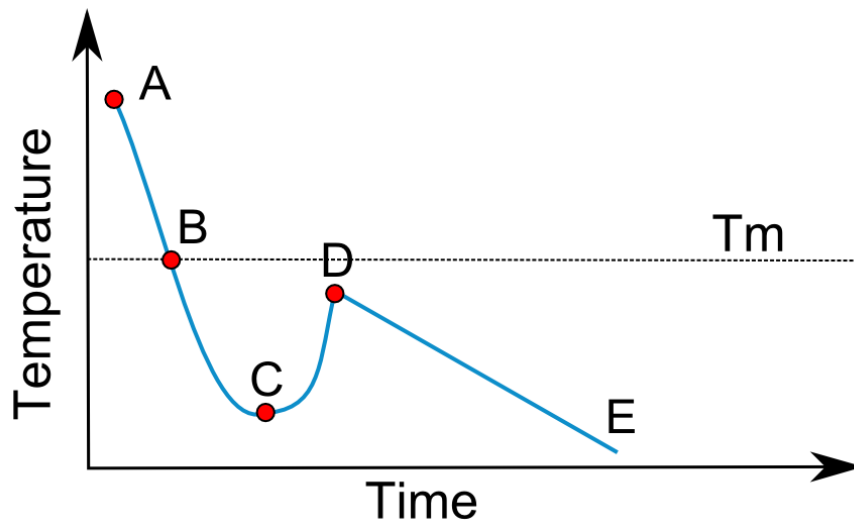


Figure 2.12. Cooling curve of a falling droplet in an atomization chamber. Undercooling (B-C), Nucleation point (C), Recalescence (C-D), Post-recalescence solidification (D-E).

2.5. Methods of characterization

One of the widely used characterization methods is optical microscopy (OM). The limitation of optical microscopy in the context of this study is that it is only useful for large precipitates (several microns in size). Scanning electron microscopy (SEM) is suitable for precipitates as small as 100nm in size. By using SEM, composition analysis through energy dispersive X-ray (EDX) analysis can be also obtained [82]. Using Transmission electron microscopy (TEM) analysis, it is possible to get information from composition, morphology, and size of individual precipitates [83]. XRD is another method which is widely used for phase identification, lattice parameter determination and thin film characterization. Basically, when the incident x-ray beam is diffracted from different planes of crystal lattice, a diffraction pattern is created which is the characteristic of the sample [84]. It has been shown that the thickness of materials required to absorb 50% of the beam ($t_{50\%}$) of the x-ray for Fe is about 0.29×10^{-5} m and for Al is about 0.53×10^{-5} m [85] which shows that XRD is a near-surface analysis. Another diffraction method that can generate information from the bulk of the sample is Neutron Diffraction (ND).

In ND, the $t_{50\%}$ distance for Fe and Al has been reported as 0.62×10^{-2} m and 7.05×10^{-2} m, respectively. Also, linear absorption in ND is much smaller than that in X-rays [85]. Neutron beam has relatively low intensity which makes it as one of the limitations of this technique. Therefore, in order to

obtain reliable information from the sample, a large volume of sample and/or longer analysis times are required. It has been reported that powder diffraction using ND technique typically takes 12 hours [85]. Same fundamental equations as X-rays are governing neutron powder diffraction. In order to produce neutrons, high energy protons collide with a heavy metal target, producing approximately 5 to 30 neutrons per proton [85].

In a powder diffraction pattern, there are a set of peaks which are placed over a varying background. Rietveld analysis technique can generate lots of useful information by fitting the ND and XRD peaks. This will be discussed next.

2.5.1. Rietveld refinement analysis

The Rietveld refinement analysis is based on a least-squares approach, which can refine a theoretical line profile until it fits the experimental diffraction profile. If one assumes that ϕ is the difference between a calculated profile, y^{calc} , and the experimental profile, y^{obs} , the Rietveld refinement principle is to minimize the function ϕ [54,82]:

$$\phi = \sum_i w_i [y_i^{obs} - y_i^{calc}]^2 = Minimum \quad \text{Eq. 2.22}$$

where w_i is the weighting factor for each observation point.

Using a diffraction pattern, it is possible to obtain information about peak positions and intensity. By finding the peak positions, it is possible to understand the unit cell dimensions, lattice parameters and space group. This is because peak positions are indicative of the crystal structure and

phase symmetry. Since peak intensities show the total diffraction from each plane in the crystal structure, therefore, peak intensities are based on the atom distribution in the crystal structure. It has been stated that the peak intensities are correlated to the phase structure [82]. Therefore, different information such as atomic positions and phase compositions (atomic occupancies) can be deduced from the peak intensities.

As previously discussed, it is possible to do quantitative phase analysis on the powders by using Rietveld refinement techniques [86]. For powders generated with IA, ND has been used for phase identification and phase quantification using the Rietveld analysis. Prasad et al. [87] were able to quantify the amount of microsegregation during rapid solidification of Al-Cu alloys. They produced Al-Cu alloys powder using IA with three compositions of 5wt.%Cu, 10wt.%Cu and 17wt.%Cu in nitrogen and helium cooling gas. Using Rietveld analysis on ND data as well as image analysis of SEM images, they were able to determine the weight percent of eutectic microstructure. They could show that by increasing composition of copper, the microsegregation decreases. They also found that there is a small effect of the cooling rate on the microsegregation. In another work, Ilbagi et al. [88] produced $\text{Al}_{68.5}\text{Ni}_{31.5}$ alloy powder using the IA method. A profile refinement using the GSAS computer code (General Structure Analysis System) on ND and XRD showed that only three phases (i.e. Al_3Ni_2 , Al_3Ni and Al) existed in the entire investigated particle range.

2.6. Thesis objective

As discussed in the previous section, undercooling and cooling rate are two important factors determining final microstructure and phases of solidifying materials. During ingot casting of tool steels, low cooling rate and undercooling values are achieved and result in formation of coarse microstructure and carbides. High undercooling and cooling rate can be achieved in atomized rapidly solidified tool steel, which can modify the final microstructure and mechanical properties. It was shown in previous sections that various rapid solidification techniques such as gas atomization, laser melting and the chill block method have been used to study the microstructure and carbide formation in some ferrous alloys. However, systematic and quantitative experimental work on rapid solidification of D2 tool steels is still lacking (especially on the effect of high undercoolings and cooling rates that can be achieved during atomization). In this work, the IA technique is used as a method to create rapidly solidified particles of D2 tool steel alloy to achieve the following goals:

- To study the effect of rapid solidification on D2 tool steel and quantitatively investigate the effect of undercooling and cooling rate on the microstructure.
- To study the effect of undercooling and cooling rate on the annealed particles to investigate the carbide precipitation behaviour of rapidly solidified D2 tool steel particles.

- To investigate the effect of rapid solidification on the microstructure of spray deposited D2 tool steel.
- To explore the possibility of using online measurement devices to measure the amount of undercooling while the droplets are cooling in free fall.

D2 tool steels are widely used in industry because of their good wear and abrasion properties and their high volume fraction of carbides. It is believed that these excellent mechanical properties can be modified by reducing microsegregation and by evenly distributing carbides during solidification processing. Understanding the rapid solidification phenomenon of D2 tool steel in order to develop particles with a fine microstructure and fine, well-distributed precipitated carbides offers a valuable opportunity to refine the microstructure of products produced from D2 steel droplets.

Chapter 3

3. Experimental Procedures

In order to study rapid solidification of D2 tool steel, both experimental and modelling efforts are needed. In the experimental work, powders of D2 tool steel were generated. To conduct a containerless solidification technique, the IA technique was used to produce rapidly solidified D2 tool steel powders. The IA technique was briefly described in the previous chapter. In this chapter a more detailed description of the atomization technique will be addressed. In addition, sample preparation and characterization methods used will be discussed. Sensors used for online measurements of the falling droplets during atomization will also be explained briefly at the end of this chapter. The online measurement tools are discussed specifically in Chapter 5. More detailed information about each experimental procedure, when required, is given in the related chapters.

3.1. The melting, atomization and spray deposition of molten D2 steel

In the previous chapter, a brief description of the IA method was given. The melting and atomization of molten D2 steel will be explained in the following section.

3.1.1. Atomization and spray deposition

The D2 steel bars (from Bohler-Uddeholm, product number C0795749) with chemical composition shown in Table 3.1 were cut into small pieces

and then ground to remove any surface paint, oxide layer and contamination, ensuring that each piece of material was clean.

Table 3.1. Chemical composition of D2 tool steel used in this study

Chemical composition (wt. %)					
Carbon	Manganese	Chromium	Molybdenum	Vanadium	Silicon
1.55	0.40	11.80	0.80	0.80	0.30

To avoid having the D2 steel react with the crucible, alumina crucibles were used with a purity of >99.6% and maximum working temperature of 1750°C (from AdValue Technology, part number AL-2250) which provides good chemical resistance at high temperatures. Since an induction furnace was used to melt D2 tool steel, a graphite crucible slightly larger in diameter than the alumina crucible was used as a susceptor. The nozzle plate at the bottom of the crucible was made of high density, high purity alumina and was drilled with 37 holes, each plate with a diameter of 100µm, 300µm and 500µm. The set of alumina-graphite crucibles were placed inside a copper coil at the top of the atomization tower. A 20kW solid-state induction power supply system VIP-1 from INDUCTOTHERM was used for heating. An alumina plunger and a Type C thermocouple (with 1% error) covered with an alumina tube were also placed inside the crucible. The atomization tower was then closed and sealed. The gas inside the tower (helium or nitrogen) was purged out and back filled three times before starting heating. The oxygen level within the tower before melting

and atomization was kept to less than 10ppm (measured using a model 2D solid state ZrO₂ sensor from Centorr Vacuum Industries). Since the alumina parts inside the setup are sensitive to thermal shock, a slow heating rate of 150°C/hour was used for the first 1.5 hours. Heating (with a higher rate) continued until the crucible contents were melted (about 500g D2 tool steel ingot).

The alloy was kept at 1600°C (about 200°C) superheat for about 30 minutes to make sure that the melt was completely homogenized. The amplitude and frequency of vibrating plunger were controlled using an impedance head (SVS Company, product number 5860B). A frequency of 80Hz was applied to the plunger to break up the liquid stream into droplets with different diameters. The droplets fell through a static inert gas atmosphere of helium or nitrogen solidifying during their free fall. The powders were solidified by the time they reached a high temperature oil quench bath 4m below the atomizing nozzle in the small tower. The oil type used was Galden perflourinated fluid – HT230 supplied by Ausimont. The small tower was used to produce the individual D2 steel powders.

The powders produced and collected in an oil beaker were washed using toluene and ethanol to remove the oil residue on the powders. The remaining ethanol was then removed by drying the particles under a fume hood. Dried powders were weighed and sieved using a RO-TAP sieving machine (model number RX-29) for 20 minutes and categorized into different particle size ranges according to ASTM E-11 [89] specifications.

A Gilson sieve set with a stainless steel frame and steel wire grid was used for sieving. After sieving, powders with different particle size ranges were weighed and kept in separate glass containers. Collected powders were then analyzed based on a log-normal distribution to calculate mass median particle size (D_{50}) and controlled log-normal standard deviations ($\sigma=D_{84}/D_{50}$).

Table 3.2 shows the atomization run conditions as well as the particle size distribution of powders from sieve analysis.

Table 3.2. Atomization run conditions as well as particle size distribution of produced powders

Run#	Atomization gas	#of holes, orifice diameter (μm)	D_{50} (μm)/ σ^*
111210	Helium	37, 300	385/1.26
111206	Nitrogen	37, 300	405/1.35
110112	Helium	3, 500	780/1.16
110118	Helium	5, 400	600/1.38
110126	Nitrogen	97, 400	500/1.16
100310	Nitrogen	37, 500	890/1.4

$$* \sigma = \frac{D_{84}}{D_{50}}$$

A schematic of the IA unit used for spray deposition is shown in Figure 3.1.a. An image of spray deposition of Cu-6wt.%Sn alloy using the IA unit is also shown in Figure 3.1.b [68].

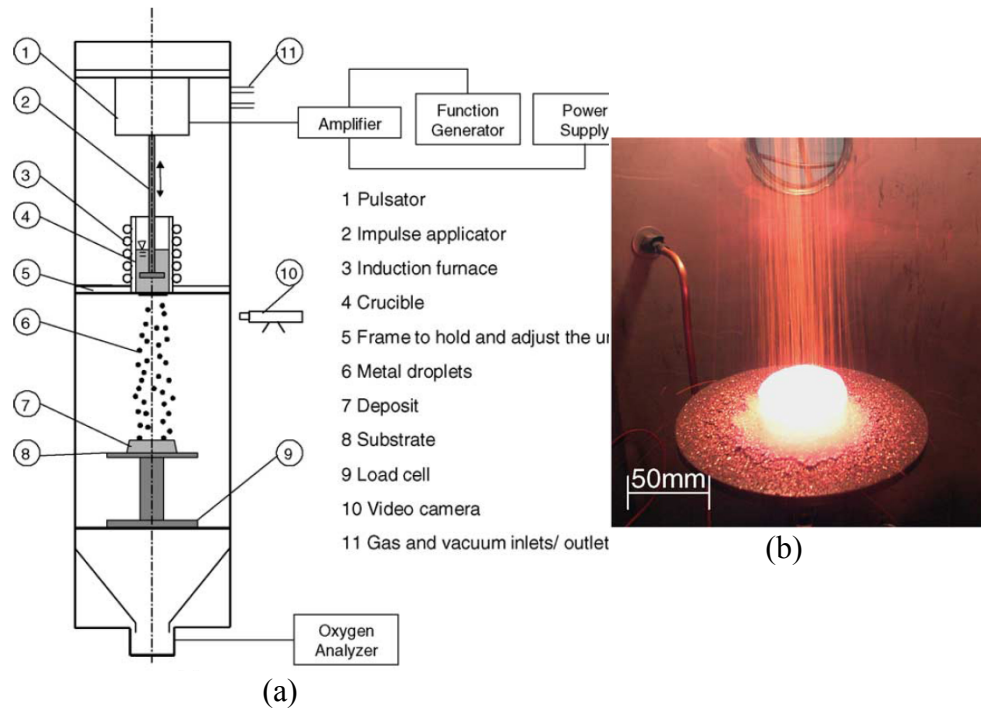


Figure 3.1. (a) schematic of spray deposition in the small tower and (b) image of spray deposition [68].

About 400g of D2 tool steel was melted in the alumina crucible, induction heated by an induction-heated graphite susceptor. A C type thermocouple (with 1% error) inside the melt showed the actual melt temperature and a K type thermocouple (with 0.4% error) showed the temperature of the atmosphere inside the tower. After reaching 1600°C, by movement of an impulse applicator, the melt was pushed through the orifice plate at the bottom of the crucible. The size of holes in the orifice plate was 300µm with 37 holes. Then, the produced droplets were cooled down through the cooling atmosphere (nitrogen) and they hit the substrate. Distances of 38cm (run name: 3810-with helium as a cooling gas), 28cm (run name: 2810-with nitrogen as a cooling gas) and 20cm (run name: 2010-with nitrogen as a cooling gas) were chosen between the orifice plate

and substrate. Plain carbon steel plate preheated to 40°C was used as substrate. An inert atmosphere with less than 10ppm oxygen was achieved in the tower by purging with inert gas.

At 20cm, another experiment was also conducted with 1000ppm oxygen, in order to investigate the effect of oxygen on the final microstructure of deposit (run name: 201000). A plunger was connected to a sensor to measure the force and acceleration of the plunger during the atomization run. Also, the substrate was placed on a load cell device measuring the weight of deposit as a function of atomization time. This is a DP41-S high performance strain gage from Omega with 0.005% accuracy of reading. Using the mass of the deposits versus time of deposition, it is possible to calculate deposition rate. Table 3.3 shows the parameters of the experiments.

Table 3.3. IA run conditions for atomized D2 tool steel deposits

Run number	120123	120210	120127	120201
Run name	3810	2810	2010	201000
Run time (s)	462	265	190	216
Cooling gas	Helium	Nitrogen	Nitrogen	Nitrogen
Oxygen level	<10ppm	<10ppm	<10ppm	1000ppm
Deposit mass (g)	152	324	320	358
Height of spray deposit (mm)	N/A	50	43	45
Avg. deposition rate (g/min)	46	77.2	165.5	94.2

Figure 3.2 shows D2 tool steel spray deposits at different distances of substrate, cooling atmosphere and oxygen levels.

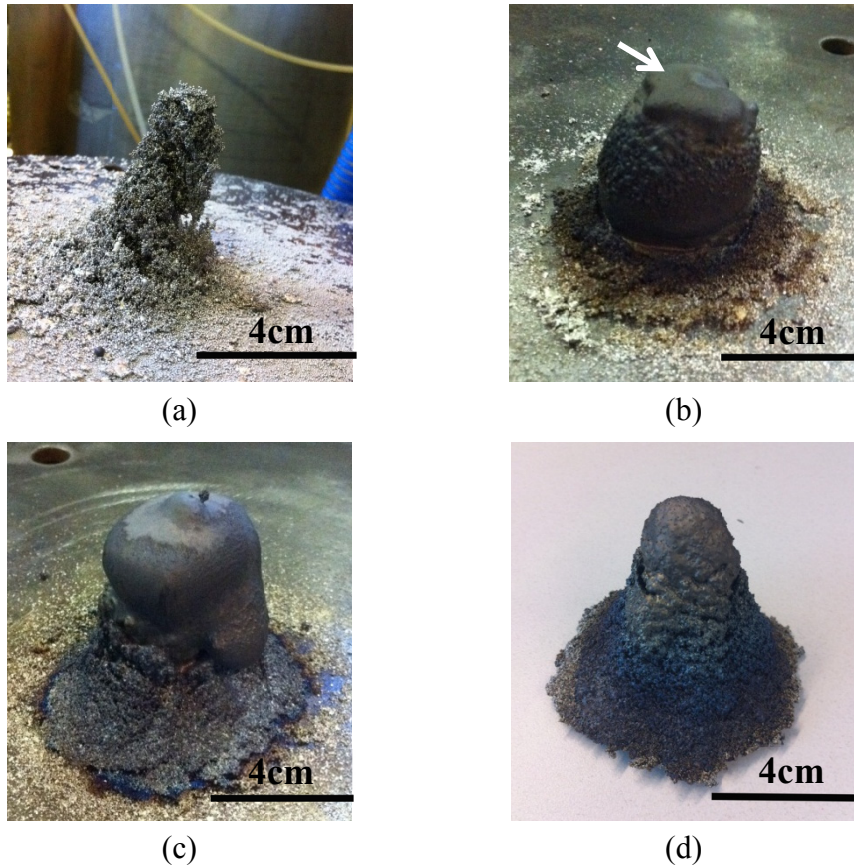


Figure 3.2. D2 tool steel spray deposits (a) IA with substrate at 38cm below the nozzle plate atomized in helium, oxygen level of 10ppm, (b) IA with substrate at 20cm below the nozzle plate atomized in nitrogen, oxygen level of 10ppm (c) IA with substrate at 20cm below the nozzle plate atomized in nitrogen, oxygen level of 1000ppm and (d) IA with substrate at 28cm below the nozzle plate atomized in nitrogen, oxygen level of 10ppm.

Sampling and characterization of deposits have been explained in Section 3.1.4. Spacing between the dendrites as well as eutectic volume fraction were measured from the bottom to top part of the deposits. The cooling rate and amount of eutectic undercooling were then measured using SDAS and eutectic volume fraction values.

3.1.2. Annealing of the particles

Atomized powders in helium and nitrogen atmospheres were given an isochronal heat treatment at different temperatures and the powders after annealing were prepared for further analysis. A Setaram Labsys Evo Differential Scanning Calorimeter device (DSC) was used to find the upper limit temperature of annealing. Powders of 600-710 μ m atomized in nitrogen were heated with the nominal 10K/min heating rate (10.5K/min actual heating rate) up to 1100°C. DSC peaks of transformation were investigated to find the temperature limit of annealing. At the high temperature limit, ferrite is transformed to austenite and it is apparent as a transformation peak in the DSC output.

Subsequent to the DSC tests described above, powders were annealed using the following three steps: first, the particles were heated up to the desirable temperature at a heat rate of 20K/min; next, the particles were heated isochronally at the desired temperature for two hours; finally, the particles were cooled to room temperature at a rate of 20K/min (19.4K/min actual cooling rate). The isochronal temperatures used for annealing were 350°C, 450°C, 550°C, 650°C, 750°C and 850°C with about $\pm 7^\circ\text{C}$ deviation from the set temperatures. Annealing was done in a Setaram Labsys Evo DSC with argon as an inert atmosphere. About $5.8 \times 10^{-7} \text{m}^3$ of powdered material was used for ND and XRD analysis.

3.1.3. Powders and spray deposits mounting, polishing and etching

As-atomized and annealed powders of the size range of interest were mounted in epoxy for SEM analysis or used as is for X-ray diffraction, neutron diffraction and high energy X-ray diffraction. To mount the powder particles, epoxy resin (West systems 10SA) and hardener (West systems 20SA) with a ratio of 2.5:1 (volume) were mixed. Powder particles and epoxy was poured into plastic moulds with a diameter of 2.54cm and left for about two hours to set. The Buehler Ecomet 250 auto grinder-polisher was used to grind and polish the mounted particles. Using 600 grit silicon carbide papers, the mounted samples were ground to obtain a flat surface. Then, nine and three micrometer diamond solution was used respectively for about 4 minutes during the polishing. $0.05\mu\text{m}$ Al_2O_3 slurry was used for the final polishing. The polished samples were carefully washed in an ultrasound device to ensure that no Al_2O_3 particles remained on the samples. Samples then were etched using a Nital etchant, 10% for about 15sec at room temperature to reveal the precipitated carbides during annealing.

Spray deposits (sample# 2810, 2010, 201000) were cut longitudinally in half for microstructural analysis. One half was ground and polished to be prepared for hardness measurements, optical and SEM analyses. The other half was cut into three different parts (Figure 3.3): the bottom part (BP), which is about 1cm from the bottom of the deposits; the middle part (MP), which is 1.5cm tall from the top of the BP; and the top

part (TP), which is the remainder of the sample. These sections were mounted separately inside the epoxy and ground and polished as described before.

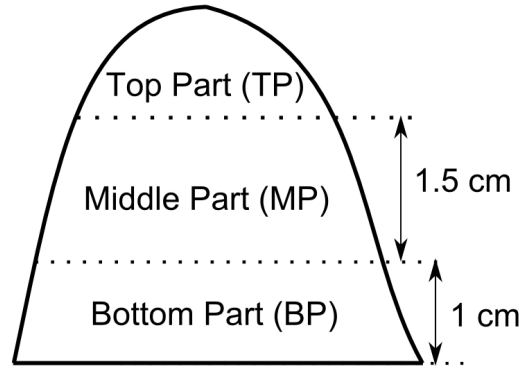


Figure 3.3. Schematic of sectioning of spray deposits.

3.1.4. Characterization

3.1.4.1. SEM

All mounted samples (powders and spray deposits) were carbon coated and analyzed with a 20kV JEOL 6301F scanning electron microscope with a resolution of approximately 3nm. This was a field emission scanning electron microscope which can provide high resolution digital images. Some images were taken using a 20kV Ziess EVO MA15 SEM with the resolution of about 5nm. The EDX analysis in this SEM was done using a Bruker Silicon Drifted Detector with an energy resolution of 125eV.

SEM analyses were also done on spray deposits on the longitudinally sectioned sample. Images have been taken from the base of the deposits (where deposits were in touch with the substrate) to the top part

of the deposits. EDX analysis in the SEM was conducted using a Bruker Silicon Drifted Detector with an energy resolution of 125eV.

- **Measuring secondary dendrite arm spacing (SDAS)**

To measure the scale of the microstructure in different particle sizes atomized in different cooling atmospheres (nitrogen or helium) and the spray deposits, SDAS and cell spacing were measured. In some samples, primary and secondary dendrites are clearly visible and distinguishable, (e.g. Figure 3.4.a). A line with known length was drawn parallel to the primary arm, by intersecting the number of secondary arms. By dividing the length of this line by the numbers of intercepts, the SDAS was calculated. In the samples in which it is not possible to distinguish the dendrite arms (e.g. Figure 3.4.b), cell spacing measurements were done to quantify the size of the microstructure [54]. ImageTool Ver. 3.0 was used to measure the length of different lines drawn inside the cells. An average and standard deviation of measured lengths were calculated by the software. SDAS and cell spacing measurements were done on more than 10 images per particle size range.

- **Measuring eutectic inter-lamella spacing**

ImageTool Ver. 3.0 was used to measure the spacing between eutectic lamella. More than 10 images per particle size range were used in order to measure the average eutectic inter-lamella spacing. The average and standard deviation of the measure lamella were calculated by the software.

- **Measurement of eutectic volume fraction**

Stereology was used to quantitatively measure the eutectic area fraction in the atomized particles and spray deposits. Stereology is the procedure used to quantify microstructural features. In this technique, a set of equations are used which can correlate the 3-D information to 2-D images [5]. A basic equation in stereology is shown in Eq. 3.1 [90]:

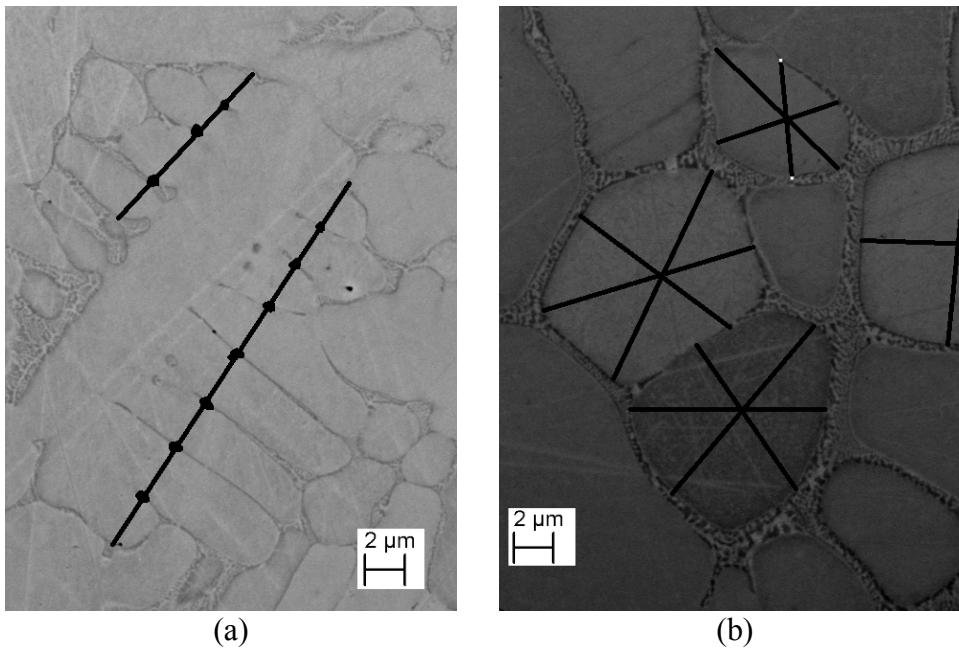


Figure 3.4. SDAS measurements for (a) 650µm particle atomized in helium (110112) and (b) 1000µm particle atomized in nitrogen (100310).

$$V_V = A_A = P_p \quad \text{Eq. 3.1}$$

where V, A and P letters are volume fraction, area fraction and the point count of a feature of interest. Eq. 3.1 means that it is possible to find the volume fraction of a feature of interest by area fraction calculation or point count analysis. According to DeHoff et al. [90], the concept of the equation $V_V=P_p$ is that if one randomly places a point within an image, the volume

fraction of a feature is equal to the statistical probability that the point falls inside that feature.

In order to calculate the volume percent eutectic in the atomized powders, a random grid was superimposed on 2-D SEM images of atomized powders using ImageJ software. There were about 580 points of grid per image (Figure 3.5). The grid intersections points that are falling in the eutectic region were then counted manually. If the point falls within the eutectic region, it was counted as 1. Points falling on the boundary of the eutectic and primary dendrites counted as 0.5. Then, using Eq. 3.2, it was possible to calculate the volume percent of eutectic in each image:

$$v_e = P_p = \frac{n_e + 0.5n_b}{n_t} \times 100 \quad \text{Eq. 3.2}$$

where v_e , n_e , n_b and n_t are the volume percent eutectic, the number of points inside the eutectic region, the number of points on the eutectic-primary phase boundary and the total number of grid points on each image (580 in Figure 3.5), respectively.

More than 10 images per particle size were used to calculate eutectic volume percent (or from specific part of the spray deposit). The average of volume percent eutectic and standard deviation were calculated based on these measurements [5].

3.1.4.2. X-ray diffraction (XRD)

About 500mg of as-atomized and annealed powder particles were used to collect XRD patterns. For spray deposits, the sectioned sample from the BP

and MP of deposits produced at different conditions (different distances from the nozzle plate and oxygen levels) was washed with ethanol to remove any possible contamination. The XRD experiments were carried out using a Rigaku Gerigerflex 2173 X-ray Diffractometer, equipped with a cobalt X-ray source. For phase identification and quantification, the XRD experimental conditions are shown in Table 3.4.

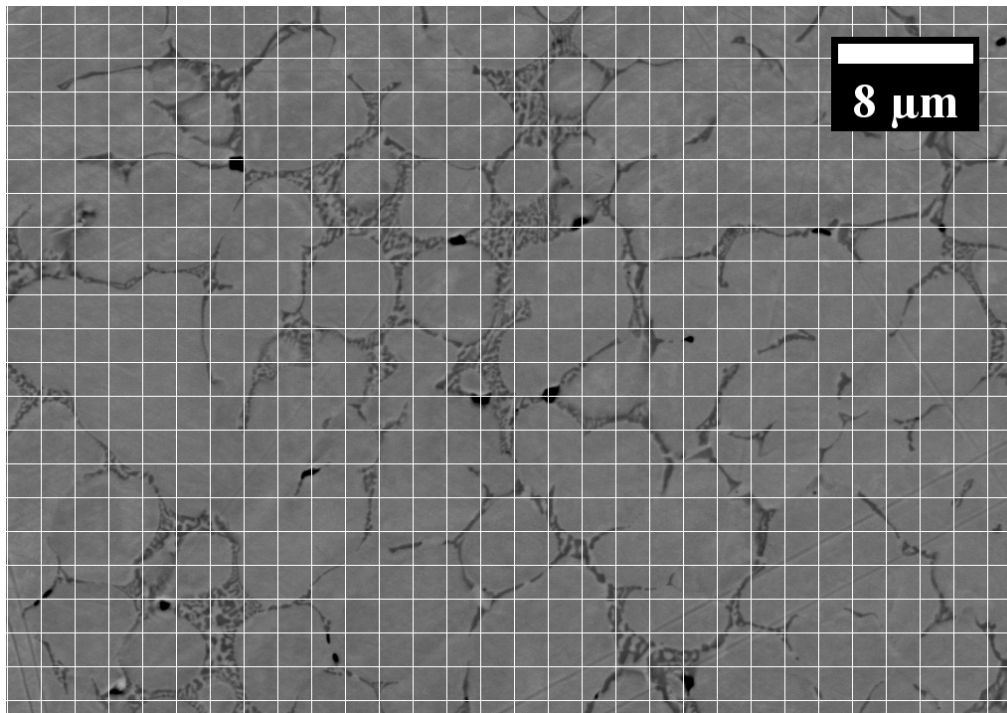


Figure 3.5. A 2µm grid is randomly superimposed on the SEM image of a 650µm droplet atomized in nitrogen (110310).

- High resolution powder diffraction

To obtain a higher resolution detection of any carbide or other formed phases in the as-atomized and annealed samples, different particle size ranges atomized in helium and nitrogen as well as the annealed particles in

650°C were sent to the Argonne National Laboratory for high energy powder diffraction analysis. Beamline 11-BM technical specifications are listed in Table 3.5. Comparing the specifications in Table 3.4 and Table 3.5, Beamline 11-BM has a resolution 1000 times that of XRD.

Table 3.4. Experimental conditions for XRD analysis

Diffractometer	Rigaki Geigerflex 2173
Radiation	Co, wavelength 0.178899nm
2θ angular range	20-120°
Resolution	1.0°(2θ)/minute
Sample holder	Quartz (zero-background plate)

Table 3.5. Summary of 11-BM technical specifications [91]

Source	Bending Magnet (BM), critical energy: 19.5 keV
Energy range	15-35 keV ($\lambda \approx 1.0-0.34\text{\AA}$)
Monochromator	Si (111) double crystal
Focusing	Sagittally bent Si (111) crystal
Beam size	1.5mm (horizontal)x0.5mm (vertical) focused at sample
Angular coverage	2θ range: 0.5°-130° at ambient temp
Resolution	min. 2θ step size=0.0001°
Capacity	Automatic robotic sample changer enables unattended collection of 100+ individual samples
Sample environments	Any inert gas or customized environment

Powders of interest were poured inside Kapton capillary tubes with the inner diameter of 0.80mm. The vials were put inside a sample mounting base, as shown in Figure 3.6. Samples were then shipped to 11-BM Beamline for high energy powder diffraction analysis.

3.1.4.3. Neutron diffraction (ND)

ND experiments were performed to obtain the weight fraction of different phases in the powder particles, and information regarding the lattice parameter of formed phases. ND was used to analyze about 5g of as-atomized particles in the size range of interest.

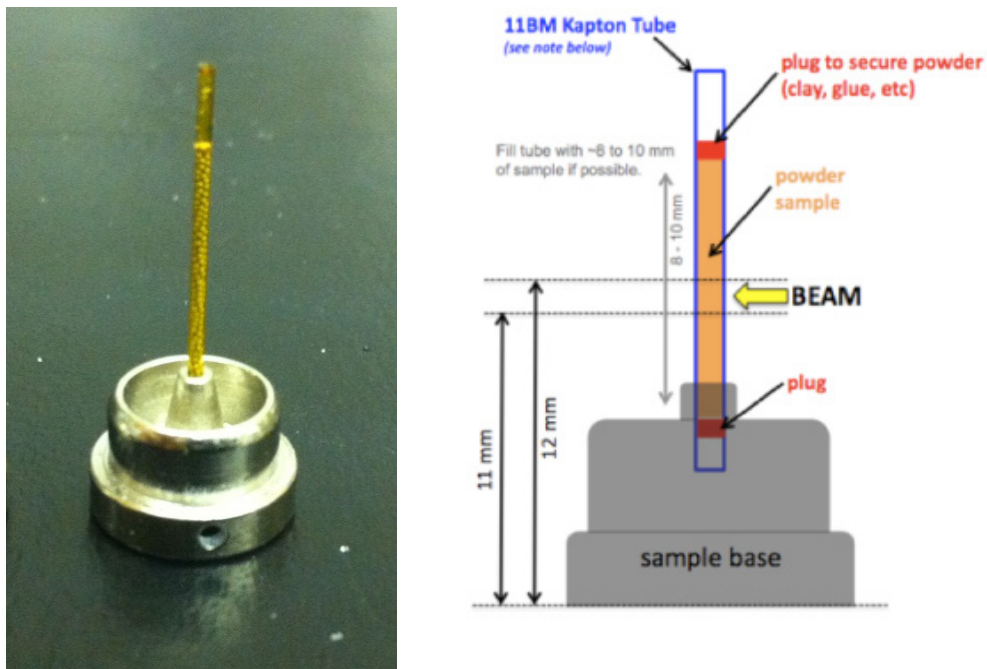


Figure 3.6. Image of a properly prepared sample for 11-BM high energy powder diffraction. Figure at right shows a sample which is properly prepared high energy powder diffraction analysis for 11-BM [92].

The ND experiments were carried out using a C2 neutron powder diffractometer at the National Research Council of Canada – Canadian

Neutron Beam Center (NRC-CNBC) in Chalk River, ON. The diffractometer of C2 neutron powder diffraction consists of an 800-wire BF3 detector which has been placed on an epoxy dance floor. For the ND analysis, a Si531 monochromator was used with a wavelength of 1.33Å. Vanadium was used as a sample holder with the volume of 10^{-6} m^3 (1 cm^3) and internal diameter of 0.005 m.

To conduct the quantification analysis on the ND peaks to determine the lattice parameter of the austenite phase, Rietveld analysis was performed using the GSAS (General Structure Analysis System) software. Crystallographic Information Files (CIF) of austenite and ferrite phases was used to perform diffraction pattern refinement using Rietveld analysis technique. This technique was also applied on the X-ray diffraction and high energy powder diffraction data of particles.

3.1.4.4. Transmission Electron Microscopy (TEM)

As-atomized powders (in helium) and powder particles annealed at 350 and 650°C were characterized by transmission electron microscopy (JEOL JEM-2010 equipped with an EDX detector operated at 200 kV). Bright field (BF) images, selected area diffraction (SAD) patterns and EDX spectra from localized regions were obtained using this TEM device. Electron transparent specimens were prepared using focused ion beam (FIB) techniques (Hitachi NB 5000, dual-beam FIB-SEM). Figure 3.7 shows an example of steps using FIB in order to remove TEM sample from a 650µm particle IA in helium. Using an energetic Ga ion, the samples were

sectioned from the regions of interest (a region containing both eutectic and matrix material). The Ga ion beam had a large beam current of 20nA to 60nA. Sectioned samples were then mounted on a copper grid and then thinned using a current of 0.7nA to 4 nA. Thinned samples were then polished using a current of <0.1nA to obtain thickness of about 100nm.

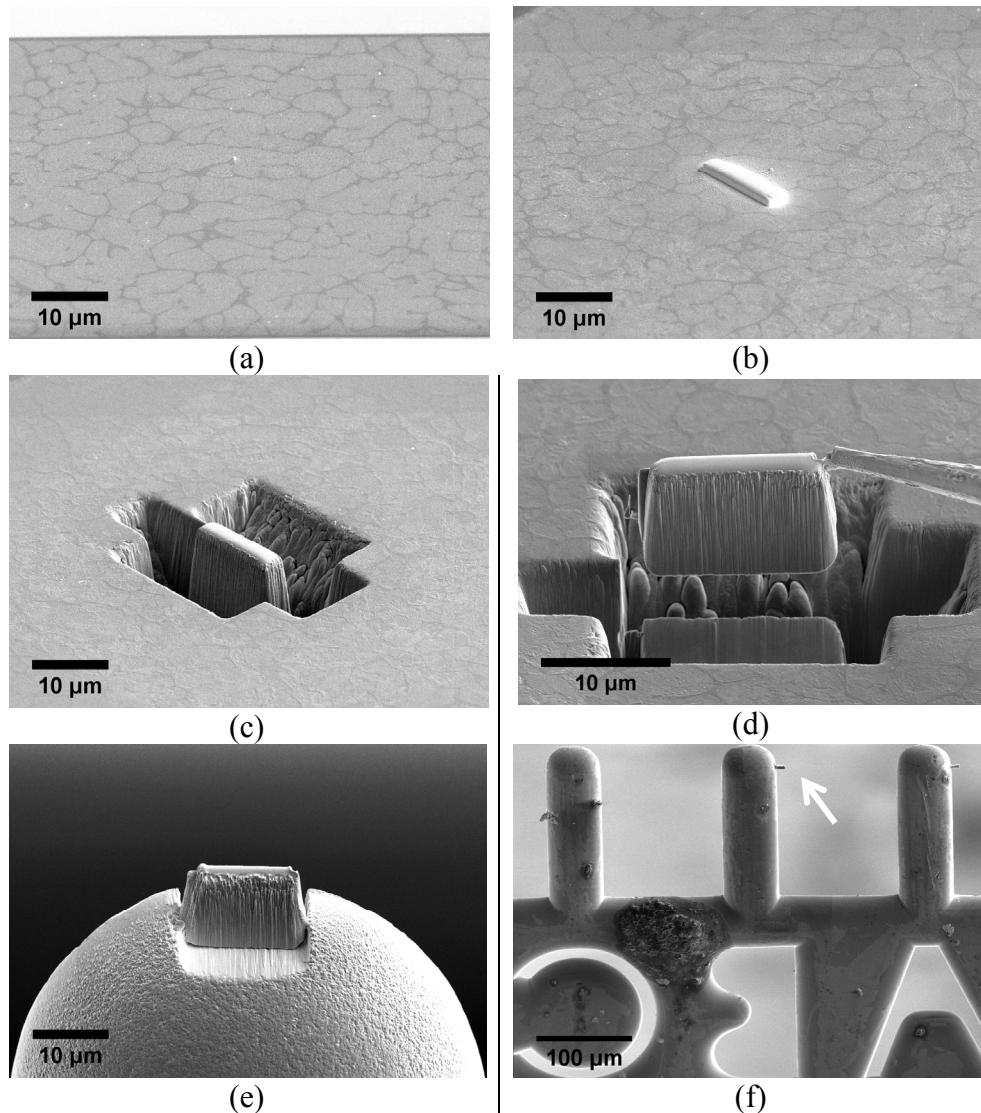


Figure 3.7. FIB steps in order to remove a TEM sample from a 650 μm IA-He particle, (a) SEM micrograph of the sample before FIB process, (b) depositing tungsten on the area of interest, (c) milling regions around the area of interest, (d) lift-out of sample piece by means of a manipulator mounted inside the FIB chamber, (e) and (f) sample mounted to a copper grid to be thinned for TEM analysis.

3.1.4.5. Hardness measurement

To study effect of rapid solidification and subsequent annealing on the mechanical properties of the particles, hardness analyses were done on the particle in different size ranges, atomized in helium and nitrogen annealed at different temperatures. Hardness measurements were done using Buehler Tukon 1102 microvickers hardness tester. Hardness of about 30 different points was measured for any sample of interest. Average and standard deviations were calculated using these measurement points.

Since the particles are mounted in an epoxy resin, a suitable load should be applied through the indenter of the hardness machine to ensure that the whole force applied from the indenter is focused on the sample. If a large amount of load is applied to the particle, it is possible that the load will deform some part of the mounting material, and no precise value of hardness will be achieved during hardness measurements. Different amounts of loads ranging from 50gf (grams-force) to 500gf were used to find the optimum value. Figure 3.8 shows hardness of 300-355 μ m as-atomized particles in helium as a function of applying the load during the hardness measurement. In this case, the optimum would be the point at which the hardness value is not smaller than the average value of hardness, and the indent is large enough to be able to measure the dimensions for the microvickers hardness calculations. Figure 3.8 shows that hardness is constant up to 100gf load, and after that, hardness decreases by increasing the applying load. This means that at the higher amount of the applying

load, epoxy resin is also deformed, which affects the measured hardness values of the particles.

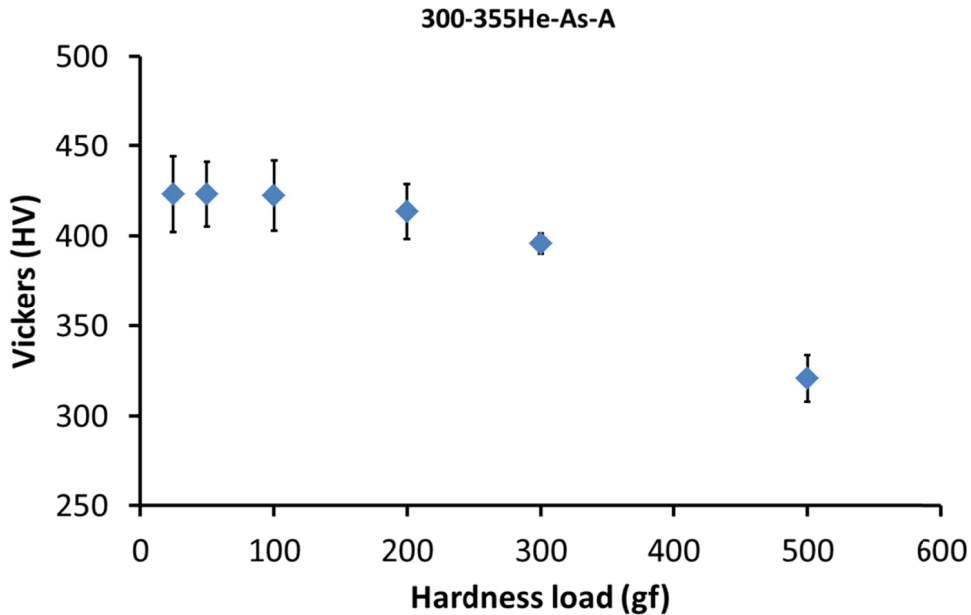


Figure 3.8. Hardness of 300-355 μ m as-atomized particles as a function of applying the load during the hardness measurement.

Microvickers hardness map was plotted from the longitudinal section of the spray deposits. For each point, the hardness of three adjacent areas was measured, and average and standard deviations of data were calculated using the measurement points.

3.1.4.6. Porosity measurement

In order to measure the amount of closed porosity, spray deposit samples were cut in half. One half was kept as a back-up for any other required analysis and the other half was sectioned according to Figure 3.9. In this

picture, “C” stands for “Centerline” of the sample and “R” stands for “Right side” of the sample.

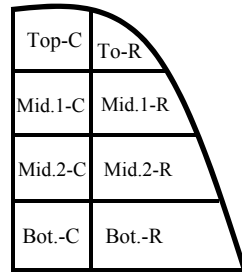


Figure 3.9. Schematic of spray deposits sectioning for porosity measurements.

All cut sections were washed with alcohol to remove any adhering foreign materials such as dirt or oxide scale. The porosity level of the sections of each spray deposit samples was then measured using Archimedes’ principle according to ASTM B962-13 using distilled water and a balance with accuracy of 0.01 mg [93].

3.1.5. Sensors on the atomization units

Previous sections focused on experiments that produced powders and spray deposits, and described the analyses on the samples. This section will describe online measurement devices installed on small and box towers (section 2.3.3), and the data generated and analyzed using these devices.

In order to collect different types of informatio from different parts of the atomization tower, several probes and sensors have been installed into the different IA units. Type C thermocouples were used to measure the temperature of the melt during melting and atomization. Type K

thermocouples also monitored the temperature of the gas atmosphere inside the IA unit. There was an oxygen sensor unit to measure the amount of oxygen in the chamber, after evacuating and purging with the inert gas. A load cell unit was placed at the bottom of the tower to collect data for the mass flow rate during atomization (under the oil beaker in the case of powder generation and under the metal substrate in the case of spray deposition).

To measure the effective radiant energy, DPV-2000 from Tecnar Automation Ltée was used, while the shadowgraph (Sizing Master Shadow from LaVision GmbH in Gottingen, Germany) was used to measure the velocity and droplet size of the copper droplets. These sensors were installed on a translation stage inside the drop tube. The stage could move in all three directions (Figure 3.10). This 3D translation stage can easily move in X, Y and Z direction, using DaVis 7.2 software (from LaVision GmbH). It can move maximum of 1 m, 0.25 m and 1 m in X, Y and Z direction, respectively. The stage at each direction can move with minimum 0.375mm/s and maximum 75mm/s velocities. The error of movement is about ± 2 mm for every 200 mm of movement. The sensors are simply attached to the stage using screws.

DPV-2000 is an optical sensing device based on a patented technology developed by the National Research Council of Canada. It uses a dual slit optical sensor that can measure the effective radiant energy of up to 800 droplets per second with a depth of field of 1.9 mm. It can measure

the radiant energy of droplets at two different wavelengths [94]. This device will be explained more in Chapter 5.

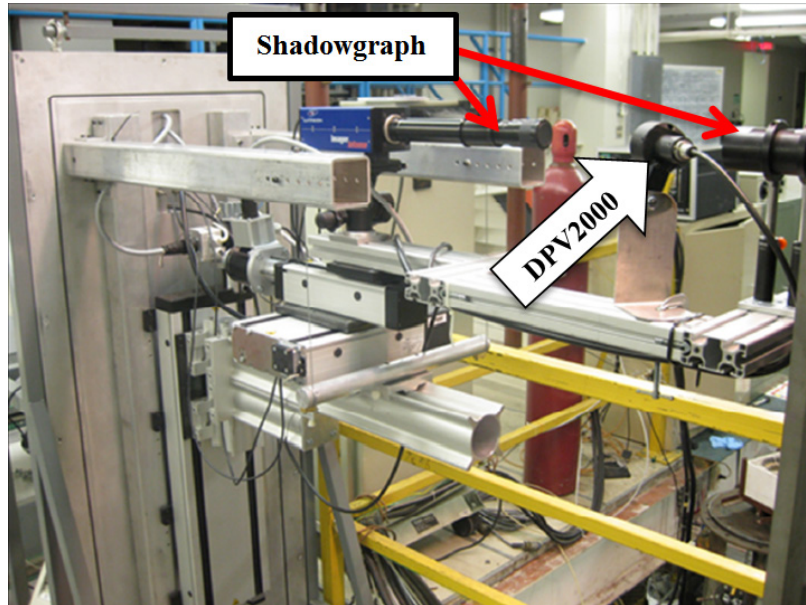


Figure 3.10. Translation stage, as well as online measurement devices, installed on the tower 's door.

Sizing Master Shadow from LaVision uses a backlighting technique to visualize droplets for image analysis. A light source, in this case a pulsed laser combined with diffuser optics, illuminates in-flight droplets 5 times per second. The backlight of droplets inside the measurement volume of $6 \times 6 \times 6 \text{ mm}^3$ is captured by a high-resolution high-speed imaging system. The shadowgraph device makes it possible to investigate droplet sizes down to $5 \mu\text{m}$.

The focal point of both shadowgraph and DPV-2000 was set to an imaginary vertical line going through the center of the bottom of the crucible. Any unfocused droplets would be rejected by the criteria set by the

operator in the respective software of each instrument. Figure 3.11 shows two rejected droplets by DPV-2000 and shadowgraph devices. Figure 3.11.a shows DPV-2000 trigger tuning screen illustrating several peaks which only the first two of them are related to an acceptable droplet. Unfocused droplets far away from the focal distance of the device will be rejected by DPV-2000. For droplet measurements, DPV-2000 acceptance criteria have been listed by TECNAR Company [95]:

- Droplet temperature: 1000-4000°C
- Droplet velocity: 5-1200m/s
- Droplet diameter: 10-300µm

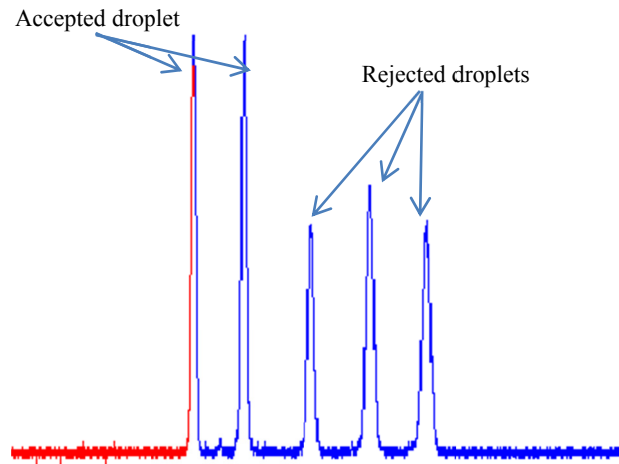
Figure 3.11.b shows some captured droplets by the shadowgraph camera. It can be seen that some of them are not measured by the software, since they do not have sharp focused edges.

3.1.5.1. Online measurements procedure

To investigate the radiation energy and temperature of falling droplets, pure copper and D2 tool steel were used for IA. Pure copper was used as a second material to test the two-colour pyrometer assumption of the DPV-2000 for the following reasons:

- Pure copper solidification parameters are known and a heat loss model can be easily applied onto the molten copper
- The melting temperature of pure copper is within the working temperature range of the DPV-2000 (1000-4000°C)

- Since no other phase forms during the solidification of copper, any heat generated when the copper droplets fall can be attributed to the copper heat of fusion.



(a)



(b)

Figure 3.11. (a) DPV-2000 trigger tuning screen showing accepted and rejected droplets and (b) shadowgraph captured picture showing unfocused rejected droplets.

For pure copper atomization, copper with 99.99% purity (Alfa Aesar) was melted in a graphite crucible (1.81 g/cm³ density and 12 vol. % porosity) using a 20kW induction furnace at the top of a drop tube-IA tower. An argon atmosphere of 90ppm oxygen was maintained in the tower during melting and atomization. After the copper was melted, it was superheated to 1400°C. The molten metal was atomized through orifices (300 µm and 500 µm) at the bottom of the crucible, forming ligaments, which spherodized into droplets in the inert argon atmosphere. The falling droplets were cooled in free fall by the argon atmosphere. The particle size distribution of falling droplets (D_{50} and D_{90}), velocity and effective radiant energy were measured at distances of 10, 30 and 50 cm from the orifices.

Also, D2 tool steel was atomized with the same atomization conditions described in section 3.1.1. The falling droplets were cooled in free fall by the nitrogen atmosphere. Particle size distribution of falling droplets (D_{50} and D_{90}), velocity and the effective radiant energy were measured at distances of 4, 18 and 28 cm from the orifices.

In this chapter, general experimental procedures used to produce powders and spray deposits, annealing of the samples and characterization methods were discussed. Online measurement techniques were also briefly addressed in this chapter. In the next chapter, effect of rapid solidification parameters such as undercooling and cooling rate will be investigated on the microstructure and phases of D2 tool steel (qualitatively and quantitatively).

Chapter 4

4. Microstructural investigation of D2 tool steel during rapid solidification¹

4.1. Introduction

D2 tool steels are widely used in industry owing to a combination of good wear and abrasion properties [7]. The D2 tool steel contains a high volume fraction of carbides that precipitate during the eutectic transformation. The spacing and size of these particles is key for mechanical properties as smaller particles that are closely spaced will result in improved wear resistance [96]. As discussed in Chapter 2, carbide size and spacing is mainly controlled by solidification kinetics, and specifically, the amount of cooling rate and eutectic undercooling. High undercooling and cooling rate result in formation of fine secondary dendrite arm spacing of the primary (Fe-rich) phase as well as less eutectic fraction. The use of a conventional casting process to create components will result in a low undercoolings and cooling rates which result in large secondary dendrite-arm spacing λ_2 and leads to coarse carbides, while a rapid solidification will refine the microstructure to ensure an even distribution of the carbides and thus improved strength [97].

¹ Chapter 4 has largely appeared in Powder Metallurgy, Vol. 57, No.1, 2014, 70-78, DOI: <http://dx.doi.org/10.1179/1743290113Y.0000000072>. Reformatted according to thesis requirements.

The effect of cooling rate on secondary dendrite arm spacing was shown in Eq. 2.5. In addition to the cooling rate, primary phase and eutectic undercoolings of the liquid prior to grain nucleation has a significant effect on the final microstructure of metallic alloys. For example, Behulova et al. [33] showed that in metal powder formed by rapid solidification, a finer microstructure was obtained at a higher level of primary phase undercooling. The importance of eutectic undercooling in modifying the final phase fractions was highlighted in work by Prasad et al. [79]. These authors demonstrated through experimentation and simulation that it was necessary to incorporate eutectic undercooling in order to accurately predict the eutectic percent. Finally, at large undercoolings greater than a critical value (ΔT_{hyp}), the melt will solidify with almost no partitioning of the solute phase, creating a highly supersaturated solid solution [25].

Crystallization of an undercooled melt occurs in two steps: (1) phase nucleation and (2) growth of the solid phase. In the rapid solidification processes, the release of latent heat associated with the growth phase plays a large role in microstructure formation due to potential for large undercoolings, and the resulting thermal recalescence once the solid nucleates [98]. It has been noted that the amount of supersaturated solid solution and the formation of other metastable phases in the solid is mostly affected by the fraction of solid that forms during recalescence, f_R [25]. Assuming that solidification during recalescence occurs under near-

adiabatic conditions, the volume fraction solidifying during the recalescence, f_R , can be calculated as follows [25],

$$f_R = \frac{\Delta T_p}{\Delta T_{hyp}} \quad \text{Eq. 4.1}$$

where ΔT_p is the primary phase undercooling, $\Delta T_{hyp} = \frac{\Delta H_f}{C_p^l}$ is the hypercooling limit, ΔH_f is the volumetric latent heat of fusion and C_p^l is the specific heat capacity of the liquid phase. Eq. 4.1 is a consequence of the fact that the heat released as part of near-adiabatic solidification during recalescence must be absorbed by the surrounding liquid without the droplet temperature exceeding the liquidus. After recalescence, the remaining melt solidifies under Scheil solidification condition (with back diffusion of solute especially interstitial solute) until the solidus or eutectic temperature is reached.

Figure 4.1 shows phase diagram showing D2 tool steel solidification path. This phase diagram has been generated using Thermocalc software v. 5.0.4.75 and the TCFE6 data bank v.6.0. Comparing this phase diagram with the phase diagram for ternary alloy of Fe-C-Cr (Figure 2.2), it can be seen that there are more complex phases form during solidification D2 steel compare to Fe-C-Cr alloy. Also, eutectic transformation temperature is also higher in Figure 4.1 than in Figure 2.2. Clearly, the net effect of alloying elements present in D2 tool steel is to increase the eutectic transformation temperature compared to the ternary alloy of Fe-C-Cr.

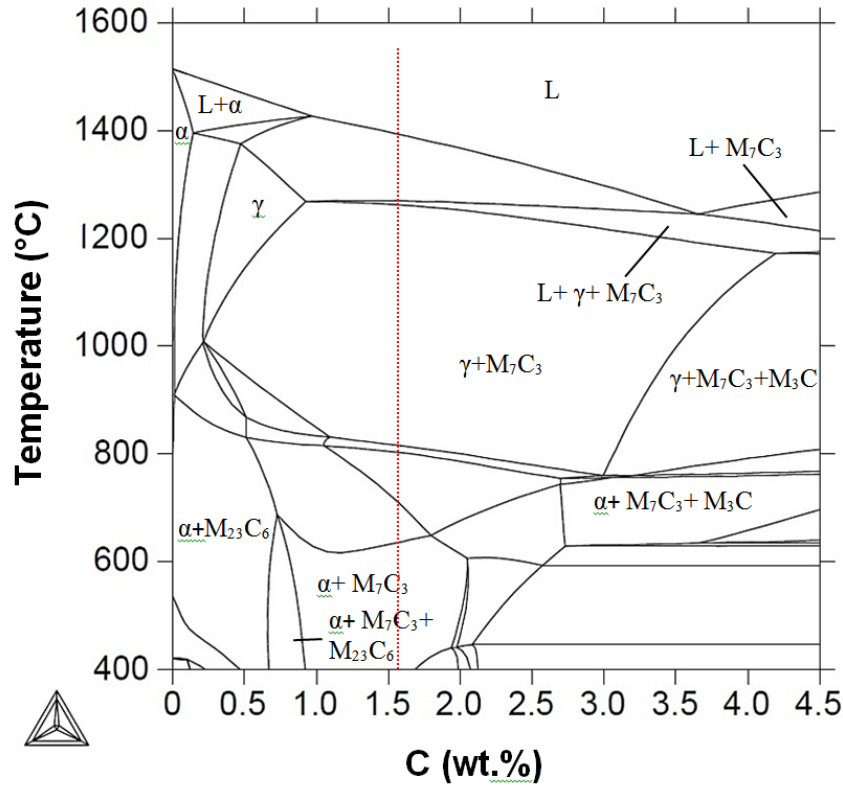


Figure 4.1. Calculated phase diagram for D2 tool steel from TCFE6 database using ThermoCalc software.

In the past few years, various rapid solidification techniques such as gas atomization [29,33], electromagnetic levitation [99,100] and laser melting [101] have been used to study the microstructure and carbide formation in ferrous alloys since these techniques allow for experimentation with a wide variation in cooling rate and casting size. The results have revealed grain refined microstructures and relatively small carbide phases created by high amount of undercooling and cooling rate. However, a systematic experimental work on the rapid solidification of D2 tool steels is still lacking. In this chapter, the effect of cooling rate and undercooling on microstructure evolution in D2 tool steel is investigated using the rapid

solidification techniques of IA and WA. Quantitative analysis has been done on measuring the volume fractions of the primary phase and eutectic in order to determine the link between microstructure, undercooling temperatures for nucleation, and cooling rate. In the future chapters, knowledge of the degree to which the matrix phase is supersaturated as a function of undercooling and cooling rate will be used to investigate carbide precipitation in rapidly solidified D2 tool steel as a result of the post solidification heat treatment.

4.2. Experimental

In order to investigate solidification microstructure under rapid cooling rates, two atomization techniques, IA and WA have been utilized. IA and WA were described in Chapter 2. The D2 tool steel powder from IA was generated using an apparatus available at the University of Alberta, while the WA powder was provided by the Hoeganaes Company.

Table 3.2 shows IA atomization run conditions as well as geometric standard deviation of particle mass distribution (σ) and median particle diameter (D_{50}), while D_{50} and σ values for WA powders were provided as 70 μm and 1.64, respectively, by Hoeganaes Company. As noted elsewhere [53,62], IA powders have spherical shape whereas WA powders are irregular in shape as shown in Figure 4.2.

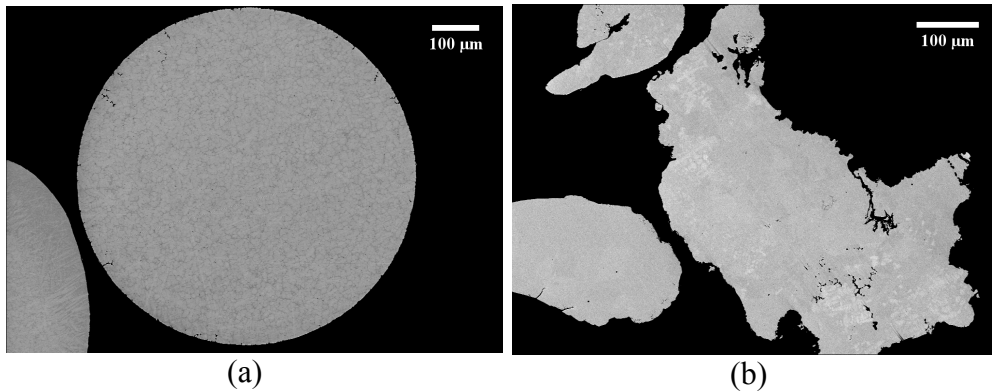


Figure 4.2. BSE images of particles of D2 tool steel atomized using: (a) IA (in helium) and (b) WA. Both particles are about 655µm.

Subsequent to atomization, washing and sieving processes, size ranges of 300-355 µm, 600-710 µm and 1000-1400 µm were chosen from the IA powder and size ranges of 90-110 µm, 300-355 µm and 600-710 µm were chosen from the WA powder for further analysis. Particle size analysis of IA particles is shown in Table 3.2. Particle ranges were chosen in order to cover the range of cooling conditions by varying particle size and gas. For each of the different powder size fractions, specimens were mounted in epoxy resin, ground, polished, and then carbon coated in preparation for metallography. SEM was performed in order to measure both the secondary dendrite arm spacing (SDAS) and the area fraction of eutectic. For the SDAS, 60 measurements per specimen were performed using the Image Tool software in order to accurately determine this parameter. For the measurement of the eutectic fraction overlaid grid method was utilized (as described in Chapter 3). Additionally, quantitative phase identification was carried out through X-ray diffraction using Co-K α radiation in a Rigaku Denki Rotaflex RU-200B X-ray system.

4.3. Results

Below is provided a concise description of the D2 tool steel microstructure that is found in powders atomized by IA and WA. First, the morphology of different particles sizes produced from IA (atomized in helium and nitrogen) and WA will be described. Then, quantification of some important microstructural and solidification parameters will be discussed. Finally, the effect of solidification parameters including cooling rate and undercooling on microstructural features will be investigated. As it was not possible to measure directly the temperature of the droplets during atomization, a methodology for estimating the amount of undercooling prior to nucleation of the primary phase and eutectic based on metallographic analysis will be presented [102,103].

4.3.1. Qualitative description of the microstructure

The images shown in Figure 4.3 are SEM micrographs of three D2 tool steel particles produced by IA: (a) a 325 μm particle cooled in helium, (b) a 325 μm particle with nitrogen, and (c) a 655 μm particle with nitrogen.

Visual observation of the particles in Figure 4.3.a and Figure 4.3.b, which are both 325 μm in size, shows that the microstructure is finer for particles solidified in helium (Figure 4.3.a) versus those solidified in nitrogen (Figure 4.3.b). Since the thermal conductivity of helium is significantly higher than that of nitrogen [104], droplets in helium solidify faster, resulting in a finer microstructure.

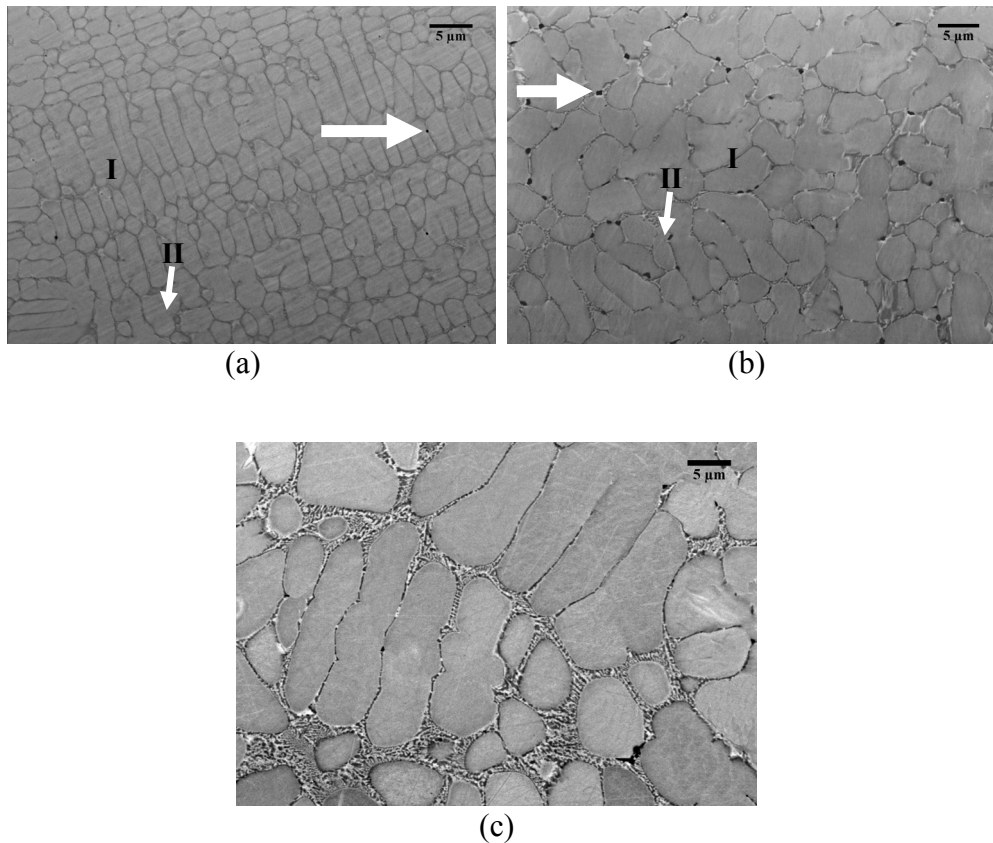


Figure 4.3. BSE images of D2 tool steel particles formed by IA: (a) 325µm particle atomized in helium, (b) 325µm particle atomized in nitrogen and (c) 655µm particle atomized in nitrogen. Arrows show porosities.

Light and dark gray regions, as well as some solidification porosity can also be seen in both images. In comparing Figure 4.3.b with Figure 4.3.c, it can also be seen that changes in the particle size also affects the scale of the microstructure since the larger particle has a comparatively coarse microstructure. This is due to the fact that heat transfer and hence cooling rate is higher in smaller particles due to their larger surface-to-volume ratio. Also, assuming a fixed number of impurities in a liquid, by dividing the liquid into smaller droplets, fewer impurities would be available per droplet. Therefore, there are less heterogeneous sites available

for nucleation in the smaller droplets. This will result in achieving high amount of undercooling in the small droplets which reduces dendrite arm spacing. The same effect was seen on the WA particles. As it can be seen in Figure 4.4, larger WA particles (Figure 4.4.b) have coarser dendrite arm spacing compare to the smaller particles which have finer dendritic microstructure (Figure 4.4.a).

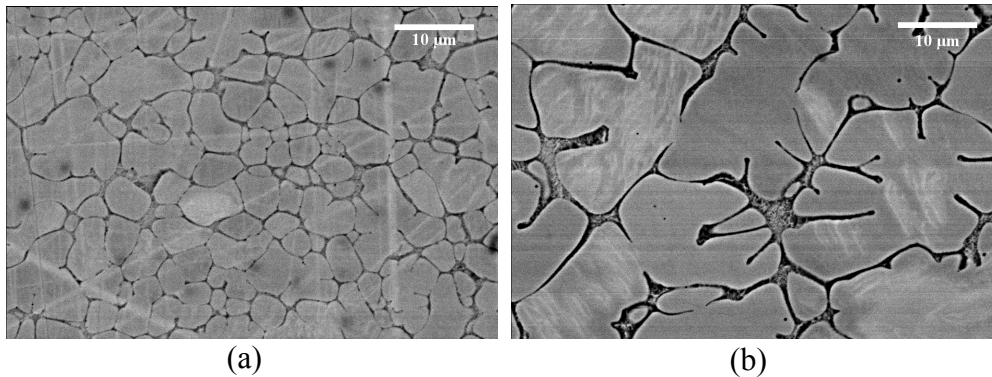


Figure 4.4. BSE images of D2 tool steel particles formed by WA: (a) 325µm particle and (b) 650µm particle (c).

EDX analysis results from different grey levels (regions I: light gray and region II: dark gray) shown in Figure 4.3 are given in Table 4.1. This table shows that during solidification the alloying elements (chromium, manganese, molybdenum and vanadium) were rejected to the dark gray region since they are higher in the dark gray phase than in the light gray region. According to the phases identified from XRD, the EDX results shown in Table 4.1 and the phase diagram, it can be concluded that the light gray phase in the IA particles shown in Figure 4.3 is iron rich phase (ferrite or austenite), and dark region between the light gray phase is the eutectic material: iron rich phase (ferrite or austenite) and a M_7C_3 carbide.

Table 4.1. EDX analysis results from dark and light gray regions in D2 steel (shown in Figure 4.3) (wt.%)

	Fe	Cr	Mn	Mo	V
Region I	89.4	9.5	0.4	0.4	0.4
Region II	74.0	21.2	1.4	1.3	2.0

Figure 4.5 shows XRD results for IA particles of 600-710 μm in diameter cooled using helium and nitrogen, as well as comparatively-sized WA particles. It can be seen from the figure that the rapid solidification of D2 steel during atomization results in the formation of supersaturated metastable retained-austenite as well as the complete suppression of ferrite and martensite. The austenite in the rapidly solidified D2 steel particles was so stable that the retained austenite did not convert to martensite even after a quench in liquid nitrogen. The reason is likely the lowering of the martensite start temperature caused by high supersaturation of austenite. Bhargava et al. [39] reported similar microstructure for rapidly solidified D2 steel using the melt spun method, and showed that the lattice parameter of austenite in melt-spun D2 steel was approximately 1.5% larger than that for gamma iron, indicating substantial opportunity for excess solution of carbon and chromium in the austenite.

Figure 4.5 also shows some small M_7C_3 peaks which can be attributed to the eutectic carbides formed in the interdendritic region. There are also some small iron oxide peaks in WA particles which can be due to oxidation of the droplets during atomizing by water.

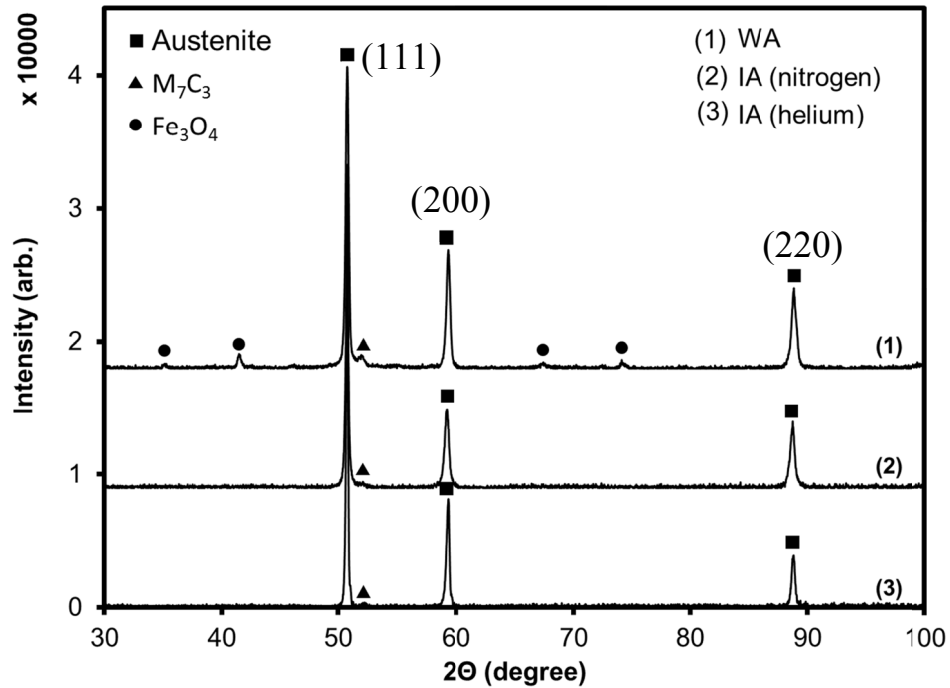


Figure 4.5. XRD patterns for 600-710 μm particles produced via IA in helium and nitrogen as well as WA.

4.3.2. Quantitative analysis

The effect of cooling rate on solidification microstructure was quantified based on the secondary dendrite arm spacing. Table 4.2 lists the SDAS (measured using Image Tool software) of WA and IA particles. For the IA particles, SDAS is also sorted as a function of particle size and cooling gas. Table 4.2 shows the average SDAS values of particles and its standard deviation as a function of particle size and cooling gas. It is shown that by decreasing particle size, and changing the cooling gas from nitrogen to helium, the SDAS decreases. Similar effect have been previously reported in the literature for Al alloy systems [88,105].

Table 4.2. SDAS as a function of particle size and cooling gas

Particle size range (μm)	Average SDAS (μm)		
	IA in helium	IA in nitrogen	WA
90-110	-	-	1.0 \pm 0.43
300-355	2.4 \pm 0.3	3.8 \pm 0.0	1.9 \pm 0.21
600-710	3.4 \pm 0.7	6.0 \pm 1.1	4.1 \pm 0.2
1000-1400	5.6 \pm 1.0	7.6 \pm 1.0	-

High magnification SEM images of the eutectic material in IA particles, shown in Figure 4.6, indicate that the eutectic structure of particles atomized in helium (Figure 4.6.a) is much finer as compared to the particles atomized in nitrogen (Figure 4.6.b) for the same particle size. Concurrently, the interlamellae spacing is higher for the case of solidification in nitrogen (0.11 \pm 0.04 μm , Figure 4.6.b) as compared to that in helium (0.22 \pm 0.05 μm , Figure 4.6.a). Based on work by Fischmeister et al. [106], the thickness of eutectic lamellae is proportional to $dT/dt_e^{-\frac{1}{4}}$, where $(dT/dt)_e$ is the average cooling rate, which is the result of multiplication of mean temperature gradient around the dendrite arm and growth rate of dendrite. Thus, the measurements of the interlamellae spacing suggest that the average cooling rate for solidification in helium is approximately 16 times higher than that in nitrogen for the 1200 μm -sized particle.

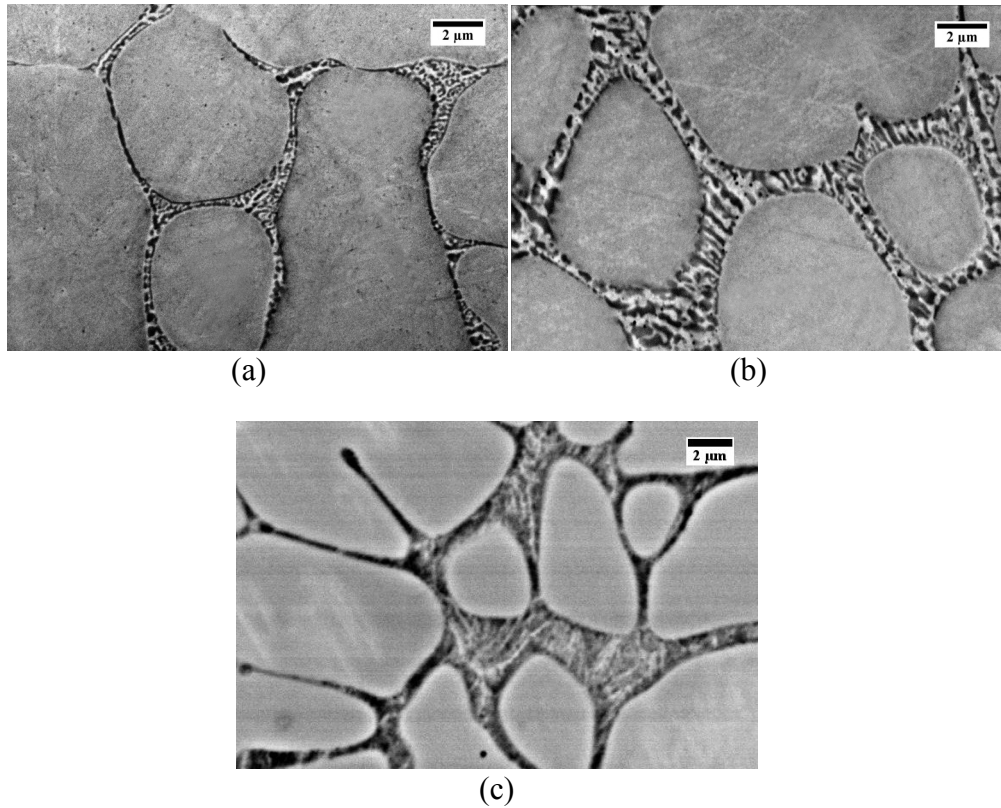


Figure 4.6. High-magnification BSE-SEM images of D2 tool steel: (a) 1200 μm IA particle in helium, (b) 1200 μm IA particle in nitrogen and (c) 655 μm WA particle.

A high magnification SEM image of the eutectic material in a 655 μm WA particle is also provided in Figure 4.6.c, for comparison purposes. In this particle, the eutectic lamellar spacing is about $0.10\pm 0.03\mu\text{m}$. Since the interlamellae spacing calculated for Figure 4.6.a and Figure 4.6.c are very similar, it can be concluded that the cooling rates during eutectic solidification in WA and IA with helium are almost the same for the same sized powder.

Figure 4.7 reports the effect of cooling gas and particle size on the amount of eutectic in WA and IA particles. First, it can be seen that the

eutectic area fraction is smaller for the small particles with higher cooling rates. Second, for the IA particles, the error bars increase with increasing particle size. This indicates that, similar to Al-Cu and Al-Fe systems [37,107], the D2 tool steel particles are less homogeneous as the particle size increases.

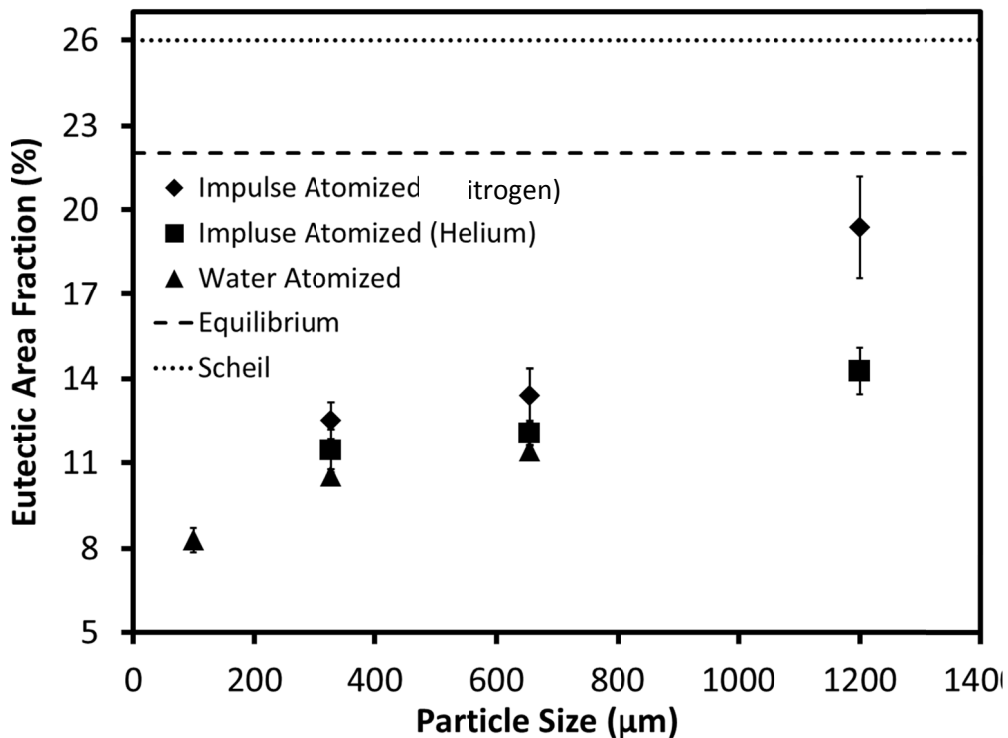


Figure 4.7. Eutectic area fraction as a function of particle size and cooling gas for IA and WA.

The equilibrium and Scheil eutectic fractions are also provided on Figure 4.7, for comparison purposes. Scheil calculations (assuming perfect mixing in the liquid and no diffusion in the solid [37]) have been done using Thermocalc software for D2 tool steel at eutectic temperature¹. As can be seen, the measured values of eutectic area fraction for D2 tool steel are

¹ Using Thermocalc ver. 5.0.4.75 software, TCFE6 v6 database and Scheil calculation feature for multicomponent alloy systems

considerably less than what is predicted by the two limiting theoretical cases. Previous atomization studies, with Al-Fe and Al-Cu, have shown that eutectic undercooling is responsible for this reduction in the fraction eutectic [37,107]. Kurz and Trivedi have shown that by increasing the solidification rate (which results in the higher growth velocity), the equilibrium phase diagram is changed so that there are reduced amounts of eutectic [108]. The same trend has been shown for rapidly solidified Al-Cu and Al-Si alloys by Sarreal and Abbaschian [109]. These authors attributed the lower amount of eutectic to both dendrite tip undercooling as well as eutectic undercooling. Formation of the eutectic can even be suppressed completely, due to formation of a metastable supersaturated solid solution [110]. This is attributed to the features of rapid solidification, as the interface velocity is higher than the solute diffusion speed in bulk phases.

4.3.3. Solidification kinetics

The measured λ_2 values shown in Table 4.2, in combination with the eutectic fraction measurements shown in Figure 4.7 can be used to provide new insights into the solidification kinetics of the D2 tool steel.

Based on the results shown in Figure 4.7, it would appear that the atomization process produces material with a wide range of eutectic fraction. For the IA process, the eutectic fraction varies from 8% to 20% as a function of particle size. In contrast, the equilibrium (lever-rule) eutectic content of a D2 tool steel with 1.55 wt.%C, based on the phase diagram shown in Figure 4.1, is approximately 22% with the transformation

occurring at 1270°C. It is possible to estimate the required undercooling prior to nucleation of the eutectic by comparing the measured values to the eutectic fractions predicted via metastable extensions of the liquidus and solidus lines below the equilibrium eutectic temperature. Metastable extension of liquidus and solidus lines were extracted using Thermocalc software (Figure 4.8).

The temperature at which the extensions of liquidus and solidus yield a eutectic fraction equal to that experimentally measured is shown in Figure 4.9. From Figure 4.9, larger undercoolings are found to occur when the eutectic fraction is small. As the eutectic fraction is inversely proportional to particle size (Figure 4.7), it can be postulated that the fine eutectic lamellae spacing observed in Figure 4.6.c and other small particles is directly related to undercooling temperature and growth rate of eutectic.

The secondary dendrite spacing, λ_2 , can be expressed as a function of the coarsening kinetics and is proportional to the cube root of time [4],

$$\lambda_2 = 5.5(Mt_{SL})^{\frac{1}{3}} \quad \text{Eq. 4.2}$$

with

$$M = \frac{-\Gamma D \ln\left(\frac{C_l^m}{C_0}\right)}{m(1-k)(C_l^m - C_0)} \quad \text{Eq. 4.3}$$

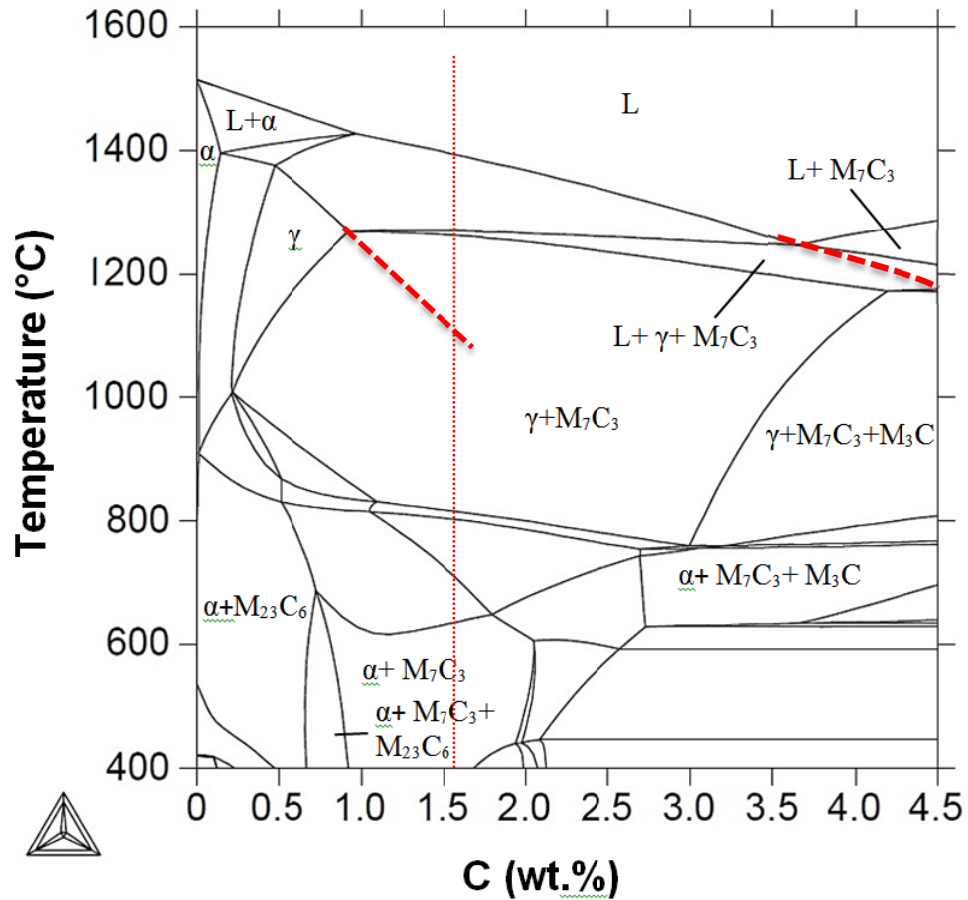


Figure 4.8. D2 tool steel phase diagram showing metastable extension of liquidus and solidus lines using Thermocalc software.

where Γ is the Gibbs-Thompson coefficient ($\Gamma=10^{-7}$ mK [111]), D is the diffusion coefficient of solute in the liquid ($D=10^{-9}$ m²s⁻¹[112]), m is the slope of the liquids line, C_1^m is the composition of the last liquid to solidify, C_0 is the overall composition, t_{SL} is the solidification time of the primary phase, k is the distribution coefficient and the units of λ_2 are m. Use of Eq. 4.2 enables an estimation of the solidification time based on the measured values of λ_2 . The results, provided in the second column of Table 4.3, indicate that there is considerable variation in t_{SL} as a function of

the atomization conditions and particle size; obviously smaller particles solidify faster.

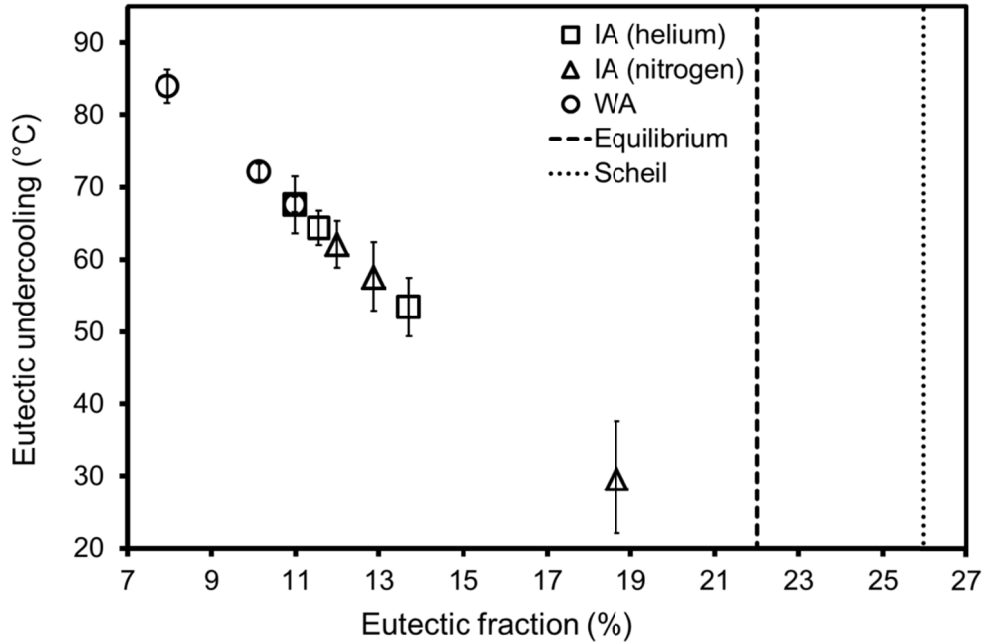


Figure 4.9. Effect of eutectic undercooling on the amount of eutectic in IA and WA D2 tool steel.

Equating Eq. 4.2 (which relates λ_2 with solute partitioning) with Eq. 2.5 (which relates λ_2 to cooling rate) and assuming $n=\frac{1}{3}$ leads to the expression below:

$$\Delta T_r = \left(\frac{B \times 10^{-6}}{5.5} \right)^3 \times \frac{1}{M} \quad \text{Eq. 4.4}$$

where $B=42.1 \mu\text{m}(\text{°C/s})^n$ [18]. This expression provides an estimate of the solidification interval of the primary phase since the temperature range ΔT_r represents the range over which the secondary dendrite arms coarsen, i.e.

$\Delta T_r = T_{primary}^{nuc.} - T_{eutectic}^{nuc.}$. Although the assumption $n = \frac{1}{3}$ is significant, it is consistent with experimentally-determined values of n for other steel alloys during rapid solidification [18]. Values of B and n will be validated in Chapter 6 as well. It should be noted that the recalescence is not considered in the coarsening equation and it is known that some recalescence is happening in reality. The resulting values of ΔT_r for the various atomized particles are provided in Table 4.3. ΔT_r is found to vary with particle size and atomization method since C_1^m term in Eq. 4.3 is not taken to be the equilibrium eutectic composition but rather the values taken from the metastable liquidus line for D2 tool steel.

Table 4.3. Solidification time and solidification temperature range for particles solidified at different conditions

Atomization method	Particle size range (μm)	Solidification time (s)	Primary temperature range for austenite ($^{\circ}\text{C}$)	f_R (Vol.%)
IA-helium	300-355	1.03×10^{-2}	55.11	72 ± 0.9
	600-710	4.63×10^{-2}	54.84	71 ± 0.5
	1000-1400	1.29×10^{-1}	53.88	68 ± 1.0
IA-nitrogen	300-355	4.15×10^{-2}	54.64	70 ± 0.8
	600-710	1.59×10^{-1}	54.25	69 ± 1.2
	1000-1400	3.02×10^{-1}	51.71	62 ± 2.1
WA	300-355	8.04×10^{-4}	56.50	84 ± 0.5
	600-710	4.86×10^{-3}	55.50	72 ± 0.3
	1000-1400	5.20×10^{-2}	55.11	67 ± 0.3

With ΔT , and the eutectic undercooling temperatures derived from the eutectic fractions, one can estimate the nucleation temperature of the primary phase and the corresponding primary phase undercooling as compared to the equilibrium phase diagram. It can be seen from Figure 4.10 that for rapid solidification, larger primary phase undercooling results in a smaller eutectic fraction. Figure 4.11 shows a direct relationship between particle size and primary phase undercooling.

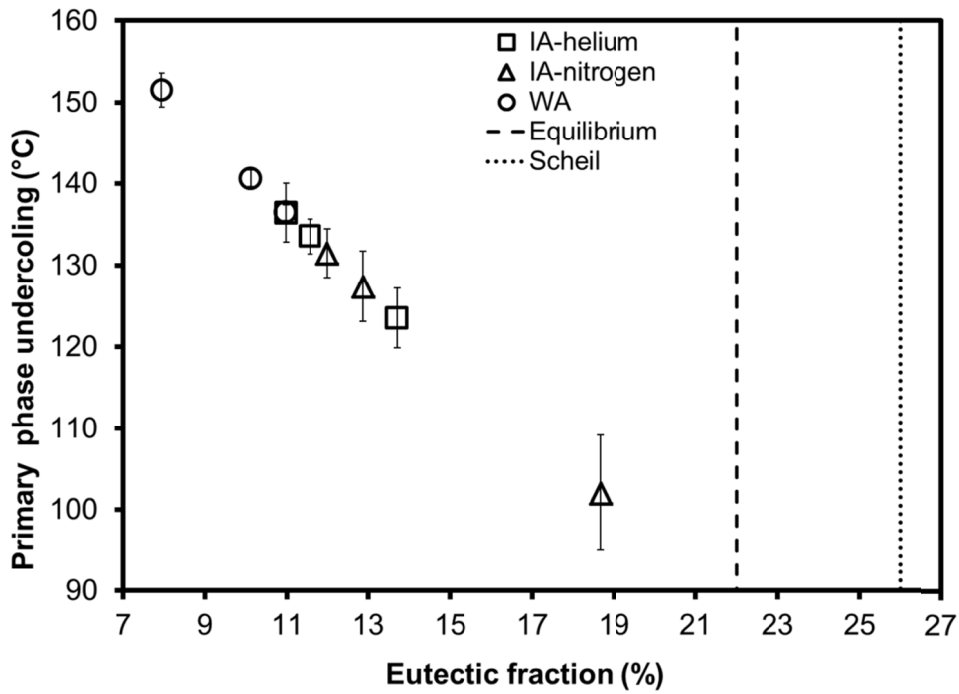


Figure 4.10. Effect of primary phase undercooling on the amount of eutectic in IA and WA D2 tool steel.

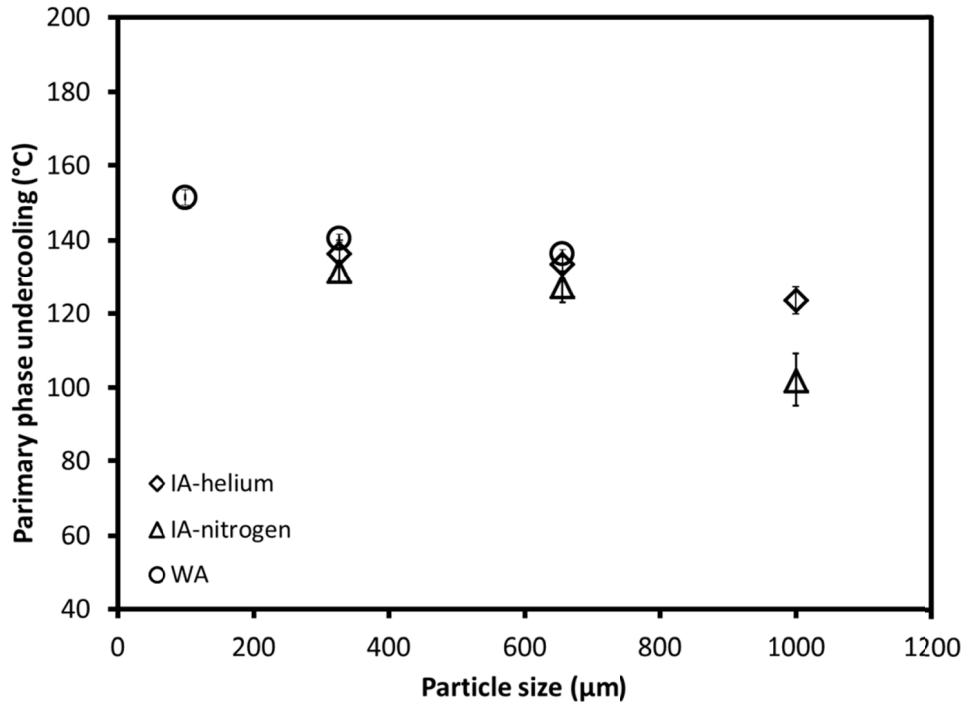


Figure 4.11. Effect of particle size on the primary phase undercooling.

As can be seen, the primary phase undercooling only slightly decreases with an increase in the particle size to 655µm. But, a further increase in particle size to 1000µm results in a significant decrease in undercooling for the case with a nitrogen atmosphere. The calculated values of ΔT and t_{SL} from Table 4.3 for different D2 tool steel particle sizes during IA in helium and nitrogen, and WA, can be used to directly determine the average cooling rate of the primary phase during atomization. These average cooling rates are provided in Figure 4.12 as a function of eutectic fraction. As is shown, the eutectic fraction is inversely proportional to the primary phase cooling rate.

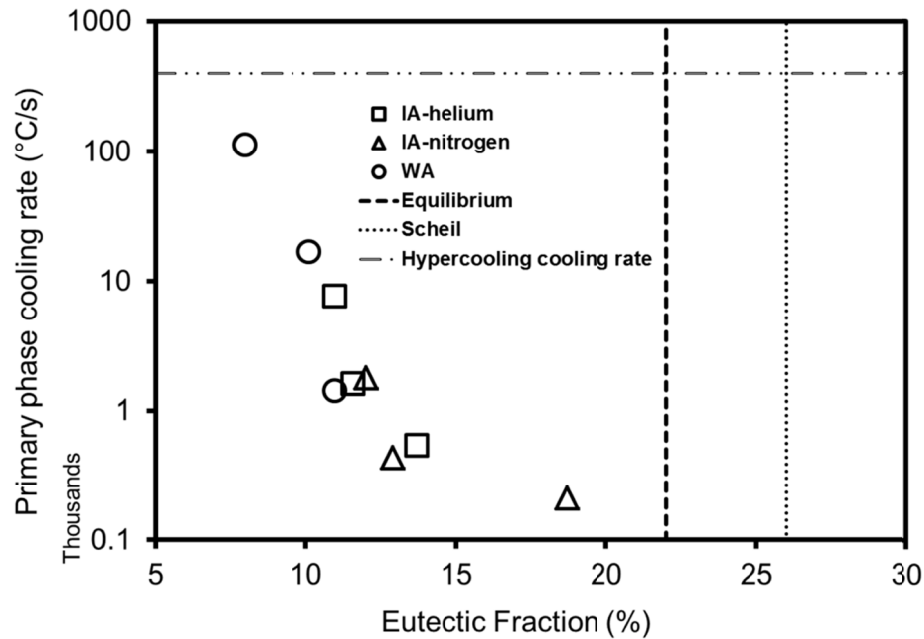


Figure 4.12. Effect of cooling rate of primary phase on the amount of eutectic in IA and WA D2 tool steel.

The methodology outlined above for calculating the solidification interval and the undercooling of the primary phases does not take into account the dendrite tip kinetics, and is therefore a significant approximation. But, as shown in Figure 4.10 and Figure 4.11, considerable variation in undercooling is predicted to occur as a function of particle size and cooling gas, matching our understanding of the atomization process. In a companion work [113] on IA rapidly solidified Al-10wt.%Cu droplets, primary phase undercooling data calculated using the coarsening model approach outlined in Eq. 4.4 was compared to results obtained from comprehensive study of eutectic undercooling that combined neutron diffraction analysis of undercooling temperature, and a microsegregation model of solidification [114]. This comparison found the coarsening

approximation to be within 10-15% of the work by Prasad et al. [79], thus validating the use of this methodology to qualitatively characterize primary phase undercooling and nucleation during solidification.

The fraction of droplet solidified during recalescence can be calculated using Eq. 4.1, and the primary phase undercoolings provided in Figure 4.11¹. The calculated f_R values for the IA droplets in helium and nitrogen as well as WA droplets are shown in Table 4.3. Considering these results, along with the primary phase undercooling presented in Figure 4.10, it can be seen in

Figure 4.13 that f_R increases with increasing primary phase undercooling. This result is consistent with the work of Prasad et al. [65], who showed using a combination of experimental and modeling activities that an increase in the primary phase undercooling for Al-Cu alloys results in an increase in the fraction of solid that forms during recalescence.

Figure 4.13 also shows that if one extrapolate the f_R up to $f_R=100$ Vol.%, primary phase undercooling would reach the hypercooling limit of 264°C. Hypercooling limit is the undercooling at which solidified fraction at the recalescence is 1 [25]. This value corresponds to a 20 μ m particle atomized in helium with 4×10^5 K/s cooling rate.

¹ The hypercooling limit of 264°C for D2 tool steel was calculated from ΔH_f and C_p^l material property values taken from Thermocalc (8.70×10^8 Jm⁻³, 3.30×10^6 JK⁻¹m⁻³)

4.3.3.1. Critical radius and activation energy of austenite nucleant

After finding an estimation of primary phase undercooling in the IA droplets, now it is possible to estimate the critical radius of the austenite nucleation (r^*), as well as its nucleation activation energy (ΔG^*). Assuming homogenous nucleation, r^* and ΔG^* are represented as Eq. 2.3 and Eq. 2.4, respectively.

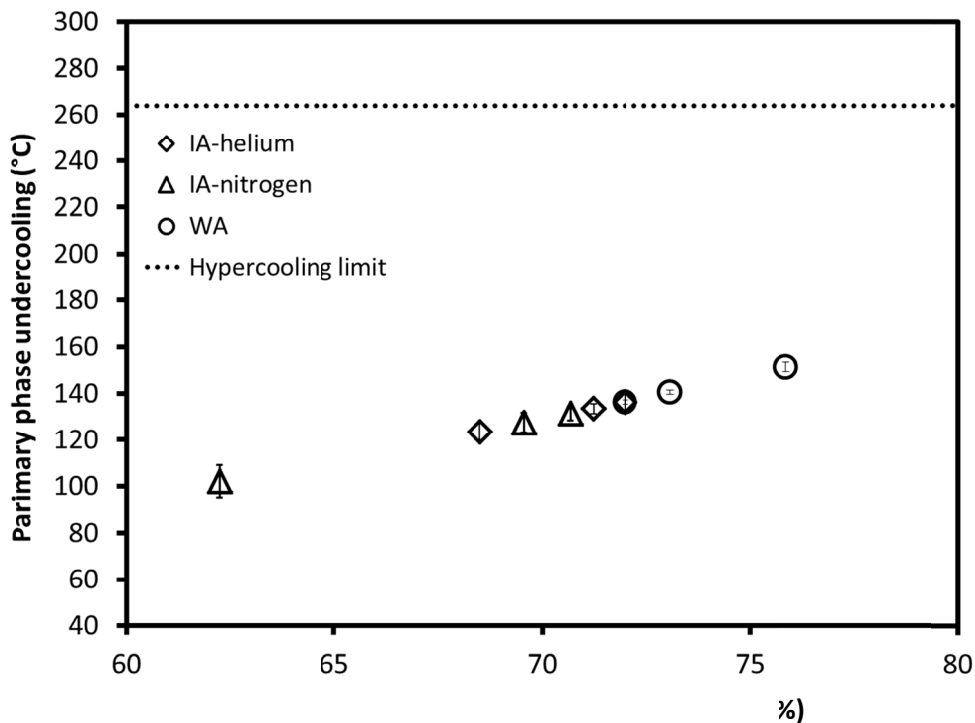


Figure 4.13. Primary phase undercooling versus fraction solidified during recalescence of D2 tool steel droplets.

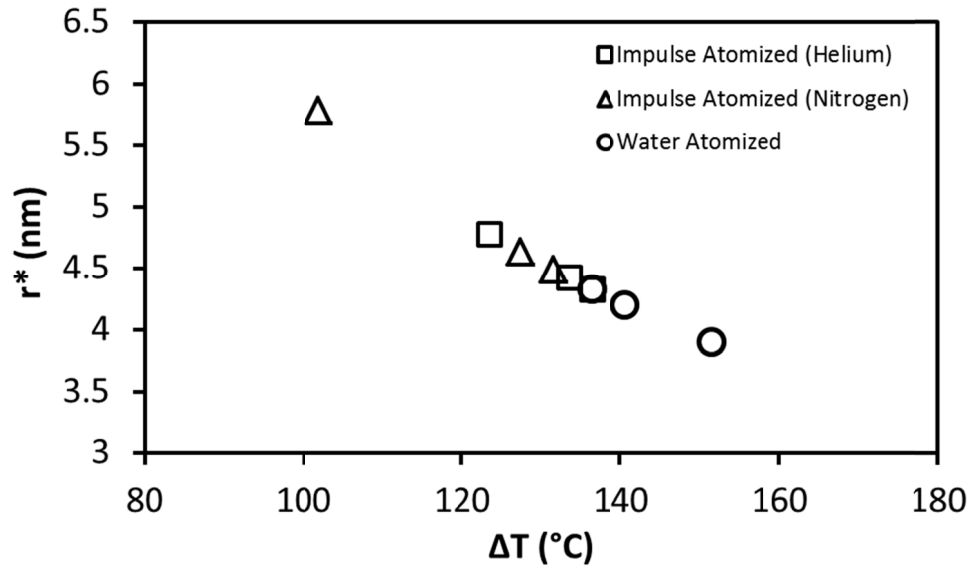
Using Thermocalc software, one can calculate the early nucleants of austenite have about 0.57 wt.% carbon when they first form in the liquid. Briefly, Thermocalc provides the chemical composition of austenite slightly below the nucleation temperature of D2 tool. Using this value and information provided by Mizukamu et al. [115], the solid-liquid interfacial

energy can be calculated as 0.154Jm^{-2} . Using primary undercooling values of IA-helium, IA-nitrogen and WA produced particles, critical radius of the austenite nucleation (r^*) using Eq. 2.3, as well as its nucleation activation energy (ΔG^*), using Eq. 2.4, can be calculated and are presented in Figure 4.14.

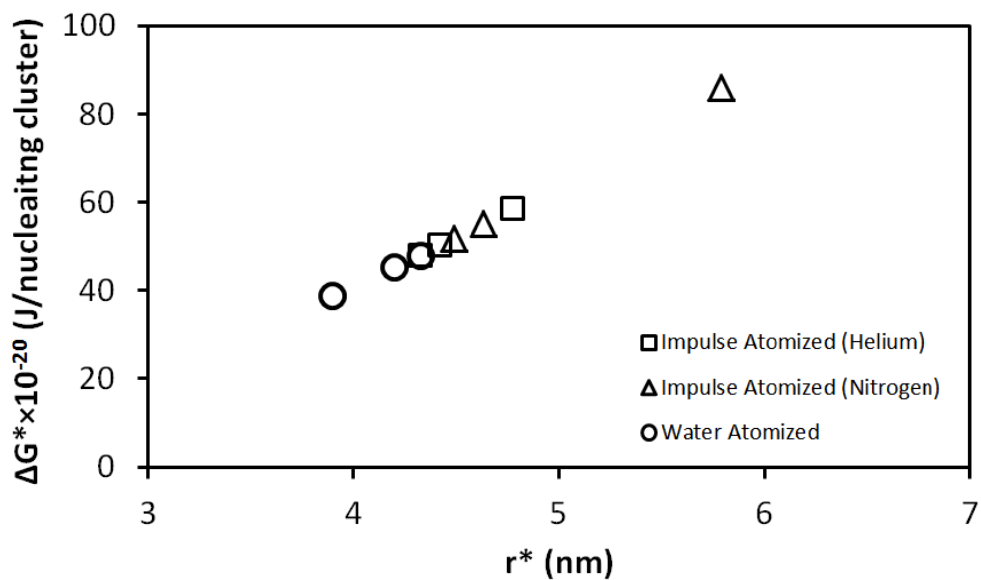
Using austenite lattice parameter as $a_\gamma = 0.358\text{nm}$ provided by Lee et al. [116], and assuming spherical nucleants of austenite, one can find the number of unit cells in a homogenous austenite nucleants, as shown in Figure 4.15. This figure shows that by increasing the primary phase undercooling, number of unit cells in the austenite nucleant decreases. It means by increasing the primary phase undercooling, less unit cells need to be joined in order to make an austenite nucleant with the critical radius. This means nucleation can proceed faster and easier by increasing the primary phase undercooling. Information provided in Figure 4.15 would be useful in modeling of nucleation stage of D2 tool steels.

4.4. Discussion

The microstructure morphology and solidification kinetics during IA and WA presented in this chapter can provide new insight into the rapid solidification of D2 tool steel, and its effect on carbide formation during subsequent heat treatment. As shown in Figure 4.11, larger undercoolings are required in the small particles prior to primary phase nucleation, which results in the formation of more austenite during the recalescence event.



(a)



(b)

Figure 4.14. (a) Critical radius of austenite nucleant as a function of primary phase undercooling, (b) Activation energy for formation of austenite nucleants as a function of critical radius of nucleants.

The degree of supersaturation is related with the eutectic undercooling as well as primary phase undercooling. Near the eutectic temperature is where the primary phase gets really supersaturated with

solute. Also according to Herlach [22], in high amount of primary phase undercooling, crystal growth velocity is much larger than atomic diffusive speed which also results in high degree of supersaturation. More liquid remained in post-recalescence period transforms under Scheil conditions which cause formation of segregation in the microstructure.

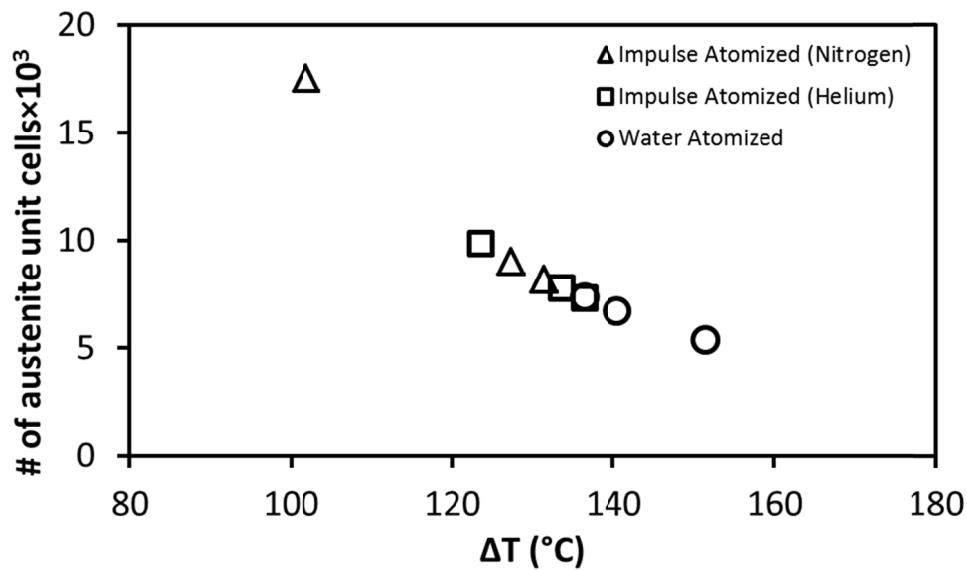


Figure 4.15. Number of unitcells in the austenite nucleants during homogenous nucleation of austenite.

In the case of primary phase undercooling, since the amount of supersaturated solid solution is affected by f_R [25], it can be hypothesized that there will be different levels of supersaturation according to the degree of undercooling achieved in different particles; smaller particles will have higher levels of supersaturation in alloying elements as compared to the larger ones. As the degree of supersaturation provides the driving force for

precipitation of secondary phases during heat treatment, smaller particles are expected to precipitate carbides on a finer scale, providing enhanced mechanical properties [117]. At the same time, there is a limit to the degree of undercooling, and hence carbide spacing, that can be achieved with rapid solidification. Although the hypercooling limit for the D2 tool steel under adiabatic solidification conditions is about 264°C, the maximum value found achieved in the IA and WA experiments is about 140°C.

The variation in λ_2 shown in Table 4.2 and in eutectic fraction shown in Figure 4.7 indicate that the microstructure is affected by the choice of cooling gas and therefore, solidification of these particles cannot be considered as completely adiabatic. But, as shown in Figure 4.11, the largest particles appear to be largely affected by the choice of cooling gas. In the smaller particles, only a slight increase in primary phase undercooling is obtained when cooling with helium as compared to nitrogen. For example, in 328 μm particles shown in Figure 4.11, the difference in primary undercooling values in helium and nitrogen is about 9°C, while this difference in 1000 μm droplets is about 25°C. Due to the small volume of the smaller particles, and therefore less latent heat of fusion, most of the heat generated during solidification is accommodated by the liquid, which minimizes the effect of the cooling gas. In the larger particles, however, the abundance of active nucleation sites can be overcome by the increased cooling power of helium, causing droplets to

begin solidification at larger undercoolings. At this size, solidification is controlled mainly by external heat extraction, as found previously in [118].

4.4.1. Sensitivity analysis on chemical composition of D2 tool steel

As shown in Table 2.2, D2 tool steel chemical composition shows a range of alloying elements. Since carbon and chromium are the major alloying elements in D2 tool steel, a sensitivity analysis has been done on the effect of carbon and chromium content on the calculated amount of eutectic undercooling using chemical composition of D2 tool steel used in this study.

To do so, phase diagrams of D2 tool steel were generated using chromium contents of 11wt.% and 13wt.% (upper and lower range of chromium in D2 tool steel). Generated D2 phase diagrams using different chromium values do not appear to be significantly different. The slope of solidus and liquidus lines remain almost same ($m_s = -234^\circ\text{C} \cdot (\text{wt.}\%)^{-1}$ and $m_l = -75^\circ\text{C} \cdot (\text{wt.}\%)^{-1}$). The only small difference is in the eutectic temperature ($\sim 8^\circ\text{C}$). The range of carbon content for D2 is from 1.40wt.% to 1.60wt.%. For this range of chromium and carbon contents, the corresponding range of eutectic undercooling values was determined to be between 2% to 10% from the eutectic undercooling values calculated using D2 tool steel composition in this study. These results show although the phase diagram is changing by changing the chromium and carbon content, but the eutectic undercooling values (and as a result primary phase undercooling) are not very sensitive to the alloying content in the D2 tool steel chemical

composition range. Thus, the assumed chemical analysis of the WA powders being the same as that of IA powders has no effect on the trends or conclusions presented in this work.

4.5. Summary

In this chapter, the effect of different rapid solidification parameters such as undercooling and cooling rate on the microstructure and formation of different phases such as retained austenite was investigated. The as-atomized microstructure of the powders contains primary retained austenite dendrites and eutectic of austenite and M_7C_3 carbides. It was found that when helium is used as a cooling gas during IA, a finer microstructure, smaller SDAS and finer eutectic lamellae are obtained as compared to using nitrogen. Similar results were observed in the smaller particles due to their higher cooling rates.

The quantitative relationship between solidification undercooling (primary and eutectic undercooling) and cooling rate and level of supersaturation of primary phase was also studied in this chapter. There is a higher amount of primary phase and eutectic undercooling in the particles with higher cooling rate. The use of helium gas and smaller droplets yield higher cooling rates.

The knowledge of primary phase supersaturation will be used in the Chapter 6 to investigate precipitation of carbides during annealing of rapidly solidified D2 tool steel.

The need exists to independently verify the primary phase undercooling temperatures estimated from the microstructural

quantification which are described in this chapter. The following chapter will cover the efforts for the online real-time diagnostics of the atomized droplets during the free fall. Chapter 5 describes efforts to find a methodology to measure the undercooling of IA droplets, using online measurement techniques and modeling.

Chapter 5

5. Online real-time diagnostics of a single fluid atomization system

5.1. Introduction

The possibility to control the morphology and microstructure can be achieved by variation of different solidification conditions (such as undercooling or cooling rate). This can substantially affect the physical and mechanical properties of alloys.

A number of models have been reported for predicting or estimating the undercooling temperature of droplets in gas and single fluid atomization systems as well as drop tubes [79,119,120]. There are no feasible experimental techniques available yet to directly validate these models or estimates. As previously shown in Chapter 4, primary and eutectic undercoolings were calculated indirectly, using volume fraction of primary phase and eutectic formed during solidification. An indirect method of validation was also presented by Prasad et al. [65]. In this approach, microtomographic images were analyzed in order to locate the region in which the growth in a particle has been initiated. The volume of this region was measured and compared with predictions based on a microsegregation model. A variable undercooling of the primary phase was incorporated in this model [79,87]. This approach has led to estimations of primary phase undercooling of about 15 to 20°C in Al-Cu droplets. The problem associated with this approach is that the initial growth region in a particle is

not always visible. This approach involves measurement errors which reduces the accuracy of final measurement. Eutectic undercooling has also been estimated by measuring the fraction of eutectic in the solidified structure either using SEM images or neutron diffraction [37,87]. The measured quantity is compared with the respective phase diagram of the system under study. Solidus and liquidus lines are extended until agreement is found between measured eutectic fraction and the extended lines on the phase diagram. The eutectic temperature corresponding to this agreement is taken to be the nucleation temperature of the eutectic. Temperature measurements of a droplet levitated in an electromagnetic field was reported by Gandin et al. [114] using a high speed pyrometer. They clearly reported primary phase and eutectic undercooling measurements of an Al-24Cu droplet with 6mm diameter.

A systematic effort on the investigation of thermal history of falling droplets in-situ during atomization is rare [121]. In addition to the thermal history, in-situ measurement of the droplet diameter in order to measure the initial and instantaneous velocity is vital in validating solidification models. This section reports on an effort to make such measurements on droplets in flight and in-situ during the atomization of copper and D2 steel. Two measuring instruments were used: a shadowgraph to measure droplet velocity and diameter and a DPV-2000 (a two color pyrometer) for droplet radiation measurements.

Shadowgraph is a high-magnification shadow imaging system which is used for visualizing particles (Figure 5.1). It is based on high resolution imaging with pulsed backlight illumination. This technique is independent of the shape and material of the particles and allows the investigation of sizes down to the micron scale.

In order to illuminate the falling droplets, a double pulse laser was used. By coupling the light source with a double frame camera, it is also possible to investigate the velocity of the particles.

Data from the shadowgraph will be used to get particle size, particle position, particle shape and velocity during free fall. The position of the shadowgraph can be controlled with a translation stage in all three axes.

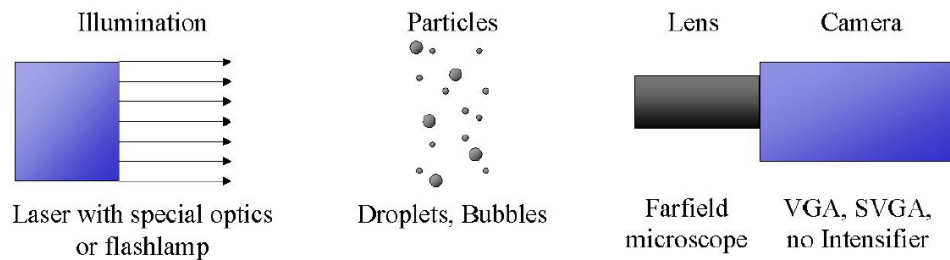


Figure 5.1. General view of a shadowgraph system [122].

A two-step segmentation algorithm is applied on the images taken by the shadowgraph. The first segmentation is to find the location of the particles which is called the bounding box. In this step, shadow picture of the droplet is subtracted from a reference image (background atmosphere image) and an inverted shadow image is then achieved (Figure 5.2). For the

first segmentation a user defined global threshold is used to detect the particles (Figure 5.3). The global threshold is relative to the difference between maximum and minimum intensity of the inverted image. The droplets images which are above the global threshold are considered for the next step (#1, #2, #3 and #4 in Figure 5.3). If peaks intensity is below the global threshold, that peak will be ignored for the further calculations.

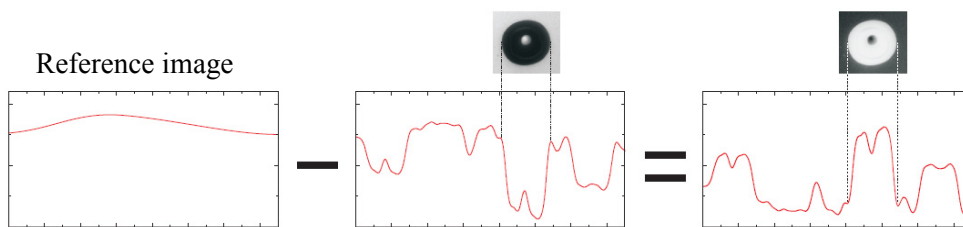


Figure 5.2. Inverting the shadow image using a reference image [122].

In the second step of the segmentation, areas of the image which are above the global threshold are selected (Figure 5.3 for particle #3). High level and low level grey counts can be determined by user based on the image focus needed for the calculations (Figure 5.4). If high values of “high level” counts and low values of “low level” counts are selected, less-focused droplets will be detected by shadowgraph which results in errors in particle size calculations. Global threshold, high level and low level values of 40%, 60% and 40% were chosen respectively in this work [122].

In order to calculate the velocity of the droplets, the shadowgraph software first applies sizing algorithm to each frame of the source images and stores information about position and size of each droplet. Pictures taken from both frames then analyzed by the software and based on the

location of the droplets in both pictures and time between each frame, the velocity of the droplet is then calculated. The droplets in two pictures are only accepted if the diameter deviation is within the given range which in this work it was $\pm 5\%$ diameter deviation [122].

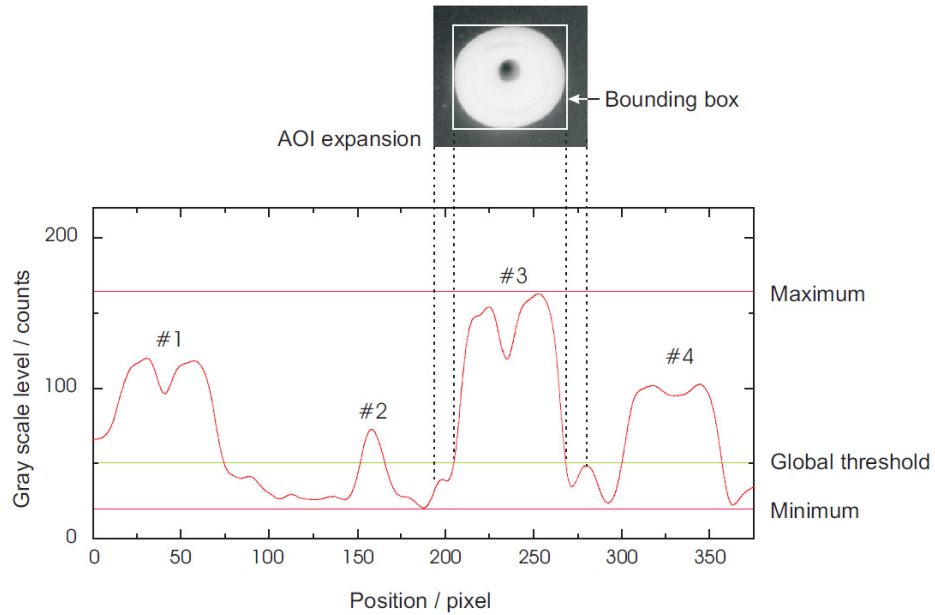


Figure 5.3. Thresholds for the first segmentation [122].

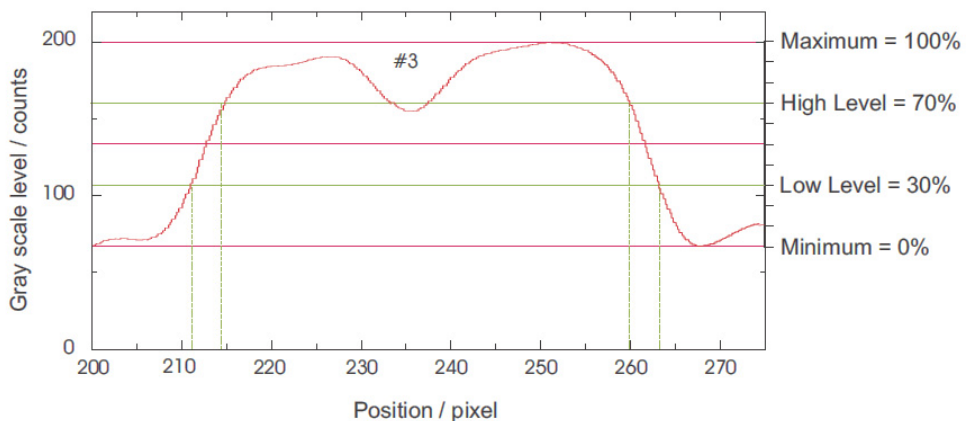


Figure 5.4. Thresholds for the first segmentation [122].

The DPV-2000 is a high-speed two colors pyrometer that measures the effective radiant energy of the particles. According to Planck's radiation law, the total energy radiated by a particle can be expressed as:

$$E(\lambda_i) = \frac{C_1 \varepsilon(\lambda_i) \lambda_i^{-5}}{e^{C_2/\lambda_i T} - 1} \quad \text{Eq. 5.1}$$

where, $C_1 = 3.74 \times 10^8 \text{ W} \cdot \mu\text{m}^4/\text{m}^2$ and $C_2 = 1.4387 \times 10^4 \text{ } \mu\text{m} \cdot \text{K}$ [123]. $\varepsilon(\lambda_i)$ is emissivity at λ_i , wavelength, and T is temperature. In two color pyrometry, a measure of the energy radiated from a body is taken at two wavelengths. It is assumed, for a two color pyrometer, that over the measured temperature and at wavelengths that are close to each other, the emissivity is not a function of wavelength. In this work, we aim to test this assumption for molten copper droplets atomized into an argon gas atmosphere. For molten droplets, Eq. 5.1 can be re-written in the following form for the DPV-2000:

$$Q(\lambda_i) = \frac{C_1 \alpha(\lambda_i) d^2 \lambda_i^{-5}}{e^{C_2/\lambda_i T} - 1} \quad \text{Eq. 5.2}$$

where $Q(\lambda_i)$ is proportional to $E(\lambda_i)$ and is the quantity measured by the DPV-2000, $\alpha(\lambda_i)$ is proportional to $\varepsilon(\lambda_i)$ and d is the droplet diameter in μm . The DPV-2000 reports measurements of Q at two specific wavelengths designed into the instrument. For these experiments these wavelengths are, λ_1 is $0.787 \text{ } \mu\text{m}$ and λ_2 is $0.995 \text{ } \mu\text{m}$. A mathematical model was also utilized to predict the temperature of falling copper droplets at different heights, which was explained in section 2.4. Thus, for a given measurement of Q for a known droplet size and distance below the nozzle, $\alpha(\lambda_i)$ at each

wavelength is the only unknown in Eq. 5.2 and will be compared for values determined at λ_1 and λ_2 . The following section addresses attempts to understand radiant energy change of droplets at different distances, due to heat loss and solidification.

5.1.1. DPV-2000 hypotheses

There are several hypotheses which are considered in DPV-2000 measurements [94]. Some of them can be considered as the principles in calculations and some of them should be explored in order to find out if they are meaningful in IA application:

- Molten droplets are considered as gray body emitters, i.e. $\varepsilon(\lambda_1) = \varepsilon(\lambda_2)$,
- Molten droplets should be spherical (or close to spherical); which in IA almost all of the droplets are spherical when atomized in an inert gas environment,
- Regardless of the size, All droplets have similar $\varepsilon(\lambda_i)$.

These hypotheses will be evaluated in this chapter in the free fall droplets condition.

Figure 5.5 shows droplets of copper and D2 tool steel at 4cm and 10cm below the nozzle plates, respectively. These images were taken by shadowgraph. It can be seen from this figure that almost all droplets are spherical at the minimum distances (4cm in D2 and 10cm in copper) from nozzle plate where DPV-2000 has been located.

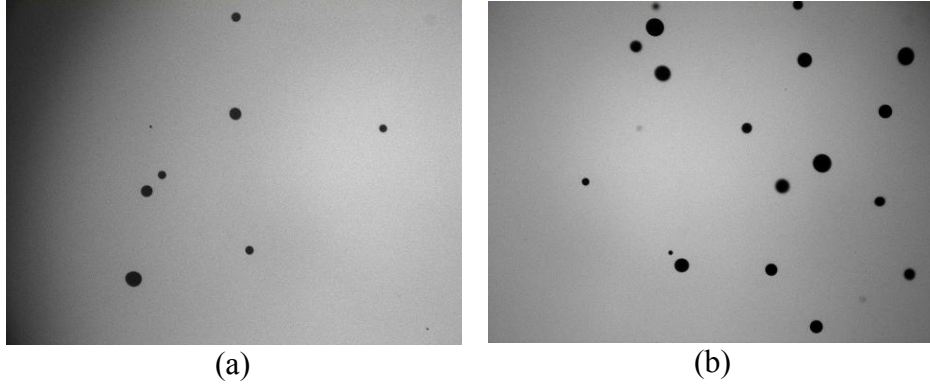


Figure 5.5. shadowgraph images of droplets during free fall, (a) molten D2 tool steel at 4cm below the nozzle plate and (b) molten copper at 10cm below the nozzle plate.

5.1.2. DPV-2000 temperature measurement

As previously mentioned, DPV-2000 is a high-speed, high precision two color pyrometer. Surface temperature of the particles, T , is then measured based on Planck's radiation law (Eq. 5.1). Assuming gray body hypothesis, λ_1 and λ_2 are chosen close enough so that $\varepsilon(\lambda_1) \approx \varepsilon(\lambda_2)$, then [94]:

$$R = \frac{E(\lambda_1)}{E(\lambda_2)} = \left(\frac{\lambda_1}{\lambda_2}\right)^{-5} \cdot e^{\frac{C_2}{T} \left(\frac{1}{\lambda_2} - \frac{1}{\lambda_1}\right)} \quad \text{Eq. 5.3}$$

$$T = \frac{C_2(\lambda_1 - \lambda_2)}{\lambda_1 \lambda_2} \left[\frac{1}{\ln R + 5 \ln \left(\frac{\lambda_1}{\lambda_2}\right)} \right] \quad \text{Eq. 5.4}$$

5.1.3. DPV-2000 diameter measurement

Using Planck's law (Eq. 5.2) and considering all droplets are spherical, one can write that the diameter of particle is:

$$d = \sqrt{\frac{E(\lambda_i)}{DC}} \quad \text{Eq. 5.5}$$

where DC is the Diameter Coefficient and equal to:

$$DC = \frac{C_1 \cdot \varepsilon(\lambda_i) \cdot \lambda_i^{-5}}{e^{C_2/\lambda_i T} - 1} \quad \text{Eq. 5.6}$$

As shown in Eq. 5.6, the diameter coefficient is dependent on the temperature of the droplet. Since at each distance, the temperature of droplet of different sizes is different, one should calibrate DPV-2000 device at each measuring distance. After calibration of DPV-2000 at each measuring distance, it has been reported by DPV-2000 manufacturer (TECNAR) [94] that precision of particle size measurement is between 7-15% and that it is greatly dependant on the validity of the initial hypotheses, especially sphericity of molten droplets.

5.2. Results and discussion

5.2.1. DPV-2000 diameter measurement calibration

The shadowgraph was used to calibrate the DPV-2000 diameter measurement. As described earlier, shadowgraph technique is independent of the shape and material of the particles. The measured particle size using shadowgraph was used to calibrate diameter measurement of DPV-2000.

During atomization, the shadowgraph was continuously collecting droplet size and velocity data at 5Hz frequency. For copper atomization run at 15cm, a total number of 5200 droplets were measured by shadowgraph during the entire atomization time of two minutes and $D_{50}=580\mu\text{m}$ has been

measured for this set of droplets at 15cm. For the same atomization run, DPV-2000 collected 295 droplets with D_{50} of 652 μm .

According to DPV-2000 reference manual [124], new Diameter Coefficient (after calibration) can be calculated using following equation:

$$\text{New DC} = \text{Current DC} \times \left[\frac{\text{Current Diameter}}{\text{Target Diameter}} \right]^2 \quad \text{Eq. 5.7}$$

where “New DC” is the diameter coefficient after calibration, “Current DC” is the diameter coefficient which is used before the calibration, “current diameter” is D_{50} measured by DPV-2000 before calibration and “Target Diameter” is D_{50} measured by shadowgraph. Before calibration, “Current DC” value was 6197. After doing the calibration according to Eq. 5.7, “New DC” value for 15cm would be 7845.

5.2.2. Online measurements

Figure 5.6 shows velocity of the falling droplets collected by shadowgraph at 15cm below the nozzle plate. It shows distribution of velocity for range of droplet sizes. This atomization run was done with pure copper (99.99% purity), 1400°C superheat, argon as cooling gas, graphite nozzle plate with 37 holes each 500 μm diameter and run number of 110408.

Using this data will result in formation of lots of noise in the following calculations based on the velocity (initial velocity and temperature). Considering that the DPV-2000 has an error in the measurement of diameter of 7%, one can find average velocities for the range of particle sizes which sit in the 7% measurement error as limited by DPV-2000. Figure 5.7

represents average velocities (as well as the standard deviation) for each range of droplet size measured by shadowgraph, which sits in 7% of DPV-2000 diameter measurement.

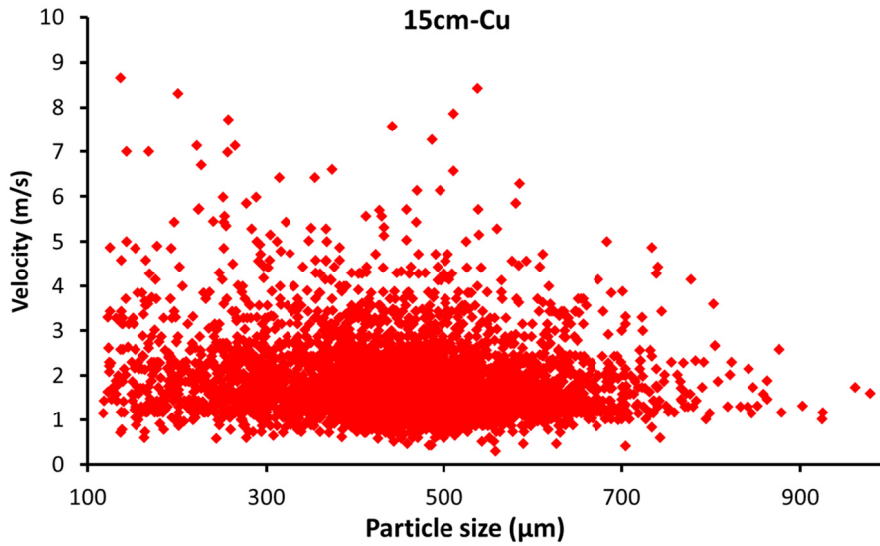


Figure 5.6. Velocity as a function of droplet size of falling droplets collected by shadowgraph system at 15cm below the nozzle plate.

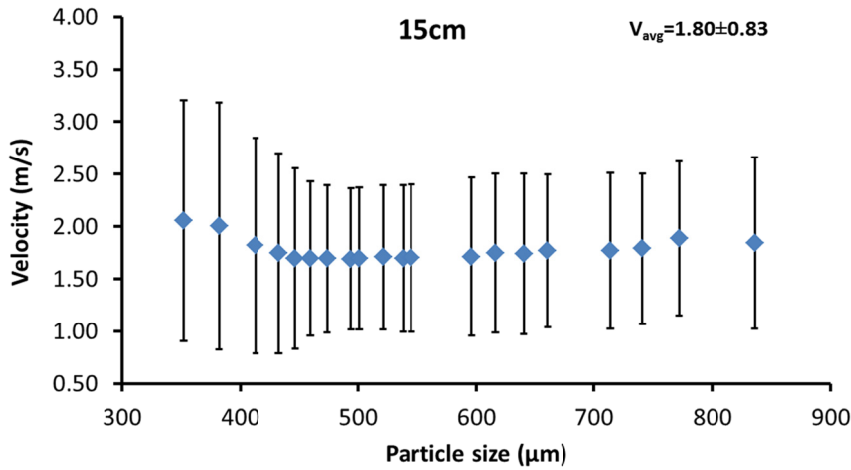


Figure 5.7. Average velocity of IA droplets of copper measured at 15cm below the nozzle plate by shadowgraph for range of droplets within 7% precision measurement range of DPV-2000.

Another approach to analyzing the data is as follows. Using statistical analysis, one can plot Q1, Q2 and Q3¹ for velocity data for different range of particle sizes in the form of a boxplot (Figure 5.8).

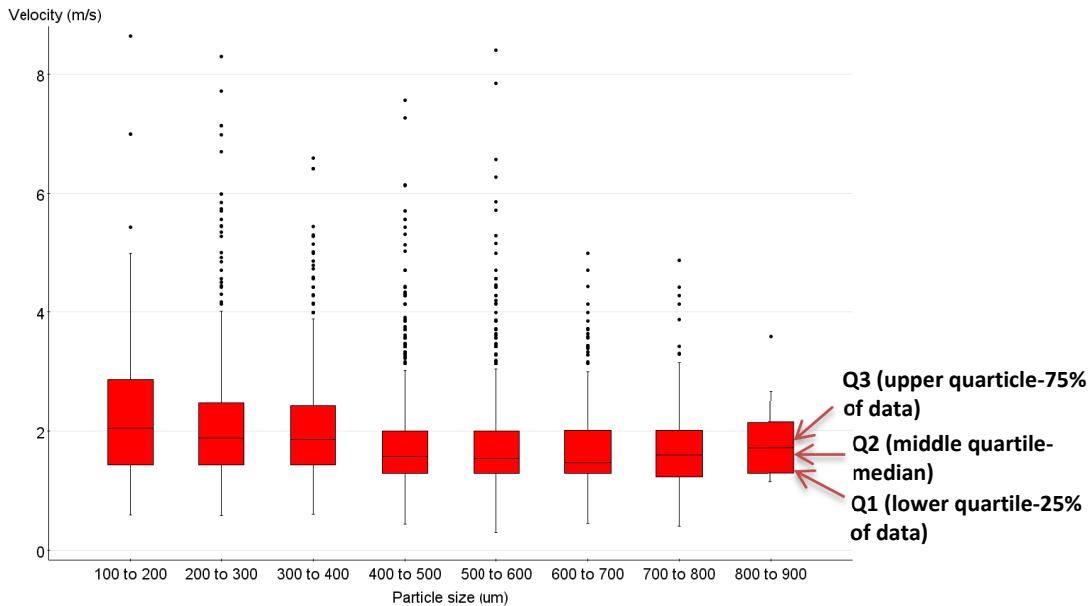


Figure 5.8. Boxplot showing velocity of copper droplets in different particle size range at 15cm below the nozzle plate.

The line in the middle of the boxes in Figure 5.8 shows the median value of velocity for each droplet size. It can be seen that at each particle size range, median values for velocity are close to each other and equal to 1.8m/s. This average velocity can be considered as the average velocity of droplets at 15cm below the nozzle plate.

The same set of data was collected for falling droplets of D2 tool steel at 4cm, 18cm and 28 cm below the nozzle plate (Figure 5.9). This figure shows that at 28cm distance, at each particle size range, median values for velocity are in the same range and the average equals 3.2m/s.

¹ Q1 is the lower quartile, Q2 is the middle quartile (median) and Q3 is the upper quartile.

This average velocity value for droplets falling at 4cm and 18cm heights are 2.3m/s and 2.6m/s, respectively.

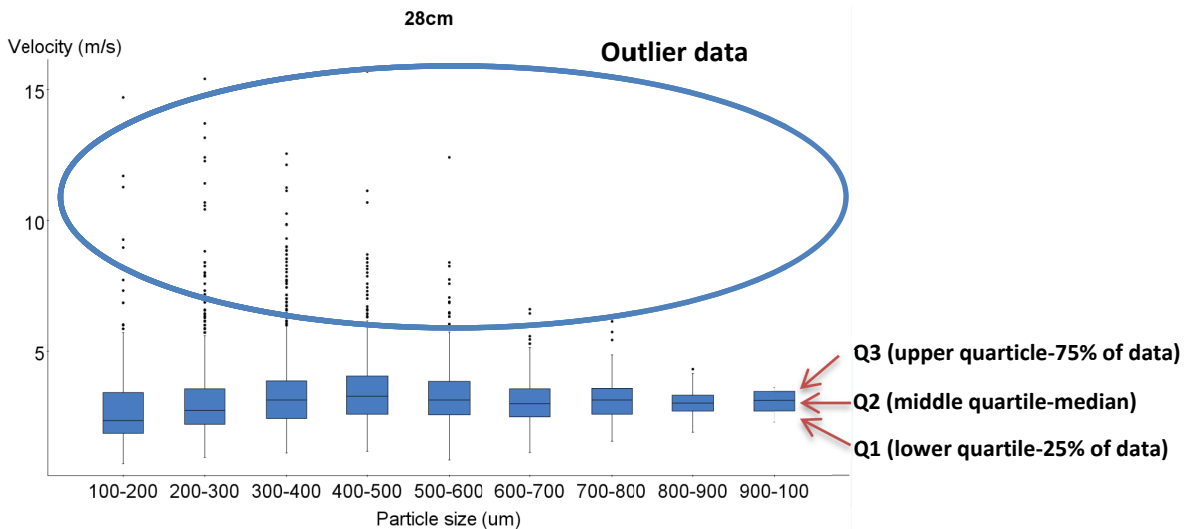


Figure 5.9. Velocity as a function of droplet size of falling droplets collected by shadowgraph system at 28cm below the nozzle plate.

While the shadowgraph was collecting the velocity and diameter of falling droplets at the center of the plume, the DPV-2000 was measuring the radiant energy of the droplets from the same location. The focal point of both shadowgraph and DPV-2000 devices was aimed to be set to the same point, so there would be a greater chance that both devices to measure the same droplets at that point. Figure 5.10.a shows the signal counts of each droplet that DPV-2000 measured at two wavelengths. The area under the curves shown in the inset of Figure 5.10.a represents the radiant energy and as such it is a dimensionless value. The radiant energies measured for different droplet sizes at two different wavelengths are shown in Figure 5.10.b. The measurement was done at 15cm below the nozzle plate

for copper droplets. It can be seen that larger droplets have higher radiant energy. Same set of data for D2 tool steel droplets at 4cm, 18cm and 28cm below the nozzle plate is also shown in Figure 5.11.a-c.

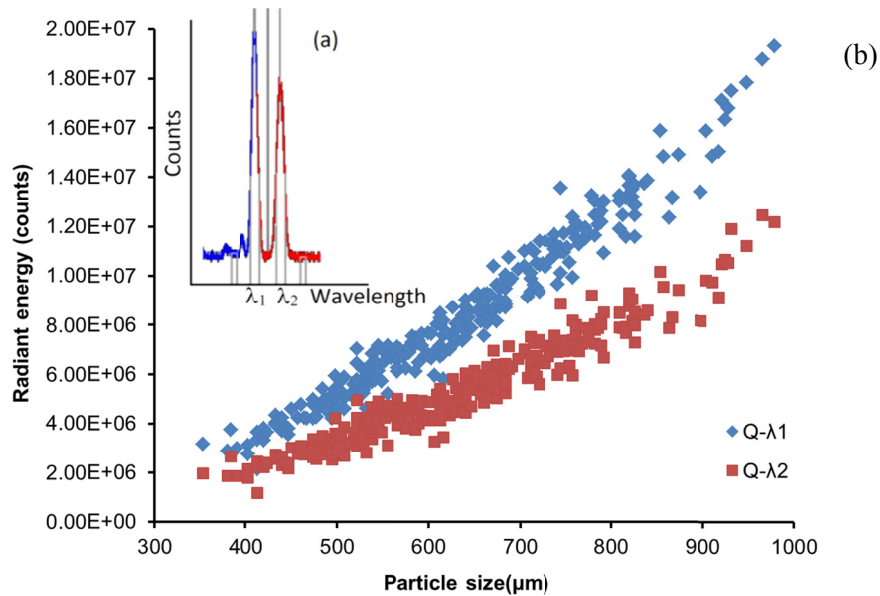
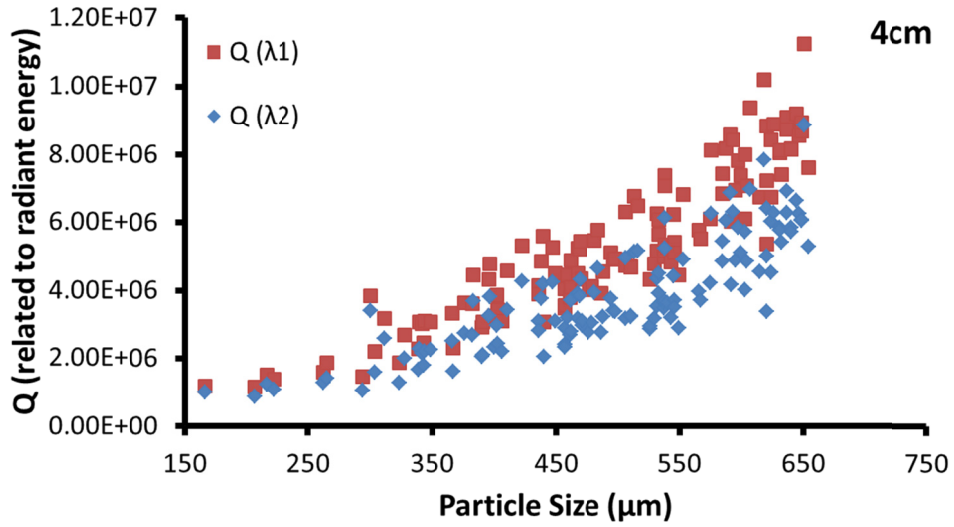
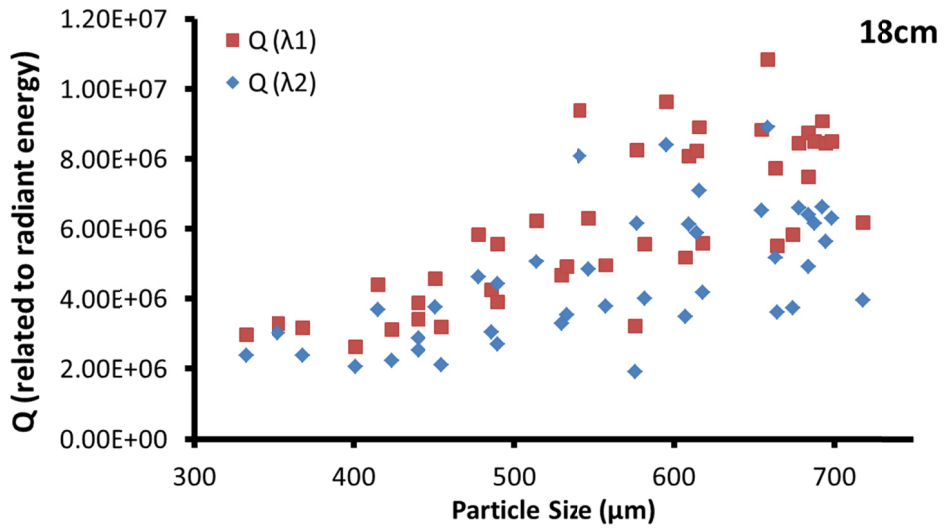


Figure 5.10. The signal counts measured at two different wavelengths for a single droplet, (b) Radiant energy vs. droplet diameter measured by DPV-2000 at 15cm below the nozzle plate (copper).

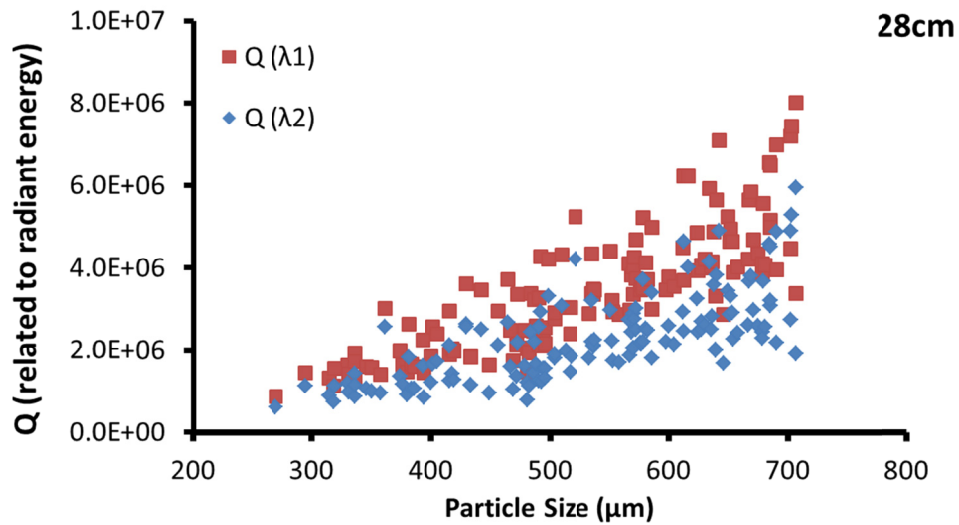
Figure 5.11.d shows power curve fitted radiant energy at wavelength 1 ($Q(\lambda_1)$) versus droplet diameter curve measured at λ_1 at different heights for the droplets that are fully liquid, including those that are undercooled (for D2 tool steel). The undercooling values used in these calculations are based on the values calculated in Chapter 4 for different droplet sizes atomized in nitrogen. The details of the calculations will be discussed in the following sections. Since $Q(\lambda_2)$ shows similar behavior as $Q(\lambda_1)$, analyses will only be shown for $Q(\lambda_1)$ results in the rest of this chapter. All the calculations for λ_2 are included in Appendix A (Figure A.1).



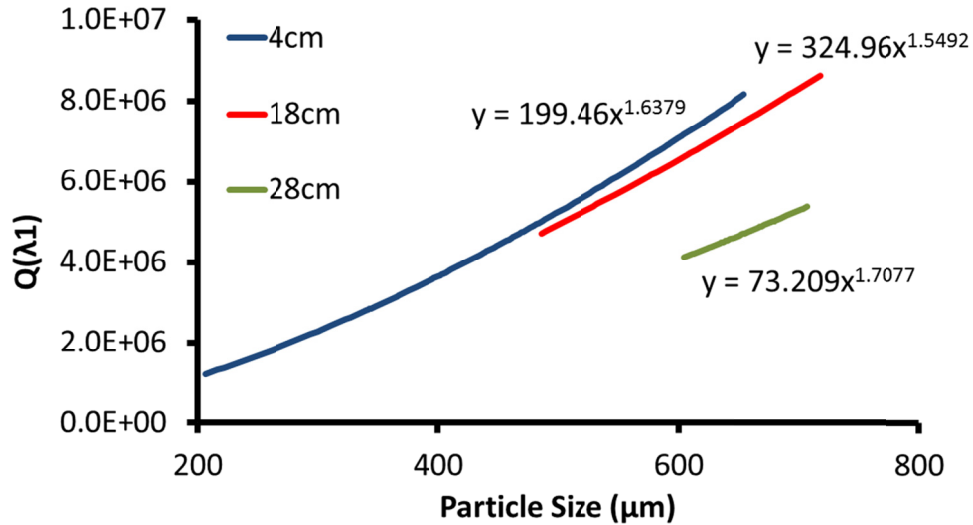
(a)



(b)



(c)



(d)

Figure 5.11. Radiant energy vs. droplet diameter measured by DPV-2000 at (a) 4cm, (b) 18cm and (c) 28cm below the nozzle plate (D2 tool steel). (d) power curve fitted radiant energy of $Q(\lambda_1)$ as a function of droplet diameter for the fully liquid D2 tool steel droplets.

Figure 5.12 also shows power curve fitted radiant energy at wavelength 1 ($Q(\lambda_1)$) versus droplet diameter curve measured at λ_1 at different heights for copper droplets that are fully liquid with no undercooling. It can be seen from the figure that $Q(\lambda_1)$ values at 10cm and 15cm distances below the nozzle plate are so close, compared to that in 50cm. This can be due to small distance between 10cm and 15cm compared to 50cm and therefore, similar $Q(\lambda_1)$ values have been achieved from DPV-2000 at these two distances. Similar graph for $Q(\lambda_2)$ values as a function of copper droplet diameter is also plotted which is shown in Figure A.2 in Appendix A.

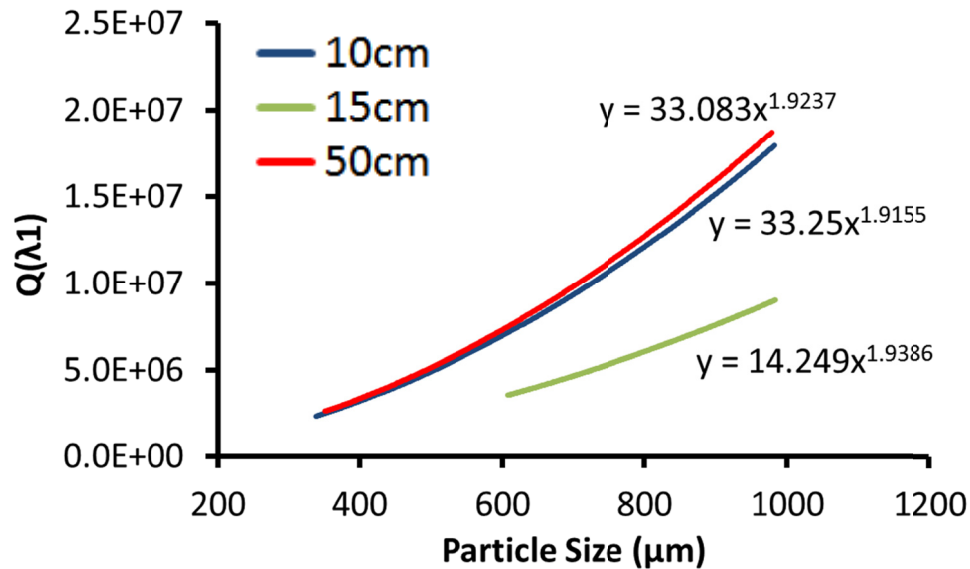


Figure 5.12. Power curve fitted radiant energy of $Q(\lambda_1)$ as a function of droplet diameter for the fully liquid copper droplets.

5.2.3. Droplets temperature calculations

In order to find the temperature of a given droplet size at different distances from the nozzle plate a heat loss model discussed in section 2.4 was used. The droplet's initial temperature (i.e. atomization temperature) and initial velocity (i.e. the exit velocity from the nozzle plate) are required. The initial temperature was 1400°C and 1600°C for copper and D2 tool steel atomization, respectively.

The following procedure is used to calculate temperature of droplets: for a given droplet size, the model is run using varying initial velocities. The initial velocity that yields the average velocity determined using the shadowgraph at 15cm below the nozzle plate is taken as the correct initial velocity for that particle size. Figure 5.13 is a plot of velocity versus distance from the nozzle plate for different droplet sizes. All of these

different trajectories yield an average velocity of 1.8m/s at 15cm below the nozzle plate as measured by the shadowgraph. These initial velocities were used along with their corresponding droplet sizes to estimate the droplet temperature at 15cm below the nozzle plate. The temperature predictions are plotted in Figure 5.14 for copper. From these results, it is apparent that all particles except 294 μm are still molten at this position. Temperature calculation for D2 tool steel will be shown in section 5.2.4.2.

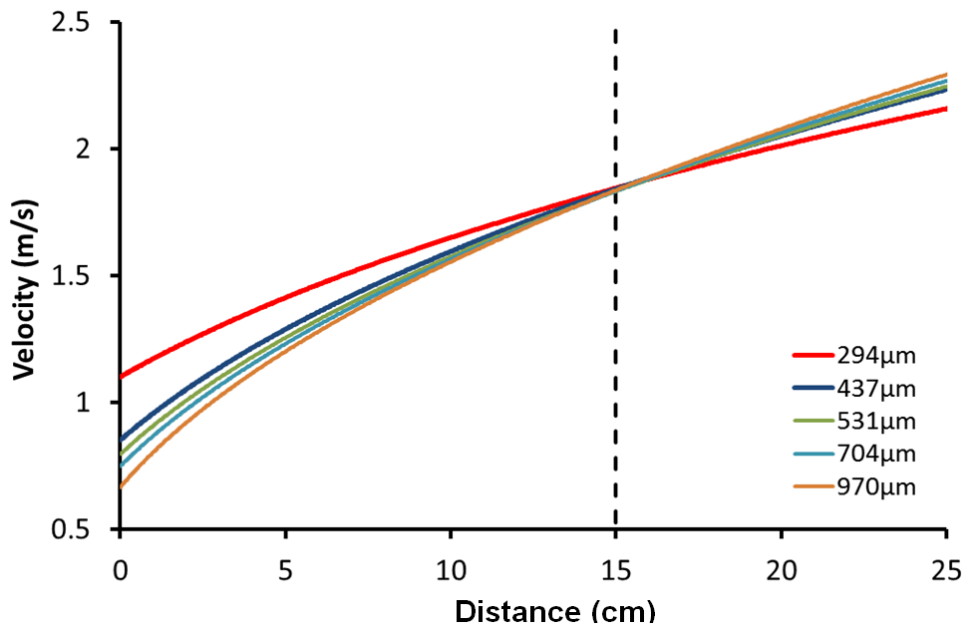


Figure 5.13. Velocity as a function of distance of droplets from the nozzle plate for different droplet sizes, generated from the model.

5.2.4. Calculated temperature and measured radiant energy correlation

5.2.4.1. Calculated temperature of Copper

Temperature of copper droplets at different falling distances from nozzle plate calculated using thermal loss model is shown in Figure 5.15. Note that

no undercooling has been considered during the temperature calculation of copper droplets.

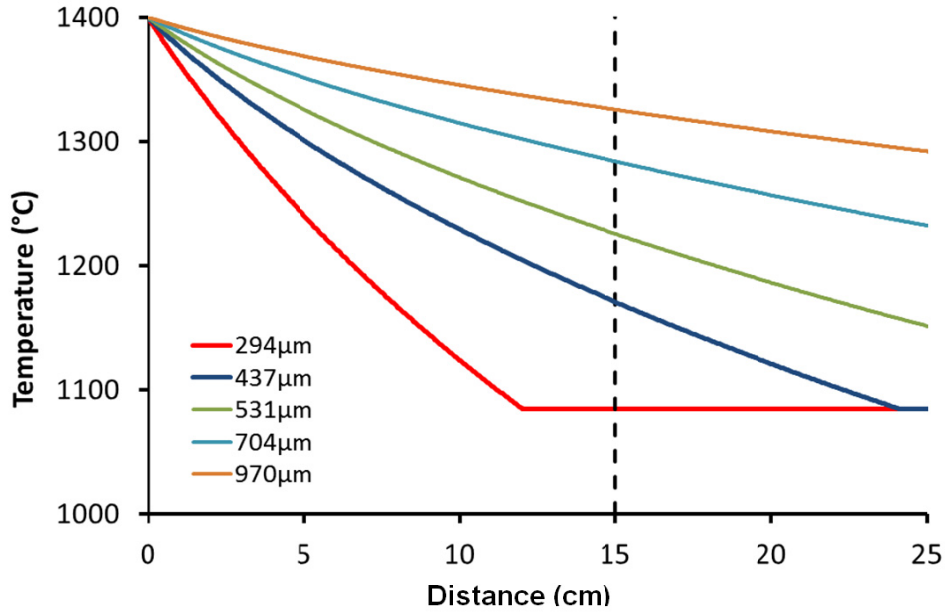


Figure 5.14. Temperature vs. distance from nozzle plate (plotted using the model), using initial velocities calculated from Figure 5.13. Dashed line shows distance from the nozzle plate (15cm).

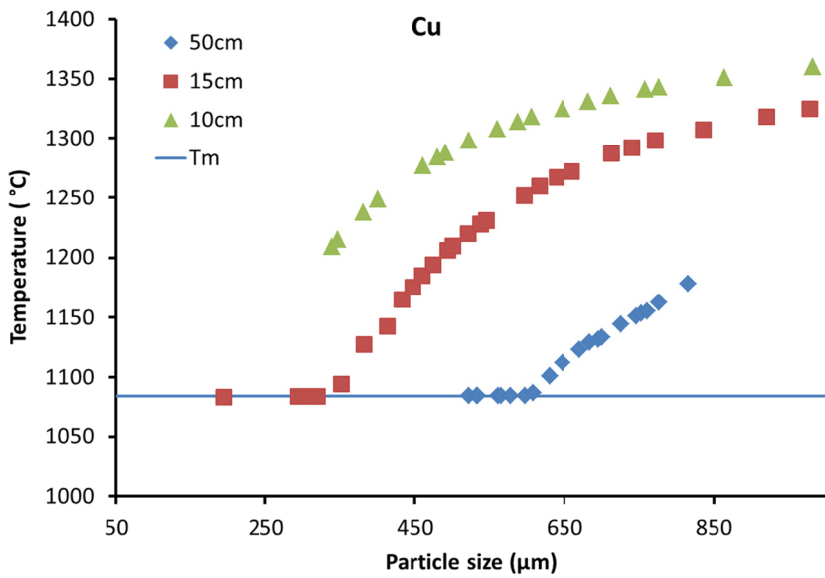


Figure 5.15. Calculated temperature of copper droplets at different falling distances.

Figure 5.15 shows that copper droplets at 10cm from the nozzle plates are all in the liquid state. By falling further down, to 15cm, finer droplets start solidifying while the large ones are still liquid. At larger falling distance (50cm), droplets as coarse as 500 microns are also solidifying. Using the heat loss model, it is also possible to calculate the fraction of solid that forms in each particle during solidification. Also, since the droplets reach their respective velocities at each distance from the nozzle plate, therefore, they should have different initial velocities when they exit the nozzle plate orifices. Figure 5.16 shows the solidified fraction of copper droplets at T_m (Figure 5.15) at 15cm and 50cm from the nozzle plate. Initial velocity of same semi-solid droplets is also shown in Figure 5.16.

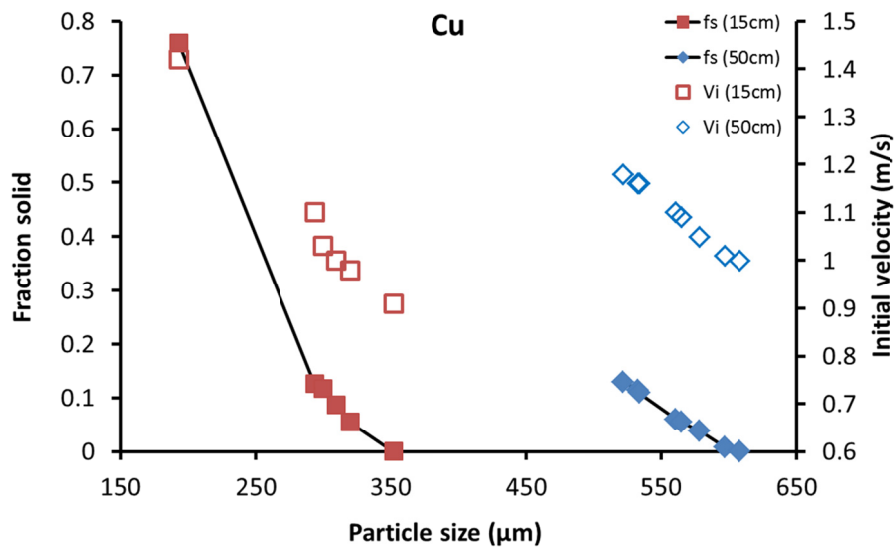


Figure 5.16. Solidified fraction of copper droplets at 15cm and 50cm of nozzle plate, as well as initial velocity of droplets exiting from the orifices.

As shown in Figure 5.16, at 15cm, particles up to 350 μ m in size are in the semi-solid format which covers fraction solid range from 0.76 to 0. At 50cm, larger droplets are in the semi-solid form while they were completely liquid at lower distances.

5.2.4.2. Calculated temperature of D2 steel

A methodology was shown in Chapter 4 where primary phase undercooling of D2 tool steel was estimated. Since it is not possible to apply that methodology to copper particles (there is no microstructural indication as primary phase and eutectic region in the pure copper), no modelling was done on copper considering primary phase undercooling. Since primary phase undercooling data are available from Chapter 4, one can model temperature behaviour of D2 droplets during their free fall considering primary phase undercooling.

In order to calculate primary and eutectic undercooling values for different particle sizes, linear regression of undercooling values (Figure 4.9 and Figure 4.10) of three particle size ranges (300-355 μ m, 600-710 μ m, 1000-1400 μ m atomized in nitrogen) was used (Figure 5.17). The primary undercooling values were used in the thermal model in order to calculate fraction solidified for different particle sizes at different distances.

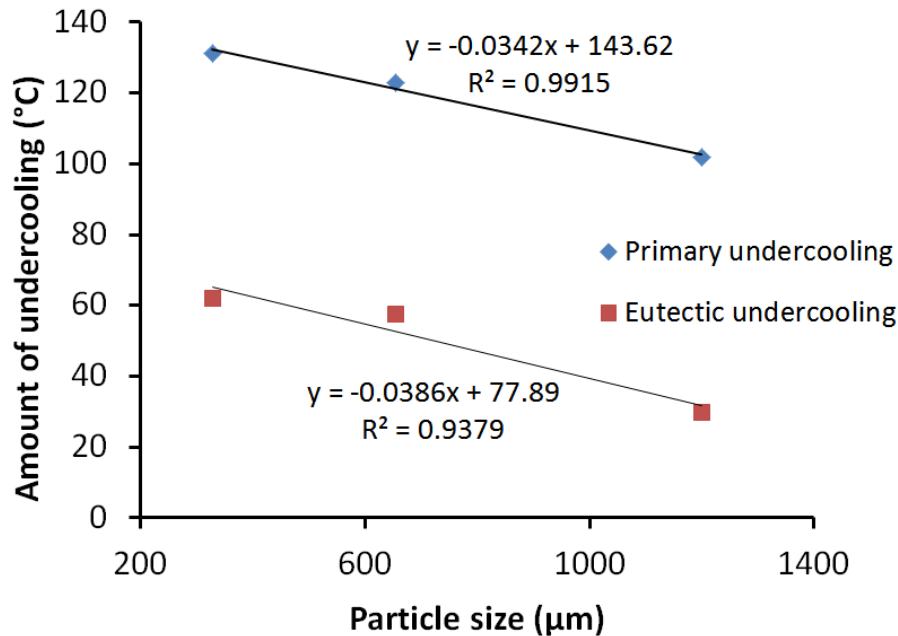


Figure 5.17. Primary and eutectic undercooling values as a function of particle size of droplets atomized in the nitrogen atmosphere.

The primary undercooling values will be used in the droplet thermal model as part of the analysis of online measurements of the falling droplets. Using the thermal model, the velocity measured by shadowgraph, and the primary undercooling temperatures, one can calculate thermal history of different size droplets at different falling heights (Figure 5.18) [80]. Figure 5.18 is a plot of droplet temperature versus particle size. For a given height below the nozzle plate, e.g. 4cm, the temperature of droplets of a given size is calculated and presented in Figure 5.18. Once the temperature falls below the liquidus temperature, that droplet is undercooled. When the experimentally determined primary undercooling is achieved for a given droplet size, solidification begins. Note that in this model, only the thermal component of solidification is accounted for. Nevertheless, recalescence is

observed by virtue of the droplet temperature rising after primary phase nucleation as seen in Figure 5.18.

Using the graph in Figure 5.18, one can identify the droplet sizes that are fully undercooled at the measuring heights. Namely these are for 4cm, 18cm and 28cm, 206 μm , 486 μm and 604 μm , respectively. These droplets will be the limit of the region where further analysis will be developed in the next section.

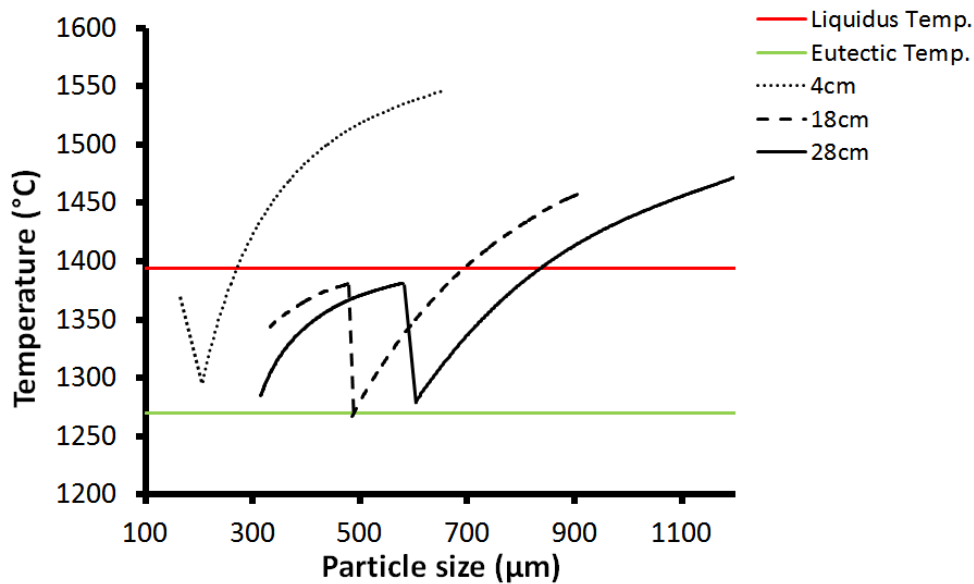


Figure 5.18. Temperature of falling D2 steel droplets in heights calculated by the heat loss model.

At 4cm, 18cm and 28cm below the nozzle plate, droplets of D2 steel finer than 270 μm , 690 μm and 850 μm are semi-solid, respectively. Larger fraction of droplet size at 18cm and 28cm are in the semi-solid temperature range compared to the 4cm droplets. Droplets at 28cm have lower temperatures compared to that at 18cm which shows fraction solidified of

D2 tool steel droplets at 4cm, 18cm and 28cm falling distances from the nozzle plate.

5.2.5. Radiant energy analysis of droplets at difference falling distances

Different factors such as temperature, size and wavelength affect the emissivity of a material [123]. In this section, the variation of emissivity for different droplet sizes will be examined.

Eq. 5.2 can be written as follows:

$$\frac{Q(\lambda_i)}{d^2} = K_i C_1 \alpha(\lambda_i) \lambda_i^{-5} \quad \text{Eq. 5.8}$$

where

$$K_i = \frac{1}{e^{C_2/\lambda_i T} - 1} \quad \text{Eq. 5.9}$$

Since in Eq. 5.8 and Eq. 5.9, C_1 , C_2 and λ_i are constants, one can plot $Q(\lambda_i)/d^2$ versus K_i at different heights. The slope of the graph at different heights for a constant droplet size is related to $\alpha(\lambda_i)$. Figure 5.19 shows $Q(\lambda_i)/d^2$ versus K_i values for the D2 steel liquid droplets at different heights during free fall. It also shows the K_i value related to the melting temperature of D2 steel (dashed vertical line). All the droplets left of the line are experiencing primary phase undercooling. Therefore, they are all in the liquid state. Note that for each of the curves in Figure 5.19, each data point represents a particle of a different size. If one joins the points representing the same size particles but at different distances below the

orifice, then one can evaluate whether $\alpha(\lambda_1)$ is constant or variable. In Figure 5.19, the points for three droplets are joined, 614 μm , 700 μm and 800 μm . The solid lines connect $Q(\lambda_1)/d^2$ values at different heights but for the same droplet size. Again, according to Eq. 5.8, $Q(\lambda_i)/d^2$ versus K_i slope (for the specific particle size) should be a linear line passing zero points of the coordinate system. This behaviour is visible between 18cm and 28cm data points. But, when it goes to 4cm data, it does not follow the trend. This needs further analysis, but it can be related to the larger variation of emissivity from 4cm to 18cm compared to that from 18cm to 28cm for the same particle size. Alternately, this may be due to the DPV-2000 sensor being affected by the radiation from the bottom of the melt crucible due to its close proximity to it at 4cm. Therefore, only the results at 18 and 28 cm will be further discussed. Also, $Q(\lambda_i)/d^2$ versus K_i slope (for the specific particle size) is changing with changing the particle size. This shows that the emissivity is also changing with particle size. An advantage of plotting $Q(\lambda_i)/d^2$ versus K_i is that direct effect of emissivity can be reduced in the calculation to only the slope of the plot and thus will not affect the subsequent analysis of droplet temperature. $Q(\lambda_i)/d^2$ versus K_i plot for wavelength λ_2 for D2 droplets is shown in Figure A.3 in Appendix A.

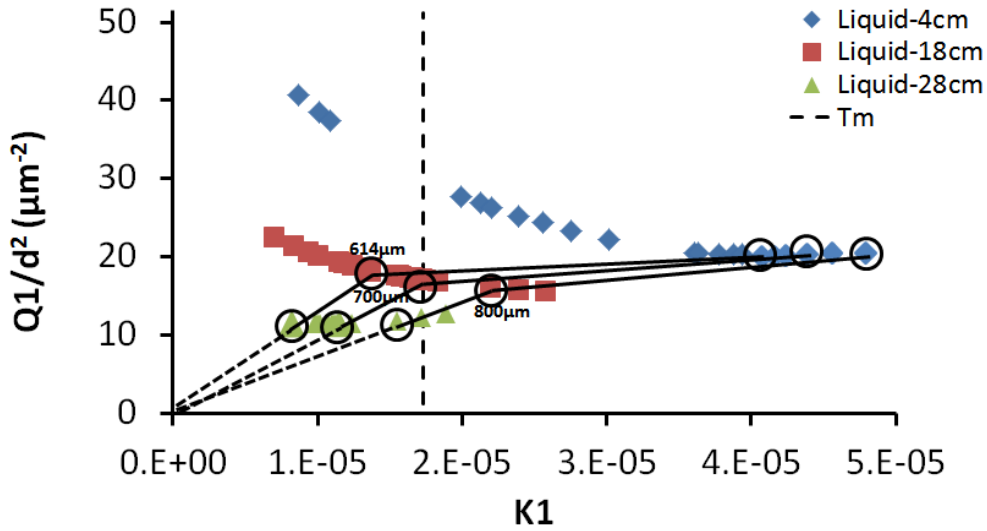


Figure 5.19. $Q(\lambda_1)/d^2$ versus K_1 graph at different heights for the D2 steel liquid droplets.

Similar to D2 tool steel, Figure 5.20 shows $Q(\lambda_1)/d^2$ versus K_1 values for copper liquid droplets at different heights during free fall.

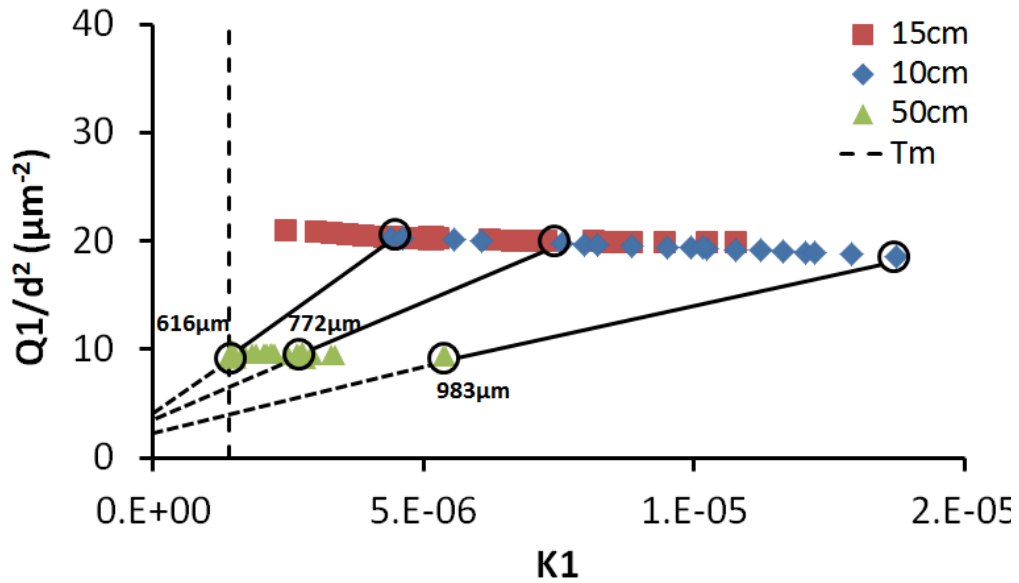


Figure 5.20. $Q(\lambda_1)/d^2$ versus K_1 graph at different heights for copper liquid droplets.

Considering the same approach discussed for D2 tool steel droplets in Figure 5.19, in copper droplets shown in Figure 5.20, the solid lines connect $Q(\lambda_1)/d^2$ values at different heights but for the same droplet sizes (616 μm , 772 μm and 983 μm). Again, according to Eq. 5.8, $Q(\lambda_1)/d^2$ slope (for the specific particle size) should be a linear line passing zero points of the coordinate system. It can be seen from Figure 5.20 that the lines are passing a point close to zero. As demonstrated in Figure 5.12, $Q(\lambda_1)$ values in 10cm and 15cm distances are so close and therefore in Figure 5.20, $Q(\lambda_1)/d^2$ values for these two distances almost cover the same K_1 range. Joining the points from these two distances representing the same size particles to 50cm (i.e. between 10cm and 50cm or 15cm and 50cm), represents a linear line passing a point close to the zero point of the coordinate system. $Q(\lambda_i)/d^2$ versus K_i plot for wavelength λ_2 for copper droplets is shown in Figure A.4 in Appendix A. Based on these results using copper and D2 at two different wavelengths, it is clear that the emissivity of droplets is a function of material, size and temperature. As an example, slope of the lines in D2 (Figure 5.19) for 614 μm , 700 μm and 800 μm droplets is $1.3 \times 10^6 \mu\text{m}^{-2}$, $1.2 \times 10^6 \mu\text{m}^{-2}$ and $6.8 \times 10^5 \mu\text{m}^{-2}$, respectively.

5.2.5.1. Estimation of droplet size and temperature at which solidification starts

After solidification starts, there is the generation of latent heat of solidification which increases the temperature of the droplets (as shows in Figure 5.18). Therefore, $Q(\lambda_1)/d^2$ versus K_1 plot would show a

discontinuous change in K_1 values. Figure 5.21 shows $Q(\lambda_1)/d^2$ versus K_1 plot for semi-solid droplets at different heights. Note that the $Q(\lambda_1)$ values used are the experimental ones that are averaged for each particle size range which lie inside the measurement accuracy of DPV-2000. The fraction solidified during solidification of droplets at different heights is also shown in this figure. It can be seen that fraction solidified is increasing toward the smaller K_1 values (lower temperatures).

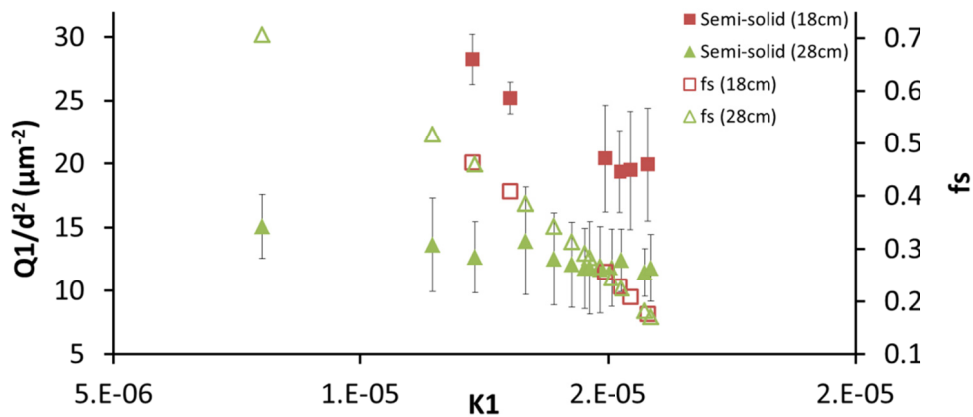


Figure 5.21. $Q(\lambda_1)/d^2$ and fraction solidified versus K_1 graphs at different heights for the semi-solid droplets.

One can superimpose the results shown in Figure 5.19 with those of Figure 5.21 in order to follow the behaviour of droplets before and after the start of the solidification (Figure 5.22). The error bars have been eliminated from the plot in Figure 5.22 for ease of presentation and for ease of identifying the average trend in the results. The error bars will be further discussed below. Figure 5.22 also shows the linear extension of the semi-solid curve and its intersection with the liquid trend data. The intersection

points at 18cm and 28cm heights correspond to 1386°C and 1376°C temperature, respectively. These intersection points seem to relate to the droplet size at which the solidification has just started (i.e. the end of recalescence). This finite solid fraction and temperature rise can be attributed to be close to when recalescence ends. The intersection temperature therefore can be equal to the maximum temperature achieved by the droplet following recalescence.

Droplet size and temperature at which solidification has just started can be used in the heat flow model (at 18cm and 28cm heights) to confirm these values. The thermal model is run for 485µm and 605µm droplets with their respective initial velocities. The droplet height when solidification begins is determined by the model. Note that the calculation accounts for the experimentally estimated primary phase undercooling. The model outputs show that at 18.5cm height, solidification is starting for 485µm droplets. Also, for 605 µm droplet, at 29.5cm, solidification starts according to the model. This information shows that the results from DPV-2000 are within 0.5cm (or within 2%) and 1.5cm (or within 5%) of the model results for 485µm droplet (at 18cm) and 605µm (at 28cm), respectively.

5.2.5.2. Discussion about DPV-2000 precision

DPV-2000 collects data from falling droplets depending on the several variables such as temperature, size, velocity and trajectory of the droplets. If any of these parameters do not meet DPV-2000 requirements (i.e. very slow droplets, not-vertically falling droplets, low temperature, etc.), DPV-2000

does not collect any information from the droplets or measures it with low precision. For example, only droplets with temperature between 1000°C to 4000°C can be detected by DPV-2000. Temperatures close to the detection limits would be measured by DPV-2000 but with low precision [94]. These cause some errors attributed to DPV-2000 calculations (error bars in Figure 5.21 for semi-solid droplets). These errors can be attributed in part to instrument and measurement errors.

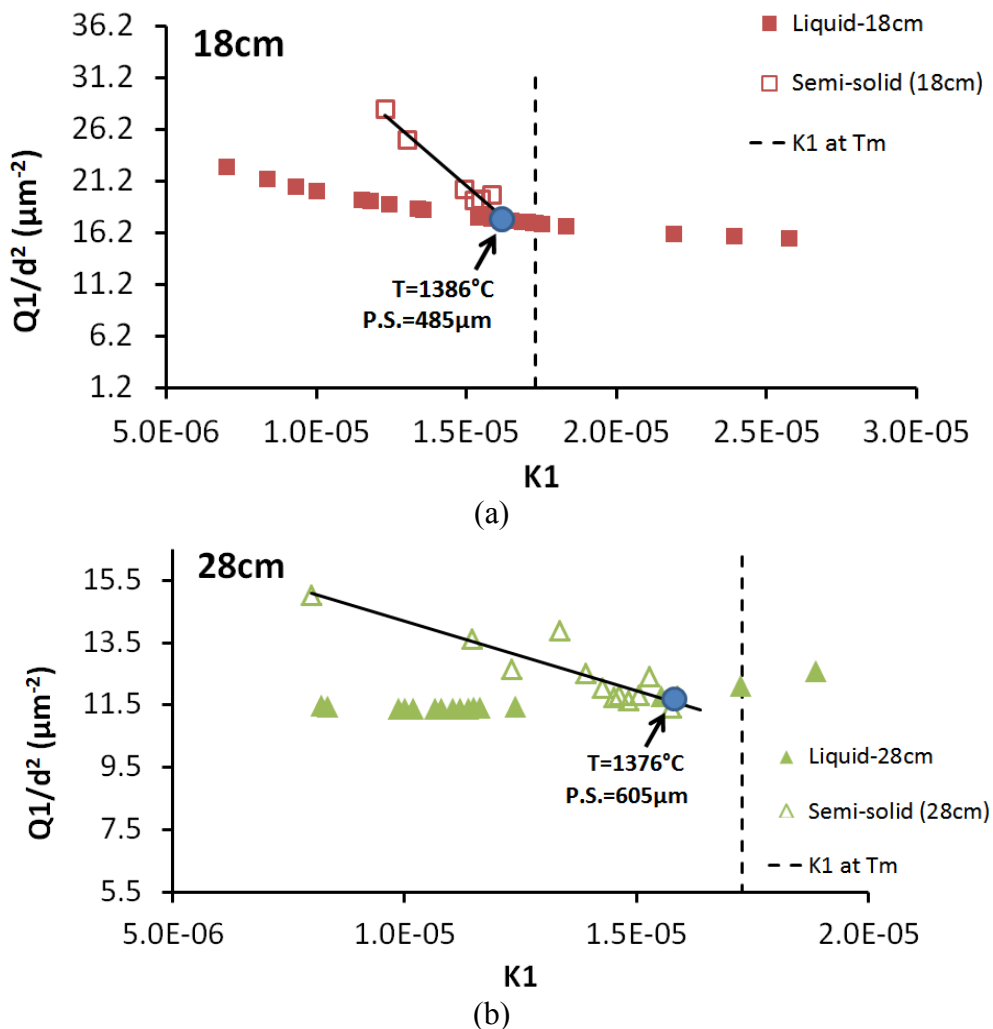


Figure 5.22. $Q(\lambda_1)/d^2$ versus K_1 graphs at different heights for the both liquid and semi-solid droplets at (a) 18cm and (b) 28cm heights.

On the other hand, nucleation is also a random phenomenon. Nucleation occurs spontaneously and randomly, and as has been shown earlier, primary phase nucleation requires undercooling of the liquid. A droplet is solidifying when nucleation requirements (i.e. chemical potential balance in the system) which are called solidification requirements.

In order to collect the solidification information using DPV-2000, both instrument and measurement errors, and solidification requirements are taking place simultaneously. Therefore, collecting information from a droplet (with the qualified properties for DPV-2000) at the precise time or position when it starts to solidify has a very low probability. Also, the time duration of recalescence from its start to its completion is much smaller than the measurement capability of DPV-2000. For example for 450 μ m droplet, the duration of recalescence is about 10^{-5} s. Also, at 28cm height, the time of flight of the same size droplet through the two sensors in DPV-2000 is about 3×10^{-6} s. Therefore, DPV-2000 cannot detect droplet's recalescence during its free fall in front of DPV-2000. This further underscores that the temperatures shown in Figure 5.22 represent the droplet temperature following recalescence for the respective droplet sizes.

5.3. Summary

In this chapter, efforts were done in order to investigate possibilities to investigate temperature behaviour of falling droplets. This was done with using DPV-2000 and shadowgraph devices measuring radiant energy, velocity and size of droplets at different distances of falling. With a help of

a thermal prediction model, a methodology was developed to correlate the radiant energy of droplets to the droplet size and temperature at which the recalescence has ended. Reasonable values were obtained comparing to the results from the heat loss model. It was also shown that droplet effective emissivities vary with material, size and temperature. In the next chapter, heat treatment of rapidly solidified D2 tool steel powders will be discussed and the effect of supersaturation on the final microstructure and phases will be investigated.

Chapter 6

6. Effect of heat treatment on microstructure and mechanical properties of rapidly solidified D2 tool steel

6.1. Introduction

A well-known high chromium and high carbon tool steel, D2 tool steel can be found in many industrial applications. Good wear and abrasion properties have been reported in these steels which are due to the formation of a high volume fraction of carbides in these steels [7]. But, microsegregation in these alloys should be reduced in order to obtain good mechanical properties.

Although the D2 tool steel has lots of applications in industry, few studies of microstructure characterization during RS processing have been done for this alloy. One set of studies reported results for RS material using splat quenching and melt spinning [34,39]. Some investigation on a cold worked tool steel produced via powder metallurgy process were reported by Blaha et al. [8], where effect of different alloying elements on final mechanical properties of cold worked tool steel was investigated. In this chapter, the effect of rapid solidification via IA and subsequent heat treatment on the microstructure and phase formation of D2 tool steel is analyzed. It was shown in Chapter 4 that droplets solidified at faster cooling rates had larger primary and eutectic undercoolings and a reduction in the fraction eutectic. Consequently, the retained austenite would be supersaturated in carbide-forming elements. In this chapter, the effects of

undercooling, cooling rate and primary phase supersaturation on the heat treated rapidly solidified in D2 tool steel are explored. Also, in order to find out how stable retained austenite is, and to trigger the martensitic transformation within the retained austenite phase, sub-zero treatment was done on the rapidly solidified particles. In addition, in order to qualitatively compare the microstructure form in low cooling rates (near equilibrium conditions) with the rapidly solidified ones, D2 tool steel samples were solidified at different low temperatures.

6.2. Experimental

6.2.1. Sub-zero treatment

As explained in Chapter 4, supersaturated retained austenite forms after rapid solidification of D2 tool steel with IA. In order to find out how stable retained austenite is, samples were quenched in liquid nitrogen. Large (1200 μm) particles atomized in nitrogen and fine (325 μm) particles atomized in helium were chosen in order to be quenched. This selection was made in order to have both the lowest and highest solidification rates. Microhardness of the powders was measured before and after quenching, using 100gf load.

6.2.2. Finding the upper limits of the temperature for annealing

Upper limit temperature for annealing (temperature at which austenite transformation starts, lower critical temperature), was found using a DSC device. Powders of 600-710 μm atomized in nitrogen were heated with a

10K/min heating rate up to 1100°C. The resulting DSC scan is shown in Figure 6.1 in section 6.3.1.

6.2.3. Annealing of D2 tool steel

Annealing of atomized powders was done using DSC which was explained in details in section 3.1.2. Results are presented in section 6.3.4.

6.2.4. Solidification at low cooling rates

Comparison has been done between the microstructure of IA samples and those solidified in near equilibrium conditions. To do so, about 50mg of IA particles of D2 tool steel with a diameter of 650 μ m were completely melted by heating to 1600°C. A Setaram Labsys Evo DSC was used for this purpose. In order to calibrate the temperature measurement of the DSC, samples of zinc, tin, Aluminum, silver, gold and nickel standard samples was used for the entire detectable temperature range. After melting the sample, solidification started at cooling rate of 0.166°C/sec. To measure the dendrite arm spacing after slow cooling of the sample, image analysis was conducted on the SEM micrographs of the solidified samples. Results are presented in Section 6.3.2. No XRD analysis was done on the slowly solidified samples. The reason is basically that only small amount of sample can be analyzed using DSC device and this quantity is not enough for XRD analysis.

6.3. Results and discussion

6.3.1. Finding the upper limits of the temperature for annealing

The DSC output was one endothermic and one exothermic peak (Figure 6.1). According to Bhargava et al. [39], the decomposition of metastable retained austenite resulted in formation of the exothermic peak, while onset of the endothermic peak indicates the temperature at which ferrite transforms to austenite which is around 840°C for D2 tool steel.

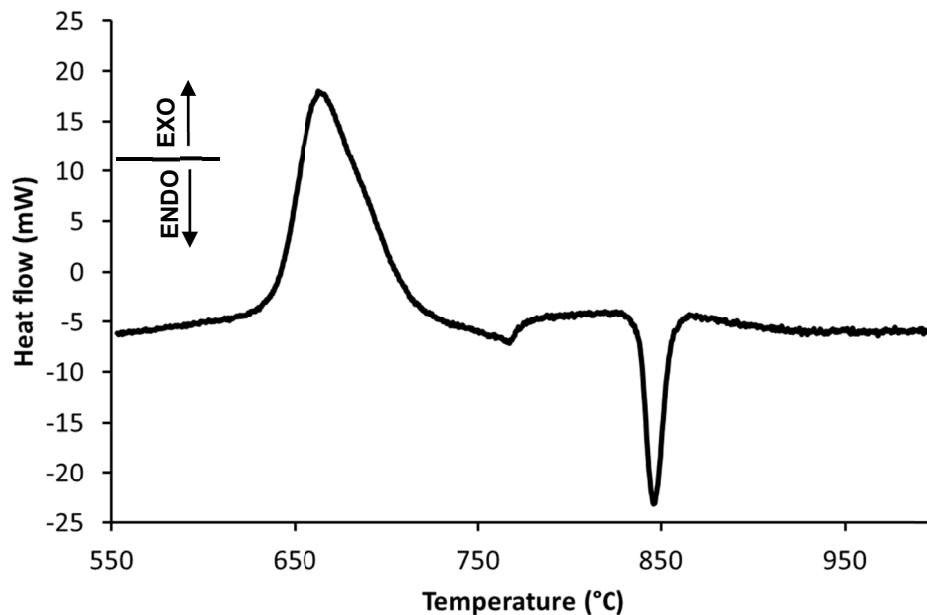


Figure 6.1. DSC graph of 600-710 μ m particles atomized in nitrogen (heating reate of 10K/min).

6.3.4

All annealing treatments have been conducted at temperatures below the austenite transformation temperature. The goal is to see the effect of the temperature on the precipitation of the supersaturated alloying element inside the non-equilibrium austenite phase in the form of carbides. That is

why the annealing temperature should not exceed the austenite transformation temperature.

6.3.2. Solidification at slow cooling rates

Figure 6.2 shows the microstructure of the D2 tool steel solidified with the cooling rate of $0.166^{\circ}\text{C}/\text{sec}$.

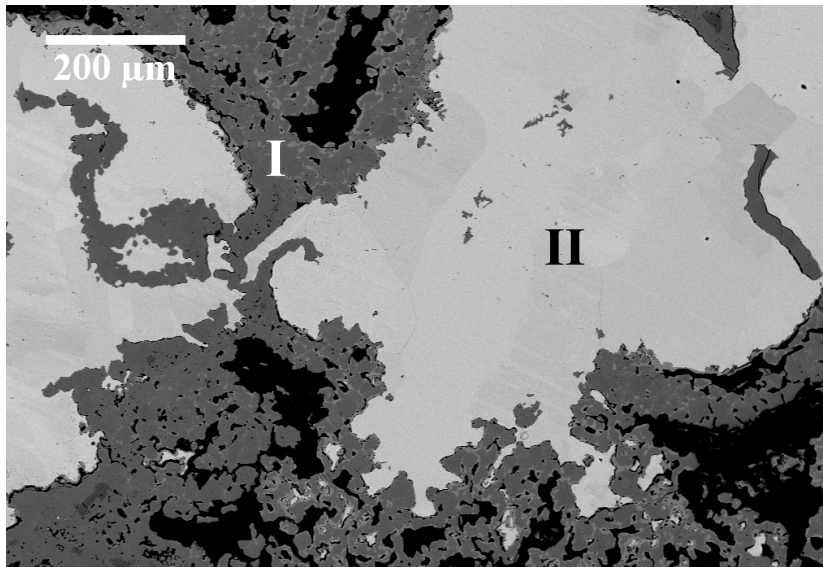


Figure 6.2. BSE-SEM micrograph of D2 tool steel under cooling rate of $0.166^{\circ}\text{C}/\text{sec}$. Black regions are the porosity in the mounting material.

Using energy dispersive X-ray (EDX) spectroscopy and the D2 tool steel phase diagram, the light phase is ferrite and the dark region is chromium carbide phase (with some vanadium content). EDX analysis of dark regions (region I in Figure 6.2) shows high amounts of both chromium and iron in region I which can be attributed to a carbide phase. The lighter phase (region II in Figure 6.2) shows high amount of iron and slight quantity of chromium which can be attributed to the ferrite phase. Slowly solidified particles also have magnetic properties which can confirm formation of ferrite instead of retained austenite (As-atomized droplets do

not have magnetic properties since as shown in Chapter 4, they have fully retained austenite in their microstructure).

It can be seen in Figure 6.2 that the entire carbide region is rejected to the outer part of the samples and some coarse grain of ferrite have been formed. It can be seen that by slow cooling the D2 tool steel melt, segregation of primary phase and carbides happens in the microstructure. This is a good example of why D2 steel parts are not produced anymore using conventional casting methods with low cooling rates.

6.3.2.1. Validation of dendrite arm spacing model

As previously mentioned, known cooling rate of $0.166^{\circ}\text{C}/\text{sec}$ was applied in the DSC. Therefore, using this known cooling rate, it is possible to calculate the values for B and n introduced in Eq. 2.5. This equation can be used in order to relate the cooling rate to the SDAS. This equation was used in Chapter 4 in order to develop an equation to calculate the solidification range and primary phase undercooling of droplets. Boccalini et al. [18] used $B=42.1\mu\text{m} (\text{C}/\text{sec})^n$ and $n=0.333$ values for high speed steels. Considering these values as well as the measured SDAS achieved from the DSC sample, it is possible to compare the imposed cooling rate with the actual value. Dendrite arm spacing was measured using ImageJ software using a few dendrites that can be seen in the D2 tool steel solidified at $0.166^{\circ}\text{C}/\text{sec}$ (Figure 6.3). Some measured dendrites are shown by white arrows in Figure 6.3. The spacing was about $85\mu\text{m}$. Then, using the dendrite arm spacing equation in Chapter 4, the cooling rate of $0.11^{\circ}\text{C}/\text{sec}$ was

calculated. It can be seen that the calculated cooling rate is close to the value of $0.166^{\circ}\text{C}/\text{sec}$ imposed by the DSC. This can prove the validity of the used values for B and n.

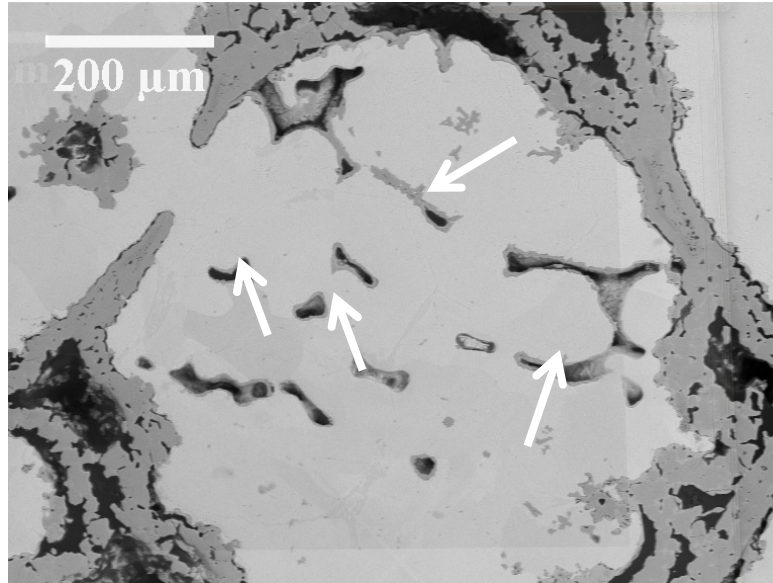


Figure 6.3. BSE-SEM micrograph of D2 tool steel under cooling rate of $0.166^{\circ}\text{C}/\text{sec}$. White arrows show some measured dendrites.

6.3.3. Sub-zero treatment of rapidly solidified particles

Figure 6.4 shows the microvickers' hardness of as-atomized and quenched particles in liquid nitrogen. First, it can be seen that the hardness of particles with higher cooling rates ($300\text{-}355\mu\text{m}$ -helium) is higher than that in particles with slower cooling rates ($1000\text{-}1400\mu\text{m}$ -nitrogen). This is because the particles with a higher cooling rate have a finer microstructure. Hardness of quenched particles in the liquid nitrogen shows that there is almost no change in the hardness of the particles after quenching.

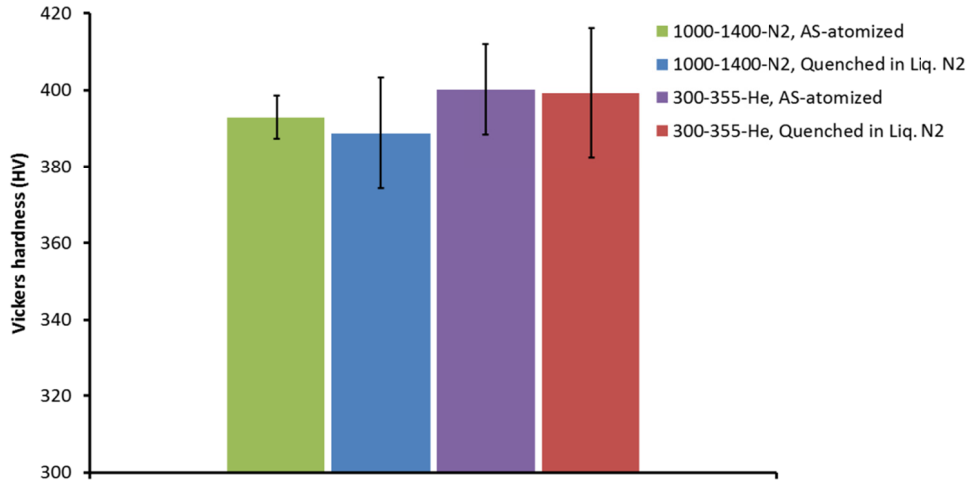


Figure 6.4. Microvickers' hardness of different sized particles as-atomized and quenched in the liquid nitrogen.

The results show no trace of martensitic transformation in the samples. It is clear that the martensitic transformation point for the refined retained austenite phase is, in fact, lower than the boiling point of nitrogen in all IA-produced powders. The main parameter affecting the M_s temperature is the composition of the steel [125]. There are different equations for M_s that has been derived empirically or by modelling. These equations are mostly for the maximum carbon and chromium content of 2.08wt.% and 13.4wt.%, respectively, which cover the D2 tool steel chemical compositions. As example, Eq. 6.1 and Eq. 6.2 shows two different empirically derived equations for martensite start temperature [125–127]:

$$M_s(^{\circ}\text{C}) = 500 - 300C - 33Mn - 22Cr - 22Si - 11Mo \quad \text{Eq. 6.1}$$

$$M_s(^{\circ}\text{C}) = 539 - 423C - 30.4Mn - 12.1Cr - 7.5Mo \quad \text{Eq. 6.2}$$

For the chemical composition of D2 tool steel, the M_s temperature for D2 tool steel using Eq. 6.1 and Eq. 6.2 would be -253.2°C and -279.8°C , respectively. This means that by lowering the temperature of austenite to the aforementioned temperatures, austenite transforms into martensite. Since the boiling temperature of liquid nitrogen is about -196°C , quenching the particles with austenite microstructure does not transform austenite into martensite. During rapid solidification of steels, the austenite phase is supersaturated with alloying elements and small grains are also formed (Figure 4.3). These factors decrease the M_s temperature even further [128,129].

It has been shown that transformation of austenite to martensite is a process requiring the nucleation stage [130]. In the rapidly solidified D2 droplets, the austenite phase directly grows from the melt during the rapid solidification process. The high amount of chromium and carbon supersaturated in this phase is an important factor for lowering the M_s temperature [131]. Furthermore, austenite stabilization happens which is due to formation of very fine austenite domains. The reason is, basically, high strength of the austenite phase (due to formation of fine austenite domains) which make it difficult to accommodate the martensite phase [130].

Zou et al. [130] reported that after quenching rapidly solidified laser melted D2 tool steel in the liquid nitrogen, no martensitic transformation

took place. In their work, XRD peaks of quenched rapidly solidified samples showed no trace of any martensite phase. Peaks only moved slightly towards lower angles. This indicates that during laser melting and quenching, a residual stress is introduced to the sample. So, although the high cooling rate of ($\sim 10^7$ K/s) has been reported in that work, after 25 pulses of surface laser melting of D2 steel, the martensitic transformation was totally suppressed.

6.3.4. Supersaturation during rapid solidification

As mentioned in Chapter 4, there would be different levels of supersaturation during rapid solidification of D2 tool steel droplets. This supersaturation is due to the high amount of undercooling and cooling rates of the droplet. In order to quantify the level of supersaturation, equilibrium composition of the alloy at different temperatures should be known. Then, by calculating the concentration of different elements in retained austenite phase as a result of rapid solidification, one can calculate the level of supersaturation at any specific temperature after complete solidification.

6.3.4.1. Equilibrium curve for M_7C_3 carbides

The temperature dependence of the solubility product (k_s) is expressed by an Arrhenius relationship [47]:

$$\log k_s = \frac{-Q}{2.303RT} + \frac{c}{2.303} \quad \text{Eq. 6.3}$$

where Q is the heat of dissolution, R is the gas constant and c is a constant.

The condensed form of Eq. 6.3 for M_7C_3 type of carbide is [47]:

$$\log k_{M_7C_3} = A - \frac{B}{T} \quad \text{Eq. 6.4}$$

where A and B are constants for a given system and T is the temperature (K). For M_7C_3 type of carbides, in general, $k_{M_7C_3}$ is defined as:

$$k_{M_7C_3} = X_{eM}^7 \cdot X_{eC}^3 \quad \text{Eq. 6.5}$$

where X_{eM} and X_{eC} are the equilibrium concentrations of M and C at a specific temperature in wt.% (Considering activity coefficient equal to 1 [47]).

In order to calculate A and B values in Eq. 6.4, one needs to know $k_{M_7C_3}$ values at least two different temperatures. Using Themocalc software, it is possible to find X_{eM} and X_{eC} at two different temperatures which can result in calculation of A and B values in Eq. 6.4 (Appendix B):

$$k_{M_7C_3} = 10^{(19.1 - \frac{18639}{T})} \quad \text{Eq. 6.6}$$

Using Eq. 6.6, it is possible to plot equilibrium curve of chromium and carbon elements in austenite at three different temperatures, 550°C, 650°C and 750°C (Figure 6.5). Figure 6.5 shows that by increasing the temperature from 550°C to 750°C, solubility of carbon and chromium is increasing inside the austenite matrix. If $[Cr]^7[C]^3$ is less than k_s , then the alloying elements remain in the solution. However if the composition is above the curve, since system wants to return to equilibrium, the excess amounts of alloying elements must precipitate out to return to the solubility line.

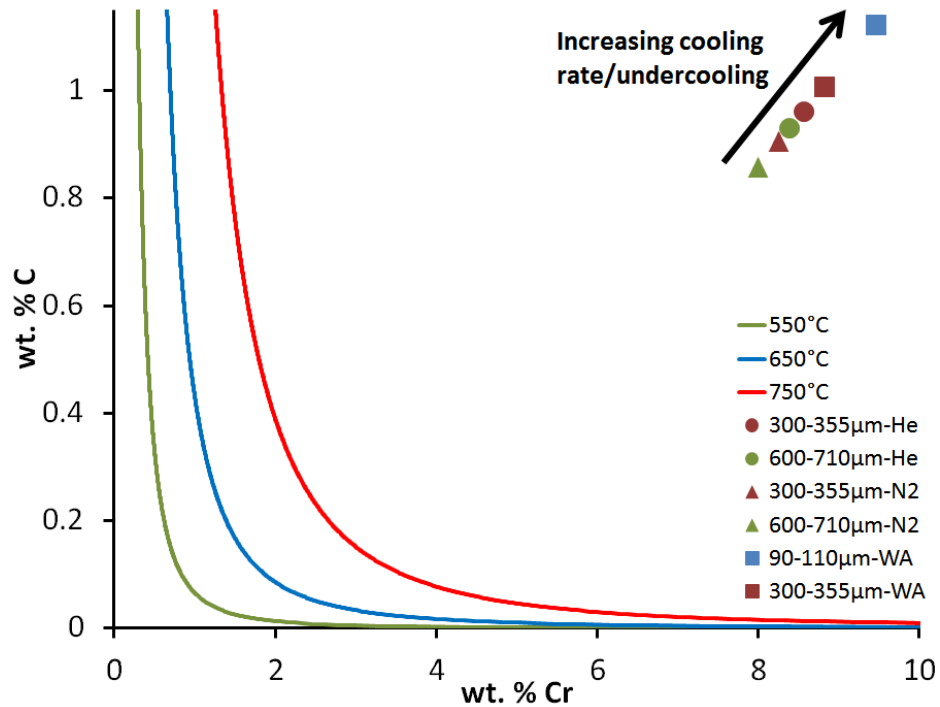


Figure 6.5. Equilibrium curve of chromium and carbon at 550°C, 650°C and 750°C in the austenite phase.

The amount of supersaturation of alloying elements at room temperature can be calculated using equilibrium concentration of alloying elements in eutectic carbide. According to D2 tool steel phase diagram (Figure 4.1), eutectic structure has about 62wt.% M_7C_3 and 38wt.% austenite. Since rapid solidification is happening during rapid cooling of the droplet, one can assume that same eutectic structure remains at room temperature, since there is not enough time for further diffusion of elements to change the constituents' percentage. Figure 4.7 shows eutectic fraction at the solidified droplets with different cooling rate. Therefore carbide fraction at each droplet can be calculated. Using Thermocalc software and

considering initial composition of D2 tool steel (Table 2.2), one can calculate supersaturated composition of chromium and carbon in the solidified droplets at room temperature. Table 6.1 shows the results of a sample calculation for three different droplet sizes IA in helium. The results are shown in Figure 6.5. Since [Cr] and [C] are above the curve, the excess amount of chromium and carbon should precipitate out in the form of precipitates during annealing.

Table 6.1. Sample calculation results for the amount of supersaturated chromium at room temperature in the retained austenite for the droplets IA in helium

Particle size range (μm)	M_7C_3 carbide eutectic fraction (wt.%)	Amount of chromium in M_7C_3 (wt.%)	Amount of chromium in austenite at room temperature (wt.%)
300-355	6.76	3.23	8.57
600-710	7.13	3.41	8.39
1000-1400	8.45	4.04	7.76

6.3.4.2. Quantification of supersaturation

Figure 6.5 shows that by increasing the undercooling/cooling rate, concentration of chromium and carbon content is increasing inside the final structure.

Generally, during rapid solidification of D2 tool steel, alloying elements do not have time to diffuse out of the austenite structure and remain supersaturated in it. These elements can then precipitate out during

subsequent annealing cycles in the form of M_7C_3 carbides. Solution supersaturation for M_7C_3 carbides ($S_{M_7C_3}$) is defined as [132]:

$$S_{M_7C_3} = \ln \left[\frac{X_M^7 \cdot X_C^3}{k_{M_7C_3}} \right] \quad \text{Eq. 6.7}$$

where X_M and X_C are supersaturated concentration of alloying elements (wt.%) in the austenite.

Using the values of alloy composition solidified with different cooling rates and equilibrium composition at temperatures from 550°C to 750°C (shown in Figure 6.5), it is possible to calculate the level of supersaturation according to Eq. 6.7. Figure 6.6 shows the level of supersaturation of carbon and chromium in the solidified D2 steel droplets with different cooling rates, at three different temperatures.

Figure 6.6 shows that by increasing the cooling rate, the amount of supersaturation also increases. It can be seen that this increase is faster at lower cooling rate and reduced at higher cooling rate. It seems that the amount of supersaturation goes into a limit at each temperature. At lower cooling rates, dissolved elements in the form of supersaturation are far below the supersaturation limit and therefore supersaturation increases faster by increasing the cooling rate at lower cooling rates. Figure 6.6 also shows that the level of supersaturation is higher at lower temperatures, since the solubility limit is smaller at lower temperatures. Therefore, with the same alloy composition, at lower temperature there is higher amount of supersaturation compared to higher temperatures.

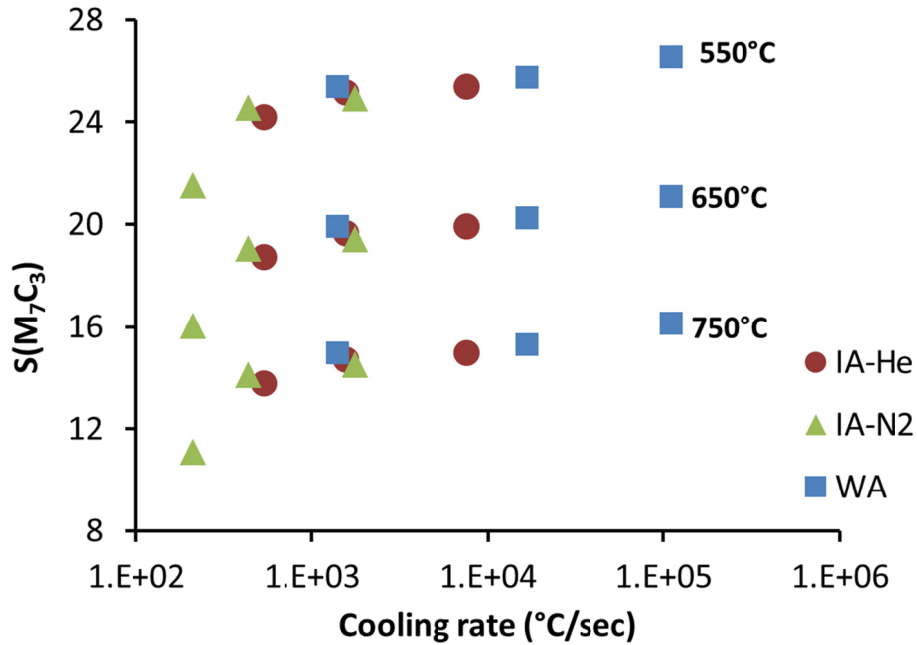


Figure 6.6. Level of supersaturation of final D2 steel structure at different temperatures as function of cooling rate.

Effect of eutectic undercooling on the amount of supersaturation is shown in Figure 6.7. Figure 6.7 shows that eutectic undercooling almost has linear effect on the amount of supersaturation. So, by increasing the eutectic undercooling, amount of supersaturation also increases linearly. Same as the effect of cooling rate, amount of supersaturation at lower temperatures is larger compared to that in higher temperatures.

The amount of supersaturation in the solution directly affects the driving force of precipitation. In general, the high concentration of supersaturated elements in the matrix leads to the larger driving force, ΔG_v , for the precipitation of carbide (i.e. M_7C_3) [133]:

$$\Delta G_V = -\frac{RT}{V_m} S_{M_7C_3} \quad \text{Eq. 6.8}$$

where V_m is the molar volume of the carbide.

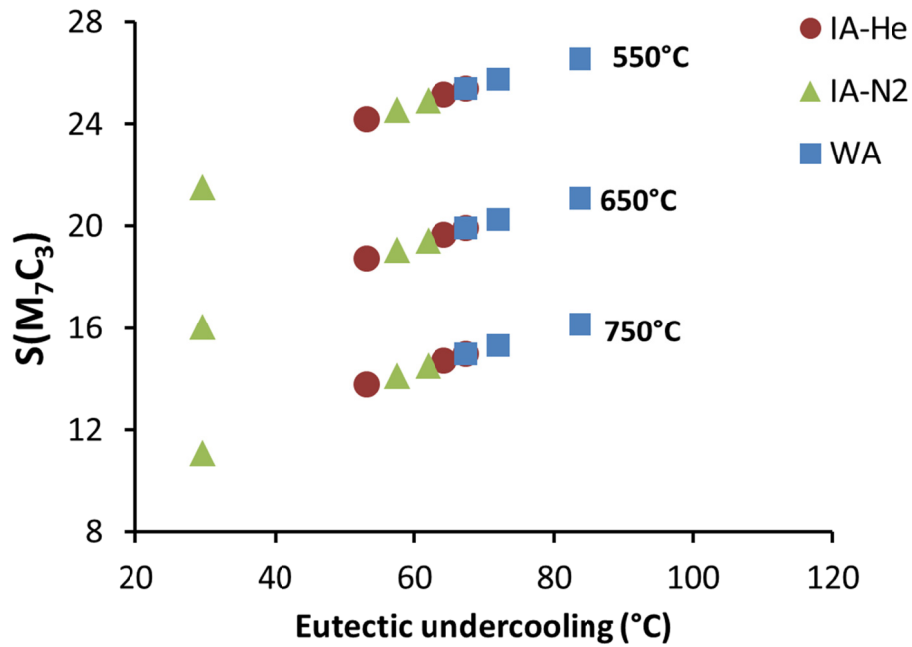


Figure 6.7. Level of supersaturation of final D2 steel structure at different temperatures as a function of eutectic undercooling.

Precipitation driving force for precipitation of M_7C_3 type of carbides from supersaturated retained austenite at 550°C and 750°C annealing temperatures as a function of droplet cooling rate and eutectic undercooling are shown in Figure 6.8 and Figure 6.9.

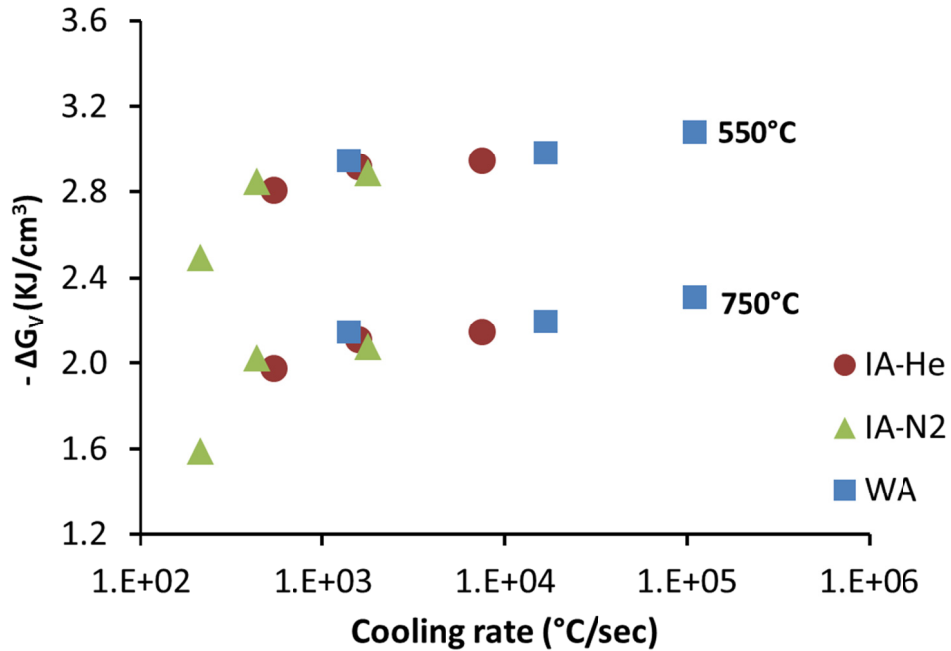


Figure 6.8. Precipitation driving force for M_7C_3 carbides in the supersaturated rapidly solidified retained austenite at different temperatures as function of cooling rate.

Figure 6.8 and Figure 6.9 show that by increasing of the droplet cooling rate (and primary phase undercooling), precipitation driving force of M_7C_3 type of carbides is increasing in a specific annealing temperature. Also, it can be seen from these figures that the precipitation driving force is larger in the lower temperatures.

After quantifying the amount of supersaturation in different undercooling and cooling rates, it would be useful to quantitatively examine the effect of this supersaturation on the microstructural features that form during annealing of rapidly solidified droplets.

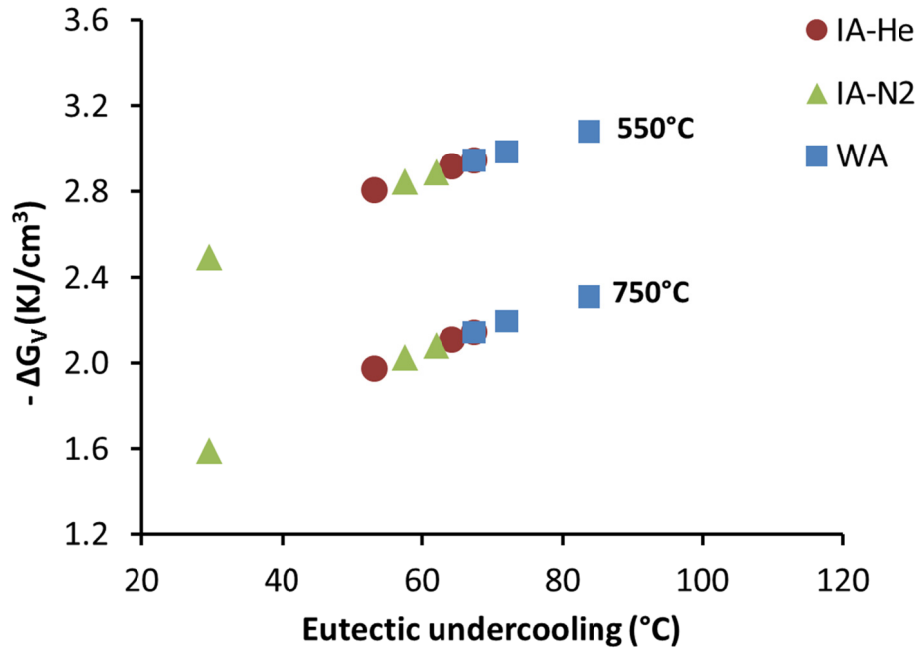


Figure 6.9. Precipitation driving force for M_7C_3 carbides in the supersaturated rapidly solidified retained austenite at different temperatures as function of eutectic undercooling.

6.3.5. Phase identification and quantification analysis of annealed particles

6.3.5.1. X-ray diffraction

Figure 6.10 shows the XRD results for as-atomized particles (300-355 μ m in helium) and particles that were heat treated at different temperatures. This figure shows XRD analysis results of 300-355 μ m IA droplets in nitrogen, in as-atomized and heat treated conditions. It can be seen that rapid solidification of D2 steel causes supersaturated metastable retained austenite to form, and completely suppresses the formation of ferrite. All extra small peaks in Figure 6.10 can be indexed to Fe_3O_4 type of oxide (as described in Chapter 4).

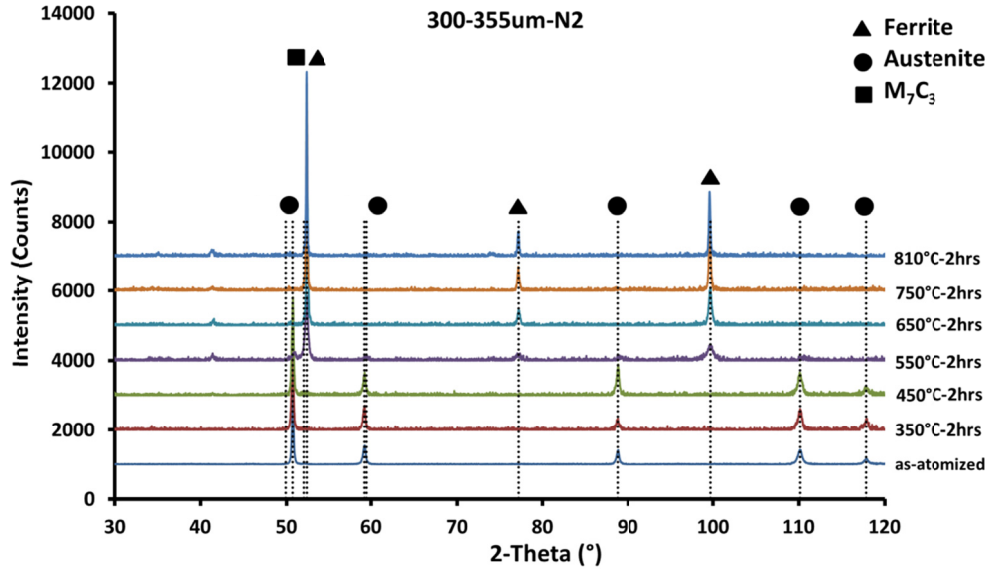


Figure 6.10. XRD patterns for 300-355 μm particles atomized in nitrogen and annealed for 2 hour at different temperatures. All extra small peaks are Fe_3O_4 type of oxide

Annealing the particles at 350°C and 450°C does not change the phases, but upon annealing at 550°C, the retained austenite has transformed to ferrite. At higher annealing temperatures (i.e. 650°C, 750°C and 810°C), only ferrite peaks are present. The austenite-to-ferrite transformation, then, has resulted in carbide precipitation. There are some small peaks which are related to Fe_3O_4 type of oxide. Carbides peaks are overlapped with ferrite and therefore it is not possible to independently identify them. The presence of carbides (M_7C_3) for these samples will be discussed later in Section 6.3.6.

Figure 6.11 shows the XRD peaks of annealed 300-355 μm particles atomized in helium as well as the as-atomized particles.

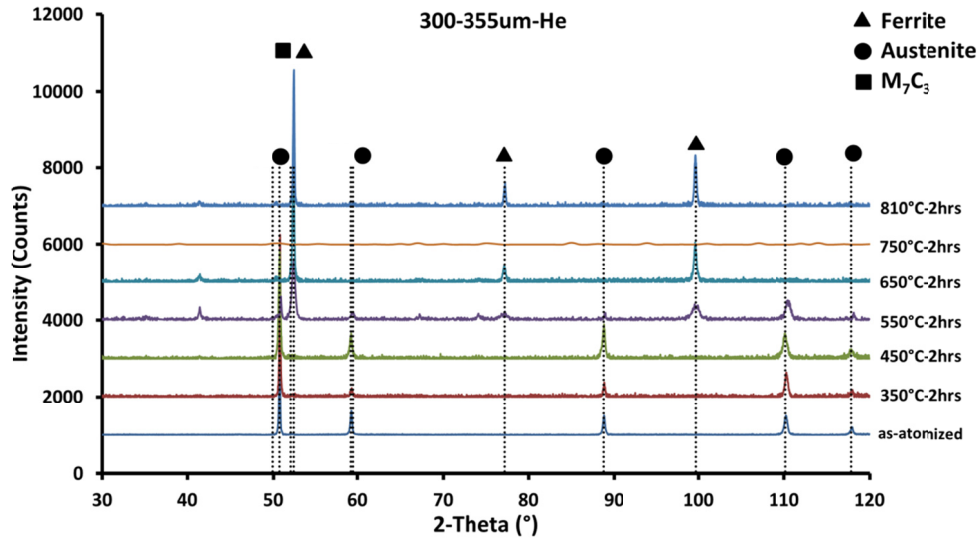


Figure 6.11. XRD patterns for 300-355 μm particles atomized in helium and annealed for 2 hours at different temperatures. All extra small peaks are Fe_3O_4 type of oxide

Figure 6.11 shows that all the formed phases at different annealing temperatures are almost same as the ones formed in 300-355 μm particles atomized in nitrogen. Figure 6.12 shows the XRD of annealed 600-710 μm particles atomized in nitrogen as well as the as-atomized particles. Same as Figure 6.10, all extra small peaks can be indexed to Fe_3O_4 type of oxide.

The phases formed in the annealed 600-710 μm particles atomized in nitrogen are the same as those formed in the smaller size particles (Figure 6.10 and Figure 6.11). Figure 6.13 shows the XRD results of 600-710 μm particles atomized in helium as well as the as-atomized ones.

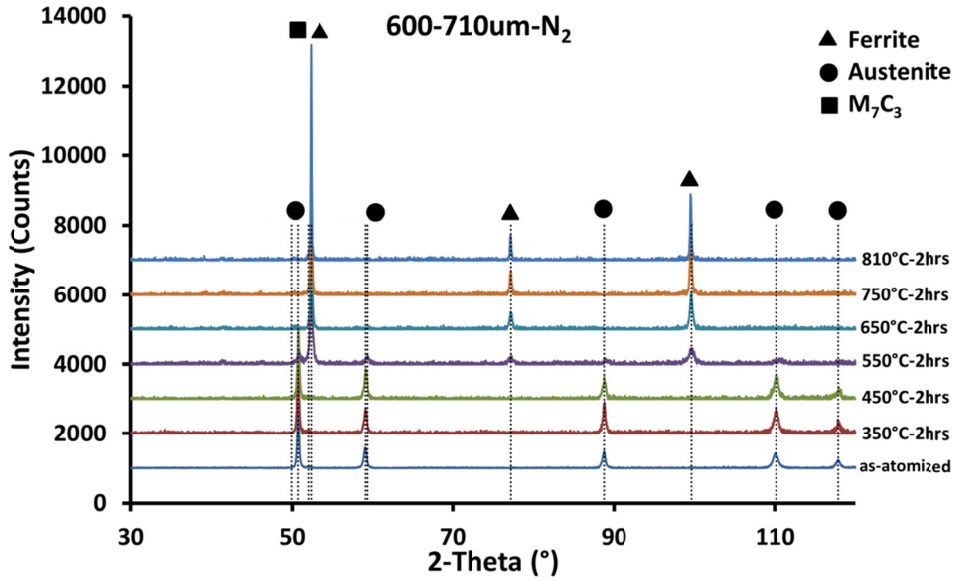


Figure 6.12. XRD patterns for 600-710 μm particles atomized in nitrogen and annealed for 2 hour at different temperatures. All extra small peaks are Fe_3O_4 type of oxide.

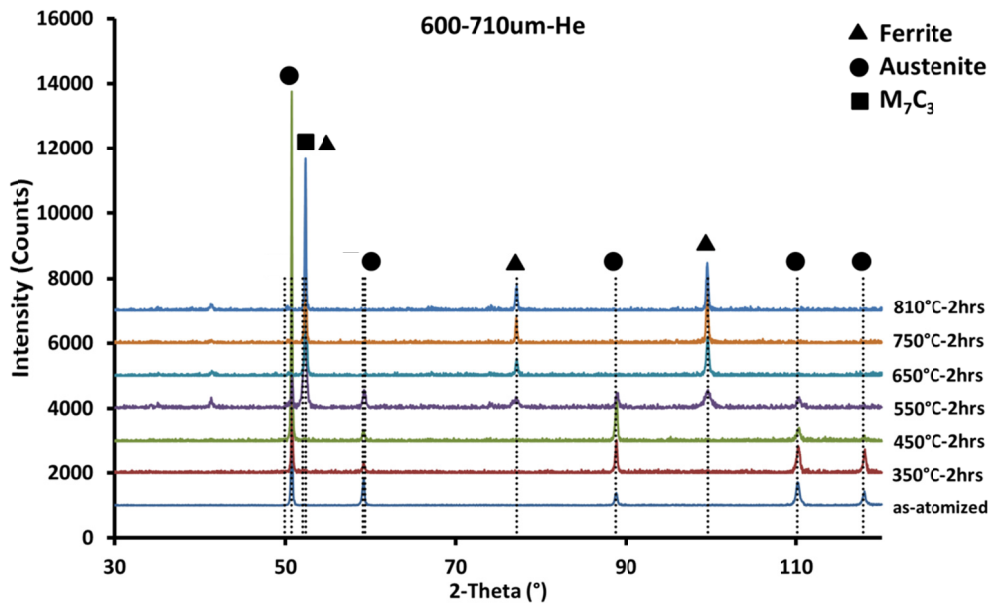


Figure 6.13. XRD patterns for 600-710 μm particles atomized in helium and annealed for 2 hour at different temperatures.

It has been reported that in the laser melted steels which have lower carbon and chromium contents than D2 tool steel, $M_{23}C_6$ carbides are also formed as well as M_7C_3 carbides [134,135]. Some other carbides, including MoC and $(Cr,V)_2C$, were also formed after 14 hours of annealing at 550°C in the steels with higher carbon and chromium contents than D2 tool steels. This resulted in secondary carbide precipitation and, therefore, secondary hardening of the alloy [136].

6.3.5.2. High energy XRD

Since XRD counts of M_7C_3 carbide are much smaller compared to those of austenite and ferrite peaks, it is difficult to characterize the carbide peaks and also not possible to conduct a Rietveld analysis. Therefore, High energy XRD (HEXRD) has been conducted on selected as-atomized and annealed particles. Figure 6.14 and Figure 6.15 show HEXRD peaks of 300-355 μ m and 600-710 μ m atomized in nitrogen particles annealed at 650°C for 2 hours, as well as as-atomized ones. It can be seen in these figures that because the HEXRD technique has higher resolution, more M_7C_3 carbides peaks are visible, but again, the peaks are small and weak compared to the austenite and ferrite peaks. The HEXRD results also confirm that ferrite and M_7C_3 carbides form during annealing of the particles at 650°C.

Similar peaks were achieved for 300-355 μ m and 600-710 μ m particles atomized in helium and annealed at 650°C during HEXRD.

Since nitrogen used as a cooling media during different IA runs, there is a possibility for nitrogen to be absorbed by liquid steel during

solidification and form some nitride phases. It should be noted that no nitride peaks were detected in HEXRD results.

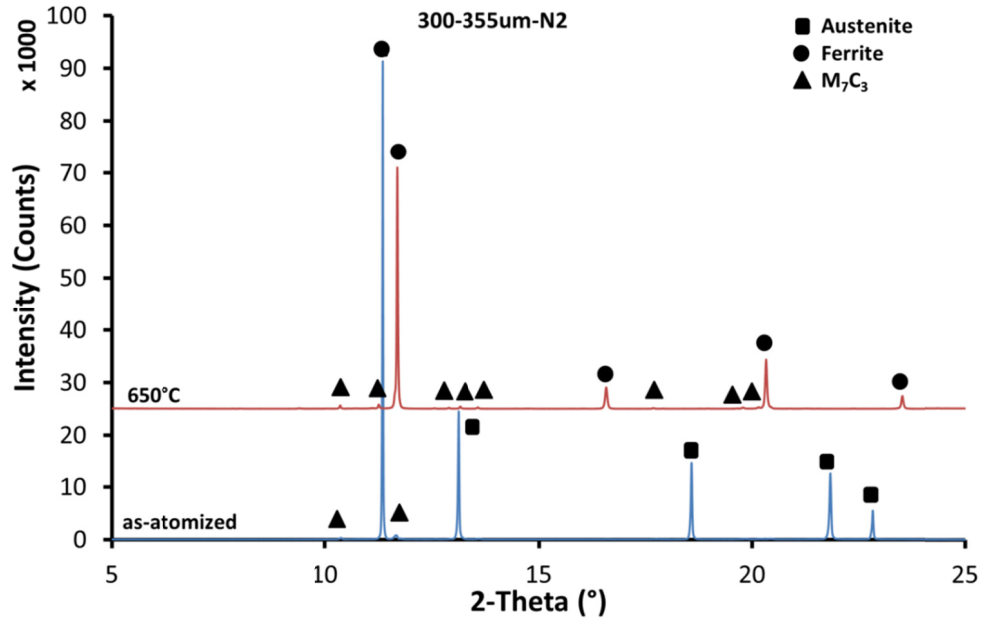


Figure 6.14. High Energy XRD patterns for 300-355µm particles atomized in nitrogen and annealed for 2 hours at 650C.

6.3.5.3. Rietveld analysis

There is a better resolution in the diffraction results from HEXRD, but, since the carbide peaks are very weak compared to austenite and ferrite peaks, it is very difficult to conduct an accurate profile refinement in order to find the phase fractions of these carbides.

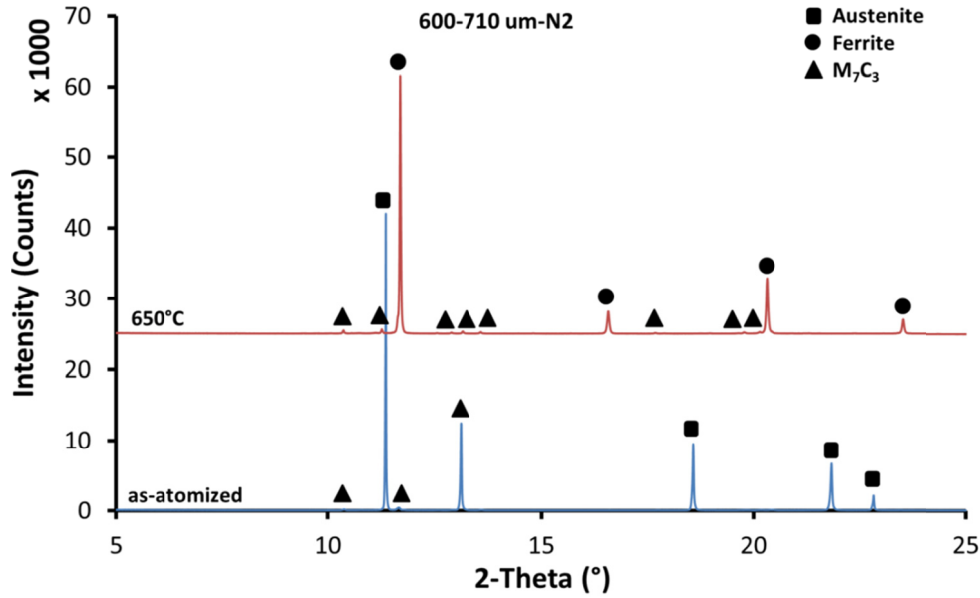
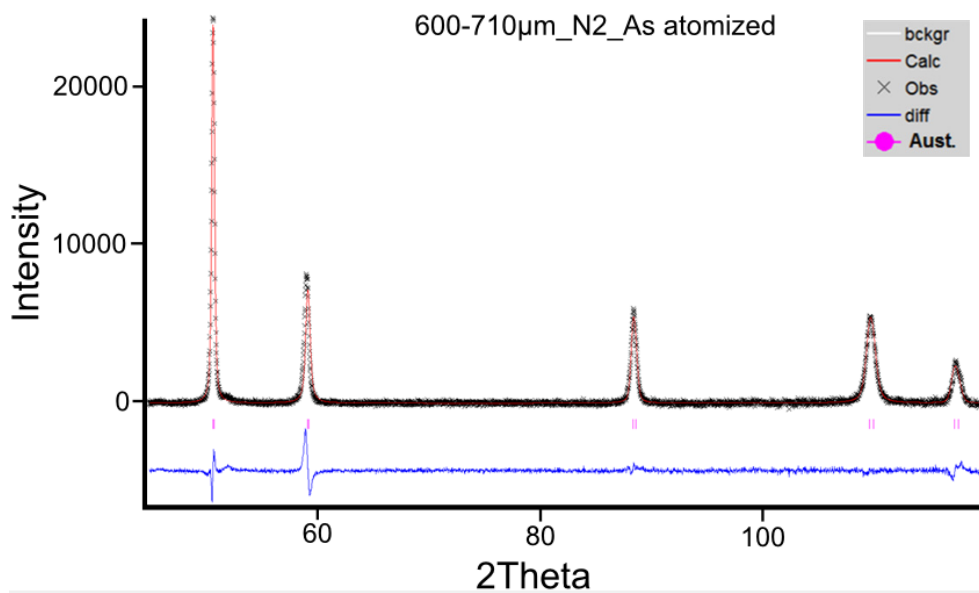


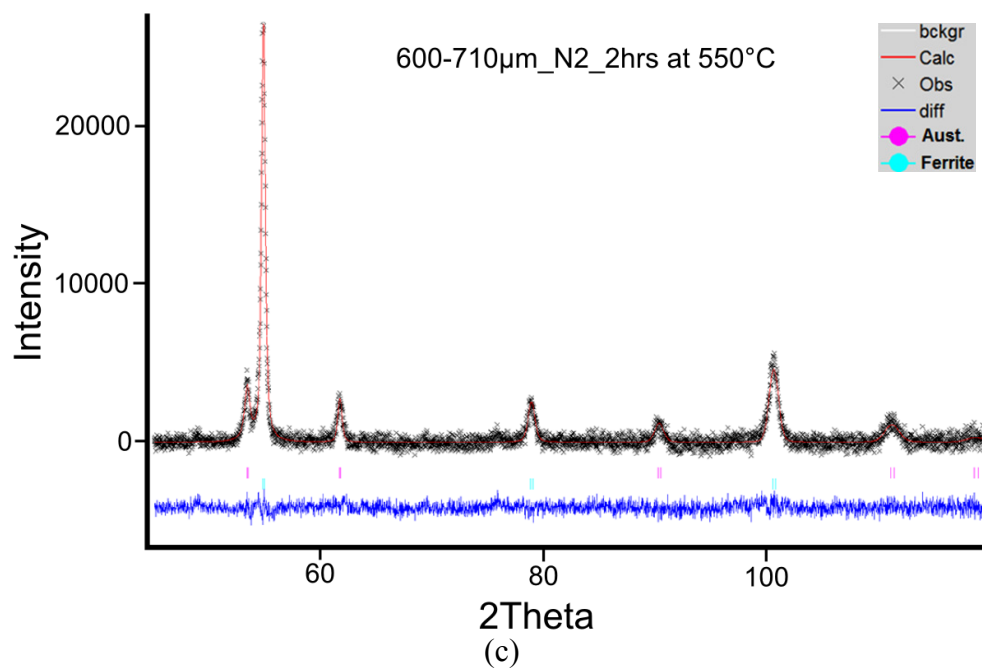
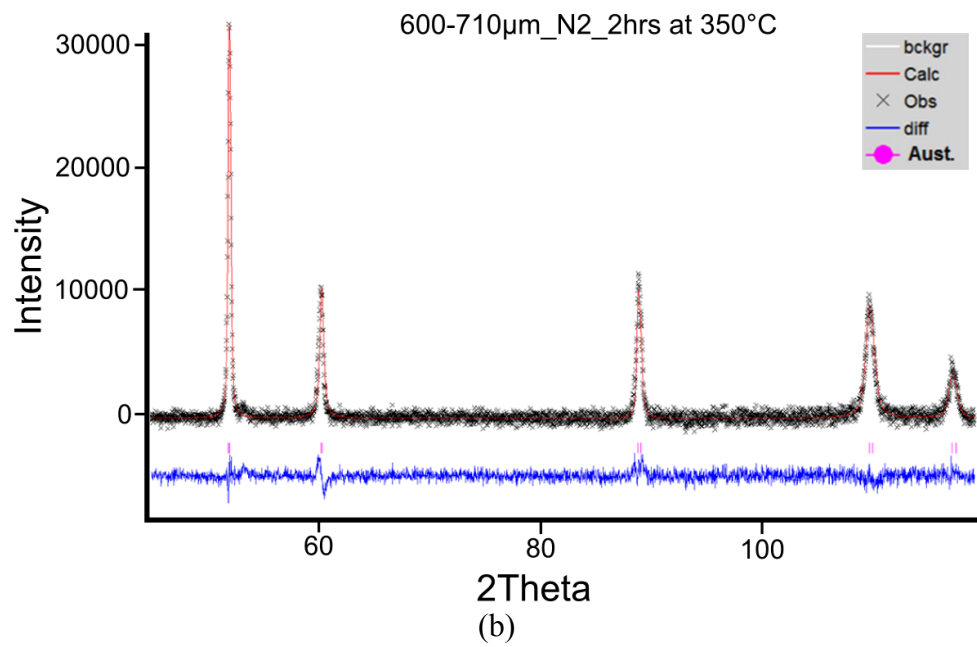
Figure 6.15. High Energy XRD patterns for 600-710 μ m particles atomized in nitrogen and annealed for 2 hours at 650°C.

Another option for conducting a Rietveld analysis of the peaks was to refine the austenite peaks at different annealing temperatures in order to solve for the value of the austenite lattice parameter at different annealing temperatures, to find out at what temperature austenite transforms to ferrite and carbide. Also, if we just ignore the presence of carbide peaks (since the peaks are so weak), it is possible to calculate the amount of ferrite and austenite at each temperature in order to estimate the percentage of phase transformation at each annealing temperature. Profile refinement was carried out using the software GSAS on XRD patterns from particles of D2 tool steels atomized in helium and nitrogen. In order to confirm values of the lattice parameter calculated from the software, HEXRD and neutron diffraction data were also used at available temperatures. Austenite and ferrite phases were identified. Refinements were conducted on as-atomized

as well as annealed particles at different temperatures. Figure 6.16 shows an example of the measured XRD pattern of IA particles with the diameter of $650\mu\text{m}$ for as-atomized and annealed temperatures, along with the calculated diffraction pattern. Images are only for four different conditions: as-atomized, annealed at 350°C , 550°C and 750°C . In this figure, the top line (red line) indicated the experimentally calculated diffraction pattern. This pattern is obtained after Rietveld analysis using GSAS software. The difference between the experimentally observed and calculated diffraction pattern is shown by the blue line (bottom line). There are some small vertical bars indicating the positions of the diffraction peaks of the austenite and ferrite phases.



(a)



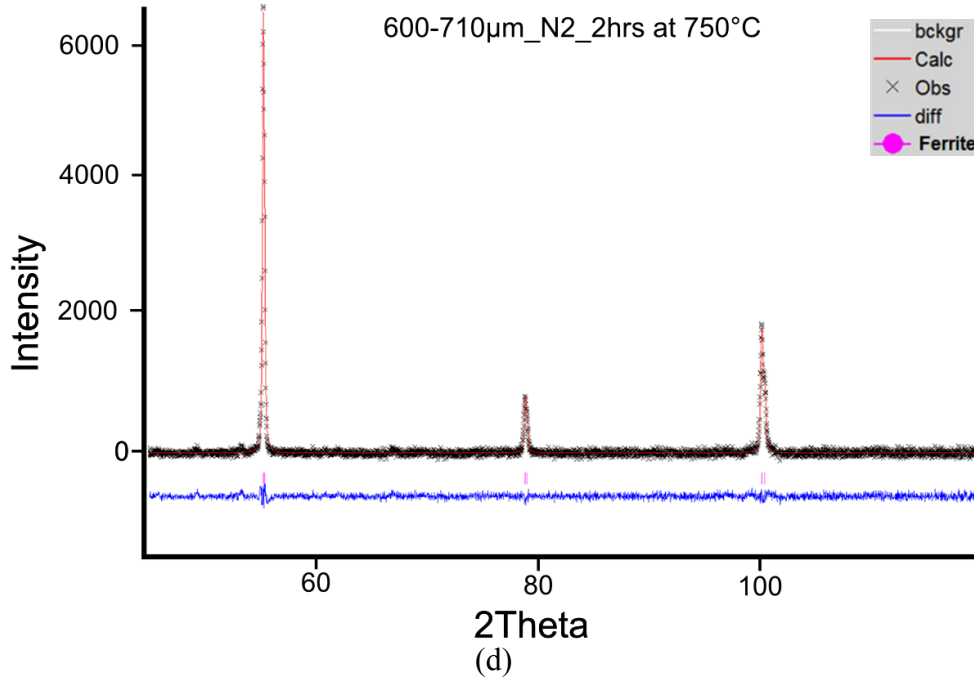


Figure 6.16. Profile refinement of D2 tool steel particles with the diameter size range of 600-710 μm atomized in nitrogen using the GSAS computer code in (a) As-atomized with $\chi^2=4.80$, (b) annealed at 350 $^{\circ}\text{C}$ with $\chi^2=1.14$, (c) annealed at 550 $^{\circ}\text{C}$ with $\chi^2=1.03$ and (d) annealed at 750 $^{\circ}\text{C}$ with $\chi^2=1.08$. Red line: the calculated diffraction pattern. Blue line: the difference between the observed and calculated diffraction pattern. Small vertical bars: the position of the austenite and ferrite the diffraction peaks.

6.3.5.4. Lattice parameter and percent transformation

Similar to Section 6.3.5.3, analyses have been conducted on neutron diffraction data of as-atomized particles in helium and nitrogen, as well as on high energy XRD data. From the Rietveld analysis results shown in Figure 6.16 (and the same results for the rest of the samples), it is possible to achieve lattice parameter of austenite during annealing. Also, by finding the fraction of austenite and ferrite at each annealing temperature, the

transformation percent can be calculated. Figure 6.17 shows the lattice parameter of the microstructure phase as a function of the annealing temperature for 600-710 μm particles atomized in nitrogen. The same graph also shows the percent transformation of austenite to ferrite.

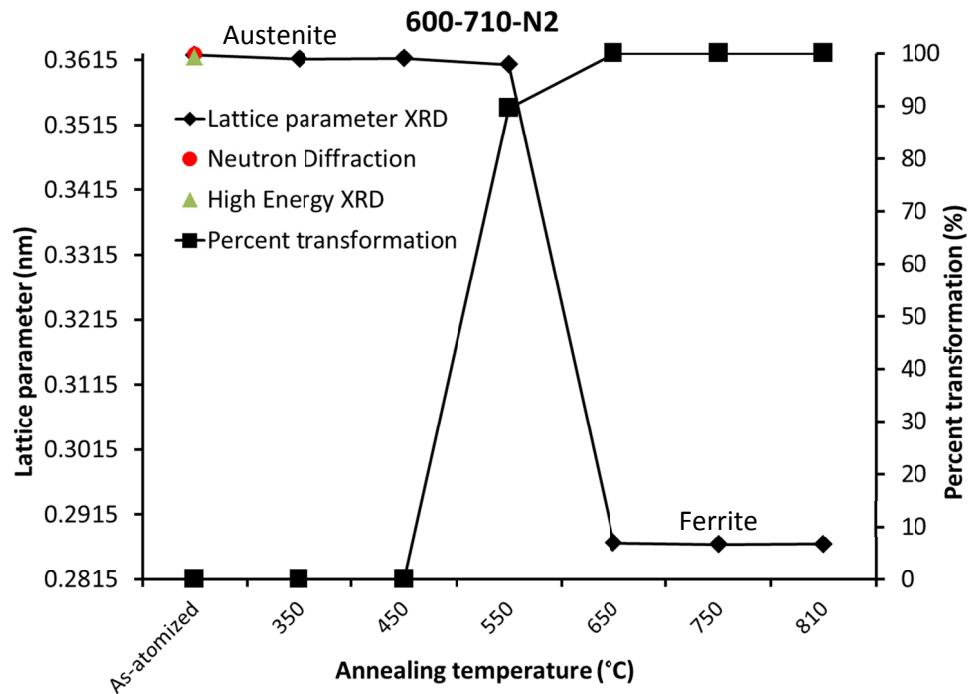


Figure 6.17. Lattice parameter of austenite and ferrite and percent transformation of austenite to ferrite as a function of annealing temperature.

Figure 6.17 shows that by annealing the sample up to 550°C, the lattice parameter of retained austenite is about 0.3623nm. Also, the percent transformation remains at zero. As the annealing increasing from 550°C to 650°C, phase transformation happens and lattice parameter values change from 0.3610nm (for austenite) to 0.2871nm (for ferrite). There is also a steep growth in the value of percent transformation from zero to 75.5%. By

annealing above 650°C, there is no substantial change in lattice parameter and percent transformation. The size of the lattice parameter for ferrite is 0.2871nm [137]. This means that at 550°C, austenite transforms to ferrite and, therefore, carbide precipitation starts. Also, it can be seen that the austenite lattice parameter calculated using ND and HEXRD at room temperature is consistent with the XRD results.

During annealing, supersaturated alloying elements diffuse out from the retained austenite structure and form M_7C_3 carbides. After the M_7C_3 carbides precipitate out inside the austenite phase, then, the austenite phase can be destabilized. This depletes the carbon and chromium from the matrix phase and as a result, lattice parameter of the austenite is then decreased (Figure 6.17). This results in increasing the M_s temperature of the austenite phase. Therefore, when the sample is cooling to the room temperature, there is more possibility for the formation of the martensite phase [135]. In the current study, the cooling rate after two hours of isochronal annealing is about 0.33°C/min which does not seem fast enough to form martensite from the depleted austenite matrix. Li et al. [135] has reported that after annealing the laser melted high chromium cast steel, austenite transforms to martensite when the samples are being air cooled. It seems that laser melted samples, cooling rate of depleted austenitic phase is high enough for formation of martensite instead of ferrite. This can be due to the heat sink effect of the sample bulk as well as air cooling effect [134,138].

Considering the same analysis for different particle sizes IA atomized in different cooling gases, one can plot the percent of transformation at 550°C (annealing for two hours) as a function of the cooling rate of droplets (Figure 6.18). This figure also shows the austenite-to-ferrite transformation data for WA particles annealed at 550°C for two hours.

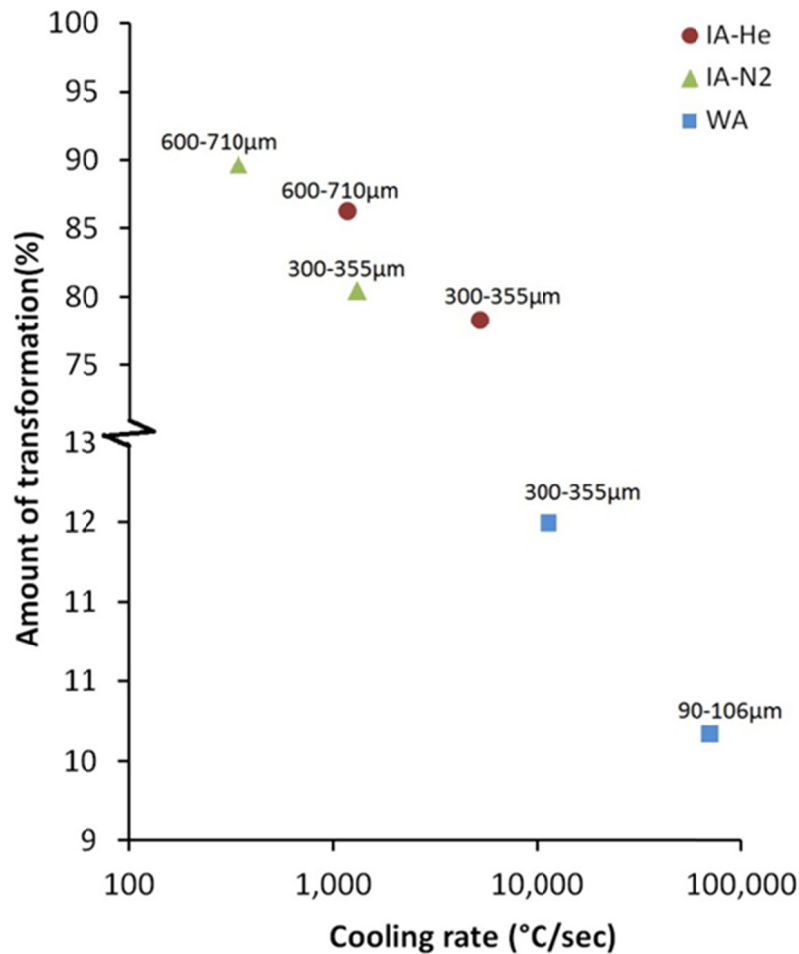


Figure 6.18. Percent of transformation of austenite to ferrite at annealed for two hours at 550°C as a function of cooling rate of droplets.

It can be concluded from Figure 6.18 that droplets with higher cooling rates have lower percent of transformation during annealing at 550°C.

In the austenite with FCC lattice, the dissolved carbon atoms only occupy octahedral interstitial position. This results in lowest amount of internal stresses and distortion. According to Figure 4.1, the maximum solubility of carbon in austenite in D2 tool steel is about 0.91wt.% \approx 4.3at.%. This indicates that among all theoretically possible positions, carbon atoms only fill about 4.5 percent of them. As an example, the amount of supersaturated carbon in 90-100 μ m WA D2 tool steel particle is calculated to be about 1.12 wt.% which increases the filled positions of austenite with carbon to about 5.6 percent. During supersaturation of austenite, where carbon filling is much denser, internal stresses in the austenite lattice is so high that the resultant elastic energy result in formation of carbides. The carbide formation depends on different parameters such as the amount of undercooling (an opportunity for austenite to lower its free energy) and the mobility of the carbon atoms. But, the mobility of the atoms decreases with increasing the amount of undercooling [40]. That can explain why precipitation does not occur at lower temperatures, but starts at around 550°C.

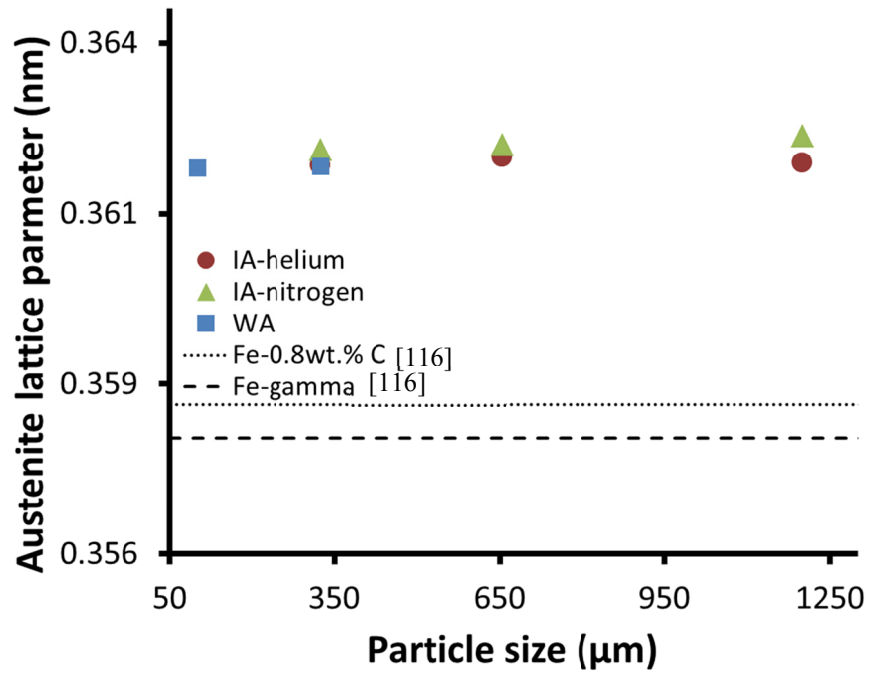
Therefore, according to the discussion provided before, the driving force of the precipitation is increased by increasing the amount of supersaturation. However, as can be seen in Figure 6.18, particles with

higher cooling rates during solidification, have higher tempering stability compared to the particles with slower cooling rates. For example, 300-355 μm particles atomized in helium have a smaller percent of transformation during annealing compared to 600-710 μm particles atomized in nitrogen. Also, there is a lag in precipitation in WA particles, which is due to their higher solidification rate and supersaturation in austenite during cooling of the droplets. Rayment et al. [139] and Peng et al. [140] showed a delay in carbide precipitation by the stabilizing effect of alloying elements in supersaturated austenite. Kishitake et al. [128] also reported that the temperature of transformation of retained austenite in rapidly solidified tool steels increases with increasing chromium and molybdenum content. They show that the retained austenite phase decomposition can be delayed by the adding the carbide former elements, but is barely affected by the amount of carbon in the retained austenite. Detailed mechanism for this temperature delay is still unknown. According to different literatures, the supersaturated alloying elements inside the austenite prevent the transformation of the austenite and hinder the carbide precipitation. Therefore, the high amount of supersaturation results in more lag in precipitation [139,144]. Also, supersaturated alloying elements change the size of the interstitial positions in the structure. This also results in an increase in the diffusive activation energy of atoms [139,140].

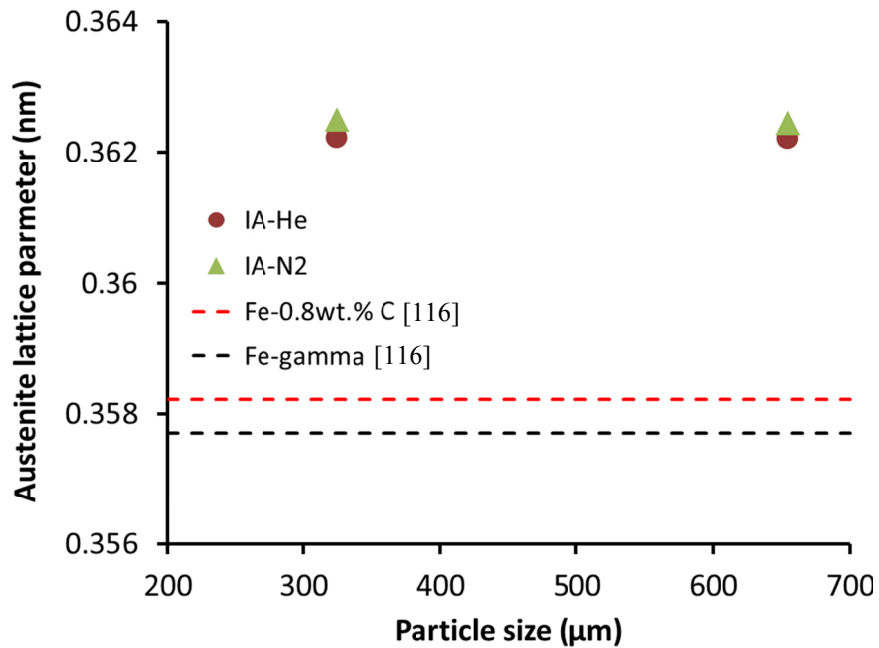
According to Li et al. [135], the high solidification rate increases the carbon and alloying elements concentration in solid solution, which is

higher in the droplets with the higher cooling rate. This elevates the range of austenite-to-ferrite transformation to the higher temperatures. Other works [141,142] also describe the effect of some alloying elements such as manganese, silicon, chromium and vanadium in the structural steels on the phase transformation kinetics during tempering. It has been reported in these works that low concentration of the alloying elements does not affect the precipitation of carbides and the transformation of retained austenite. However, temperature range of precipitation of carbides and austenite-to-ferrite transformation shifts toward higher temperatures when there are higher concentrations of these elements in the composition.

A spherical atom with diameter of 0.52\AA can be fit inside an octahedral interstitial position in gamma-iron. Therefore, carbon atom with the atomic radius of 0.77\AA , or a nitrogen atom with the atomic radius of 0.71\AA sitting in the octahedral void will expand the lattice [143]. Lattice parameter of austenite for particles WA and IA in helium and nitrogen, as well as the iron FCC lattice parameter, based on the Rietveld analysis of XRD and ND results are shown in Figure 6.19.a and Figure 6.19.b, respectively. Both XRD and ND represent almost same values for lattice parameter of supersaturated austenite in different IA and WA particles.



(a)



(b)

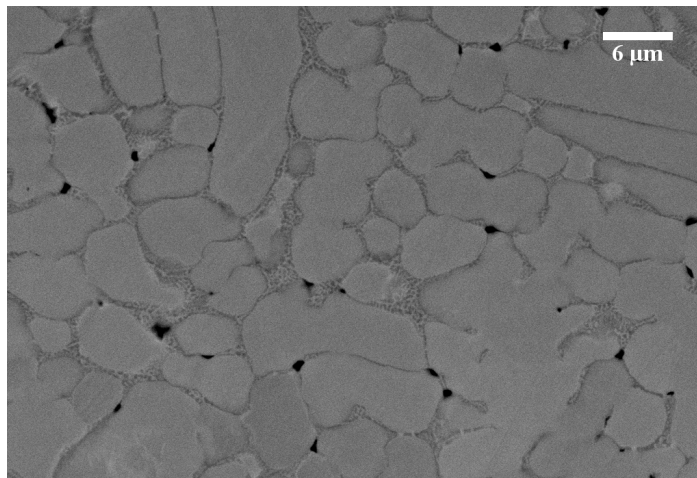
Figure 6.19. Austenite lattice parameter of different-sized droplets WA and IA in helium and nitrogen, using Rietveld analysis of (a) XRD and (b) ND. Fe-0.8wt.% C and Fe-gamma lattice parameters are also shown.

Rapid solidification of the particles does not let carbon and other alloying elements diffuse out of austenite lattice; they remain as supersaturated elements inside the austenite lattice and the lattice is expanded. Therefore, in the rapidly solidified droplets, austenite lattice parameter is much larger compared to that in the Fe- γ or steel with 0.8wt.% carbon. It should be noted that the supersaturated carbon, chromium and other alloying elements has been considered in the calculated austenite lattice parameter.

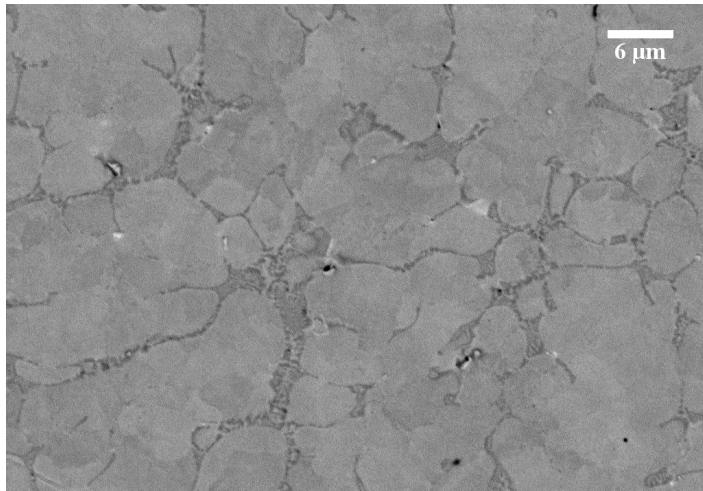
6.3.6. Microstructure of annealed particles

6.3.6.1. SEM

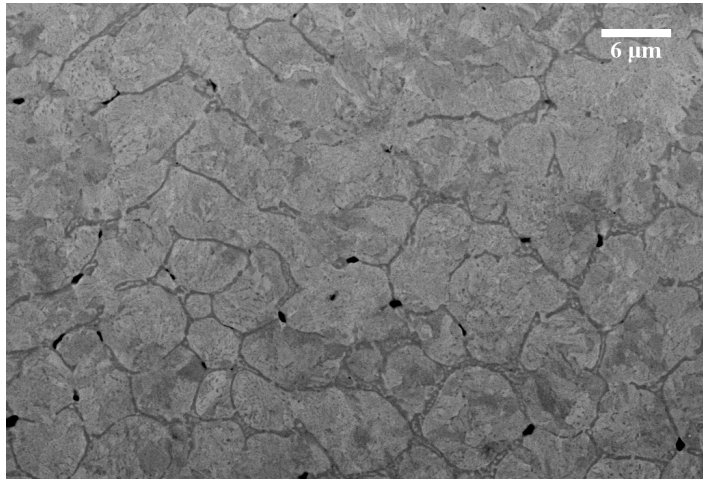
According to the XRD analysis (section 6.3.5), precipitates form in the annealing temperature of 550°C. Figure 6.20 shows a SEM micrograph of an un-etched 650 μm particle atomized in nitrogen and annealed for 2 hours at different annealing temperatures (550°C, 650°C, 750°C and 810°C).



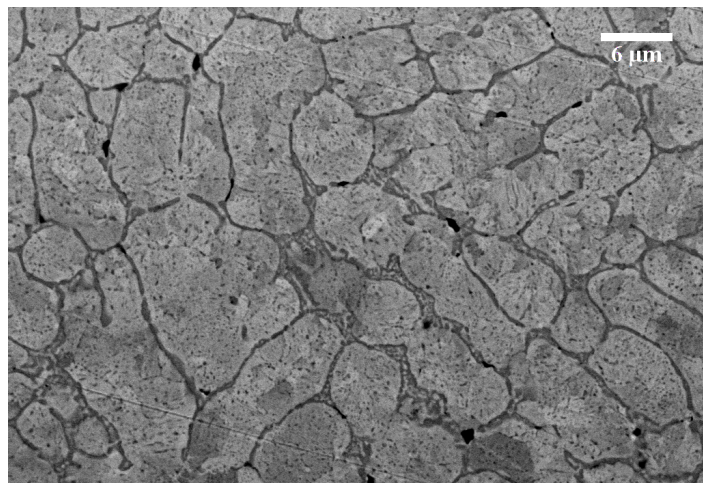
(a)



(b)



(c)

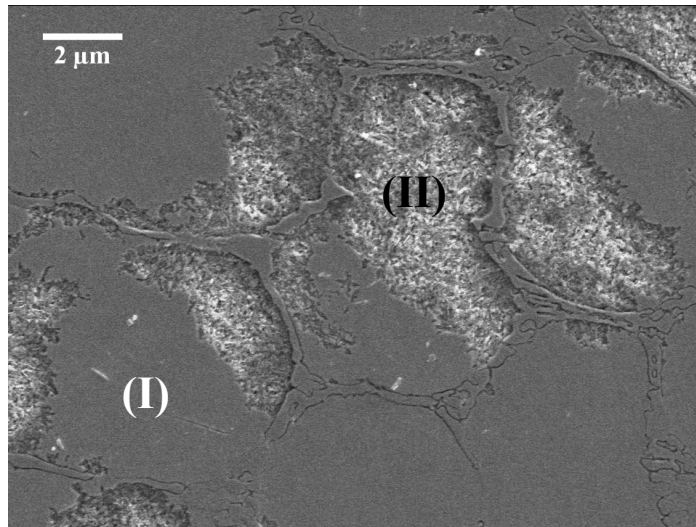


(d)

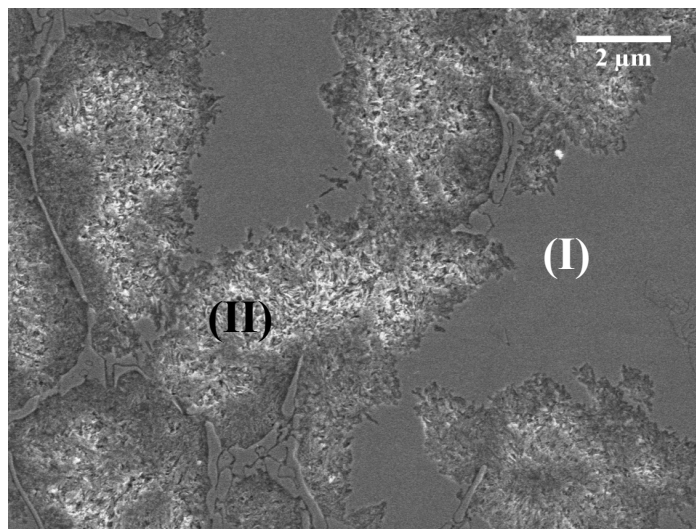
Figure 6.20. BSE-SEM image of 650µm D2 steel atomized in nitrogen, annealed for 2 hours at (a) 550°C, (b) 650°C, (c) 750°C and (d) 810°C.

The microstructure of the particle annealed at 750°C and 810°C (Figure 6.20.c,d) shows some rod-shaped precipitates inside the primary phase. Closer examination of the particle annealed at 650°C shows some barely visible features within the primary phase. No precipitate can be seen in the un-etched particles annealed at 550°C (Figure 6.20.a). The XRD results (Figure 6.10) also show precipitation at 550°C. That is probably why the precipitates are so fine at this annealing temperature, and why higher magnification analysis is needed to characterize the microstructure of the 550°C and 650°C particles.

Figure 6.21 shows a SEM image of the 600-710µm samples atomized in nitrogen and then annealed at 550°C for 2 hours. Primary grains can be seen with the surrounding eutectic, which have been formed during the solidification of the droplet. According to the XRD data for the particle annealed at 500°C (Figure 6.12), austenite and ferrite should be present at this annealing temperature. Region (I) is the retained austenite phase while the area with the white phase inside (Region (II)) contains the transformed ferrite + chromium carbides. The eutectic carbides do not transform because, according to the XRD data, these carbides are M_7C_3 and hence equivalent to that which forms during annealing.



(a)

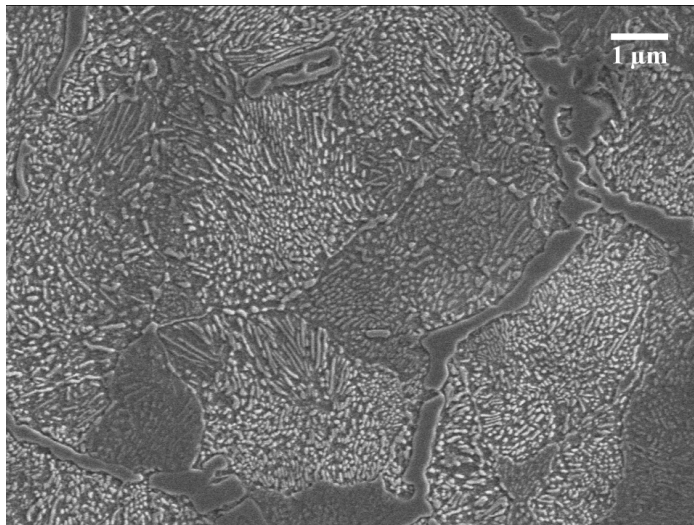


(b)

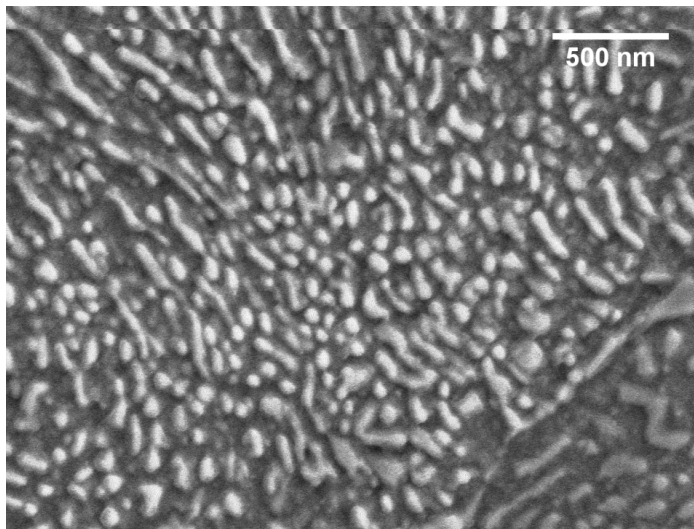
Figure 6.21. SE-SEM image of 600-710µm particle atomized in nitrogen and then annealed at 550C for 2 hours. Region (I) is austenite and Region (II) is ferrite + carbides

Figure 6.22 shows 600-710µm samples atomized in nitrogen and annealed at 650°C. It shows that almost all previously austenite grains (region (I) in Figure 6.21) are now transformed to ferrite and carbides (Figure 6.22.a). The higher magnification micrograph (Figure 6.22.b)

indicates that almost all of the retained austenite (Region (I) in Figure 6.22.a) has transformed to ferrite and carbide when an annealing temperature of 650°C is applied, and that the precipitates are very fine and rod-shaped with a diameter of about 50nm.



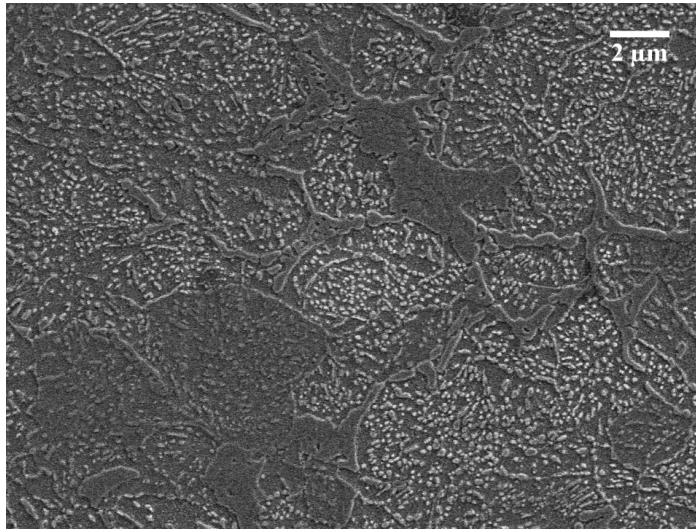
(a)



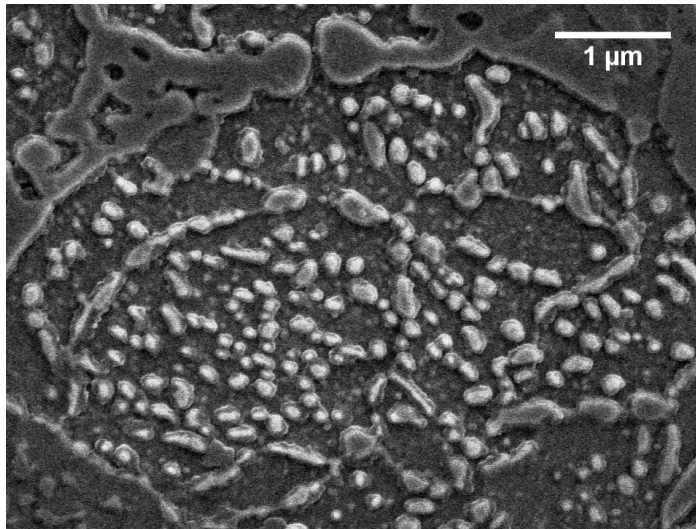
(b)

Figure 6.22. SE-SEM image of a 600-710μm particle atomized in nitrogen and then annealed at 650°C for 2 hours. (b) is the higher magnification view of image (a).

Figure 6.23 and Figure 6.24 show SEM images of a 600-710 μm particle atomized in nitrogen and then annealed at 750 $^{\circ}\text{C}$ and 810 $^{\circ}\text{C}$ for 2 hours. Precipitated carbides in the matrix as well as previously eutectic carbides (eutectic carbides) are visible in the image.

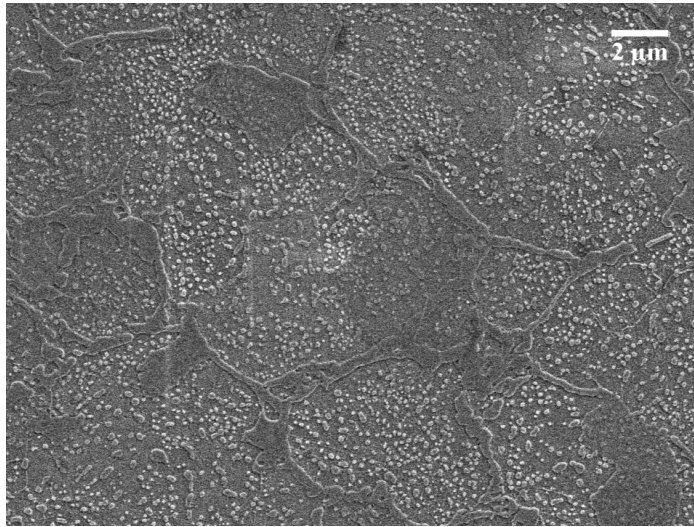


(a)

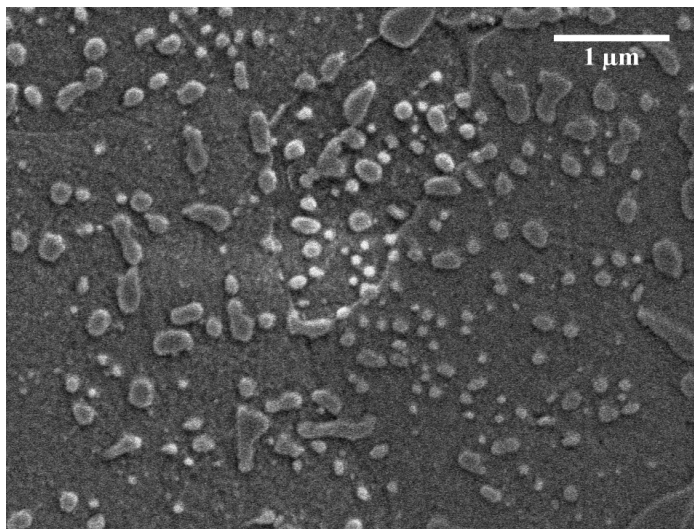


(b)

Figure 6.23. (a) SE-SEM image of 600-710 μm particle atomized in nitrogen and then annealed at 750 $^{\circ}\text{C}$ for 2 hours and (b) higher magnification.



(a)



(b)

Figure 6.24. SE-SEM image of 600-710 μm particle atomized in nitrogen and then annealed at 810 $^{\circ}\text{C}$ for 2 hours and (b) higher magnification.

It can be seen that by increasing the annealing temperature, precipitates are increasing in size, and the distance between them is also increasing.

Figure 6.25 also shows SEM images of 600-710 μm particle atomized in helium and then annealed at 810°C for 2 hours.

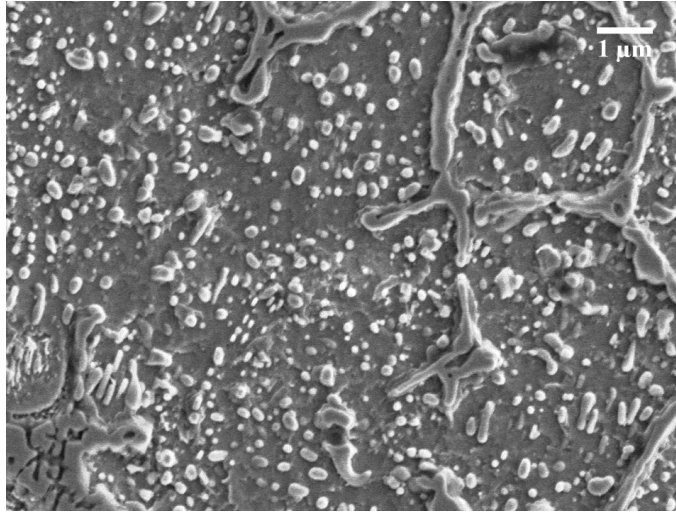


Figure 6.25. SE-SEM image of 600-710 μm particle atomized in helium and then annealed at 810°C for 2 hours.

As can be seen in Figure 6.25, the same shape precipitates are also formed in the particle atomized in helium. There is only a small difference in the size of precipitates which will be discussed in the next section.

By looking to Figure 6.23 to Figure 6.25, one can see that the globular precipitates are formed at the higher annealing temperature (except at 650°C, the temperature at which the precipitates are in rod shapes). In order to be able to see the shape of the precipitates, the SEM stage was tilted at 40° angle and some pictures were taken. Figure 6.26 shows a high magnification of precipitates in a 655 μm particle atomized in helium and annealed at 810°C for two hours.

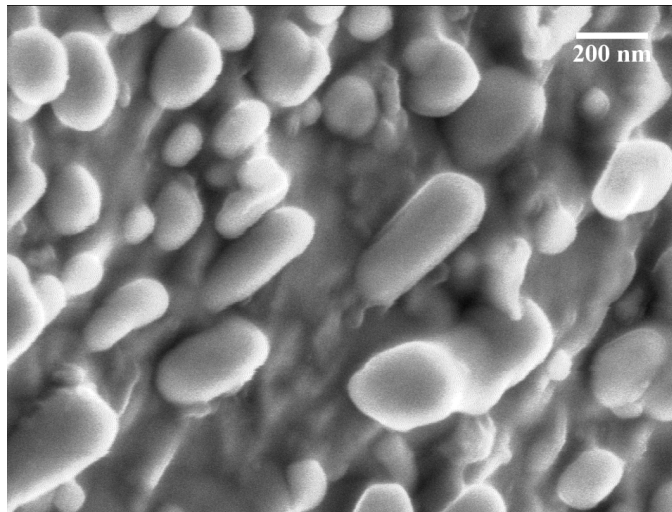
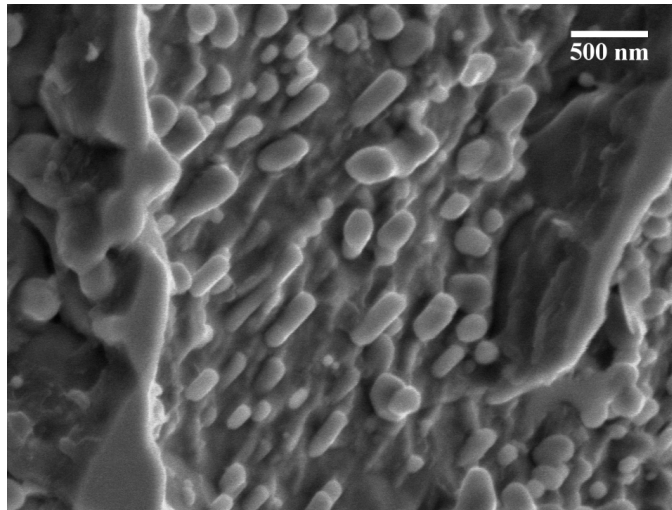


Figure 6.26. SE-SEM image of 600-710 μm particle atomized in helium and then annealed at 810 $^{\circ}\text{C}$ for 2 hours (samples tilted at 40 $^{\circ}$ angle).

Figure 6.26 shows that the precipitates are still in the rod shape at the 810 $^{\circ}\text{C}$ annealing temperature. In Figure 6.24, cross sections of precipitates are visible, which is why the precipitates look spherical. Therefore, precipitates, even after coarsening at the high temperature, are still in the rod shapes.

6.3.6.2. TEM

More detailed microstructural analysis was done using TEM of FIB specimens extracted from specific regions in the different microstructures. Figure 6.27 shows a TEM bright field (BF) micrograph from the interdendritic region and also the primary phase of a particle annealed at 350°C (Figure 6.27.a) and a selected area diffraction (SAD) pattern from the matrix or primary phase (Figure 6.27.b). The diffraction pattern can be indexed to austenite with an orientation close to the $[11\bar{2}]$ zone axis. The austenite primarily consists of iron with about 10wt.% chromium and smaller amounts of vanadium (<1 wt.%). No precipitation has occurred in the primary austenite phase at this annealing temperature. The interdendritic region represents the eutectic component, which consists of two phases, austenite and carbide.

Figure 6.28 shows the interdendritic (eutectic) region at a higher magnification at a different tilt angle. The second phase is iron and chromium rich (~33 wt.% chromium) with smaller but significant amounts of vanadium and molybdenum (4-5 wt.% of both). The SAD pattern in Figure 6.28.b is from both the austenite and the second phase, so there are two overlapping patterns. The spots corresponding to austenite are circled in red (the orientation is close to a $[0\bar{1}3]$ zone axis). The other spots are from the second phase, which can be indexed to M_7C_3 (close to a $[1\bar{1}7]$ zone axis), where M is iron and chromium, as well as vanadium and

molybdenum. These two phases, austenite and M_7C_3 , are consistent with previous work [144].

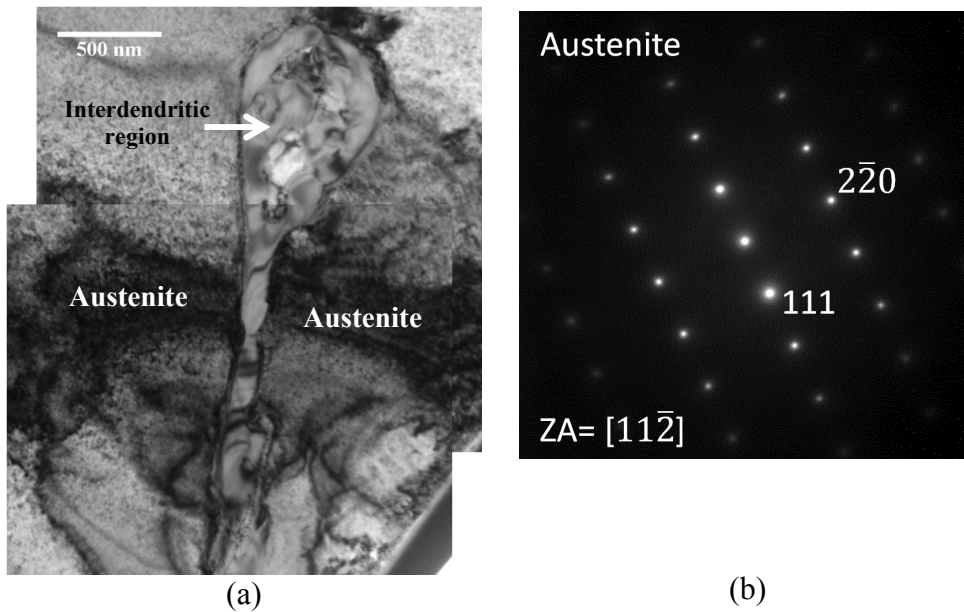


Figure 6.27. TEM BF image of the interdendritic region of a 655µm particle of D2 tool steel, atomized in helium and annealed for 2 hour at 350°C. (b) SAD pattern from the austenite primary phase.

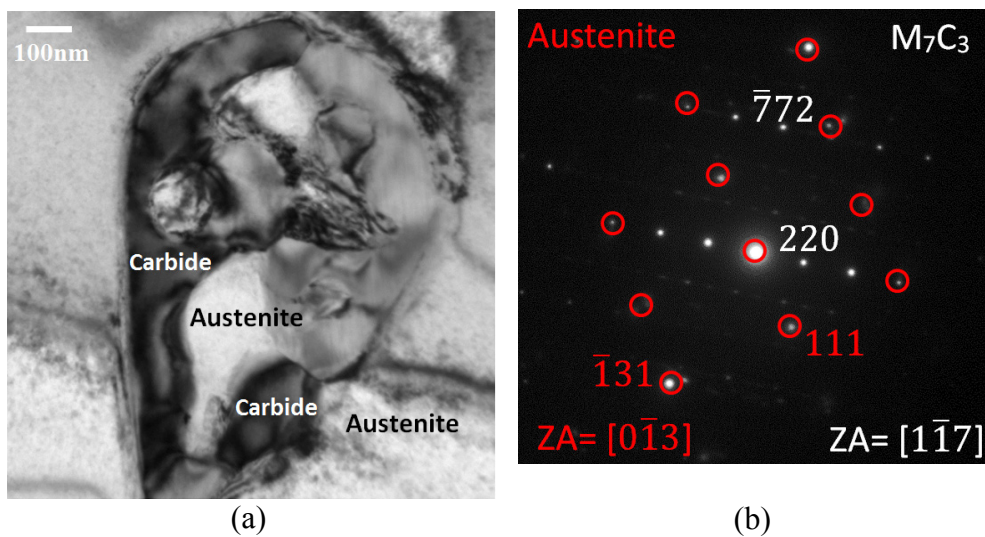


Figure 6.28. (a) Higher magnification TEM BF image from the eutectic area of the sample annealed at 350°C (Figure 6.27), (b) SAD pattern from the interdendritic (eutectic) region.

Figure 6.29 shows a TEM BF micrograph of a 600-710 μm particle annealed at 650°C. Figure 6.22 shows a SEM image from the same sample. The original primary austenite phase, which has transformed to ferrite and carbide precipitates (after annealing), and the eutectic region are indicated by arrows in Figure 6.29. A higher magnification image of the transformed phase is shown in Figure 6.29.b. After annealing at 650°C, rod-like carbides have precipitated within the primary phase; these were not visible in the SEM image (Figure 6.20.b). In fact, the primary phase is no longer austenite, but ferrite plus the precipitates. The precipitates are 200-300nm long and less than 50nm in width. SAD patterns from a ferrite grain and the carbides precipitated within the ferrite grain are shown in Figure 6.29.c and Figure 6.29.d, respectively. Figure 6.29.d shows a partial ring pattern for M_7C_3 carbides as well as spots from the ferrite matrix.

The precipitated carbides are iron and chromium rich (with about 24 wt.% chromium) with smaller amounts of vanadium and molybdenum (about 0.4 wt.% for both) in the substitutional solid solution. The ring pattern of these carbides can be indexed to M_7C_3 . Patterns were also obtained from other regions and at other orientations which confirmed the identity of the carbides. SAD patterns show that the carbides in the as-atomized particles (interdendritic area) and particles annealed at 650°C (precipitated during annealing) are both M_7C_3 . But, EDX results show that interdendritic carbides in the as-atomized sample have higher amounts of chromium (~33 wt.% chromium) compared to the carbides precipitated

within the transformed austenite grains (~24 wt.% chromium). This is basically because interdendritic carbides are formed from the rejected carbon and chromium in the interdendritic region. This provides a higher amount of chromium in the interdendritic eutectic carbides. EDX results also show that the amount of vanadium dissolved in the matrix decreases from ~0.6 wt.% in the as-atomized sample to ~0.2 wt.% in the annealed sample. The excess vanadium is present in the precipitated carbides. Also, elemental analysis using TEM shows that chromium content in retained austenite in as-atomized particles is about 9.21wt.% and in the ferrite region in the annealed particle in 650°C, it is about 3.4wt.%. This shows that when the carbides are precipitating during annealing, chromium diffuses from the austenite grain to new carbide precipitate, which reduces amount of chromium in the matrix of annealed particles compared to the as-atomized ones.

From Figure 6.28 and Figure 6.29, one can see that there is an orientation relationship between the precipitated carbides and the matrix phase. Analysis and understanding of this orientation relationship is a topic of ongoing research.

6.3.6.3. Quantification of microstructure

Using Thermocalc software, it is possible to calculate the equilibrium percent of carbide that should be formed at each temperature, considering the phase diagram of D2 steel. The equilibrium amount of carbides at

annealing temperatures of 650°C, 750°C and 810°C has been calculated.

The results are shown in Table 6.2.

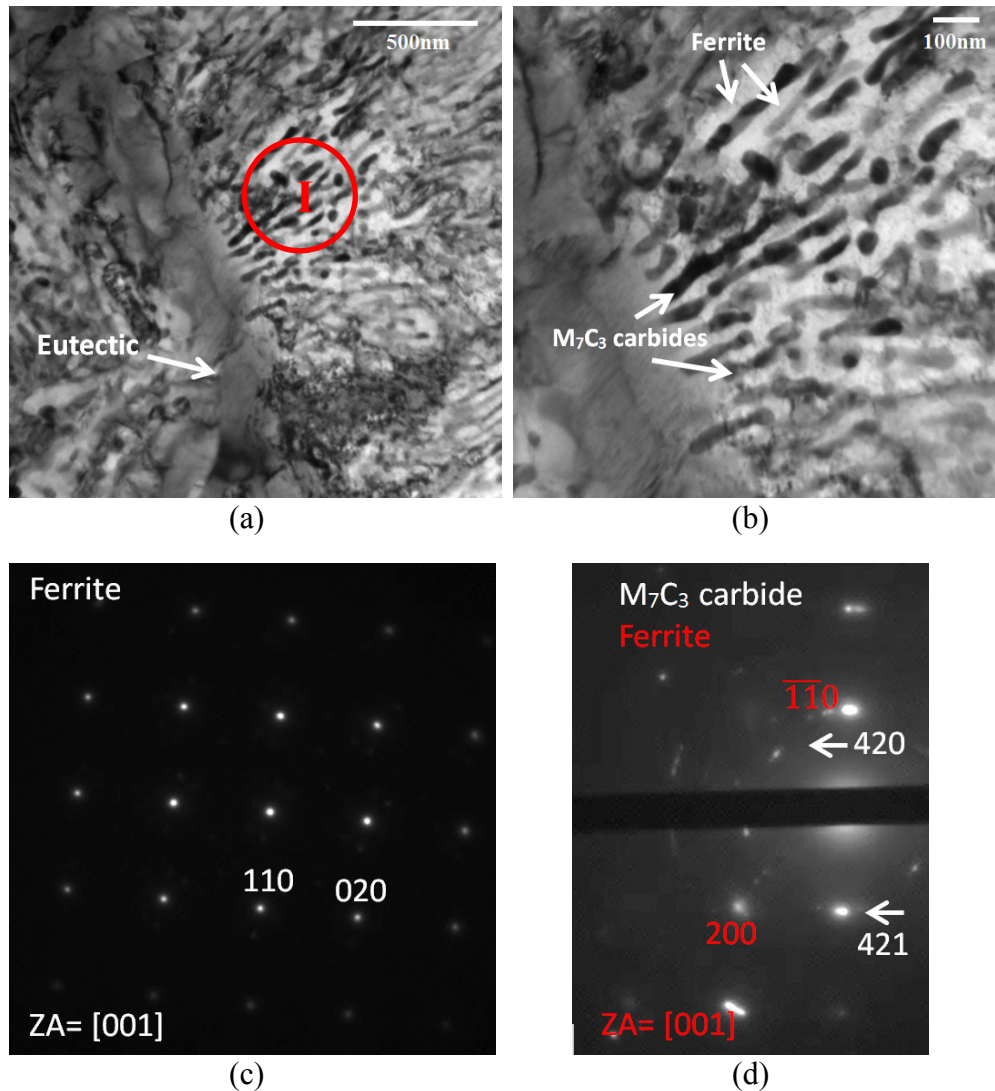


Figure 6.29. (a) and (b) TEM-BF images of a 655µm D2 tool steel sample, annealed at 923 K. SAD patterns from (c) a ferrite grain; (d) ferrite and carbide. Region I shows area with carbides used for the SAD pattern in (d).

Using the grid counting method, the volume fraction of total carbides at each annealing temperature (considering previously formed eutectic carbides during solidification and precipitated carbides inside the

transformed grains) has also been measured. Table 6.2 shows the weight fraction of carbides measured using the grid counting method for the droplets atomized in nitrogen.

Table 6.2. Weight percent of carbides at different annealing temperature for droplets atomized in nitrogen as well as equilibrium amount of carbides at those temperatures.

Solidification Condition	300-355 μm -nitrogen		600-710 μm -nitrogen		Equilibrium		
	750	810	750	810	650	750	810
Annealing temp ($^{\circ}\text{C}$)							
Formed phases	$\alpha+\text{M}_7\text{C}_3$	$\alpha+\text{M}_7\text{C}_3$	$\alpha+\text{M}_7\text{C}_3$	$\alpha+\text{M}_7\text{C}_3$	$\alpha+\text{M}_7\text{C}_3+$ M_{23}C_6	$\alpha+\text{M}_7\text{C}_3$	$\alpha+\text{M}_7\text{C}_3$
wt.% of carbides	20.0 \pm 1.0	18.9 \pm 1.5	19.4 \pm 1.5	18.6 \pm 1.7	18.5	17.8	17.7
Vol. fraction of carbides	0.22 \pm 0.01	0.21 \pm 0.01	0.21 \pm 0.01	0.20 \pm 0.01	0.2	0.19	0.19

Table 6.2 shows that fraction of carbides after annealing process is almost similar to the equilibrium fraction of carbides

As previously mentioned, precipitated carbides are rod-shaped. Since it is so difficult to measure the length of these rod precipitates, the diameter of precipitates was chosen in order to have a scale measuring size of precipitates. Figure 6.30 shows the diameter of rod precipitates that was measured for droplet with different cooling at different annealing temperatures.

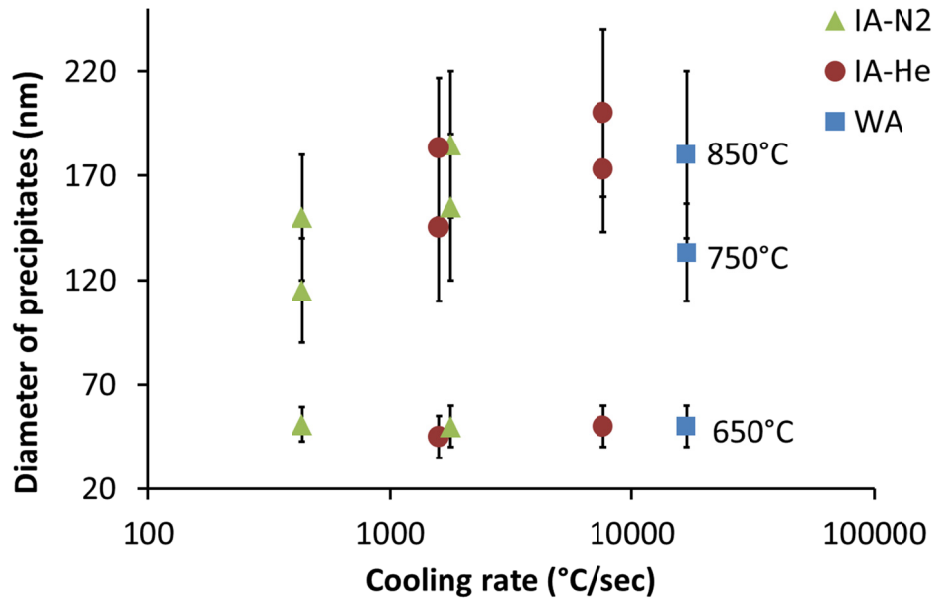


Figure 6.30. Precipitates diameter as a function of droplets cooling rates for different annealing temperatures.

From Figure 6.30, one can see that increasing the annealing temperatures, increases the diameter of the precipitate. The diameter of the precipitated carbide rods at the annealing temperature of 650°C in all samples is about 50nm. By increasing the annealing temperature, particles with higher cooling rates show a larger increase in the precipitate diameter compared to the particles with slower cooling rates (except WA samples). For example, 300-355µm droplets atomized in helium (which has the highest cooling rate among all IA samples) show the larger precipitate diameter compared to 600-710µm droplets atomized in nitrogen (which has the lowest cooling rate among all IA samples). Figure 6.18 showed that particles with the higher cooling rate also have less of an austenite-to-ferrite transformation at 550°C annealing temperature. As mentioned before, this is

due to the higher amount of supersaturation in the samples with the higher solidification rate, which results in changing the transformation temperature toward the higher temperature. But, because the ferrite-to-austenite transformation starts later in more rapidly cooled droplets (compared to less rapidly cooled droplets), one should expect finer precipitate in faster solidified particles.

In the initial stages after nucleation, the precipitates grow, a process that is faster in the particles with the higher solidification rates. This can be related to the effect of supersaturation of alloying elements on the driving force of the precipitates' growth during annealing. Droplets with higher cooling rates have large amounts of supersaturation of austenite with alloying elements. This greater amount of supersaturation translated to a greater amount of driving force during the growth of carbides. So, carbides in droplets with high cooling rates (larger supersaturation) grow faster in size. Therefore, at a specific annealing temperature, carbides of higher cooling rate droplets are bigger compared to the droplets with lower cooling rates. In the 650°C annealing temperature, precipitation is started later in the particles with the high cooling rate. But, because faster cooled particles have higher driving force for precipitates' growth, precipitates are almost in the same size as the slower cooled particles. It has been reported [145] that diffusion of chromium in ferrite is more faster than most metallic alloying elements. This results in formation of Cr_7C_3 during tempering. Also, coarsening rate of chromium carbide is higher compared to other carbides

(like vanadium carbide). Therefore, more chromium supersaturated in the austenite will cause the precipitates to coarsen more quickly in droplets with higher cooling rates.

In the growth stage of precipitates, according to Eq. 6.9, a higher amount of supersaturated elements in the matrix $c(t)$ results in higher growth rate of precipitates. So, in more rapidly solidified droplets where there are higher amount of supersaturation, precipitates grow faster. As a result, larger precipitates form at a certain annealing time and temperature.

$$\frac{dR}{dt} = \frac{D}{R} \ln\left(\frac{c(t) - c_E}{c_\beta - c_E}\right) \quad \text{Eq. 6.9}$$

where c_E is the equilibrium concentration, c_β is the concentration at the interface of the precipitate, c_t is the supersaturated composition, D is the diffusion coefficient, R is the precipitate radius and dR/dt is the growth rate [146].

Formation of some fine $M_{23}C_6$ carbides during tempering of retained supersaturated austenite has been reported [129,134,135,145]. The formation of these carbides significantly depends on the composition of tool steel. For example, slightly less carbon and chromium content result in a peritectoid reaction of $\gamma + M_7C_3 \rightarrow M_{23}C_6$ in the Fe-C-Cr phase diagram and formation of some $M_{23}C_6$ carbides during the tempering of laser surface melted steel [134,135]. Also, there have been reported that $M_{23}C_6$ forms in low carbon-high chromium content steel after tempering [129]. Generally, adding of tungsten encourages this carbide to form by allowing it to

nucleate faster, while vanadium tends to stabilize Cr_7C_3 by decreasing the rate of release into the solution of chromium and carbon needed for the growth of Cr_{23}C_3 [145]. Using Thermocalc, it can be seen that at 550°C and 650°C , a slight amount of M_{23}C_6 is available (about 3wt% at 550°C and about 2wt% at 650°C). Although according to equilibrium, there should be some M_{23}C_6 carbide, most likely the small weight fraction of this carbide means that it is not possible to detect M_{23}C_6 in XRD and TEM analyses. Also, since there is no tungsten and a considerable amount of vanadium (about 0.8wt.%) in the chemical composition of D2 tool steel, there is less of a probability that this carbide will form.

6.3.6.4. Hardness of annealed particles

Hardness measurements have been done on the as-atomized and annealed samples in order to see the effect of rapid solidification and subsequent annealing on the mechanical properties of the particles.

Because the samples are in the form of powder particles mounted inside the epoxy resin, the first step in the hardness measuring process was to figure out a suitable hardness load, because a high amount of load could deform the epoxy and show incorrect hardness values. Therefore, on one of the samples (300-355 μm atomized in helium), hardness measurements were done using different amount of loads. Figure 3.8 shows the effect of the amount of load on the hardness of 300-355 μm as-atomized in helium. To be consistent in all other hardness measurements and in order to have stable

results and more visible indents (to ease the measurements), a load of 100gf was chosen during the hardness measurement.

The effect of isochronal (2 hour) heat treatment on the microhardness of IA D2 steel is shown in Figure 6.31. The particles with the highest and lowest cooling rates, 300-355 μm atomized in helium and 600-710 μm atomized in nitrogen, respectively, and 300-355 μm water atomized particles were chosen. As-atomized 300-355 μm atomized in helium shows a slightly higher hardness, which can be attributed to its fine microstructure compared to the larger particles atomized in nitrogen. The hardness plots show an initial decrease in hardness, likely due to the relief of internal stresses introduced by rapid solidification [39]. At the 550°C annealing temperature, where the precipitation of carbides and the transformation of austenite to ferrite begin, hardness also increases. At 750°C and 810°C annealing temperatures, because of the coarsening of precipitates and also grain growth, hardness decreases considerably.

Since at 550°C, a larger percentage transformation has happened in 600-710 μm -nitrogen particles, a larger fraction of precipitates is available at this temperature compared to that in 300-355 μm -helium particles. Therefore, annealing at 550°C results in greater hardness in 600-710 μm -nitrogen particles (about 650HV) compared 300-355 μm -helium (about 512HV). At higher temperatures, due to coarser precipitate and less volume fraction of carbides, both samples experience a drop in hardness.

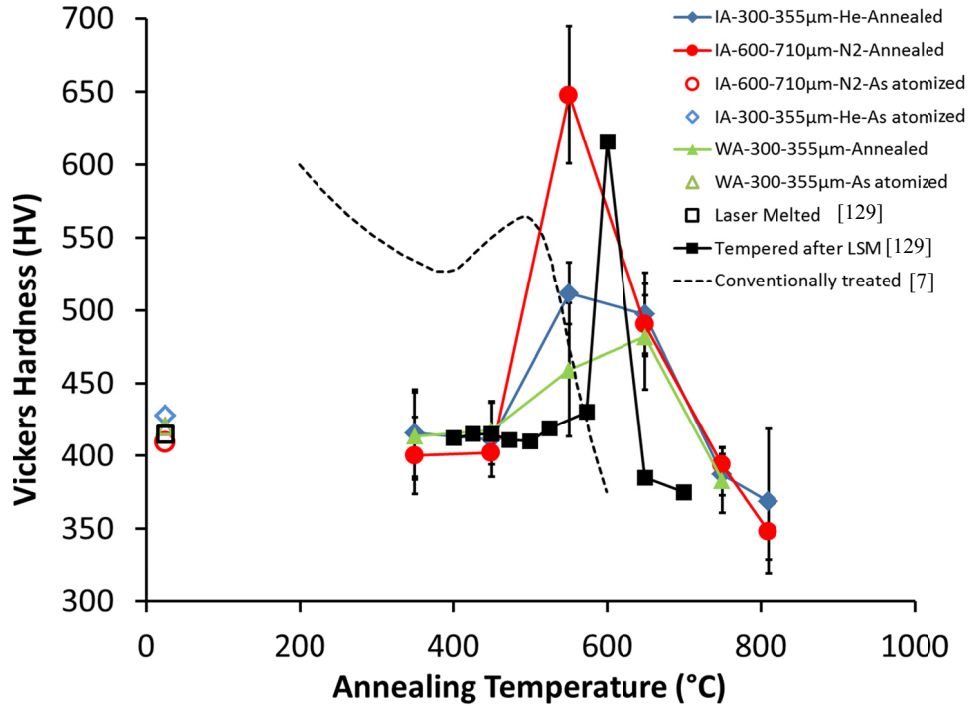


Figure 6.31. Vickers hardness of as-atomized droplets in different size ranges atomized in different atmospheres, as well as annealed samples at different temperatures.

Figure 6.31 shows that annealing of 300-355µm water atomized particles at 350°C and 450°C, does not change the hardness of the particles. It is mainly because there is no precipitation in the particles during annealing at these temperatures. Further annealing at 550°C and 650°C results in an increase in the hardness which is followed by a drop in hardness by annealing at 750°C. According to Figure 6.18, only about 12 percent of phase transformation ($\gamma \rightarrow \alpha + \text{carbides}$) happens at 550°C for 300-355µm water atomized particles. This amount of transformation results in a little increase in the hardness of particles at 550°C annealing temperature. Since more transformation happens at higher temperature, higher hardness

values would be expected at higher temperatures annealing where more transformation is taking place. The maximum hardness value for 300-355 μ m water atomized particles would be between 550°C and 650°C annealing temperatures where larger fraction of transformation has happened and also precipitates are not coarse to reduce the hardness.

Figure 6.31 also shows the variation in hardness as a function of the tempering temperature of the steel after laser surface melting (LSM) [129] and after conventional quenching from an austenitization temperature of 1025°C [7]. After LSM, the maximum hardness value is about 620HV appearing at 600°C. But, after conventional hardening, the secondary hardening peak temperature is about 570HV at 500°C.

In IA and LSM steels, the retained austenite is different from that after conventional hardening. Decomposition of the retained austenite formed after conventional hardening because happens during tempering at 200-350°C temperature range [129]. But, in IA and LSM steels, transformation of retained austenite starts after tempering at 550°C and 600°C, respectively. According to Colaco et al. [129], after M_7C_3 precipitates within the austenite phase, the destabilization of austenite happens.

Different studies have been done on composites with in-situ phases (for example Al-Si [147]) or external reinforcement phases (for example alumina particles in magnesium matrix [148]). It has been shown by Singh et al. [149] that interparticle spacing of second phase has an important effect

in strengthening of materials, which by reducing the interparticle spacing, a material became stronger. Khan et al. [147] have done an investigation on the effect of shape and distribution of silicon precipitate in aluminum-silicon alloy. They propose the following model to relate precipitate spacing and hardness of the material:

$$H = H_0 + A_p r_p^{-d} \quad \text{Eq. 6.10}$$

where H_0 is the initial hardness value, A_p is the known area at which measurements have been done in μm^2 , r_p is spacing between precipitates in μm and d is a constant dependent on the shape of the precipitates. This equation shows that larger spacing between precipitates results in lower Vickers hardness values.

Considering the diameter of precipitates and knowing total volume fraction of carbides as well as eutectic carbides, the spacing between the precipitates at different atomization and annealing conditions can be estimated. The initial hardness value of ferrite, H_0 , is assumed to be 62HV [150]. Therefore, one can plot $\log (H-H_0)$ versus $\log (r_p)$ (Figure 6.32), where H is the hardness of the material.

Figure 6.32 shows that precipitate spacing is larger in the particles annealed at higher temperatures. This figure also shows that hardness of the D2 steel decreases when the spacing between precipitates increase. This behaviour also has been seen in composite systems. Since precipitated carbides are hard phases compared to soft ferrite matrix phase, they can be considered as reinforcement phases in the composites. Based on the

hardness trendline shown in Figure 6.32 and Eq. 6.10, the value of d for rod shape precipitates (see Figure 6.26) identified to be 0.38. d values for the angular, flaky and fibrous silicon in a Al-Si alloy have been calculated as 0.50, 0.22 and 0.10, respectively [147]. These show that the d value for the rod shape precipitates stands between the angular and flaky type of precipitates.

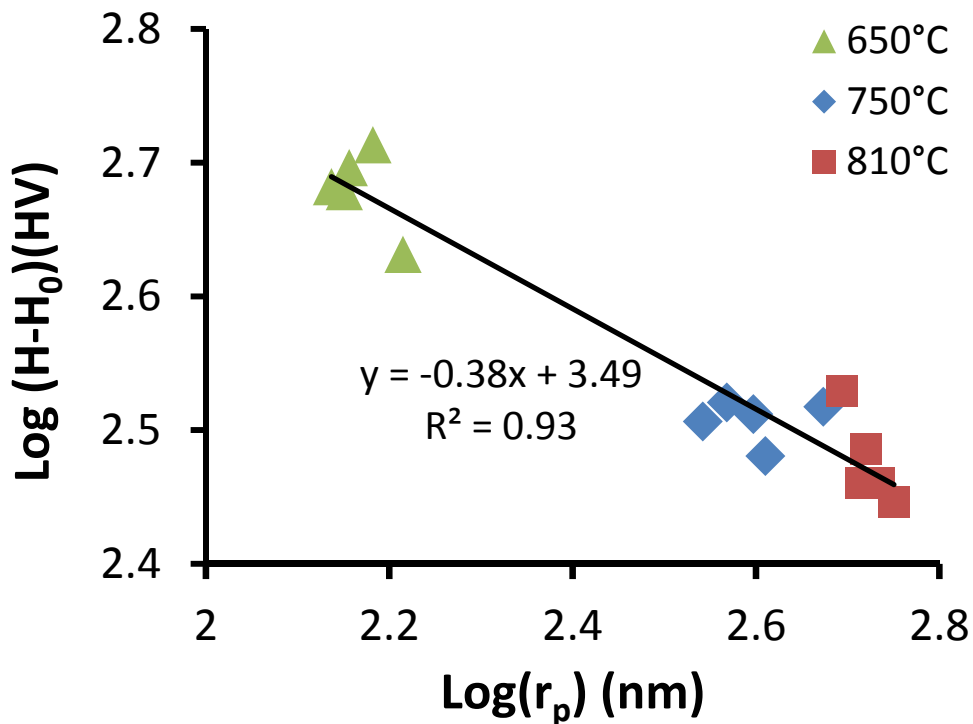


Figure 6.32. Hardness as a function of precipitate spacing of particles annealed at different temperatures.

6.4. Summary

Heat treatment of rapidly solidified D2 tool steel particles was investigated in this chapter. Effect of undercooling, cooling rate and annealing temperature on formation of precipitates and final mechanical properties were also studied. It was possible to correlate the amount of

supersaturation to the amount of primary and eutectic undercooling during solidification of IA droplets. It was found that by increasing the amount of undercooling (primary phase and eutectic), the amount of supersaturation of alloying elements inside the primary phase (retained austenite) increases as well. Amount of supersaturation of alloying elements inside the primary phase then can be attributed to the precipitation behaviour of particles during the annealing cycles. During annealing of the powder particles, the amount of austenite to ferrite transformation is smaller in the powders with higher undercooling and cooling rate. Since powder particles with higher undercooling and cooling rate have higher amount of supersaturation, precipitates then grow fast which results in coarser carbide precipitates at the end of tempering process. Hardness evaluation of the annealed powders showed that highest amount of hardness occurs at a temperature in which fine precipitate of carbide formed with larger fraction.

Using the information provided in this chapter and Chapter 4, effect of rapid solidification on the microstructure and mechanical properties of spray deposited D2 tool steel will be investigated in next chapter.

Chapter 7

7. Spray deposition of D2 tool steel

7.1. Introduction

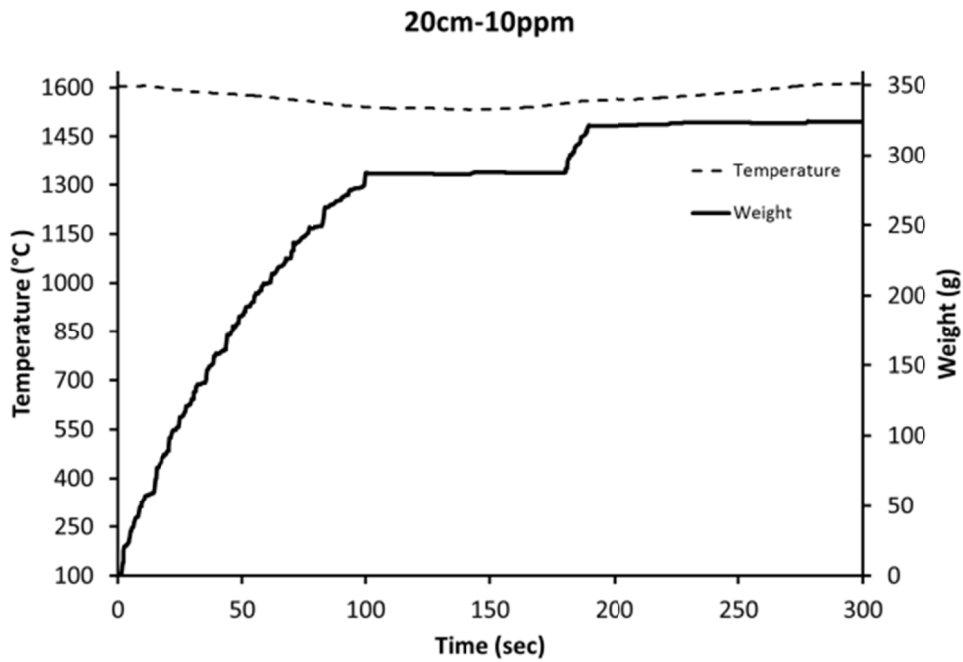
Samples produced using the spray deposition technique have benefits of both rapid solidification and near-net shape capabilities. Deposited droplets on the substrate can be in the form of fully liquid, fully solidified or semi-solid. As discussed in section 2.3.4, a very fine microstructure, low levels of segregation, fine precipitates and extended solid solubility of the alloy can be achieved using spray deposition. Also, in contrast to ingot casting which provides low amount of undercooling, it will be shown in this chapter that during spray deposition, eutectic undercooling values similar to individual droplets can be achieved. This will be done by a quantitative comparison of eutectic fraction and eutectic undercooling between solidified D2 powders and spray formed samples, in order to investigate solidification mechanism of the sprayed droplets in the spray deposited samples. Also, in this chapter, effect of different parameters such as substrate distance from the nozzle plate and the oxygen level inside the cooling media on the microstructure and formed phases during solidification has been investigated.

7.2. Results and discussion

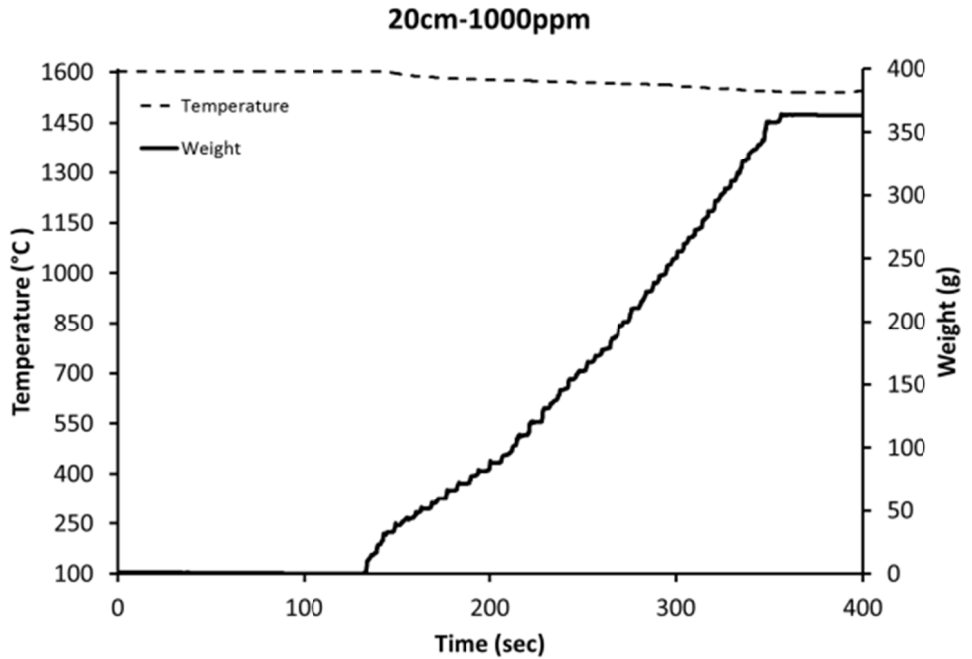
As previously mentioned, four spray deposit samples have been made by IA. The deposit produced at 38cm distance from the nozzle plate in the helium atmosphere has lots of porosities, and due to these porosities, the

deposit was not stable and collapsed during handling of the sample. In fact, the deposit was made of previously solidified particles of D2 steel making a structure on the substrate. No further analyses could be done on this deposit.

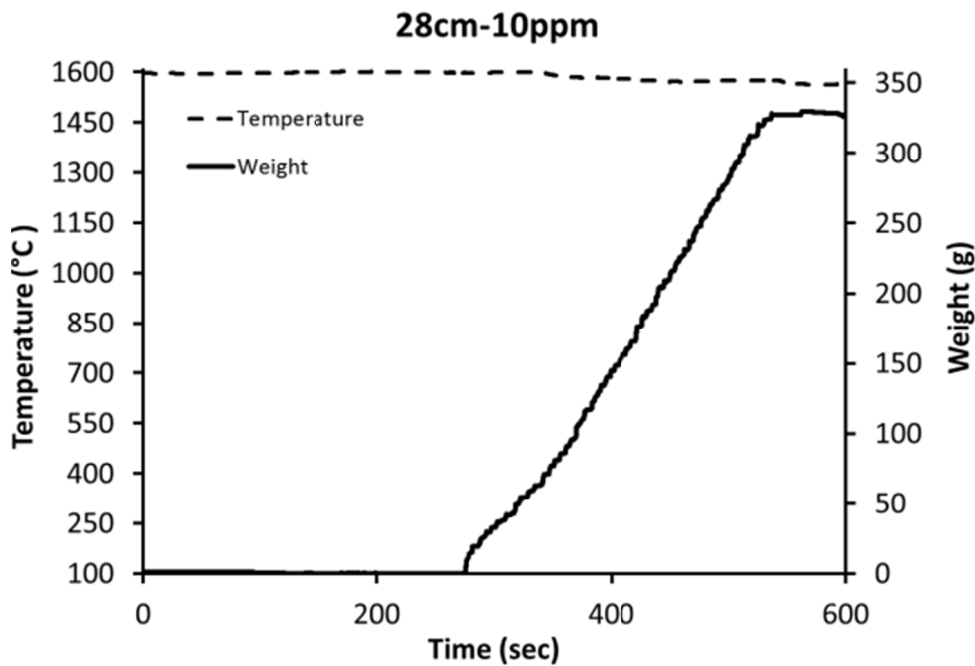
Figure 7.1 shows temperature of melt as a function of time of atomization. Load cell data also collected weight of deposits at different times. The temperature of the melt was held close to 1600°C during the atomization with about 25°C tolerance. This figure shows that the flow rate of the spray and temperature of the melt are stable during different spray deposition experiments.



(a)



(b)



(c)

Figure 7.1. Temperature of the melt and weight of deposit as a function of time of atomization, for deposit at (a) 20cm below the nozzle plate at 10ppm oxygen level, (b) 20cm below the nozzle plate at 1000ppm oxygen level and (c) 28cm below the nozzle plate at 10ppm oxygen level.

Figure 7.1 shows that atomization of samples 201000 and 2810 starts after 140s and 280s of plunger movement, respectively. There is a constant atomization rate up to the point that the atomization is stopped and spray deposited samples are prepared. In sample 2010, atomization starts exactly after the start of the plunger with a constant atomization rate, and then stops at about 100s. Atomization starts again after 80s with almost the same atomization rate and atomization stops again a little bit after that. The second atomization in sample 2010 resulted in formation of an excess part on top of the sample that is marked by an arrow in Figure 3.2.b.

7.2.1. Modeling of solid fraction and temperature of droplets

Using the heat loss model, it is possible to model the temperature history of droplets during free fall in IA. There is a range of particle size produced during each atomization runs. Using a 300 μm orifice hole, D_{50} of the produced droplets are about 360 μm . Therefore, a droplet size of 360 μm was chosen to use in the model, as a representative of the particle size with a superheat of 205°C. Figure 7.2 shows the temperature of the droplet and distance of the droplet from the nozzle plate as a function of the solidified fraction, for 360 μm droplet atomized in nitrogen and calculated by the model.

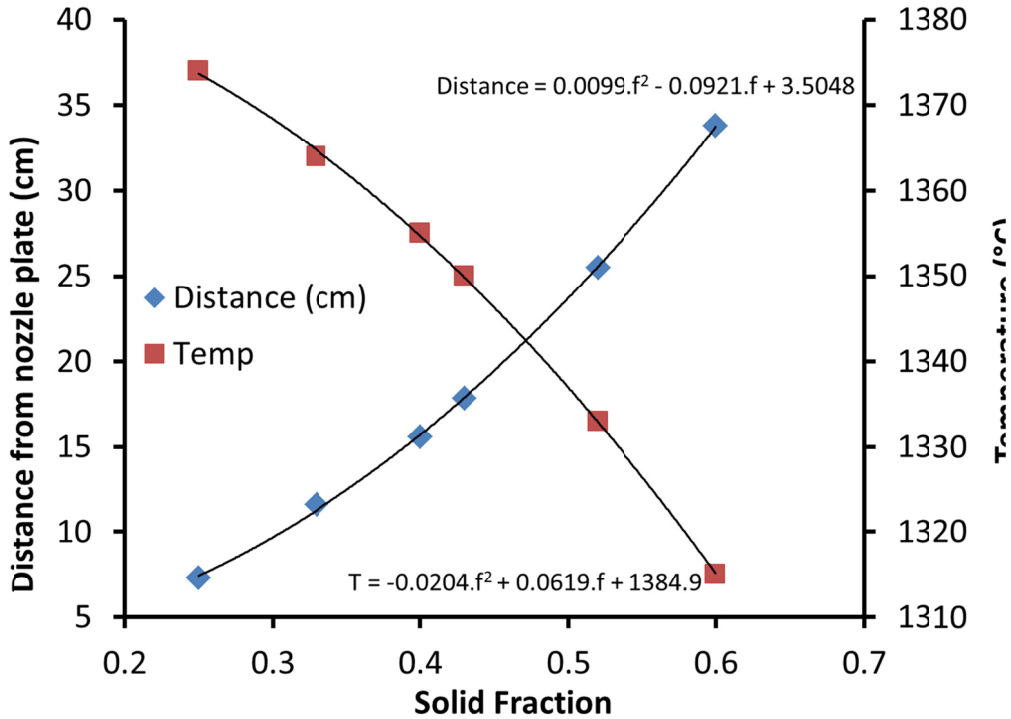


Figure 7.2. Temperature of the droplet and distance of droplet from nozzle plate as a function of fraction solidified in the droplets, for 360 μ m droplet atomized in nitrogen, with the superheat of 205 $^{\circ}$ C without undercooling calculated by the model.

For 360 μ m droplet atomized in nitrogen at 20cm distance from the nozzle plate, the temperature is about 1344 $^{\circ}$ C and the solid fraction is about 0.46. Also, at 28cm distance from the nozzle plate, the temperature is about 1327 $^{\circ}$ C and the solid fraction is about 0.55. It shows that at a shorter distance from the nozzle plate (20cm), there is more liquid in the droplets when they hit the substrate compared to the droplets that hit the substrate 28cm from nozzle plate. Therefore, there is a possibility that more porosity is available in the 28cm distanced sample. Porosity level of the deposits will be investigated more in section 7.2.3. Also, when deposition is conducted at shorter distances from the nozzle plate, the temperature of the droplets is

higher and therefore a lower cooling rate would be expected in the deposits compared to the deposits that are produced at longer distances. This effect will be discussed in the following sections.

There are different parameters that can affect the solid fraction of droplets during free fall at a specific distance. Two important parameters are the amount of superheat and particle size. Superheat has been chosen because during the atomization run, melt temperature has a fluctuation of about 25°C from 1600°C. Figure 7.3 shows the effect of droplet size and superheat on the distance from the nozzle plate at which 0.4 fraction solid forms.

Three different superheats of 50°C, 100°C and 200°C and three different particle sizes of 180, 360 and 595µm were chosen in order to see the effect of these parameters on the distance at which fraction solidified is 0.4.

From Figure 7.3, one can see that superheat does not have significant effect on the distance at which 0.4 fraction solid is achieved. Increasing the superheat from 50°C to 200°C changes the distance of 0.4 fraction solid only about 0.2cm. As described in [120,151], the cooling rate of falling droplets depends on the temperature of the droplet and surrounding gas. When the temperature of the droplet increases, there would be a larger difference between the droplet and surrounding gas and therefore a larger cooling rate would be achieved. On the other hand, with a lower amount of superheat, falling droplets also have a lower temperature

and, therefore, it is easier for them to reach a specific temperature. Balancing these two reasons would result in having an almost same solid fraction at a specific distance from the nozzle plate. Therefore, it seems superheat is not a significant parameter in considerable change of solid fraction of droplets.

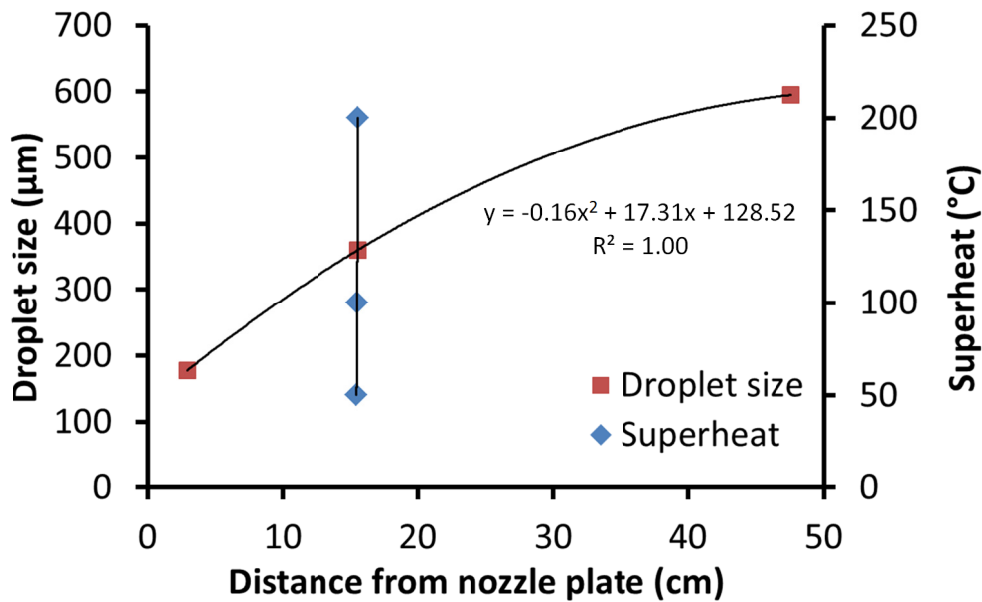


Figure 7.3. Effect of droplet size and superheat on the distance at which 40% solid forms in a nitrogen atmosphere.

Another important parameter would be the size of the droplets during free fall. From Figure 7.3, it can be seen that a slight change in droplet size considerably changes the distance at which 0.4 fraction solid is achieved. According to Zheng et al. [151] and Zeoli et al. [120], the cooling rate largely depends on the size of droplets. In the heat loss equation described in their works, the cooling rate of droplets is proportional to $1/d^2$ (where d is the particle size of falling droplet) and any small increase in the

particle size of droplets considerably decreases the cooling rate. During IA, there is a range of particle sizes ($D_{10}=180\mu\text{m}$, $D_{50}=360\mu\text{m}$ and $D_{90}=595\mu\text{m}$). When the droplets reach to the substrate, they have a different liquid portion inside which causes different solidification behaviour for each droplet. Very fine droplets can be completely solidified at the time they reach the substrate, while some large droplets can have a significant fraction of liquid when they hit the substrate.

7.2.2. Formation of different phases in deposits

Figure 7.4 shows XRD results of the BP and MP of IA deposits. XRD peaks of ferrite, austenite and M_7C_3 carbides are also shown in the graph. In all samples, austenite and ferrite phases have been formed during spray deposition.

At the eutectic temperature, the liquid remaining between dendrite arms would form eutectic of austenite and M_7C_3 carbide, as shown by XRD shown in Figure 7.4. Because of the rapid cooling effect in the spray deposits adjacent to the substrate, austenite would retain in the final microstructure. Deposition of hot droplets on the previous deposited layers can cause in-situ annealing effect on the previous layers and transformation of austenite to ferrite and M_7C_3 . It can be seen in Figure 7.4 that the intensity of the main peak of ferrite in the samples from the lower section of the deposit is a bit higher than that in the middle samples. The probable reason may be formation of ferrite and carbide from austenite in the bottom part as a result of the heat coming from the new hot deposited layers on top

of the bottom part. This heat may be sufficient as to cause transformation of some austenite to ferrite.

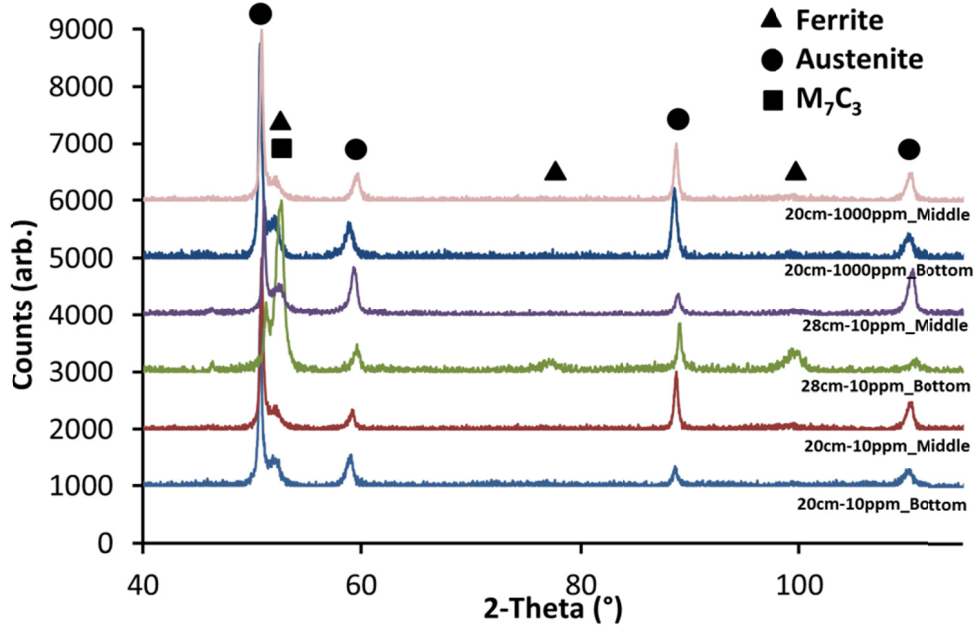


Figure 7.4. XRD graphs of bottom and middle part of impulse atomized deposits. XRD peaks of ferrite, austenite and M₇C₃ carbides are also shown in the graph.

Other parameters such as distance of substrate from nozzle plate and oxygen level in the atomization chamber also affect microstructure evolution. The following sections will discuss effect of these variables on the microstructural and mechanical properties of the spray deposits.

7.2.3. Microstructure of spray deposits

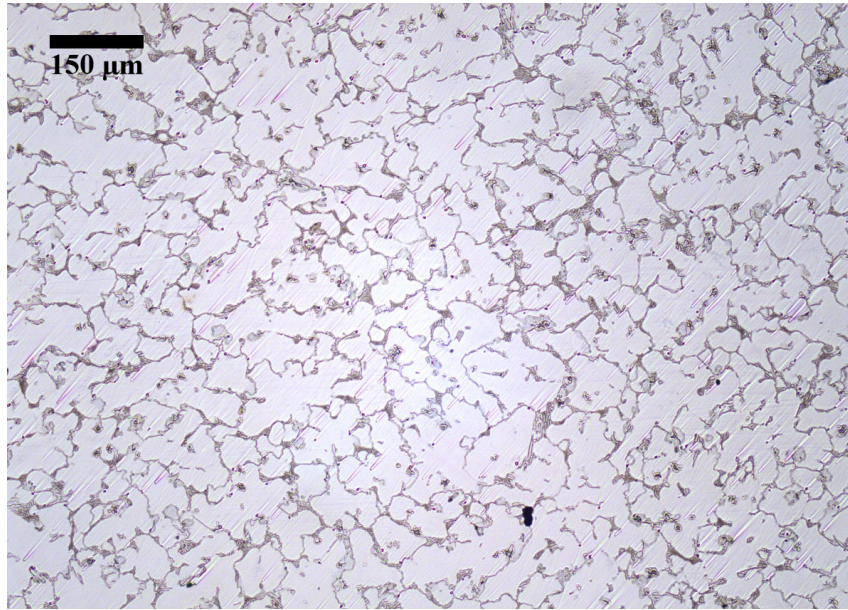
7.2.3.1. Qualitative analysis

Figure 7.5 shows OM images from 2010 and 2810 samples at 15mm distance from the bottom of the sample. This figure shows that in the sample spray deposited at 28cm, the microstructure is finer than that in the

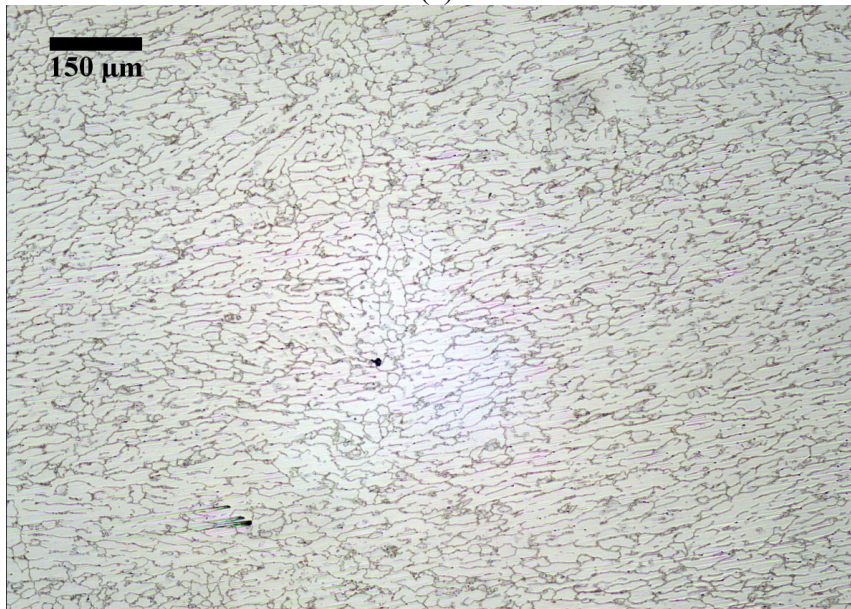
sample spray deposited at 20cm which might be due to a higher cooling rate and colder media in the 2810 sample.

The temperature of the droplets is a function of their distance from originating place (orifice plate). As their distance from the nozzle plate increases, their temperature decreases. Therefore, droplets that hit the substrate at 20cm should have a higher temperature and more liquid than the droplets that reach the substrate at 28cm. So, cooler droplets hit the substrate or deposit at longer distances should result in less enthalpy to be removed from the deposit and should have more solid formed in the droplets prior to deposition. As a result, a higher cooling rate is experienced for deposits that form at 28cm than at 20 cm. This yields a finer microstructure in deposits spray at 28cm of the nozzle plate compared to the microstructure of deposits formed at 20cm distance (Figure 7.5).

Figure 7.6 shows SEM micrographs of IA spray deposited samples at 20cm from the nozzle plate and a 655 μ m particle IA in nitrogen. Figure 7.6 shows that the microstructure of D2 tool steel spray deposits is coarser but has similar features to the IA D2 tool steel powder particles. It contains the primary phase dendrite, and between the dendrites, a eutectic structure has been formed. According to XRD results, the primary phase should be non-equilibrium retained austenite. Higher magnification of the eutectic structure is also shown in Figure 7.6.b which consists of layers of M_7C_3 carbides and austenite.

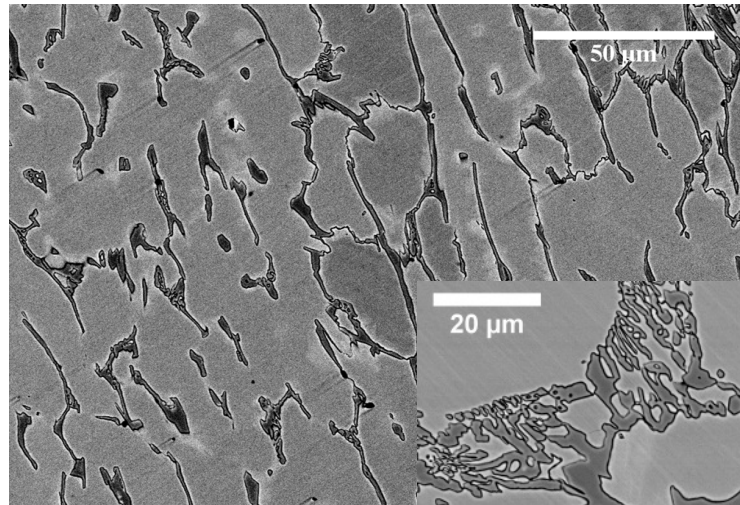


(a)

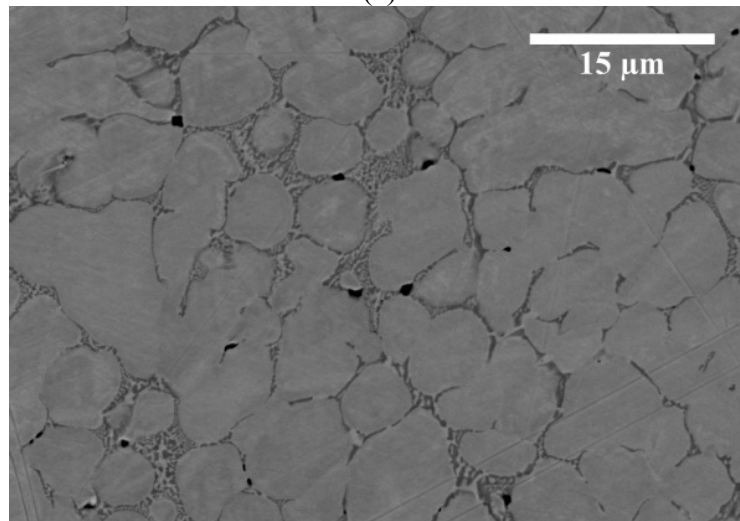


(b)

Figure 7.5. OM images of IA spray deposits at (a) 20cm and (b) 28cm distances from nozzle plate.



(a)



(b)

Figure 7.6. BSE-SEM micrograph of IA spray deposits, (a) 2810 and (b) 2010 samples.

Another factor which is effective in the size of microstructure is the height of the deposit. In fact, the distance from the cooling media (heat sinks) is a factor in the cooling rate and size of the microstructure in the deposits. As an example, Figure 7.7 shows the OM microstructure of 201000 sample at different parts of the sample, from the bottom to the top. The arrow shows the direction from bottom to top part of the sample.

As can be seen in Figure 7.7, the microstructure of the samples is fine in the regions that are close to the substrate. By going toward top part of the sample, microstructure gets coarser. Again, the area close to the top part of deposit has finer microstructure.

When the falling droplets first hit the substrate, substrate is cold (about 40°C) and fine microstructure forms. After deposition of some layers, since droplets are hot when they hit the substrate (according to the model, droplets with 360µm diameter have temperature about 1340°C), temperature of the substrate goes up and this causes a lower cooling rate for the rest of the droplets. Finally, droplets falling on top part of the deposit are in contact with the cooling atmosphere and this causes a higher cooling rate compare to the lower parts of deposits and therefore the microstructure gets finer. Since the microstructure is much finer at the bottom part compared the top part, it can be concluded that the cool substrate is more effective on the cooling rate compared to that from cooling media.

7.2.3.2. Quantitative analysis

- Secondary dendrite arm spacing and cooling rate

Figure 7.8 shows secondary dendrite arm spacing of different IA spray deposited samples at different heights of deposits. SDAS of individual IA droplets in nitrogen with different diameters are also shown in this figure.

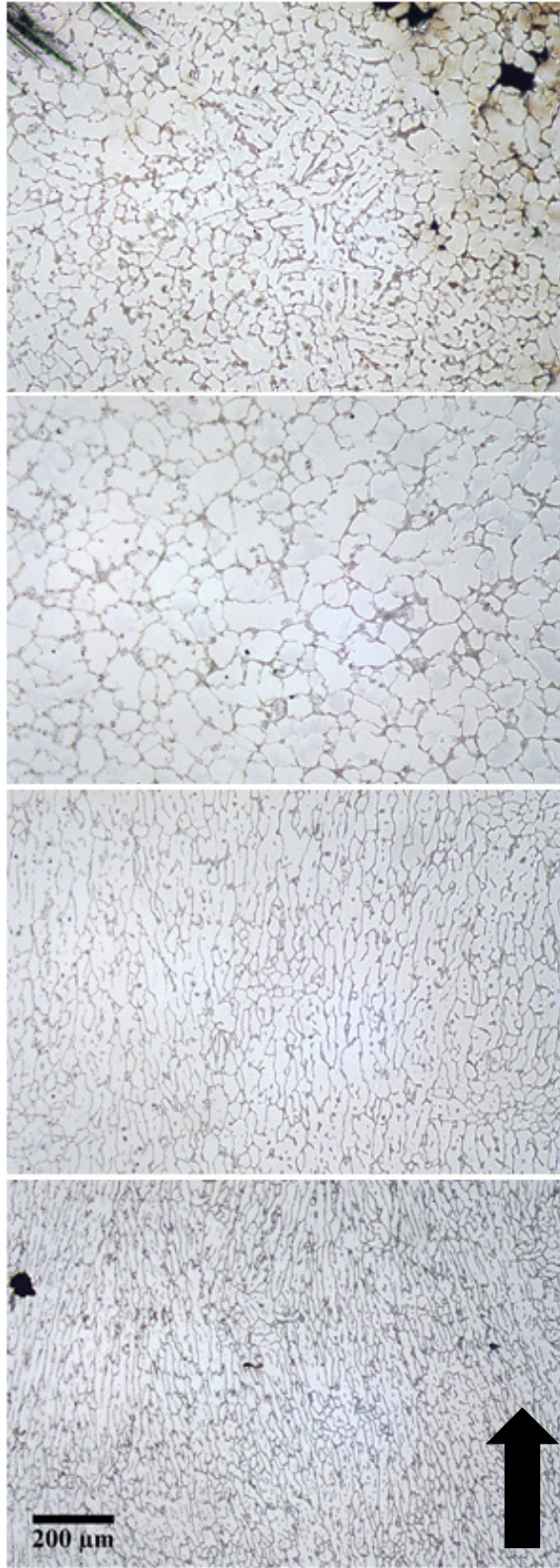
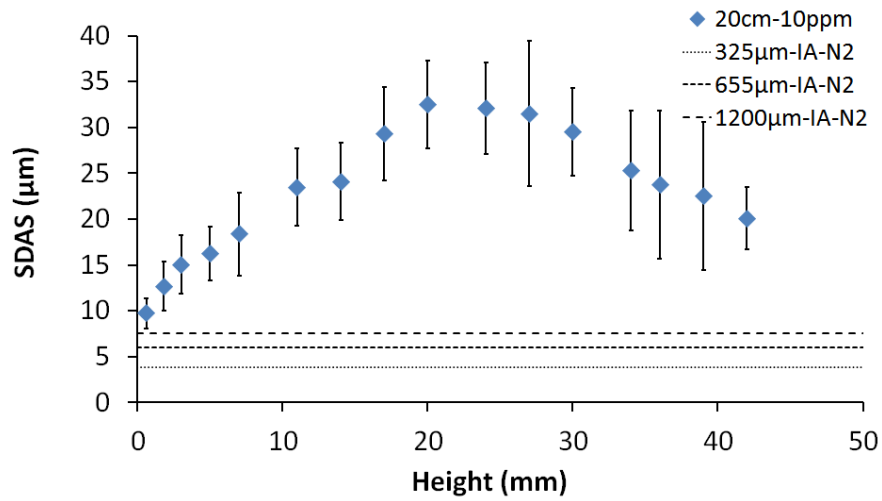
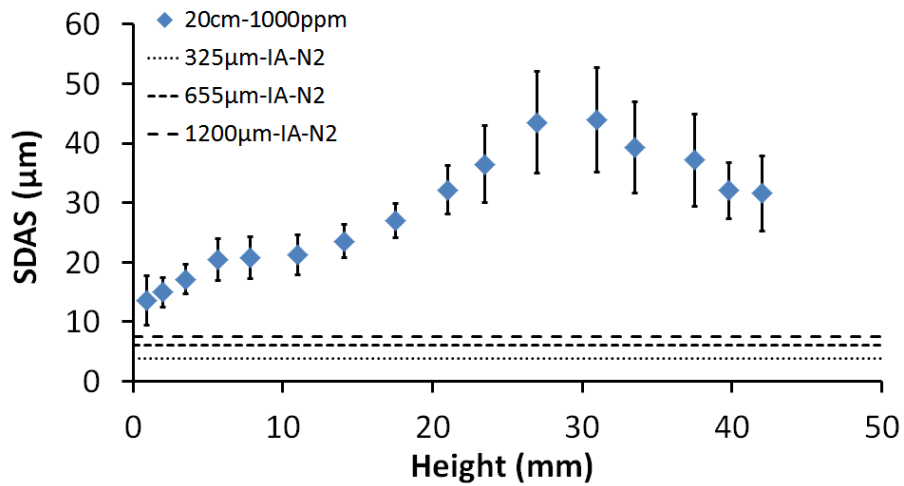


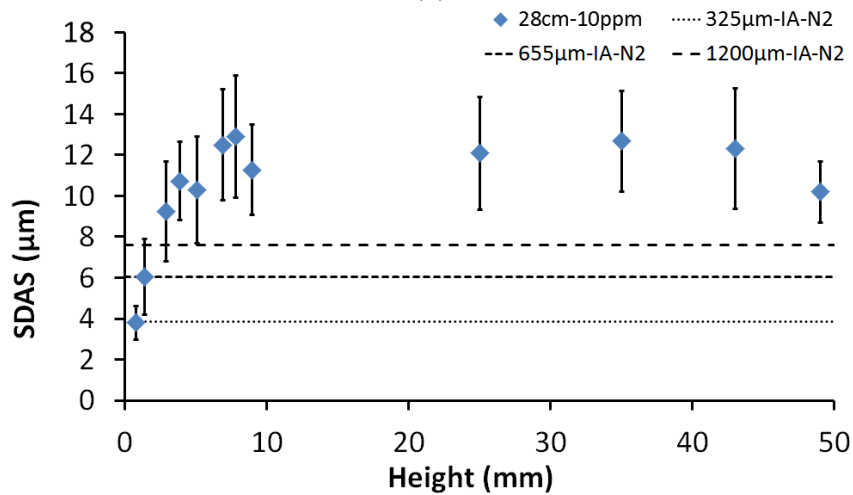
Figure 7.7. OM o IA spray deposited sample at 28cm from the bottom of the sample to the top. The arrow shows the direction to the top part of the sample.



(a)



(b)



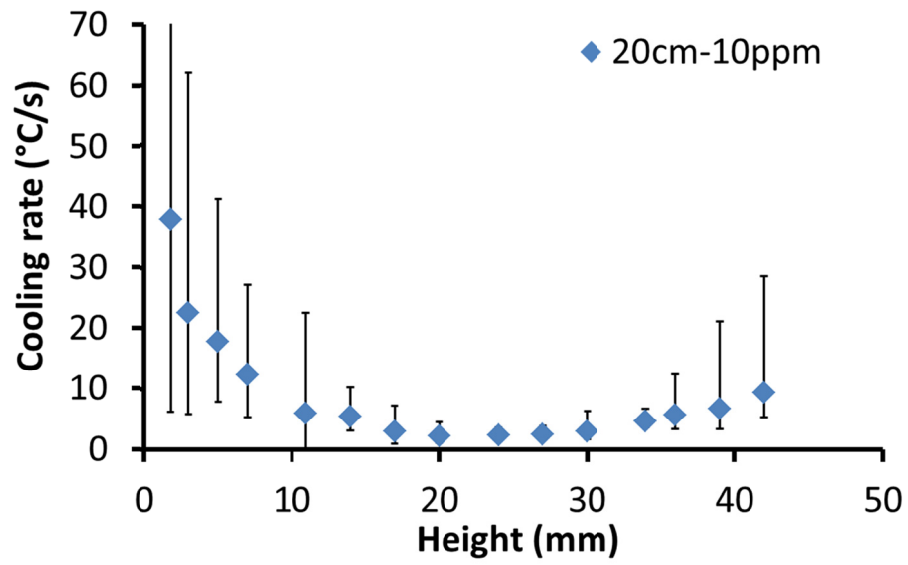
(c)

Figure 7.8. SDAS at the center line of the deposits for (a) 2010, (b) 201000 and (c) 2810.

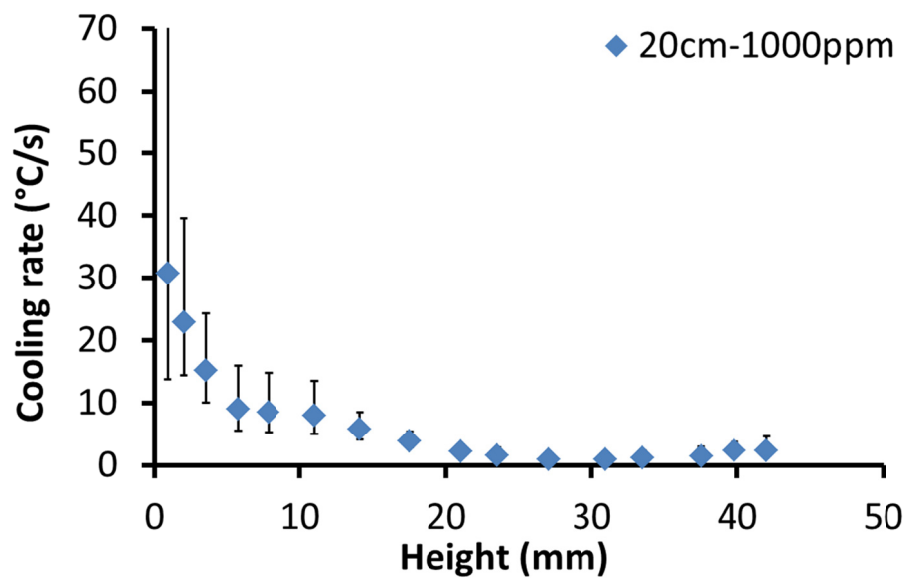
SDAS values of spray deposit samples confirms qualitative observation that microstructure is finer at the bottom of the sample and coarsen by going toward top part of the sample. At the regions close to the top part of deposits, SDAS is slightly decreasing.

Comparing SDAS for different IA droplets (reported in Table 4.2) with SDAS at different heights of spray deposits, it can be clearly seen that, based on IA droplet size and height of spray deposits, the cell spacing in spray deposits is nearly 2-10 times larger than those for powders. This is further confirmed by the model predictions of the cooling rate of a spray deposit in IA reported by Ellendt et al. [68]. In this work, a mathematical model of the cooling at the mid-section of a spray formed Cu-6Sn IA ingot was developed. It was reported that when the substrate thickness is 1mm, the maximum cooling rate of the deposit adjacent to the substrate at the mid-section is 2.5°C/s. This is two orders of magnitude smaller than the coarsest droplet size (1mm) cooling in a gas in IA [21,78].

The cooling rate of the spray deposits were measured at different heights from the bottom of the deposit using SDAS values. This was done using $\lambda=B(dT/dt)^{-n}$, where λ is SDAS in μm , dT/dt is cooling rate in $^{\circ}\text{C}/\text{sec}$ and B and n are constants equal to 42.1 and 0.33, respectively. Figure 7.9 shows cooling rate as a function of height from the bottom of the IA spray deposits.



(a)



(b)

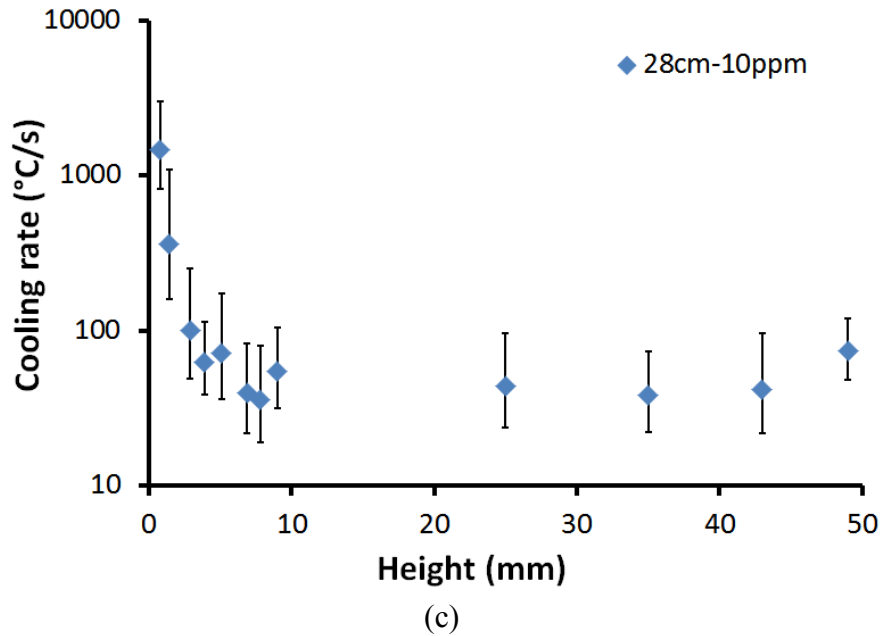


Figure 7.9. Cooling rate of IA and GA spray deposits as a function of height of deposits. (a) 2010, (b) 201000 and (c) 2810.

Cooling rate is high in the bottom of the deposit and then it decreases by increasing the height of the deposit and again at an area close to the tip of deposit, cooling rate increases a little bit. A high cooling rate at the bottom of the deposit can be related to a high degree of heat extraction through the cool substrate. At the top of the deposit, the cooling rate is also a bit higher since the deposit is in touch with the cooling atmosphere, but still much less than heat conduction at the bottom of the deposit. Ellendt et al. [68] showed that by increasing the height of the deposit, the solidification rate of IA spray deposited Cu-Sn alloy also decreases. This is due to less heat transfer at higher height of the deposit. Slightly higher solidification rate at the top of their spray deposits was related to the fact that at the end of atomization, melt flow slightly decreases which leads to a

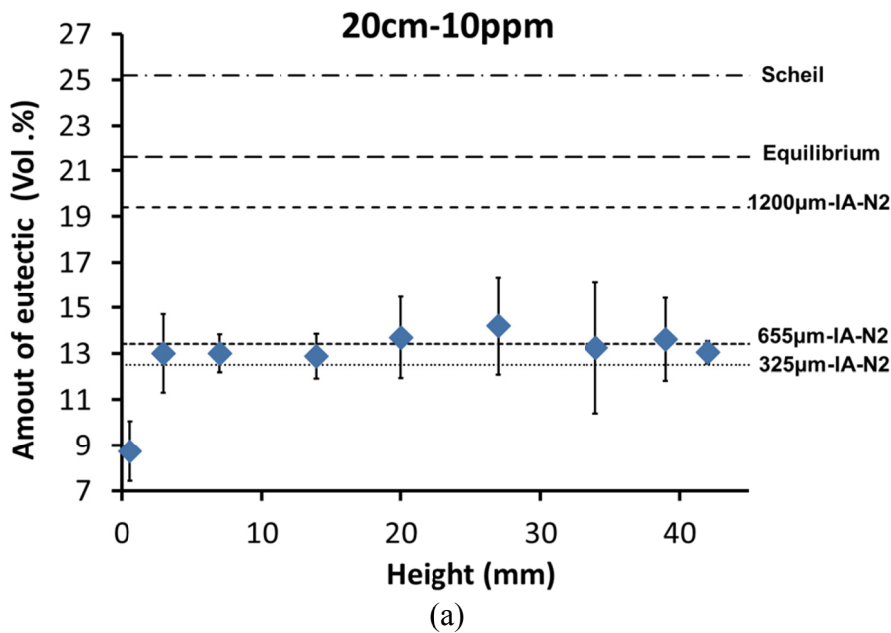
decrease in the heat flow and increase in solidification rate. This is much less than the heat flow that happens due to conduction from substrate material.

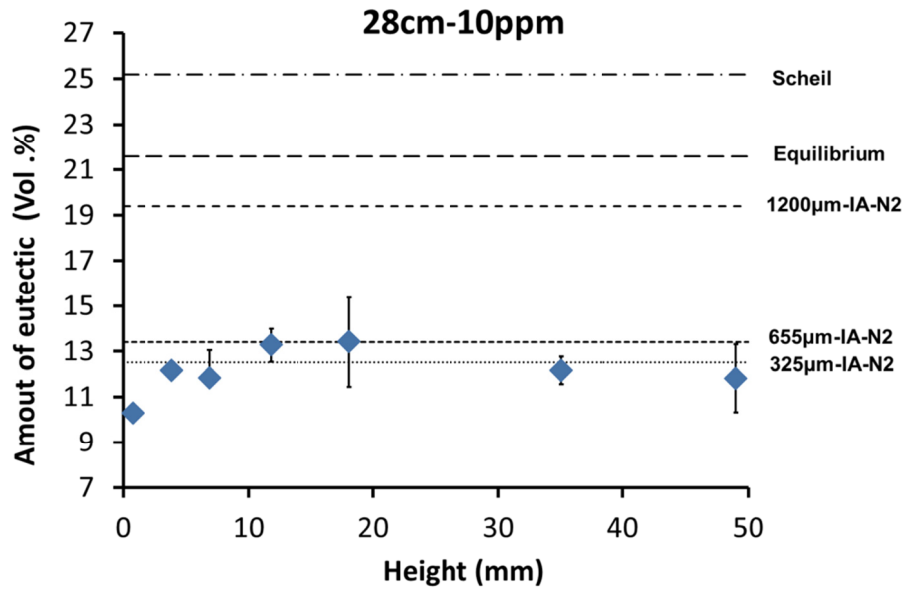
As discussed before, droplets that hit the substrate at 20cm should have a higher temperature and more liquid than the droplets that reach the substrate at 28cm. So, cooler droplets hit the substrate or deposit at higher distances should result in less enthalpy to be removed from the deposit and should have more solid formed in the droplets prior to deposition. As a result, a higher cooling rate is experienced for deposits that form at 28cm than that in 20 cm deposits. This yields a finer microstructure in deposits spray at 28cm of the nozzle plate compared to the microstructure of deposits formed at 20cm distance. Figure 7.8 shows average SDAS values of 32 μm , 12 μm and 40 μm in 2010, 2810 and 201000 deposits, respectively, at the height of 25-30cm. This also quantitatively confirms finer microstructure in the deposit formed at higher distance from the nozzle plate. Also, SDAS values of all spray deposit samples showed that microstructure is finer at the bottom of the sample and coarsen by going toward top part of the sample. At the regions close to the top part of deposits, SDAS is slightly decreasing. By comparison, SDAS in the largest particle size (1200 μm atomized in nitrogen) was reported to be less than 8 μm (Figure 7.8). SDAS gets even smaller for smaller particle sizes. Comparing SDAS in the spray deposits and individual droplets indicates that there is much higher cooling rate in the individual droplets compared to

the spray deposits resulting in a finer microstructure in the individual droplets.

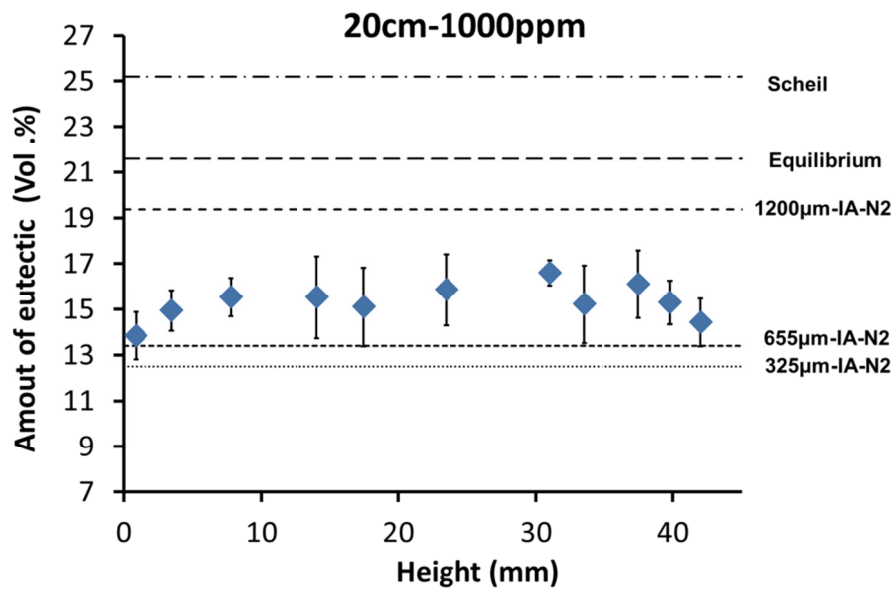
- Volume fraction of eutectic

Volume fraction of eutectic in different heights of spray deposits were measured using image analysis of SEM micrographs. Eutectic fractions of IA droplets as well as eutectic equilibrium value and Scheil prediction of eutectic fraction are also shown in Figure 7.10. It is evident that in all spray deposited samples, the eutectic fraction is nearly the same to the IA powders of 655 μm and 325 μm atomized in nitrogen. The eutectic fractions are significantly lower than either equilibrium or Scheil-Gulliver predictions.





(b)



(c)

Figure 7.10. Eutectic volume fraction of impulse atomized deposits, (a) 2010 sample, (b) 2810 sample and (c) 201000 sample.

Eutectic fraction in the spray deposits is considerably different from either equilibrium values or Scheil-Gulliver calculation as shown in Figure 7.10, while eutectic fraction in spray deposits (mostly 2010 and

2810) is nearly the same as that in particles with 325 μm and 655 μm . This will be discussed further in the discussion section. The 201000 sample also has a higher fraction of eutectic compared to the 2010 sample. Eutectic fraction and undercooling measurements have been done on the wide range of droplets (from 325 μm to 1200 μm). Yuan [152] reported that during IA of Zn-Pb alloy, IA in the air would result in formation of larger powders compared to IA in a nitrogen environment. The reason given was that by formation of the oxide layer on the liquid droplets, droplets cannot breakup further due to Rayleigh instability. As a result, larger droplets are expected in the 201000 sample. These will also have lower cooling rate in the spray deposit and larger eutectic fraction compared with the 2010 and 2810 samples.

Assuming equilibrium phase diagram (Figure 4.1), it is possible to estimate the required undercooling prior to nucleation of the eutectic by comparing the measured eutectic fraction values to the eutectic fractions predicted via metastable extensions of the liquidus and solidus lines below the equilibrium eutectic temperature. Metastable extension of liquidus and solidus lines were extracted using Thermocalc software version 5.0.4.75 using TCFE6 v.6 database for steels and Fe-alloys. The results are provided in Figure 7.11.

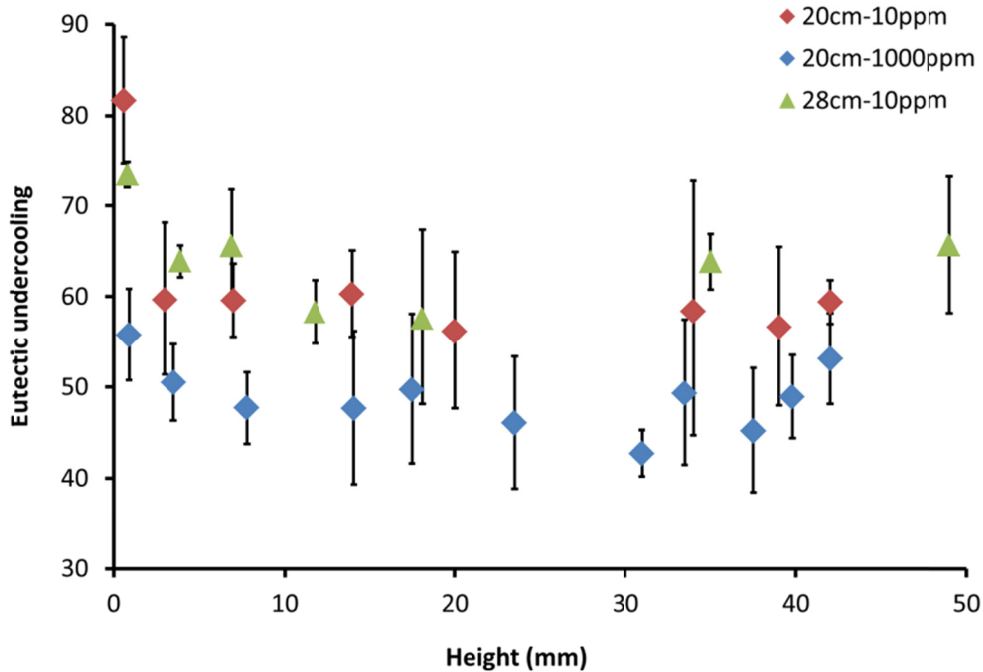


Figure 7.11. Eutectic undercooling of spray deposit as a function of height of samples.

According to Figure 7.2, fraction of solid in the falling droplets at 20cm and 28cm distance from nozzle plate is about 45% and 55%, respectively. Also, using experimental data and modeling calculations, it was found from Chapter 4 that, depending on the particle size, minimum 62 Vol.% of primary phase forms during recalescence. Therefore, at 20cm and 28cm distances from nozzle plate, eutectic transformation has not been initiated yet and it will start after semi-solid droplets are deposited on the substrate.

Although there is a difference between the cooling rate in powders and spray deposits, there is a similarity between the eutectic fraction of spray deposits and IA droplets. It can be seen in Figure 7.11 that a lower

amount of eutectic undercooling is achieved in the 201000 sample compared to the other samples which is due to its higher eutectic fraction. It can be seen that in Figure 7.11 in 2010 and 2810 samples, almost the same amount of eutectic undercooling has been achieved as 325 μm and 655 μm droplets atomized in nitrogen. These results suggest that the mechanism of eutectic undercooling is almost same in both spray deposits and droplets. Based on this mechanism, during solidification of the spray deposit, liquid remained in droplets cannot merge to each other as described by Henein as the Slushy Balloon Model (SBM) [69].

- Slushy Balloon Model

Briefly, this model can be explained as follows: oxygen content in the atomizing chamber results in formation of a nano-thick oxide layer on the falling droplets. Primary phase undercooling occurs while droplets are falling in the tower. Nucleation of the solid phase results in recalescence and growth of the primary phase. When the droplets hit the substrate, they still can have a significant amount of liquid (Figure 7.2). This depends on the size of the droplets, amount of superheat and falling distance. There is also a possibility that for fine droplets, due to their higher cooling rate, almost completely solidified droplets reach the substrate. The droplets will deform when they hit the substrate. But, the oxide layer on the droplets will not break in most of the droplets. Therefore, there would be some “droplet regions” in the deposit [69]. Solidification of these regions will be independent of adjacent regions, (not thermally independent). By further

cooling of the deposit, when the eutectic undercooling is achieved, eutectic formation will be started in each “droplet region”. In this mechanism, falling droplets are similar to the balloons filled with slush and therefore, Slushy Balloon Model (SBM) is the name for this mechanism. According to this model, there is no solute impact from the solute segregation of each region on the adjacent solidifying region. This model was successfully developed based on droplets and spray deposits of Cu-6Sn [68] and Al-0.61wt%Fe [37] using the IA method. Also, it has been noted that even for GA in which movement of droplets are very fast, the SBM model can be expected to occur. In GA spray deposition technique, droplets hit the substrate with higher speed and force. But, since GA particles are smaller compared to IA, oxide layer on the droplets will not be expected to break. As a result, in each droplet region formed due to GA, extended solubility and metastable phases can be also expected in each droplet region [69].

Further investigation on microstructure images of deposits shows the existence of some regions which can be attributed to the “droplet region” formed during spray deposition. Figure 7.12 shows OM images of 201000 and 2810 spray deposit samples. Some deformed-elongated sections have been formed in the sample perpendicular to the spray direction.

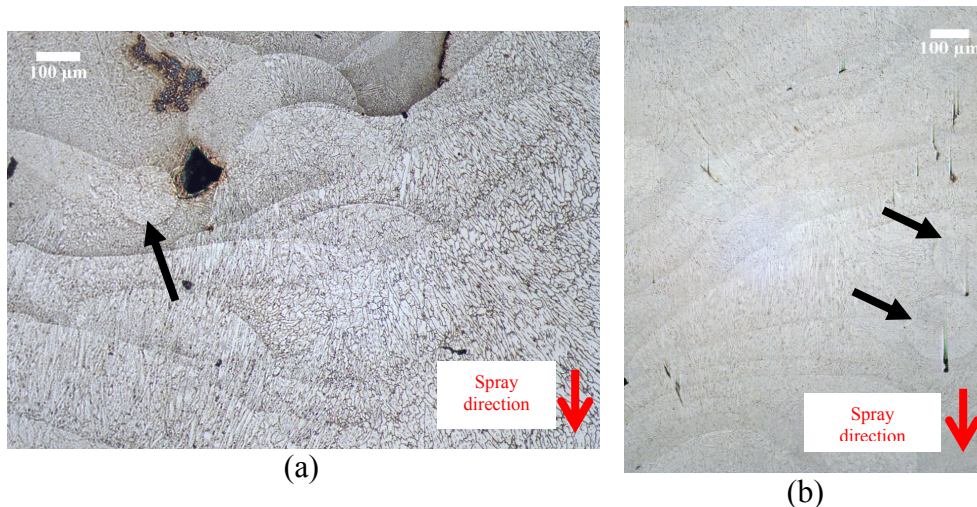


Figure 7.12. BSE-SEM micrograph of spray deposited samples at middle section of deposits, (a) 201000 and (b) 2810 samples. Red arrows show spray direction.

It seems that the deformed-elongated sections are those “droplet regions” which have been formed during falling of droplets and after reaching the substrate, they have been deformed. But the oxide coating has not been broken and results in solidification of slushy balloons inside the spray deposits. As mentioned before, the liquid fraction of falling droplets at the time when they hit the substrate is a function of different parameters, most importantly droplet size. Smaller droplets, due to their higher cooling rate, have a larger fraction solid at the time they reach to the deposit. There is a possibility that fine particles are completely solidified during free fall and when they reach the deposit, small solid powder particles are placed between the other deformed “droplet regions.” Arrows in Figure 7.12 show solid powders that have been trapped between layers of droplet regions in the spray deposits.

- Hardness of IA spray deposits

Hardness of IA spray deposits at 20cm from nozzle plates has been measured in every 5mm² of the sample (Figure 7.13).

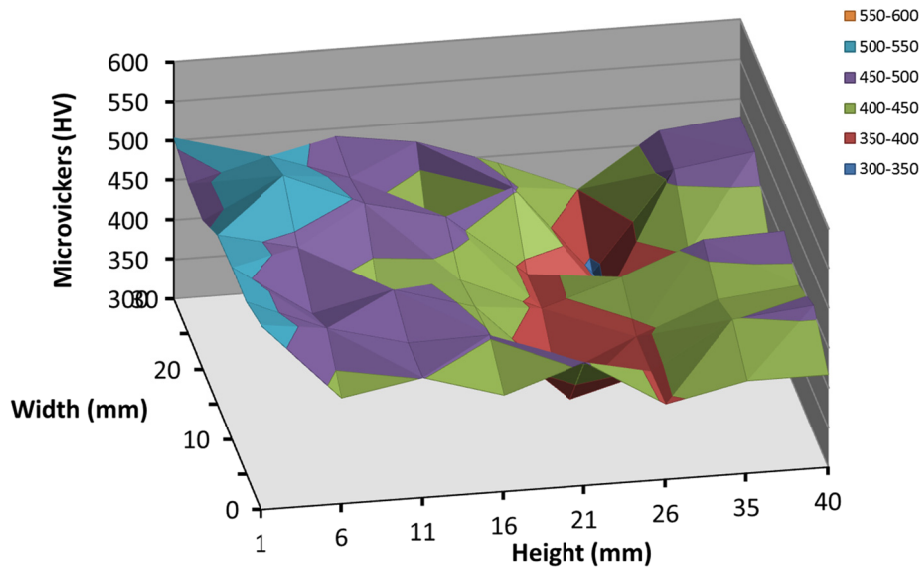


Figure 7.13. Hardness map of IA 2010 spray deposits.

The hardness map of 2010 sample shows that the hardness value is about 500Hv in the bottom part of the sample, where the deposit is in contact with substrate. By increasing the height of the sample, hardness decreases. This can be attributed to coarsening of SDAS in that direction. At top of the sample, again hardness increases a bit which again can be attributed to the finer microstructure at the top of the deposit due to the higher cooling rate as a result of cooling atmosphere.

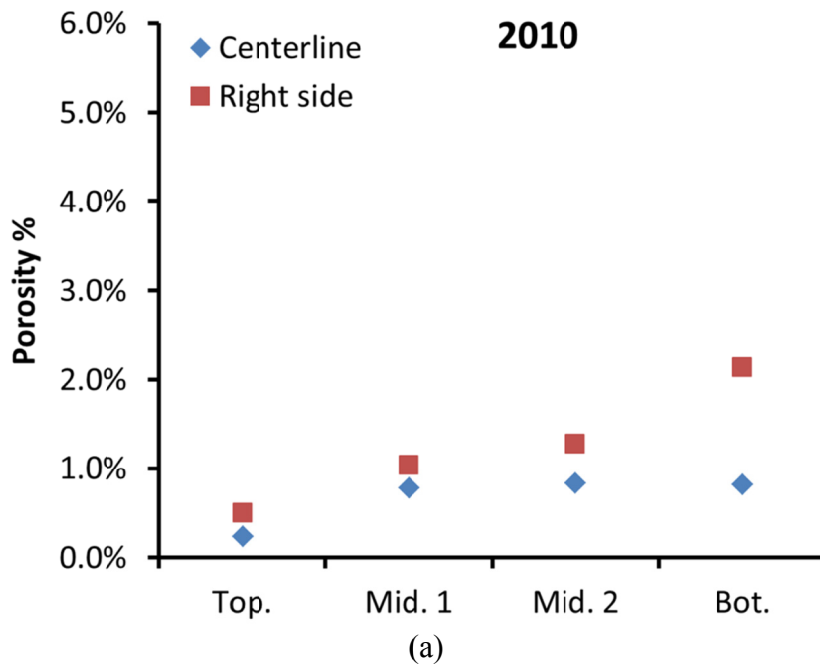
It was shown in Figure 6.31, hardness of as-atomized IA-655 μ m-nitrogen particles is about 410HV. By annealing this particle at 550°C for

two hours, hardness reached its maximum at about 650HV. Comparing the hardness of individual solidified as-atomized and annealed droplets with the hardness of spray deposits shows that hardness of spray deposits are higher than those for as-atomized droplets atomized in nitrogen, especially at the top and bottom of deposits where larger hardness value has been measured. In the 2010 sample, the average hardness value is in the range of hardness of 600-710µm-nitrogen particles annealed at 650°C. Note that the hardness measurement has been done on the as-received spray deposits, without any post-processing treatment. High hardness in spray deposits compared to individual annealed droplets is due to the fact that, as mentioned before, there is a self-annealing effect in the spray deposited sample which newly-hot deposited layers at the top of the previous layer heat the previous layers and can cause in partly-annealing of deposits which can increase hardness of deposits compared to as-atomized individual droplets. Since there is not enough time for complete annealing of deposits, due to heat dissipation from deposits, hardness of spray deposits do not reach to the maximum value that has been reported for IA-655µm-nitrogen. This shows that another short annealing of the deposits may result in a further increase in hardness. Further study is required to demonstrate this. This can be proposed as a future work to be confirmed.

- Porosity measurement of spray deposits

Figure 7.14 shows porosity of spray deposited samples at different heights in different locations of the samples. This figure shows that by going down

from top toward the bottom part of all spray deposits, porosity level also increases in both centerline and side of the deposits. Also, it can be seen that almost in all samples and locations, porosity level of right side (outer part of the deposits) is higher than that in the centerline (inner part of the deposits). Comparing Figure 7.14.a and Figure 7.14.c with Figure 7.14.b shows that overall porosity levels of sample 2010 are the lowest of the three samples. It can be seen that higher amount of oxygen during spray deposition results in higher amount of porosity in the samples deposited at 28cm from the nozzle plate. It seems in the atmosphere with higher amount of oxygen, the oxide film forming on the droplets is thicker and therefore the droplets cannot deform easily. This effect seems to be higher in the outer side of the deposits since droplets joining outer part of the deposit have larger surface area in contact with the atmosphere.



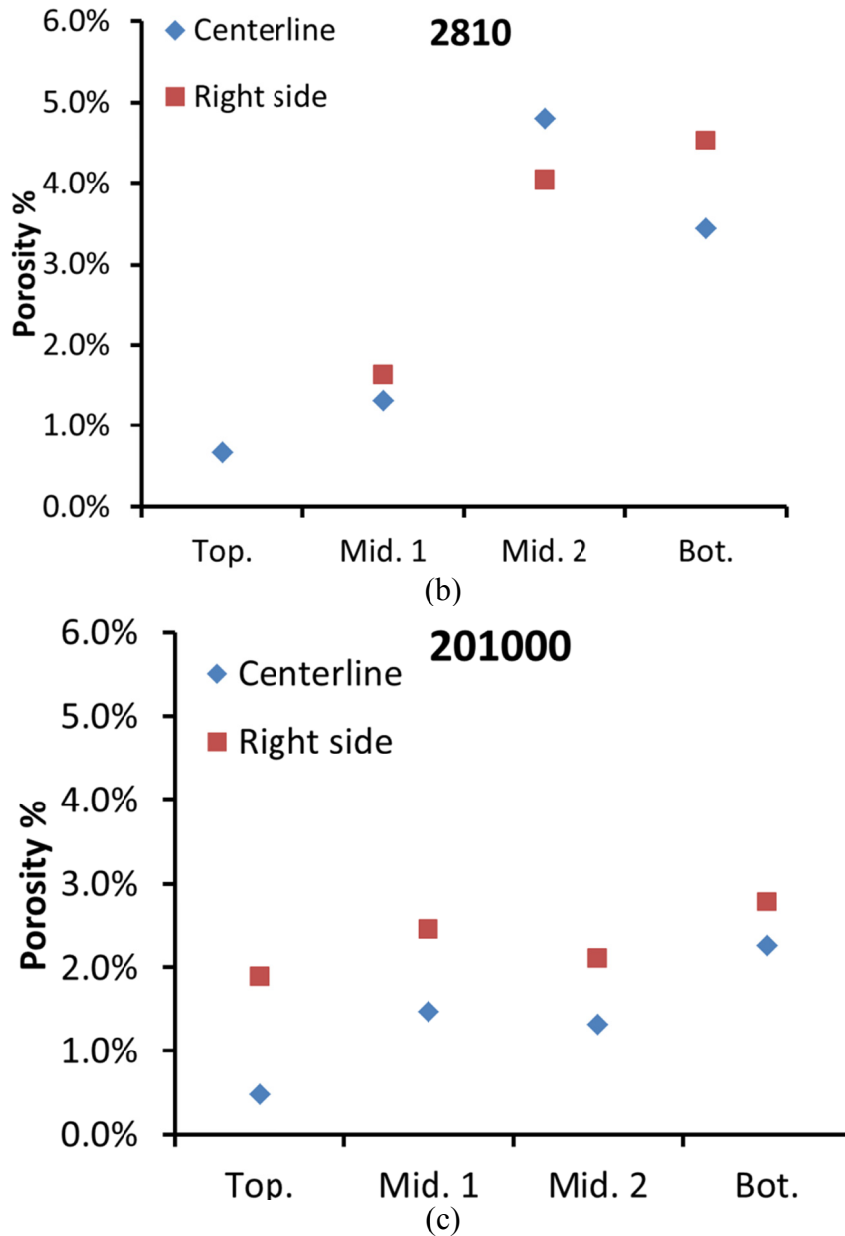


Figure 7.14. Porosity of D2 steel spray deposits at different locations according to the sample sectioning shown in Figure 3.9, (a) 2010 sample, (b) 2810 sample and (c) 201000 sample.

As discussed in Chapter 2, one of the main factors affecting the porosity level is the liquid fraction of droplets on deposition. Since falling droplets have larger liquid fraction lower porosity level is also expected in

the deposits formed in the lower distances. Also, there would be more liquid fraction in the droplets hitting the top part of the deposits compared to the ones contacting the substrate. Therefore, larger liquid fraction in the droplets makes it easier for droplet to deform when they hit the substrate and fill the spaces between the droplets which results in lower porosity level at the top part of the deposit compared to the bottom part.

According to Figure 7.14, porosity is increasing by increasing the radial distance from the centerline. If we assume that the droplet trajectory is perpendicular to the deposit surface in the center part of the deposit, there would be an impact angle where the droplets hit the outer part of the deposit. Uhlenwinkel and Ellendt [71] showed that there is a correlation between the porosity level and the impact angle. They reported that by going from centerline to outer part of the deposit, impact angle of the deposits increase. They showed that if the impact angle is below 25°, the porosity level is not affected. Porosity level scattering has been reported for the higher impact angles. In order to reduce the amount of porosity in the final product, higher values of impact angle should be avoided [71].

7.3. Summary

In this chapter, rapid solidification during spray deposition of D2 tool steel was investigated. Effect of different process parameters such as substrate distance and oxygen level was studied on the final microstructure and porosity level of deposits. Comparing with rapid solidification in individual IA droplets, it was shown that spray deposits have almost similar eutectic

undercooling values, although they have less cooling rates and coarser microstructure. Also, in the spray deposits, both austenite and ferrite phases and well as M_7C_3 carbides were formed. This is due to the tempering effect of new hot deposited layers on the previous layers. This also causes higher hardness in the spray deposits compared to that in the as-atomized droplets. Microstructural analysis of the deposits showed fine microstructure at the bottom of the deposits. This is attributed to the high cooling rate at the point adjacent to the cold substrate. Also, using slushy balloon model, it was possible to explain why eutectic fraction formed in the spray deposits is close to the value formed in the individual droplets.

In the next chapter, conclusions will be made on the rapid solidification of D2 tool steel based on all the information provided in the previous chapters, with some discussions about the results.

Chapter 8

8. Conclusion and future work

8.1 Conclusions

A microstructural investigation of D2 tool steel during rapid solidification has been carried out in this work. Effect of high undercooling and cooling rate values achieved using IA on the microstructure and properties of D2 tool steel was investigated. Characterization was then performed by electron microscopy to study the phase fraction formed during falling of different droplets sizes in helium or nitrogen media. The as-atomized microstructure of the powders contains primary retained austenite dendrites and eutectic of austenite and M_7C_3 carbides. Results showed that increasing the cooling rate (fine particles and/or helium cooling gas) reduces the amount of dendrite arm spacing. With a mean of D2 tool steel pseudobinary phase diagram and measured eutectic fraction from SEM, eutectic undercooling values could be calculated for particles with different cooling rates. It was found that in the droplets with higher amount of eutectic undercooling, less eutectic fraction was achieved during solidification. Combination of eutectic undercooling values and dendrite coarsening model, it was possible to calculate primary phase undercooling reached during solidification of falling droplets. It was also found that higher amount of primary undercooling resulted in formation of finer microstructure. The primary phase undercooling values were then used during online measurement of falling droplets characteristics.

Since measurement of actual undercooling and cooling rate of the falling droplets has long been a goal for scientists working on melt atomization, systematic measurement of particle in-flight characteristics also performed at various heights, in order to investigate the sensitivity of the measurement devices (Chapter 5). The result of such measurements coupled with the phase fraction analysis can improve the accuracy of the solidification model. DPV-2000 and shadowgraph were used in order to collect radiant energy, droplet size and velocity of the falling droplets of D2 steel. A heat loss model was then utilized with the droplets characteristics measured by online measurement devices and primary phase undercooling values from microstructural evaluation study. As a result, it was possible to find the temperature of specific particle size at the end of the recalescence. In a proposed future work, using this temperature, one can calculate fraction of primary phase formed after recalescence using Scheil method. Using measured fraction of total primary phase (from SEM analysis) and calculated fraction of primary phase after recalescence (from Scheil equation), fraction of primary phase formed during recalescence can be calculated. The advantage of this method is to understand the temperature behaviour of droplets and recalescence fraction, without using assumption and complexity of microsegregation model.

In Chapter 6, effect of undercooling and cooling rate during rapid solidification of droplets was investigated on the carbide precipitation and phase transformation during annealing. As described in Chapter 4, eutectic

and primary phase undercooling have important effect on the amount of superstation of the primary phase with alloying elements. Amount of supersaturation at room temperature then can be correlated to the amount of primary and eutectic undercooling during solidification of IA droplets (Figure 8.1). This figure shows that increasing the primary phase and eutectic undercooling results in increasing the amount of supersaturation inside the primary phase as a result of rapid solidification. This figure shows that the effect of eutectic undercooling on the supersaturation of primary phase is higher than that from primary phase undercooling. It shows that for achieving specific amount of supersaturation, lower amount of eutectic undercooling is required compared to primary phase undercooling.

Amount of supersaturation of alloying elements inside the primary phase then can be attributed to the precipitation behaviour of particles during the annealing cycles.

It was shown that the amount of austenite to ferrite transformation during annealing is smaller in the powders with higher undercooling and cooling rate. It was shown that supersaturated alloying elements increase the atoms' diffusive energy which results in changing the transformation temperature toward the higher temperature. As soon as precipitation of secondary carbide begins, destabilization of austenite occurs by depleting the carbon and chromium content of the matrix next to the precipitated carbides. Since powder particles with higher undercooling and cooling rate

have higher amount of supersaturation, precipitates then grow fast which results in coarser carbide precipitates at the end of tempering process. Hardness evaluation of the annealed powders showed that highest amount of hardness occurs at a temperature in which fine precipitate of carbide formed with larger fraction. The temperature at which maximum hardness occurs is shifting to the higher temperatures by increasing the undercooling and cooling rate of the solidified droplets.

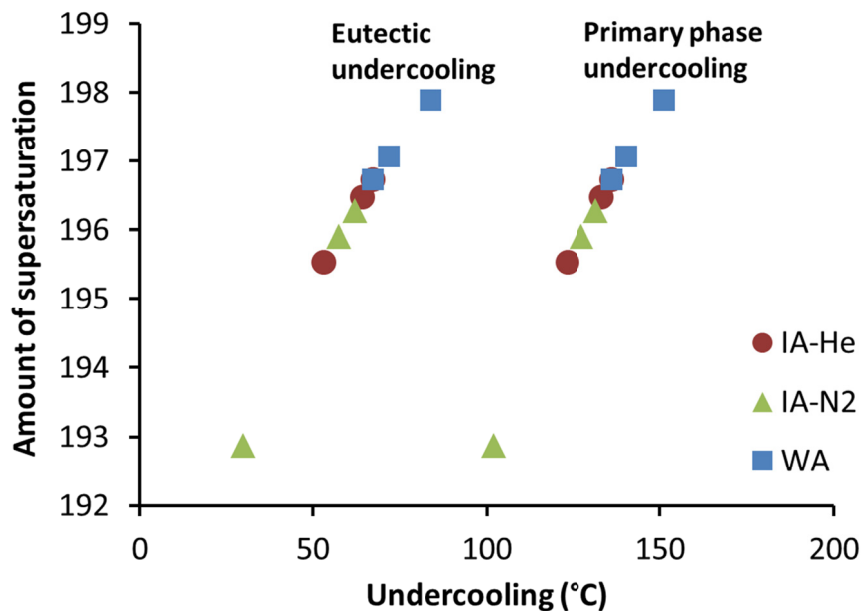


Figure 8.1. Effect of primary phase and eutectic undercooling on the amount of supersaturation of the primary phase.

The information developed in Chapters 4 to Chapters 6 from a rapid solidification method with high undercooling and cooling rate, undercooling values was then used to develop new casting methods, such as spray forming, as described in Chapter 7. During spray deposition of D2 tool

steel, undercooling values similar to individual droplet solidification achieved. This results in formation of almost same amount of eutectic as compared to individual droplets. But since there is lower cooling rate in spray deposition compared to atomization, coarser microstructure is formed in spray deposits. Also, in the spray deposits, both austenite and ferrite phases and well as M_7C_3 carbides were formed. This is due to the new hot deposited layers which cause in-situ tempering of the layers. This effect can be compared with the tempering effect of new welding passes which tempers previous passes of a weld. Hardness of spray deposits is higher than those for as-atomized droplets which is due to the self-annealing effect in the spray deposits. Microstructural analysis of the deposits showed fine microstructure at the bottom of the deposits which is attributed to the high cooling rate at the point adjacent to the cold substrate. Also, eutectic fraction formed in the spray deposits is close to the value formed in the individual droplets which can be explained using Slushy Balloon Model.

With a quantitative study, correlation between undercooling and cooling rate and the microstructure and heat treatment behaviour of rapidly solidified D2 tool steel was investigated in this work. This could help to better understand and develop new near-net shape techniques in order to have advantages of rapid solidification in the final product.

Based on the data developed in this study, it is possible to control the spray deposition parameters in a way that droplets with a specific size range are deposited on the substrate. Since annealing and hardness

behaviour of particles (with different size) annealed at different temperatures were studied in this work, it is possible to have the optimized heat treatment on the deposit (produced with specific size range). This results in getting reproducible and predictable mechanical properties from a spray deposit. Based on the results from the current study, it was found that medium-size powders (600-710 μm) atomized in nitrogen have highest hardness during annealing at 550°C. Also, it was found that at 20cm spray deposition distance, lowest porosity along with good hardness properties can be achieved in the deposit. Combining atomization of medium-size droplet on a substrate with 20cm distance from nozzle plate and annealing at 550°C can result in spray deposits with high mechanical properties along with low porosity values. Further studies need to be done on heat treatment and mechanical properties of spray deposit to be able to draw final conclusion.

8.2 Future work

Based on the finding of the present work, the following subjects would be recommended in particular for further studies:

1. Microsegregation modeling of high-carbon high-chromium steels in order to better understand and investigate effect of various degree of undercooling on the formed phases and transformations in the system.

2. Investigation of mechanical properties of the produced D2 steel bulk samples (either from spray deposition or powder metallurgy method), in order to understand effect of production and solidification parameters on

the final properties of the alloy in its application, especially wear properties and tensile strength.

3. Measurement of growth velocity as a function of different amount of undercooling values using low cooling rate-high undercooling technique (for example electromagnetic levitation). This will be beneficial in order to better understand effect of different levels of undercooling on the final properties.

References

- [1] D.A. Porter, K.E. Easterling, Phase transformations in metals and alloys, 2nd Editio, Chapman & Hall, London, 1992.
- [2] H.D. Brody, Microsegregation, Casting, in: ASM Handbook, Vol. 15, ASM International, 2008: pp. 338–347.
- [3] C. Beckermann, Macrosegregation, Casting, in: ASM Handb. , Vol. 15, ASM International, 2008: pp. 348–352.
- [4] W. Kurz, D.J. Fisher, Fundamentals of solidification, Enfield Publishing & Distribution Company, 1998.
- [5] A. Prasad, Microsegregation studies of rapidly solidified binary Al–Cu alloys, University of Alberta, 2006.
- [6] D. Eskin, Q. Du, D. Ruvalcaba, L. Katgerman, Experimental study of structure formation in binary Al–Cu alloys at different cooling rates, Mater. Sci. Eng. A. 405 (2005) 1–10.
- [7] G. Roberts, G. Krauss, R. Kennedy, Tool steels, 5th ed., ASM International, Ohio, 1998.
- [8] J. Blaha, C. Kremaszky, E.A. Werner, Carbide distribution effects in cold work tool steels, in: 6th Int. Tool. Conf., Karlstad, 2002: pp. 289–298.
- [9] Enrique J. Lavernia, Yue Wu, Spray atomization and deposition, Jown Wiley & Sons Ltd., Chichester, 1996.
- [10] K.H.J. Buschow, R.W. Cahn, M.C. Flemings, B. Ilschner, E.J. Kramer, S. Mahajan, Encyclopedia of Materials - Science and Technology, Volumes 1-11, (2011) 9384–9389.
- [11] A. (Ayooq) Arain, Heat treatment and toughness behaviour of tool steels (D2 and H13) for cutting blades, University of Toronto, 1999.
- [12] R. Wilson, Metallurgy and Heat Treatment of Tool Steels, Mcgraw-Hill Publication, 1975.
- [13] M. Behúlová, M. Lipták, P. Grgač, W. Löser, H.-G. Lindenkreuz, Comparison of microstructures developed during solidification of undercooled tool steel in levitation and on a substrate, J. Phys. Conf. Ser. 144 (2009) 012099.

- [14] A. Lesko, E. Navara, Microstructural Characterization High-Carbon Ferrochromium, *Mater. Charact.* 36 (1996) 349–356.
- [15] D. Viale, J. Béguinot, F. Chenou, G. Baron, Optimizing microstructure for high toughness cold-work tool steels, in: 6th Int. Tool. Conf., Karlstadt, 2002: pp. 299–318.
- [16] M. Durand-Charre, *The Microstructure of Steel and Cast Iron*, Springer, 2004.
- [17] A.M. Bayer, T. Vasco, L.R. Walton, Wrought Tool Steels, Properties and Selection: Irons, Steels, and High-Performance Alloys, in: *ASM Handb.*, ASM International, 1990: pp. 757–779.
- [18] M. Boccalini, H. Goldenstein, Solidification of high speed steels, *Int. Mater. Rev.* 46 (2001) 92–115.
- [19] W. Püttgen, B. Hallstedt, W. Bleck, P.J. Uggowitzer, On the microstructure formation in chromium steels rapidly cooled from the semi-solid state, *Acta Mater.* 55 (2007) 1033–1042.
- [20] M.C. Flemings, *Solidification processing*, 1st Editio, Mcgraw-Hill, 1974.
- [21] J.B. Wiskel, K. Navel, H. Henein, E. Maire, Solidification study of aluminum alloys using impulse atomization: part II. effect of cooling rate on microstructure, *Can. Metall. Q.* 41 (2002) 193–204.
- [22] D.M. Herlach, Metastable materials solidified from undercooled melts, *J. Phys. Condens. Matter.* 13 (2001) 7737.
- [23] T.Z. Kattamis, M.C. Flemings, Dendrite structure and grain size of undercooled melts, *Trans. TMS-AIME.* 236 (1966) 1523–1532.
- [24] J. Li, Y. Zhou, G. Yang, Mechanical properties of undercooled Cu 70 Ni 30 alloy, *J. Mater. Sci.* 35 (2000) 5581–5585.
- [25] D. Herlach, D. Holland-Moritz, P. Galenko, *Metastable solids from undercooled melts*, Pergamon, 2007.
- [26] Y. Wu, T.J. Piccone, Y. Shiohara, M.C. Flemings, Dendritic growth of undercooled nickel-tin: Part I, *Metall. Trans. A.* 18 (1987) 915–924.
- [27] W.J. Boettinger, Microstructural variations in rapidly solidified alloys, *Mater. Sci. Eng.* 98 (1988) 123–130.

- [28] J. Perepezko, Solidification reactions in undercooled alloys, *Mater. Sci. Eng. A.* 179-180 (1994) 52–56.
- [29] N.H. Pryds, A.S. Pedersen, Rapid solidification of martensitic stainless steel atomized droplets, *Metall. Mater. Trans. A.* 33 (2002) 3755–3761.
- [30] N.H. Pryds, Rapid solidification of 12% Cr steel, Risø National Laboratory, Technical University of Denmark, 1997.
- [31] P.J. M. Pavlickova, D. Vojtech, P. Stolar, Properties of rapidly solidified niobium-alloyed tool steel, *Met. Mater.* 40 (2002) 126–134.
- [32] P. Grgac, R. Moravcik, M. Kusy, I. Toth, M. Miglierini, E. Illekova, Thermal stability of metastable austenite in rapidly solidified chromium–molybdenum–vanadium tool steel powder, *Mater. Sci. Eng. A.* 375-377 (2004) 581–584.
- [33] M. Behulova, R. Moravcik, M. Kusy, L. Caplovic, P. Grgac, L. Stancek, Influence of atomisation on solidification microstructures in the rapidly solidified powder of the Cr–Mo–V tool steel, *Mater. Sci. Eng. A.* 304-306 (2001) 540–543.
- [34] A.K. Bhargava, A.N. Tiwari, Some microstructure aspects of melt-spun D2 steel, *Trans. Indian Inst. Met.* 58 (2005) 41–47.
- [35] D. Das, a. K. Dutta, K.K. Ray, On the refinement of carbide precipitates by cryotreatment in AISI D2 steel, *Philos. Mag.* 89 (2009) 55–76.
- [36] T.S. Srivatsan, T.S. Sudarshan, Rapid solidification technology: an engineering approach, Technomic Publishing Company Inc., Pennsylvania, 1993.
- [37] H. Henein, V. Buchoud, R. Schmidt, C. Watt, D. Malakov, C. Gandin, et al., Droplet solidification of impulse atomized Al-0.61Fe and Al-1.9Fe, *Can. Metall. Q.* 49 (2010) 275–292.
- [38] J. Chen, U. Dahlborg, C.M. Bao, M. Calvo-Dahlborg, H. Henein, Microstructure evolution of atomized Al-0.61 wt pct Fe and Al-1.90 wt pct Fe alloys, *Metall. Mater. Trans. B.* 42 (2011) 557–567.
- [39] A.K. Bhargava, A.N. Tiwari, Effect of rapid solidification and heat treatment on D2 steel, *Int. J. Rapid Solidif.* 7 (1992) 51–66.

- [40] Hoganas, Hoganas handbook for metallography, <http://hoganas.com/Documents/Handbooks/Handbook%20No.6.pdf>.
- [41] J.G. Zhang, H. Bin Xu, H.S. Shi, J.S. Wu, D.S. Sun, Microstructure and properties of spray formed Cr 12 MoV steel for rolls, *J. Mater. Process. Technol.* 111 (2001) 79–84.
- [42] Metal Ravne d.o.o. steel selector, Cold work tool steel information, <http://www.metalravne.com/selector/steels/OCR12VMS.html>. (2011).
- [43] M.F. McGuire, Stainless steels for design engineers, in: ASM International, Materials Park, Ohio, 2008: p. 304.
- [44] P. V Morra, A.J. Böttger, E.J. Mittemeijer, Decomposition of iron-based martensite: a kinetic analysis by means of differential scanning calorimetry and dilatometry, *J. Therm. Anal. Calorim.* 64 (2001) 905–914.
- [45] H. Djebaili, H. Zedira, a. Djelloul, a. Boumaza, Characterization of precipitates in a 7.9Cr–1.65Mo–1.25Si–1.2V steel during tempering, *Mater. Charact.* 60 (2009) 946–952.
- [46] H.O. Andrén, S. Karagöza, C. Guangjun, L. Lundin, H. Fischmeister, Carbide precipitation in chromium steels, *Surf. Sci.* 246 (1991) 246–251.
- [47] T. Gladman, The physical metallurgy of microalloyed steel, The Institute of Materials, London, 1997.
- [48] V.N. Eremenko, V.R. Sidorko, Thermodynamic properties of chromium carbides, *Sov. Powder Metall. Met. Ceram.* 12 (1973) 395–398.
- [49] J. M.W. Chase, C.A. Davies, J.R. Downey, D.J. Frurip, R.A. McDonald, A.N. Syverud, JANAF thermochemical tables, in: *J. Phys. Chem. Ref. Data*, 3rd Editio, 1985.
- [50] D.R. Gaskell, Introduction to the thermodynamics of materials, 4th Editio, Taylor & Francis Publication, 2003.
- [51] H. Jones, Rapid solidification of metals and alloys, Institution of Metallurgists, 1987.
- [52] H.H. Liebermann, Rapidly solidified alloys: processes-structures-properties-applications, CRC Press, 1993.

- [53] H. Henein, Single fluid atomization through the application of impulses to a melt, *Mater. Sci. Eng. A.* 326 (2002) 92–100.
- [54] A. Ilbagi, Non-equilibrium containerless solidification of Al-Ni alloys, University of Alberta, 2012.
- [55] A.J. Yule, J.J. Dunkley, Atomization of metals for powder production and spray deposition, 2nd Editio, Oxford University Press Inc., New York, 1994.
- [56] A. Ünal, D.D. Leon, T.B. Gurganus, G.J. Hildeman, Production of aluminum and aluminum-alloy powder, metal powder production and characterization, in: *ASM Handbook*, Vol. 7, ASM International, 1998: pp. 148–159.
- [57] A. Ünal, Liquid break-up in gas atomization of fine aluminum powders, *Metall. Trans. B.* 20 (1989) 61–69.
- [58] J.J. Dunkley, D. Norval, Atomisation of ferroalloys, in: *Tenth Int. Ferroalloys Congr.*, Cape Town, 2004: pp. 541–547.
- [59] J. Ting, J. Connor, S. Ridder, High-speed cinematography of gas-metal atomization, *Mater. Sci. Eng. A.* 390 (2005) 452–460.
- [60] A. V Freyberg, H. Henein, V. Uhlenwinkel, M. Buchholz, Droplet solidification and gas-droplet thermal coupling in the atomization of a Cu-6Sn alloy, *Metall. Mater. Trans. B.* 34 (2003) 243–253.
- [61] P.R. Brewin, P.I. Walker, P.D. Nurthen, Production of high alloy powders by water atomization, *Powder Metall.* 29 (1986) 281–285.
- [62] J. Hamill, C. Schade, N. Myers, Water atomized fine powder technology, Cinnaminson, New Jersey, n.d.
- [63] A.J. Pinkerton, L. Li, The behaviour of water- and gas-atomised tool steel powders in coaxial laser freeform fabrication, *Thin Solid Films.* 453-454 (2004) 600–605.
- [64] D. Yuan, H. Henein, J. Fallavollita, Method for producing droplets, U.S. Patent 5,609,919, 1997.
- [65] A. Prasad, H. Henein, E. Maire, C. a. Gandin, X-ray tomography study of atomized Al-Cu droplets, *Can. Metall. Q.* 43 (2004) 273–282.

- [66] P. Mathur, D. Apelian, A. Lawley, Analysis of the spray deposition process, *Acta Metall.* 37 (1989) 492–443.
- [67] P.S. Grant, Spray forming, *Prog. Mater. Sci.* 39 (1995) 497–545.
- [68] N. Ellendt, R. Schmidt, J. Knabe, H. Henein, V. Uhlenwinkel, Spray deposition using impulse atomization technique, *Mater. Sci. Eng. A.* 383 (2004) 107–113.
- [69] H. Henein, Why is spray forming a rapid solidification process?, *Materwiss. Werksttech.* 41 (2010) 555–561.
- [70] P. Grant, W.. Kim, B. Cantor, Spray forming of aluminium-copper alloys, *Mater. Sci. Eng. A.* 134 (1991) 1111–1114.
- [71] V. Uhlenwinkel, N. Ellendt, Porosity in spray-formed materials, *Mater. Sci. Forum.* 534-536 (2007) 429–432.
- [72] D.J. Schaeffler, A. Lawley, D. Apelian, Spray casting of high-strength low-alloy steels, *Adv. Powder Metall.* 2 (1989) 161–186.
- [73] E.J. Lavernia, T. Ando, N.J. Grant, Structures and properties of lithium containing X2020 aluminum alloys produced by liquid dynamic compaction, in: *ASM's Int. Conf. Rapidly Solidified Mater.*, San Diego, California, 1986: pp. 29–44.
- [74] B.P. Bewlay, B. Cantor, The spray deposition of a stainless steel, in: *Rapidly Solidified Mater.*, 1986.
- [75] D. Apelian, A. Lawley, P. Mathur, Spray deposition: A fundamental study of droplet impingement, spreading and consolidation, Drexel University, 1989.
- [76] P.S. Grant, B. Cantor, Microstructure and thermal conditions during spray forming of Al-4%Cu, in: J.J. Moore, E.J. Lavernia, F.H. Froes (Eds.), *Adv. Synth. Eng. Struct. Mater.*, ASM International, 1993: p. 263.
- [77] S. Annavarapu, D. Apelian, A. Lawley, Processing effects in spray casting of steel strip, *Metall. Mater. Trans. A.* 19 (1988) 3077–3086.
- [78] J.B. Wiskel, H. Henein, E. Maire, Solidification study of aluminum alloys using impulse atomization part I. heat transfer analysis of an atomized droplet, *Can. Metall. Q.* 41 (2002) 97–110.

- [79] A. Prasad, S. Mosbah, H. Henein, C.-A. Gandin, A solidification model for atomization, *ISIJ Int.* 49 (2009) 992–999.
- [80] P. Delshad Khatibi, A. Ilbagi, D. Beinker, H. Henein, In-situ characterization of droplets during free fall in the drop tube-impulse system, *J. Phys. Conf. Ser.* 327 (2011) 012014.
- [81] J.H. Hattel, N.H. Pryds, J. Thorborg, P. Ottosen, A quasi-stationary numerical model of atomized metal droplets. I: Model formulation, *Model. Simul. Mater. Sci. Eng.* 7 (1999) 413–430.
- [82] J. Lu, Quantitative microstructural characterization of microalloyed steels, University of Alberta, 2009.
- [83] J.B. Wiskel, D.G. Ivey, H. Henein, The effects of finish rolling temperature and cooling interrupt conditions on precipitation in microalloyed steels using small angle neutron scattering, *Metall. Mater. Trans. B.* 39 (2007) 116–124.
- [84] Sadiq Shah, Strategy for selecting analytical approaches, in: *ASM Handbook, Vol. 13A*, ASM International, Western Illinois University, 2003: pp. 992–998.
- [85] W.B. Yelon, F.K. Ross, A.D. Krawitz, Neutron diffraction, in: *ASM Handb.*, Vol. 10, ASM International, 1986: pp. 420–426.
- [86] R.J. Hill, C.J. Howard, Quantitative phase analysis from neutron powder diffraction data using the Rietveld method, *J. Appl. Crystallogr.* 20 (1987) 467–474.
- [87] A. Prasad, H. Henein, K. Conlon, Quantification of microsegregation during rapid solidification of Al-Cu powders, *Metall. Mater. Trans. A.* 37 (2005) 1589–1596.
- [88] A. Ilbagi, H. Henein, A.B. Phillion, Phase quantification of impulse atomized Al68.5Ni31.5 alloy, *J. Mater. Sci.* 46 (2010) 6235–6242.
- [89] Standard specification for woven wire test sieve cloth and test sieves, *ASTM Stand. E11.* (2013) 1–9.
- [90] R.T. DeHoff, F.N. Rhines, Quantitative microscopy, 1st editio, McGraw-Hill Book Company, New York, 1968.
- [91] Argonne National Laboratory: Advanced Photon Source, Technical Description of Beamline 11-BM: High Resolution Powder Diffraction, [Http://11bm.xor.aps.anl.gov/description.html](http://11bm.xor.aps.anl.gov/description.html).

- [92] Argonne National Laboratory: Advanced Photon Source, Beamline 11-BM: High Resolution Powder Diffraction-Sample Preparation for Mail-In Users., Http://11bm.xray.aps.anl.gov/users_prep.html.
- [93] Standard test methods for density of compacted or sintered powder metallurgy (PM) products using archimedes ' principle, (2013) 1–7.
- [94] Tecnar Automation Ltée, DPV-2000 calculation principles, 2011.
- [95] Tecnar Automation Ltée, Individual particle characterization device for thermal/cold Spray processes, <http://tecnar.com/index.php/dpv-Evolution>.
- [96] Y. Luan, N. Song, Y. Bai, X. Kang, D. Li, Effect of solidification rate on the morphology and distribution of eutectic carbides in centrifugal casting high-speed steel rolls, *J. Mater. Process. Technol.* 210 (2010) 536–541.
- [97] Y. Dai, M. Yang, C. Song, Q. Han, Q. Zhai, Solidification structure of C2.08Cr25.43Si1.19Mn0.43Fe70.87 powders fabricated by high pressure gas atomization, *Mater. Charact.* 61 (2010) 116–122.
- [98] A. Ilbagi, P. Delshad Khatibi, H. Henein, C.A. Gandin, D. Herlach, Quantification of primary phase undercooling of rapidly solidified droplets with 3D microtomography, in: *Int. Conf. 3D Mater. Sci.*, TMS, Seven Springs, Pennsylvania, 2012.
- [99] P. Grgac, M. Liptak, M. Behulova, L. Caplovic, H.-G. Lindenkreuz, W. Löser, Influence of melt undercooling on the microstructure of levitated Cr–Mo–V tool steel, *Mater. Sci. Eng. A.* 449-451 (2007) 658–661.
- [100] M. Behúlová, M. Lipták, P. Grgač, W. Löser, H.-G. Lindenkreuz, Comparison of microstructures developed during solidification of undercooled tool steel in levitation and on a substrate, *J. Phys. Conf. Ser.* 144 (2009) 012099.
- [101] K.Y. Benyounis, O.M. Fakron, J.H. Abboud, Rapid solidification of M2 high-speed steel by laser melting, *Mater. Des.* 30 (2009) 674–678.
- [102] A. Bogno, P. Delshad Khatibi, H. Henein, C.A. Gandin, Quantification of primary dendritic and secondary eutectic undercoolings of rapidly solidified Al-Cu droplets, in: *Mater. Sci. Technol. 2013, Symp. Light Met. Transp.*, Motreal, 2013.

- [103] P. Delshad Khatibi, H. Henein, A.B. Phillion, Microstructural investigation of D2 tool steel during rapid solidification, *Powder Metall.* 57 No.1 (2014) 70-78.
- [104] W.M. Rohsenow, J.P. Hartnett, *Handbook of heat transfer*, 3rd ed., McGraw-Hill, 1998.
- [105] L. Han, X. Nie, D. Northwood, H. Hu, Effect of cooling rates on the microstructure evolution and eutectic formation of as-cast Mg-Al-Ca alloys, in: *SAE World Congr. Exhib.*, Detroit, 2009.
- [106] H.F. Fischmeister, R. Riedl, S. Karagöz, *Solidification of high-speed tool steels*, 20 (1989).
- [107] A. Prasad, H. Henein, E. Maire, C. Gandin, Understanding the rapid solidification of Al-4.3Cu and Al-17Cu using x-ray tomography, *Metall. Mater. Trans. A.* 37 (2006) 249–287.
- [108] W. Kurz, R. Trivedi, Eutectic growth under rapid solidification conditions, *Metall. Trans. A.* 22 (1991) 3051–3057.
- [109] J.A. Sarreal, G.J. Abbaschian, The effect of solidification rate on microsegregation, *Metall. Trans. A.* 17 (1986) 2063–2073.
- [110] N.S. Miroshnichenko, *Quenching from the Liquid State (in Russian)*, Moscow, 1982.
- [111] R. Hashimoto, Y. Shibuta, T. Suzuki, Estimation of solid-liquid interfacial energy from gibbs-thomson Effect: a molecular dynamics study, *ISIJ Int.* 51 (2011) 1664–1667.
- [112] J. Miettinen, Thermodynamic-kinetic simulation of constrained dendrite growth in steels, *Metall. Mater. Trans. B.* 31 (2000) 365–379.
- [113] A. Bogno, P. Delshad Khatibi, H. Henein, C.A. Gandin, Quantification of primary and eutectic undercoolings of impulse atomized Al-Cu droplets, in: *Mater. Sci. Technol. 2013*, Montreal, Quebec, Canada, 2013.
- [114] C.A. Gandin, S. Mosbah, T. Volkman, D.M. Herlach, Experimental and numerical modeling of equiaxed solidification in metallic alloys, *Acta Mater.* 56 (2008) 3023–3035.

- [115] H. Mizukami, K. Hayashi, M. Numata, A. Yamanaka, Prediction of solid-liquid interfacial energy of steel during solidification and control of dendrite arm spacing, *ISIJ Int.* 52 (2012) 2235–2244.
- [116] S.J. Lee, Y.K. Lee, Quantitative analyses of ferrite lattice parameter and solute Nb content in low carbon microalloyed steels, *Scr. Mater.* 52 (2005) 973–976.
- [117] P. Delshad Khatibi, D.G. Ivey, H. Henein, Effect of rapid solidification and heat treatment on D2 tool steel, in: *TMS Annu. Meet.*, Orlando, FL, United States, 2012: pp. 505–512.
- [118] A.L. Genau, Microstructural development in Al-Si powder during rapid solidification, Iowa State University, 2004.
- [119] A. Prasad, H. Henein, Droplet cooling in atomization sprays, *J. Mater. Sci.* 43 (2008) 5930–5941.
- [120] S.K. N. Zeoli, S. Gu, Numerical modelling of metal droplet cooling and solidification, *Int. J. Heat Mass Transf.* 51 (2008) 4121–4131.
- [121] C. Cui, U. Fritsching, A. Schulz, Q. Li, Mathematical modeling of spray forming process of tubular preforms, *Acta Mater.* 53 (2005) 2775–2784.
- [122] LaVision, Sizing master manual, (2005).
- [123] J.P. Holman, Heat transfer, 8th Editio, McGraw Hill Inc., 1997.
- [124] Tecnar Automation Ltée, DPV-2000 reference manual, Saint-Bruno, Québec.
- [125] M. Arjomandi, H. Khorsand, S.H. Sadati, H. Abdoos, Prediction of martensite formation start temperature in steels using artificial neural networks, *Defect Diffus. Forum.* 273-276 (2008) 329–334.
- [126] G. Ghosh, G.B. Olson, Computational thermodynamics and the kinetics of martensitic transformation, *J. Phase Equilibria.* 22 (2001) 199–207.
- [127] G. Ghosh, G.B. Olson, Kinetics of BCC to FCC heterogenous martensitic nucleation: part I. The critical driving force for athermal nucleation, *Acta Metall. Mater.* 42 (1994) 3361–3370.

- [128] K. Kishitake, H. Era, F. Otsubo, Structures and tempering behavior of rapidly solidified high-carbon iron alloys, *Metall. Trans. A.* 22 (1991) 775–782.
- [129] R. Colaco, R. Vilar, Effect of laser surface melting on the tempering behaviour of DINX42Cr13 stainless tool steel, *Scr. Mater.* 38 (1997) 107–113.
- [130] J. Zou, T. Grosdidier, K. Zhang, C. Dong, Mechanisms of nanostructure and metastable phase formations in the surface melted layers of a HCPEB-treated D2 steel, *Acta Mater.* 54 (2006) 5409–5419.
- [131] T. Sourmail, C. Garcia-Mateo, Critical assessment of models for predicting the Ms temperature of steels, *Comput. Mater. Sci.* 34 (2005) 323–334.
- [132] C. Leguen, Prior austenite grain size controlled by precipitates, The National Institute of Applied Sciences of Lyon, 2010.
- [133] B. Dutta, E.J. Palmiere, C.M. Sellars, Modelling the kinetics of strain induced precipitation in Nb microalloyed steels, *Acta Mater.* 49 (2001) 785–794.
- [134] M. Li, Y. Wang, B. Han, W. Zhao, T. Han, Microstructure and properties of high chrome steel roller after laser surface melting, *Appl. Surf. Sci.* 255 (2009) 7574–7579.
- [135] M.Y. Li, Y. Wang, B. Han, The kinetics of phase Transformations during tempering in laser melted high chromium cast steel, *J. Mater. Eng. Perform.* 21 (2011) 1091–1098.
- [136] J. Wang, R.L. Zuo, Z.P. Sun, C. Li, H.H. Liu, H.S. Yang, et al., Influence of secondary carbides precipitation and transformation on hardening behavior of a 15 Cr–1 Mo–1.5 V white iron, *Mater. Charact.* 55 (2005) 234–240.
- [137] I. Swainson, Saskatchewan Research Council, Private communication, (2011).
- [138] H.M. Wang, H.W. Bergmann, Annealing laser-melted ductile iron by pulsed Nd : YAG laser radiation, 196 (1995) 171–176.
- [139] J.J. Rayment, B. Cantor, The as-quenched microstructure and tempering behavior of rapidly solidified tungsten steels, *Metall. Trans. A.* 12 (1981).

- [140] Q.F. Peng, Z.F. Shi, I.M. Hancock, A. Bloyce, Energy beam surface treatment of tool steels and their wear, *Key Eng. Mater.* 46-47 (1990) 229–244.
- [141] G. Zając, J. Pacyna, The kinetics of phase transformations during tempering in structural steels with nickel, *J. Mater. Process. Technol.* 162-163 (2005) 442–446.
- [142] J. Pacyna, A. Jedrzejwska-Strach, M. Strach, The effect of manganese and silicon on the kinetics of phase transformations during tempering - Continuous Heating Transformation (CHT) curves, *J. Mater. Process. Technol.* 64 (1997) 311–318.
- [143] GateMT, GATE Metallurgical Engineering, IISc-Bangalore, IIT-Bombay, IIT-Kanpur IIT- Madras. (n.d.) <http://gatesolution-metallurgicalengineering.blogs>.
- [144] X. Wu, G. Chen, Microstructural characteristics and carbide transformation of laser-cladded Fe-Cr-W-Ni-C coatings during high-temperature tempering, 17 (1998) 1849–1852.
- [145] M. Maalekian, The effects of alloying elements on steels, Technische Universität Graz, Christian Doppler Laboratory for Early Stages of Precipitation, 2007.
- [146] J. Burke, The kinetics of phase transformations in metals, Pergamon Press, 1965.
- [147] S. Khan, A. Ourdjini, Q.S. Hamed, M.A. AlamNajafabadi, R. Elliot, Hardness and mechanical property relationships in directionally solidified aluminium-silicon eutectic alloys with different silicon morphologies, *J. Mater. Sci.* 28 (1993) 5957–5962.
- [148] S. Kawamori, K. Kuroda, Y. Kasuga, M. Yokouchi, H. Fujiwara, K. Ameyama, Effect of alumina content on the mechanical properties of alumina particle dispersion magnesium, *Mater. Trans.* 51 (2010) 1893–1900.
- [149] S.B. Singh, R. Goswami, K. Chattopadhyay, Hardness behavior of ultrafine dispersed materials with soft dispersoids: The case of rapidly solidified Zn-Bi immiscible alloy, *Scr. Metall. Mater.* 28 (1993) 1507–1512.
- [150] Pure Irons: Atlas of Fractographs, Fractography, in: *ASM Handbook*, Vol. 12, ASM International, 1987: pp. 219–224.

- [151] B. Zheng, Y. Lin, Y. Zhou, E.J. Laverna, Gas atomization of amorphous aluminum: part I. thermal behavior calculations, *Metall. Mater. Trans. B.* 40 (2009) 768–778.
- [152] D. Yuan, *The novel impulse atomization process*, University of Alberta, 1997.

Appendix

9. Appendix A

Figure A.1 shows power curve fitted radiant energy at wavelength 2 ($Q(\lambda_2)$) versus droplet diameter of D2 tool steel measured at λ_2 at different heights for the droplets that are fully liquid, including those that are undercooled.

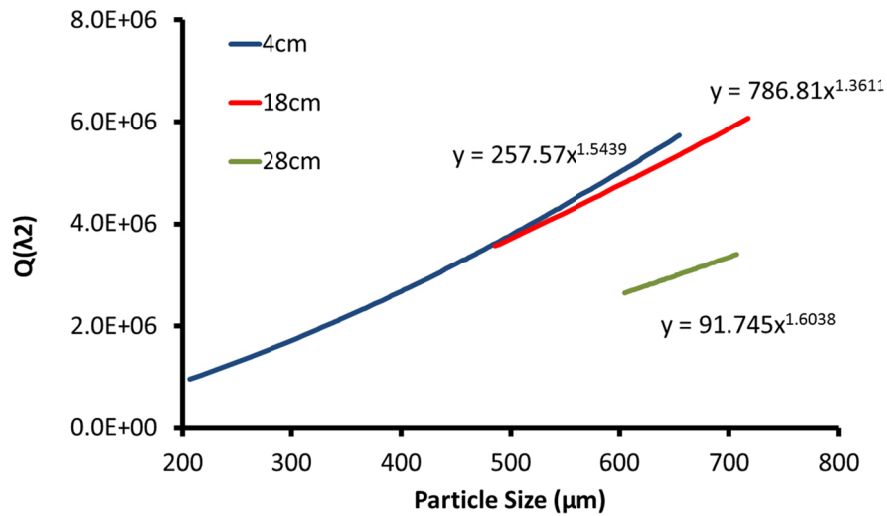


Figure A.1. Power curve fitted radiant energy of $Q(\lambda_2)$ as a function of D2 tool steel droplet diameter for the fully liquid droplets.

Figure A.2 shows power curve fitted radiant energy at wavelength 2 ($Q(\lambda_2)$) versus droplet diameter of copper measured at λ_2 at different heights for the droplets that are fully liquid, without undercooling.

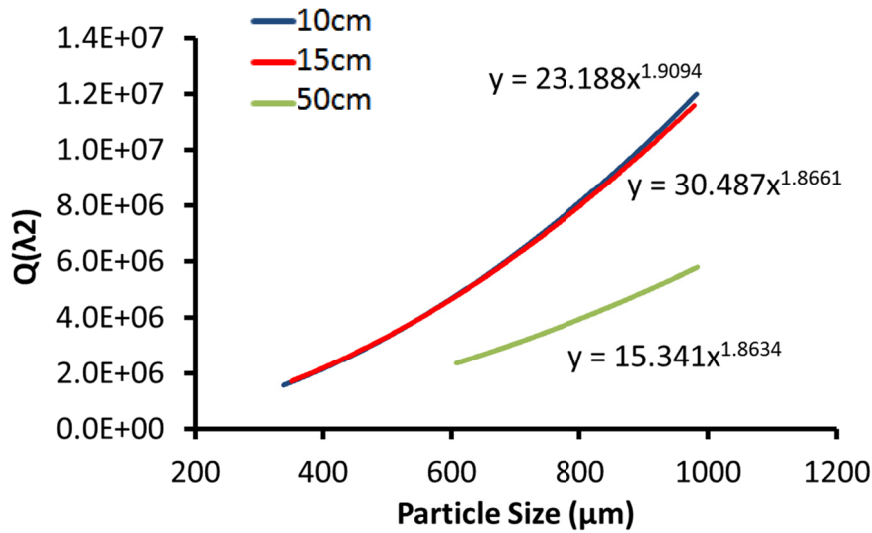


Figure A.2. Power curve fitted radiant energy of $Q(\lambda_2)$ as a function of copper droplet diameter for the fully liquid droplets.

Figure A.3 shows $Q(\lambda_1)/d^2$ versus K_1 values for the D2 tool steel liquid droplets at different heights during free fall. The points for three droplets are joined, 614 μm , 700 μm and 800 μm . The solid lines connect $Q(\lambda_2)/d^2$ values at different heights but for the same droplet size.

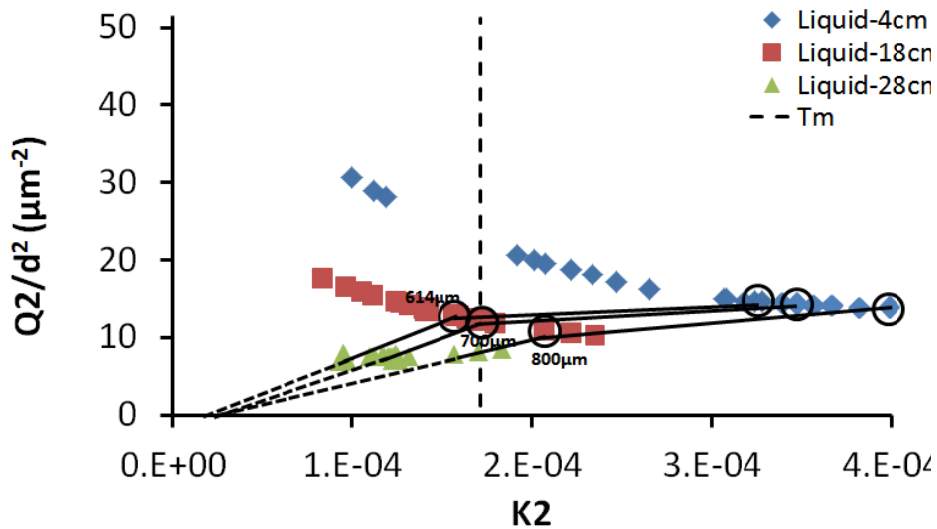


Figure A.3. $Q(\lambda_2)/d^2$ versus K_2 graph at different heights for the D2 tool steel liquid droplets.

Figure A.4 shows $Q(\lambda_2)/d^2$ versus K_2 values for copper liquid droplets at different heights during free fall. The points for three droplets are joined, 616 μm , 772 μm and 983 μm . The solid lines connect $Q(\lambda_2)/d^2$ values at different heights but for the same droplet size.

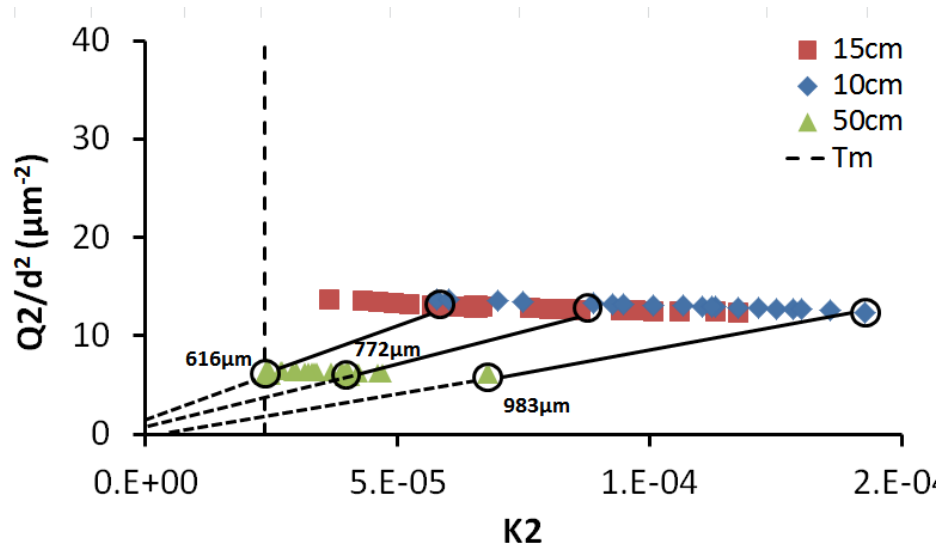


Figure A.4. $Q(\lambda_2)/d^2$ versus K_2 graph at different heights for the copper liquid droplets.

10. Appendix B

In order to calculate A and B values in Eq. 6.4, one needs to know equilibrium concentration of M and C at minimum two temperatures. Therefore, Thermocalc software ver. 5.0.4.75 was used in order to find the equilibrium concentration of different alloying elements in austenite at two temperatures of 650°C and 750°C. First, in order to get information about austenite at these two temperatures, ferrite formation was suppressed by removing ferrite from the list of final phases. As a result, austenite was present at two selected temperatures. Then equilibrium concentration of chromium, carbon and other alloying elements at 650°C and 750°C was calculated using the software, as shown in Table B.1.

Table B.1. Equilibrium concentration of alloying elements in austenite at 650°C and 750°C

Element	Equilibrium concentration in austenite (wt.%)	
	650°C	750°C
Chromium	1.72	2.62
Molybdenum	0.05	0.21
Vanadium	0.01	0.02
Carbon	0.054	0.1

Using values shown in Table B.1, one can calculate values of A and B in Eq. 6.4.